

Electroanalysis of Small Molecule Therapeutics at Nanostructured Electrode Surfaces

A thesis submitted by

Eoghain Murphy B.Sc (Hons)

to the

National University of Ireland, Maynooth

For the degree of Master of Science



**Maynooth
University**

National University
of Ireland Maynooth

Volume 1 of 1

Based on research carried out in the
Department of Chemistry, Faculty of Science and Engineering,
National University of Ireland, Maynooth
under the supervision and direction of

Dr. Eithne Dempsey

Head of Department – Prof. Denise Rooney

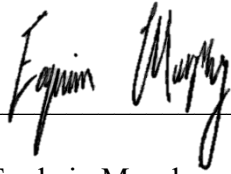
February 2023

Abstract

The outbreak of COVID-19 in Wuhan, China in December 2019, resulted in the evolution of a global pandemic which caused thousands of deaths worldwide. As little was known about this new coronavirus, many existing drugs were repurposed with the goal to effectively treat the infection. Two such candidates were dexamethasone (DEX) and N-acetyl-L-cysteine (NAC). Relatively few articles have been published relating to their electrochemical determination, and in this project the use of metal nanoparticles, microparticles and films alongside various carbon nano-onions (CNOs) were explored as chemical modifiers in order to maximize their electrochemical responses. Bare, copper microparticle (CuMPs) and copper film (CuF) modified glassy carbon electrodes were exploited in Chapter 2 to examine the DEX electroreduction response, resulting in sensitivities of $2.00 \times 10^2 \mu\text{A cm}^{-2} \text{mM}^{-1}$ and $1.13 \times 10^2 \mu\text{A cm}^{-2} \text{mM}^{-1}$ for the CuF and CuMP modified GCEs respectively. Pharmaceutical samples in the form of a cream and a solid-state dose, were analysed with recoveries 77.46 – 87.91 %, with 1.93 – 4.97 % variance. Various types of CNOs were electrochemically characterised of which, oxi-BN-doped-CNOs was selected and combined with gold nanoparticles (AuNPs), resulting in an AuNP/oxi-BN-doped CNO/GCE for NAC quantitation (sensitivity $476 \mu\text{Q cm}^{-2} \text{mM}^{-1}$ in acetate buffer). Following design and optimisation, a solid dose form of NAC was quantitatively analysed, resulting in 89 – 105 % \pm 6.75 % recovery, thus validating the sensors.

Declaration

This is to certify that the material presented within this thesis has not been submitted previously for a Degree to this or any other University. All material presented herein, except where acknowledged and cited appropriately, is the work of the author.



Eoghain Murphy

National University of Ireland, Maynooth

2022

Acknowledgments

I would like to thank my supervisor, Dr. Eithne Dempsey, for the support and guidance that she gave me throughout my Research Master's degree, as she encouraged and motivated me to challenge my curiosity and to branch out and broaden my horizons. I would also like to thank and acknowledge my parents, Ruth and Mick, Clara Evans and Dr. Saurav Kumar Guin for their help and support in my endeavour.

Chapter 1: Introduction and Literature Review

Figure 1. Structure of the SARS-CoV-2 virus²².20

Figure 2. (A) Schematic of the primary structure of the SARS-CoV-2 spike protein, where the single sequence (SS), N-terminal domain (NTD), the receptor binding domain (RBD), subdomain 1 (SD1), subdomain 2 (SD2), the S1/S2 protease cleavage site, S2' protease cleavage site, the fusion peptide (FP), heptad repeat 1 (HR1), central helix (CH), connector domain (CD), heptad repeat 2 (HR2), the transmembrane domain TM and the cytoplasmic tail (CT) are indicated. (B) Cryo-EM structures of the spike protein in the closed state (left) and open state (right)³⁰.21

Figure 3. Chemical structures of various types of carbon nanomaterials¹⁰⁶.33

Figure 4. p-CNO and BN-doped-CNO synthesis through the thermal annealing of detonation nanodiamonds, with acid treatment in 3 M nitric acid yielding , oxi-CNOs and oxi-BN-doped-CNOs.....35

Figure 5. HR-TEM image of carbon nano-onions (left) with their structure (right) shown¹²⁵.35

Figure 6. Schematic of two-electrode (left) and three-electrode (right) systems that can be used in electrochemical sensors, indicating the positions of the working electrode (WE), auxiliary (counter) electrode (CE) and reference electrode (RE)...40

Figure 7. Plots of (A) time vs potential for cycle 1 – 3 (red, purple, and blue arrows) and (B) potential vs current density of the third cycle of the cyclic voltammogram of 5 mM [Fe(CN)₆]^{3/4+} in 0.1 M KCl at the bare GCE from -0.2 – 0.6 V vs Ag/AgCl at 100 mV s⁻¹.44

Chapter 2: Electrochemical Determination of Dexamethasone at Unmodified and Copper Modified Glassy Carbon Electrodes

Figure 1. Voltammetry of a deaerated solution of 1 mM DEX in 0.1 M LiClO₄ in MeOH (black) vs the electrolyte background (red) at a bare GCE from -1.8 V to 1.5 V at 100 mV s⁻¹. A clear oxidation peak can be seen at 1.3 V (I) with weak reduction at -1.3 V (II) vs. Ag/Ag⁺.74

Figure 2(A) Overlaid voltammograms of 1 mM dexamethasone in 0.1 M LiClO₄ in methanol at the bare GCE, from -1.8 V to 1.8 V at scan rate 10-200 mV s⁻¹. **(B)** Graph showing the square root of scan rate vs current density for the oxidation peak of 1 mM dexamethasone in (A). **(C)** Graph showing log *J* vs log *n* resulting in a linear plot with slope 0.567, confirming the process was diffusion controlled.75 – 76

Figure 3 (A) Voltammetry of DEX (0.45 -3.07 mM) in 0.1 M LiClO₄ / MeOH with the background electrolyte (black) (degassed by bubbling with N₂) at a bare GCE from -1.8 V to 1.5 V at 100 mV s⁻¹. **(B)** Calibration curve showing linear relationship between dexamethasone concentration and anodic current density with sensitivity 5.42 x 10² μA cm⁻² mM⁻¹ over the range examined.....77

Figure 4 (A) Voltammetry of 1 mM dexamethasone (red) in 0.1 M sodium acetate buffer pH 4.45 (black) at 100 mVs⁻¹. **(B)** Voltammetry of 1 mM DEX in 0.1 M NaOH (red) supporting electrolyte (black) at 100 mV s⁻¹.79

Figure 5 (A) Overlaid voltammograms' for degassed 1 mM dexamethasone in 0.1 M NaOH (pH 13.0) from -0.05 V to 1.8 V over scan rates 10 – 200 mV s⁻¹. **(B)** Graph showing the scan rate vs current density for the reduction of 1 mM dexamethasone with dependence up to 50 mV s⁻¹. **(C)** Graph showing the square root of scan rate vs current density for the reduction of 1 mM dexamethasone.....80 – 81

Figure 6 (A) Calibration of DEX at GCE in 0.1 M NaOH pH 13 (deaerated), over the range 0.0781 – 5.0 mM DEX with potential range 0.05 – -1.8 V at 100 mV s⁻¹. **(B)** Corresponding calibration curve resulting in a sensitivity of 2.76 × 10⁻⁵ A mM⁻¹ (n=3).....81 – 82

Figure 7 (A) Voltammetry of 10 mM Cu(Ac)₂ in 0.1 sodium acetate buffer (pH 4.5, deaerated) at the bare GCE from -1.2 V to 0.7 V at 20 mV s⁻¹. **(B)** Chronoamperometry trace of 10 mM Cu(Ac₂) from -0.06 V to -0.47 V with current-time display to be used for the selection of the nucleation and growth pulses for Cu particle deposition in Methods I and II.....84

Figure 8 (A) Potential-time input signal where the reduction potential was varied from -0.08 V to -0.55 V over the timescale 100 to 5 s with schematic showing the growth of the CuNPs through radial diffusion **(B)** Chronoamperometry of 10 mM Cu(Ac)₂ where the electrode was initially pre-treated, followed by the application of the growth pulse. **(C)** Voltammetry of the Cu modified GCE in 0.1 M NaOH from -0.9 – 0.05 V at 100 mV s⁻¹.....85 – 86

Figure 9 (A) Voltammetry of the Cu film in 0.1 M NaOH from -1.0 – 0.05 V from 10 – 200 mV s⁻¹ (first (dashed) and last (red) curves shown). **(B)** Graph of current density vs scan rate for each peak I – IV (black, blue, red, green respectively), from which the surface coverage was calculated to lie within the range $\Gamma = 1.480 - 3.492 \times 10^{-9}$ mol cm⁻². **(C)** DEX (1 mM) response for E₁ and E₂ pulse conditions outlined in **Table 2**.....87 – 88

Figure 10 (A) Optimised three step electrodeposition of copper nanoparticles (CuNPs) (E₁ = 0.7 V for 5 s, E₂ = -0.47 V for 5 ms and E₃ = -0.265 for 50 s) **(B)** Schematic illustrating CuMP electrodeposition onto a GCE surface via the triple pulse potentiostatic method (Method II). **(C)** Overlaid Voltammetry of the CuMPs formed from Method II (black curve) vs those formed from Method I (red curve) in 0.1 M NaOH from 0.05 V to -1.8 V at 100 mV s⁻¹, where peaks I – IV are associated with copper electrochemistry. **(D)** Scan rate study *J* vs *n* plots for the copper processes I – IV (black, blue, red, green respectively), using Method II.....90 – 91

Figure 11. Bar chart monitoring the DEX cathodic response at the bare and each CuMP modified GCE.....93

Figure 12. (A) Nyquist plots of the bare (black), Cu particles realised using Method I modified (red) and CuMPs formed using Method II (purple) GCEs in 0.1 M NaOH, with $E_{app} = -0.177$ V and *frequency range* 0.01 – 100,000 Hz at an amplitude of 5 mV (average of $n=2$). (B) Voltammetry of $[Fe(CN)_6]^{3/4-}$ in 0.1 M NaOH at the bare (blue), Cu particle (Method I – dual pulse method) (red) modified and Cu particle (Method II –triple pulse method) (purple) modified GCEs from -0.2 – 0.6 V at 100 mV sec⁻¹. (C) EIS of the bare GCE (black), Cu particle modified GCE (Method I) (red) and the Cu particle modified GCE (Method II) (blue) in 5 mM $[Fe(CN)_6]^{3/4-}$ in 0.1 M NaOH with n from 0.01 – 100,000 Hz with an amplitude of 5 mV. $E = 0.202$ V, 0.217 V and 0.228 V for the bare GCE, Cu particles Method I and Cu particles Method II, respectively, with (D) a zoomed in view of the hemispherical regions of the CuF/GCE and CuMP/GCE. Bode plots of (E) the gain and (F) the negative phase angle vs log₁₀ of the frequency.....96 – 98

Figure 13. SEM image of the (A) Cu deposition at GCE (dual pulse potentiostatic electrodeposition) with EDS (B) Cu nanoclusters at GCE (triple pulse potentiostatic electrodeposition) with EDS providing confirmation of copper.....100 – 102

Figure 14. Particle size distribution of the CuMP modified GCE.....104

Figure 15. (A) Voltammetry of 1 mM dexamethasone at the bare (black) and Method I Cu particle (red) GCEs from -1.8 V to 0.05 V at 100 mV s⁻¹. (B) Voltammetry of 1 mM DEX (red) in 0.1 M NaOH (black) at the Cu particle modified GCE from -1.8 – 0.05 V at 100 mV sec⁻¹.....106

Figure 16 (A) Voltammetry of 1 mM DEX at the CuF modified GCE from -1.7 – 0.05 V at 20 – 150 mV s⁻¹ (20 and 150 mV s⁻¹ shown as the black line and red dashed line respectively. Plots of the (B) peak current vs v , (C) peak current vs $v^{1/2}$ and (D) peak potential vs v , where the signal V cathodic response was shown in black and the signal VI cathodic response was shown in red.....107 – 108

Figure 17 (A) CV of increasing dexamethasone 0.0781 – 5 mM in 0.1 M NaOH at the Method I modified GCE over the range 1.5 to -1.8 V in the reverse direction monitoring peak V. (B) Corresponding plot of peak potential at -1.6 – -1.4 V vs concentration confirming the cathodic shift in the forward direction monitoring peak V with DEX additions. (C) CV of increasing dexamethasone 0.0781 – 5 mM in 0.1 M NaOH at the copper modified GCE over the range 1.5 to -1.8 V with (D) Corresponding dexamethasone calibration curve with resulting sensitivities of $2.00 \times 10^2 \mu A cm^{-2} mM^{-1}$ peak V (red) and $1.13 \times 10^2 \mu A cm^{-2} mM^{-1}$ for the CuF/GCE and CuMP/GCE respectively (calibration at the bare GCE shown in orange with sensitivity $2.76 \times 10^1 \mu A cm^{-2} mM^{-1}$). ($n = 3$).....109 – 110

Figure 18 (A) Voltammetry of dexamethasone extracted from 1.0 g of 3 cream samples (0.0 % (black), 0.25 % (red), 0.35 % (purple) and 0.5 % (blue) w/w dexamethasone) in 0.1 M LiClO₄ in MeOH zoomed in on the anodic response. (B) Voltammetry of DEX extracted from the tablet samples containing 6 (orange), 10 (grey) and 15 (yellow) mg DEX (return sweep only shown).....112

Chapter 3: Electrochemical Characterisation of Carbon Nano-Onions and their Decoration with Gold Nanoparticles for the Electrochemical Determination of N-Acetyl-L-Cysteine

Figure 1. Schematic of the AuNP electrodeposition process with respect to pulse potential vs time.....129

Figure 2. Voltammetry of 1 mM NAC (red curve) in 0.1 M sodium acetate buffer (pH 4.45) at the bare GCE (A) and bare AuE (B) from 0.0 – 1.5 V at 100 mV s⁻¹. Black curve represents background electrolyte voltammetry in each case.....131 – 132

Figure 3. Voltammetry of 1 mM NAC in 0.1 M phosphate buffer (pH 7.15) at the bare GCE (A) and bare AuE (B) from 0.0 – 1.5 V at 100 mV s⁻¹.....132 – 133

Figure 4. Voltammetry of 1 mM NAC in 0.1 M carbonate buffer (pH 10.35) at the bare GCE (A) and bare AuE (B) from 0.0 – 1.5 V at 100 mV s⁻¹.....133 – 134

Figure 5 (A) Voltammetry of 1 mM NAC in 0.1 M sodium acetate buffer (pH 4.45) at the bare GCE from 20 – 200 mV s⁻¹ over the range 0 – 1.7 V vs Ag/AgCl (20 mV s⁻¹ and 200 mV s⁻¹ shown in red and black, respectively).....135

Figure 6 (A) Voltammetry of 1 mM NAC in 0.1 M sodium acetate buffer (pH 4.45) at the bare AuE from 10 – 200 mV s⁻¹ over 0 – 1.7 V vs Ag/AgCl. **(B)** Corresponding plot of the scan rate vs current density of the NAC oxidative response from 40 – 200 mV s⁻¹.....136

Figure 7. Voltammetry of 1 mM HAuCl₄ in 0.1 M HCl at the bare GCE from -0.4 – 1.5 V at 100 mV s⁻¹, with the electrodeposition pulse potentials indicated (red arrows).....138

Figure 8 (A) Chronoamperometry of 1 mM HAuCl₄ at the bare GCE for E_i = 0.8 V, E_c = -0.13 V, t_c = 0.01 s **(B)** Schematic of illustrating linear vs hemispherical diffusion of Au³⁺ ions towards an unmodified GCE surface, a microelectrode surface and nanoparticle modified GCE surface **(C)** Schematic illustrating the hemispherical diffusion of Au³⁺, ions to the GCE surface via hemispherical diffusion zones around seeded Au nuclei.....138 – 139

Figure 9 (A) Chronoamperometry of 1 mM HAuCl₄ at the bare GCE for 3 consecutive cycles where E_i = 0.8 V, E_a = 0.92 V, E_c = -0.13 V, t_c = t_a = 0.01 s. **(B)** Magnified image of the first cathodic transient of the first cycle. **(C)** Chronoamperometry of 1 mM HAuCl₄ at the bare GCE for 3 consecutive cycles where E_i = 0.8 V, E_a = 0.92 V, E_c = 0.55 V, t_c = t_a = 2 s. **(D)** Magnified image of the first cathodic transient of the first step.....140 – 141

Figure 10 (A) Bar chart monitoring the NAC oxidative response at the bare GCE, AuE and each AuNP/GCE for conditions 1-8 as per **Table 1** The optimum AuNP electrodeposition parameters were P₁ = -0.13 V for 60 ms, P₂ = 0.92 V for 5 ms, P_m = 0.55 V for 1 s and P_n = 0.92 V for 2.5 ms. **(B)** Voltammetry of 1 mM NAC (red) in 0.1 M H₂SO₄ (black) at the optimum AuNP/GCE from 0.4 – 1.5 V at 100 mV s⁻¹...144

Figure 11 (A) Voltammetry of the AuNP/GCE from 0.4 – 1.5 V in 0.1 M H₂SO₄ from 10 – 200 mV s⁻¹. **(B)** Plot of the scan rate vs current density of the AuNP/GCE.....146

- Figure 12** (A) Voltammetry of 5 mM $[\text{Fe}(\text{CN})_6]^{3/4-}$ in 0.1 M NaOH at the bare GCE (black) and AuNP/GCE (red) from -0.2 – 0.6 V at 100 mV s^{-1} . (B) Nyquist plot of the bare GCE (black) and the AuNP/GCE (red) in 5 mM $[\text{Fe}(\text{CN})_6]^{3/4-}$ in 0.1 M NaOH with n from 0.01 – 100,000 Hz with an amplitude of 5 mV. Simulated EIS data is shown by the dashed line. $E = 0.221$ V and 0.207 V for the bare and AuNP/GCEs, respectively. (C) Zoomed in image of the Nyquist plot highlighting the arc from the AuNP modified GCE with overlaid solid line representing simulation (Randles circuit data).....147 – 148
- Figure 13.** Corresponding experimental (solid lines) and simulated (dashed lines) Bode plots of the AuNP/GCE (red) and bare GCE (black) in 5 mM $[\text{Fe}(\text{CN})_6]^{3/4-}$ in 0.1 M NaOH with n from 0.01 – 100,000 Hz with an amplitude of 5 mV, where (A) shows the log of the frequency vs gain, and (B) shows the log of the frequency versus the phase angle.....150
- Figure 14.** HR-SEM images of the electrodeposited AuNPs at the GCE surface at (A) 5,000 \times (B) 10,000 \times (C) 25,000 \times (D) 50,000 \times magnifications with the corresponding EDS (E) spectrum and (F) layered image.....152 – 153
- Figure 15.** AuNP particle size distribution where particles between 300 – 319 nm accounted for 33 % of all particles followed by 320 – 339 nm (16.6 %) and 280 – 299 nm (7 %)......154
- Figure 16.** Voltammetry of 0.1 M KCl at the bare GCE (black) and at the (A) p-CNO, (B) BN-doped CNO, (C) oxi-CNO and (D) oxi-BN-doped CNO modified GCE with a 0.1416 mg cm^{-2} surface loading (all CNO modified GCEs are shown as the red line) from -1.0 V to 1.0 V at 100 mV s^{-1}155
- Figure 17.** CV overlay of 0.1M KCl at the (A) p-CNO, (B) BN-doped CNO, (C) oxi-CNO and (D) oxi-BN-doped CNO modified GCE from -1.0V to 1.0V, vs Ag/AgCl over scan 10 – 100 mV sec^{-1}157
- Figure 18** (A) Current density vs scan rate plots for the p-CNO (blue), BN-doped CNO (orange), oxi-CNO (green) and oxi-BN-doped CNO (red) modified GCEs (current measured at 0.5 V vs. Ag/AgCl), over a potential range of -1.0 – 1.0 V vs. Ag/AgCl from 10 – 200 mV s^{-1} in 0.1 M KCl resulting in 5.28×10^{-4} F cm^{-2} . Specific capacitance measured as a function of scan rate with maximum at 10 mV s^{-1} for the (B) p-CNOs, (C) BN-doped-CNOs, (D) oxi-CNOs and (E) oxi-BN-doped CNOs.....159
- Figure 19.** Cyclic Voltammetry at the (A) bare GCE, (B) p-CNO, (C) BN-doped CNO, (D) oxi-CNO and (E) oxi-BN-doped CNO modified GCEs relative to the background in 1 mM $[\text{Fe}(\text{CN})_6]^{3/4-}$ (red curves) in 0.1 M KCl at 100 mV s^{-1} (black curves).....161 – 162
- Figure 20.** Cyclic Voltammetry at the (A) bare GCE, (B) p-CNO, (C) BN-doped CNO, (D) oxi-CNO and (E) oxi-BN-doped CNO modified GCEs (red curves) relative to the background (black curve) in presence of 1 mM $[\text{Ru}(\text{NH}_3)_6]^{2+}$ in 0.1 M KCl at 100 mV s^{-1}163 – 164
- Figure 21.** Chronoamperometry and corresponding Cottrell plots of the (A – B) p-CNO, (C – D) BN-doped CNO, (E – F) oxi-CNO and (G – H) oxi-BN-doped CNO/GCEs.....166 – 167
- Figure 22.** Voltammetry of 1 mM NAC (red) and 10 mM NAC (purple) in 0.1 M H_2SO_4 (black) at the bare (A) GCE, (B) bare AuE and GCEs modified with 10 μL of

(C) 1 mg mL⁻¹, (D) 0.1 mg mL⁻¹, (E) 0.05 mg mL⁻¹ and (F) 0.02 mg mL⁻¹ oxi-BN-doped CNOs from 0 – 1.4 V at 100 mV s⁻¹.....169 – 171

Figure 23. Bar charts showing the oxidative response of (A) 1 mM and (B) 10 mM NAC at the bare GCE, bare PtE, bare AuE and GCEs modified with 10 μL of 1 mg mL⁻¹, 0.1 mg mL⁻¹, 0.05 mg mL⁻¹ and 0.02 mg mL⁻¹ oxi-BN-doped CNOs. The NAC response was recorded between 1.36 – 1.45 V at the bare and each oxi-BN-doped CNO modified GCE while the NAC peak was measured at 1.12 and 1.11 V for the bare PtE and bare AuE respectively.....172

Figure 24. Voltammetry of 1 mM NAC (red) and 10 mM NAC (purple) in 0.1 M H₂SO₄ (black) GCEs modified with 10 μL of (A) 1 mg mL⁻¹, (B) 0.1 mg mL⁻¹, (C) 0.05 mg mL⁻¹ and (D) 0.02 mg mL⁻¹ oxi-BN-doped CNOs and the optimised AuNPs from 0 – 1.5 V at 100 mV s⁻¹.....174 – 175

Figure 25. Bar charts showing the oxidative response of (A) 1 mM and (B) 10 mM NAC at the bare GCE, bare AuE and AuNP@ 10 μL of 1 mg mL⁻¹, 0.1 mg mL⁻¹, 0.05 mg mL⁻¹ and 0.02 mg mL⁻¹ oxi-BN-doped CNO/ GCEs.....176

Figure 26 (A) Voltammetry of the AuNP@oxi-BN-doped CNO/GCE in 0.1 M H₂SO₄ from 0.4 – 1.5 V from 10 – 200 mV s⁻¹. **(B)** Plot of scan rate vs current density monitoring the anodic and cathodic faradaic Au responses of the AuNP@oxi-BN-doped CNO/GCE.....178

Figure 27 (A) Voltammetry of 5 mM [Fe(CN)₆]^{3/4-} in 0.1 M NaOH at the bare (black) and AuNP@oxi-BN-doped CNO/GCE (purple) from -0.2 – 0.6 V at 100 mV s⁻¹. **(B)** Nyquist plot of the bare GCE (black) and the AuNP@oxi-BN-doped CNO/GCE (red) in 5 mM [Fe(CN)₆]^{3/4-} in 0.1 M NaOH with n from 0.01 – 100,000 Hz with an amplitude of 5 mV. Simulated EIS data is shown by the dashed line. E = 0.221 V and 0.209 V for the bare and AuNP@oxi-BN-doped CNO/GCEs, respectively. **(C)** Zoomed in image of the Nyquist plot highlighting the arc from the AuNP@oxi-BN-doped CNO/GCE.....179 – 180

Figure 28. Corresponding experimental (solid lines) and simulated (dashed lines) Bode plots of the AuNP@oxi-BN-doped CNO/GCE (purple) and bare GCE (black) in 5 mM [Fe(CN)₆]^{3/4-} in 0.1 M NaOH with n from 0.01 – 100,000 Hz with an amplitude of 5 mV, where (A) shows the log of the frequency vs gain and (B) shows the log of the frequency vs the phase angle.....181

Figure 29. HR-SEM images of the AuNP@oxi-BN-CNO/GCE at 5,000 × (A), 10,000 × (B), 25,000 × (C) and 50,000 × (D) magnifications.....183

Figure 30. Voltammetry of 1 mM NAC (red) in 0.1 M H₂SO₄ (black) at the AuNP@oxi-BN-doped CNO/GCE from 0 – 1.5 V at 100 mV s⁻¹.....184

Figure 31 (A) Voltammetry of 1 mM NAC in 0.1 M H₂SO₄ at the AuNP@oxi-BN-doped CNO/GCE from 0.4 – 1.5 V at 100 mV s⁻¹. **(B)** Plot of the scan rate vs current density. **(C)** plot of the scan rate vs peak potential.....185 – 186

Figure 32 (A) Voltammetry of 1 mM NAC in 0.1 M H₂SO₄ at the AuNP@oxi-BN-doped CNO/GCE from 0.4 – 1.5 V at 100 mV s⁻¹ for 15 cycles, cycles 1 and 15 shown in black and red respectively. **(B)** Plot monitoring the NAC response over 15 cycles.....187

Figure 33 (A) Coulometry of 0.199 – 2.53 mM NAC in 0.1 M H₂SO₄ at the AuNP@oxi-BN-doped CNO/ GCE **(B)** Corresponding calibrations of 0.199 – 2.53 mM NAC in 0.1 M H₂SO₄ at the oxi-BN-doped CNO (black) AuNP@oxi-BN-doped CNO (red) modified GCE and bare AuE (purple) with E = 1.15 V for 5 s. (n = 3)....189

Figure 34 (A) Coulometry of 0.199 – 2.53 mM NAC in 0.1 M sodium acetate buffer (pH 4.45) at the AuNP@oxi-BN-doped CNO/GCE **(B)** Corresponding calibrations of 0.199 – 2.53 mM NAC in 0.1 M acetate buffer (pH 4.45) at the oxi-BN-doped CNO (black) and the AuNP@oxi-BN-doped CNO (red) modified GCE with E = 1.15 V for 5 s. (n = 3).....190

Figure 35 (A) Coulometry of an NAC sample (blue) with 5 subsequent additions of a 0.1 M NAC standard in 0.1 M sodium acetate buffer (pH 4.45) at the AuNP@oxi-BN-doped CNO/GCE **(B)** Corresponding plot showing the NAC concentration series, where the sample concentration was observed where y = 0.....192

Chapter 1: Introduction and Literature Review

N/A

Chapter 2: Electrochemical Determination of Dexamethasone at Unmodified and Copper Modified Glassy Carbon Electrodes

Table 1. Assignment of redox processes and surface coverage for copper electrochemistry.....88

Table 2. Method I dual pulse optimisation of copper deposition conditions with corresponding effect on DEX (1 mM) response for peak at -1.34 V (see **Figure 8 (C)**).....89

Table 3. Various CuNP electrodeposition parameters which were screened with 1.0 mM dexamethasone to identify the optimum method. The parameters that were changed are highlighted in red.....92

Table 4. Showing the $\Delta E_p(V)$, $E_{1/2}(V)$ and $J_{p(a)}/J_{p(c)}$ of the bare GCE, CuF/GCE and CuMP/GCE.....95

Table 5. Impedance data showing the R_s , R_{CT} , C_{dl} and Gain Margins (where applicable) for the bare, CuF/GCE and CuMP/GCE.....99

Table 6. Comparison of copper electrodeposited electrode response for Method I and II relative to the bare GCE response.....111

Table 7 (A) Theoretical dexamethasone concentration extracted from 1.0 g of commercial hydrocortisone cream and reconstituted into 10 mL MeOH, the average sample concentrations measured and % recovery (n=3) **(B)** Displaying the theoretical concentration and signal, the average E_p and I_p values, variance, standard deviation, recovery, and percentage recovery for tablets containing 2 – 15 mg DEX.....114

Chapter 3: Electrochemical Characterisation of Carbon Nano-Onions and their Decoration with Gold Nanoparticles for the Electrochemical Determination of N-Acetyl-L-Cysteine

Table 1. Electrodeposition parameters used for the optimisation of the gold nanoparticle deposition for NAC quantitation.....143

Table 2. Summary of the optimised AuNP electrodeposition process.....145

Table 3. Comparison of the peak heights and potentials of 5 mM $[\text{Fe}(\text{CN})_6]^{3/4-}$ at the bare and AuNP/GCEs.....150

Table 4. Comparison of the R_s , R_{ct} , capacitances, Gain Margins and Phase Margins obtained from the EIS spectra for both simulated and experimental data obtained at the bare and AuNP/GCE.....	151
Table 5. Comparison of capacitances, electroactive surface areas and surface coverages for each of the CNOs, with the oxi-CNOs having the highest capacitance, greatest electroactive surface area and surface coverage calculated for the faradaic waves associated with oxi- functional groups.....	160
Table 6. Comparison of the oxidation and reduction peak heights and potentials, ΔE_p 's, $E_{p1/2}$'s and J_p ratios of 1 mM $[\text{Fe}(\text{CN})_6]^{3/4-}$ at the bare and each of the CNO/GCEs.....	164
Table 7. Comparison of the oxidation and reduction peak heights and potentials, ΔE_p , $E_{p1/2}$ and J_p ratios of 1 mM $[\text{Ru}(\text{NH}_3)_6]^{2+}$ the bare and each of the CNO/GCEs. The bare GCE showed the largest peak oxidation value, whereas the oxi-BN-doped CNO/GCE gave the highest reduction signal. The oxi-CNO and oxi-BN-doped CNO/GCEs showed the largest peak separation.....	164
Table 8. Comparison of the peak heights and potentials of 5 mM $[\text{Fe}(\text{CN})_6]^{3/4-}$ at the bare and AuNP@oxi-BN-doped CNO/GCEs.....	182
Table 9. Comparison of the R_s , R_{ct} and capacitances obtained from the EIS spectra for both simulated and experimental data obtained at the bare and AuNP@oxi-BN-doped CNO/GCE.....	182
Table 10. Comparison of the sensitivities, LOD's and LOQ's of the oxi-BN-doped CNO modified GCE and the AuNP@oxi-BN-doped CNO/GCE in 0.1 M sodium acetate buffer (pH 4.45).....	191
Table 11. NAC sample analysis showing the expected NAC concentration, the NAC recovered and the % recovery of samples 1 – 5.....	193

Chapter 1: Introduction and Literature Review

Structure 1. Chemical structure of dexamethasone (DEX).....	26
Structure 2. Chemical structure of N-acetyl-L-cysteine (NAC).....	28
Structure 3. Chemical structure of glutathione (GSH), showing the position of it's amino acid components.....	29

Chapter 2: Electrochemical Determination of Dexamethasone at Unmodified and Copper Modified Glassy Carbon Electrodes

Scheme 1. Depicting the electrooxidation of DEX occurring at the C11 alcohol group, resulting in the formation of a ketone group at this position.....	74
Scheme 2. Depicting the electroreduction of DEX at the C20 ketone group, resulting in the formation of an alcohol group.....	79
Scheme 3. Depicting the two step DEX reduction process observed at the Cu modified GCEs, where in the first step, DEX undergoes electroreduction at the C20 ketone, producing an alcohol group. In the second reduction step, the C3 keytone group is reduced, resulting in a dimerization of two adjacent DEX molecules.....	104
Scheme 4. Depicting possible surface interactions between DEX and the Cu nanostructure modified GCEs at C20.....	105

Chapter 3: Electrochemical Characterisation of Carbon Nano-Onions and their Decoration with Gold Nanoparticles for the Electrochemical Determination of N-Acetyl-L-Cysteine

Scheme 1 Electrooxidation of N-acetyl-L-cysteine to disulfide N,N'diacetylcystine.....	124
-----------------------------------------------------------------------------------------------	-----

Chapter 1: Introduction and Literature Review

Table of Contents

1.1.0.	Introduction	18
1.2.0.	COVID-19	19
1.2.1.	Mechanism and Transmission	20
1.2.2.	Symptoms and Long-Term Effects	23
1.2.3.	Therapeutic Agents Effective in COVID-19 Treatment	24
1.3.0.	Dexamethasone	25
1.3.1.	Dexamethasone Treatment in COVID-19 Patients	26
1.3.2.	Dexamethasone Mechanism of Action	27
1.3.3.	Dexamethasone quantitation	28
1.4.0.	N-acetyl-L-cysteine	28
1.4.1.	N-acetyl-L-cysteine Treatment in COVID-19 Patients.....	29
1.4.2.	N-acetyl-L-cysteine Mechanism of Action	30
1.4.3.	N-acetyl-L-cysteine Quantitation	31
1.5.0.	Nanomaterials of Interest	31
1.5.1.	Carbon nanomaterials.....	32
1.5.2.	Carbon Nano-onions	33
1.5.3.	Metal Nanostructures	35
1.5.4.	Metal Nanoparticles, Microparticles and Films	36
1.5.5.	Metal Nanostructure Formation	37
1.6.0.	Electrochemical sensors	39
1.6.1.	Categories of Electrochemical Sensors	40
1.6.2.	Electrochemical and Analytical Techniques Applied	41
1.6.2.1.	Cyclic Voltammetry.....	42
1.6.2.2.	Chronoamperometry and Chronocoulometry	44
1.6.2.3.	Electrochemical Impedance Spectroscopy	46

1.6.2.4.	Scanning Electron Microscopy	47
1.7.0.	References	50

1.0. Introduction

Electrochemistry refers to the study of chemical processes that cause electrons to move, resulting in the oxidation (loss of electrons) or reduction (gain of electrons) of an atom or molecule in question, resulting in the change of the oxidation state¹. Electrochemistry is a broad and widely applicable branch of chemistry, with a wide array of applications such as in battery and capacitor development², fuel cells³ and sensor design⁴. This project will focus on the latter with sensors designed to quantitatively analyse two therapeutic agents, dexamethasone (DEX) and N-acetyl-L-cysteine (NAC), which have shown to be effective in the treatment of COVID-19⁵⁻⁷.

Firstly, electrochemical sensors account for the largest group of sensors, representing approximately 55% in total. Other types of sensors include optical (24%), mass (12%) and thermal (6%) sensors. Electrochemical sensors can be applied in both aqueous and non-aqueous systems, where they are categorised based on their transducer type. Electrochemical sensors can thus be categorised accordingly: potentiometric, amperometric and impedimetric electrochemical sensors⁴, which will be discussed in section 6.1.

Electrochemical sensors have been used in a wide array of applications. The enzymatic glucose sensor is an example of a well-known biosensor used for the determination of glucose levels in blood in diabetic patients^{8, 9}. Electrochemical sensors are also applicable to the environment, where various sensors have been developed to detect chemicals and ions, such as pesticides¹⁰, trace levels of lead¹¹ and uranium¹² in contaminated water samples, while others have been used to evaluate and analyse drugs in pharmaceutical formulations¹³⁻¹⁵. With consideration for the applications of the various electrochemical sensors mentioned, the overarching goal of this project was to identify small molecule therapeutics relevant to the treatment of COVID-19 and develop electrochemical sensors specific for each drug with high sensitivities with the goal to accurately quantify each drug extracted from pharmaceutical samples.

1.2.0. COVID-19

In December 2019, an outbreak of an unknown form of pneumonia was reported in Wuhan, Hubei Province, China. These cases were linked to the Huanan Seafood Wholesale Market. This new disease was identified through inoculation of respiratory samples into human respiratory epithelial cells, where it was isolated and shown to be a novel form of coronavirus related to SARS-CoV, and thus this new virus was named severe acute respiratory syndrome coronavirus 2 (SARS-CoV-2), a form of betacoronavirus under the subgenus Sarbecovirus. The rapid global spread of this coronavirus caused coronavirus disease (COVID-19) and led to thousands of deaths worldwide, and thus on 12th March 2020, the World Health Organization (WHO) declared a global pandemic¹⁶.

At the beginning of the COVID-19 pandemic, very little was known about the SARS-CoV-2 however clear observations were made relating to how quickly the virus spread from person to person and on the range of symptoms relating to the virus ranged from mild to severe. To combat this, various strategies were implemented to avoid the spread of COVID-19. Measures taken involved handwashing, physical distancing of 2 meters, the avoidance of mass gatherings and wearing facemasks. Lockdown and stay at home strategies were also implemented to help flatten the transmission curve, which involved the closure of schools, offices, and retail, where deemed “non-essential”. Teaching and office work resumed shortly after the implementation of lockdowns, where classes and work were carried out remotely. Retail involving the wholesale sale of food, beverages and newspapers in non-specialised and specialised stores, consumer products necessary to maintain the safety and sanitation, pharmacies and chemists, fuel stations and heating fuel providers, the sale of essential items for the health and welfare of animals, including animal feed and medicines, animal food, pet food and animal supplies including bedding laundries and drycleaners, banks, post offices and credit unions, and the retail of safety supply stores were all deemed essential and could remain open¹⁷⁻¹⁹.

1.2.1. Mechanism and Transmission

SARS-CoV-2 is a single positive-strand RNA coronavirus that has been shown to cause severe respiratory syndrome in humans. Coronaviruses have been shown to cause potentially life-threatening respiratory, gastrointestinal and diseases of the central nervous system in both humans and animals. Coronaviruses have the capacity to mutate and adapt to new environments. Coronaviruses are also programmed to modify the host's response to the virus, therefore making threats long-term and constant²⁰. It has been shown by Liu et al that SARS-CoV-2 cell tropism (the type of cell when infection is established) was identified in cells from multiple organs, thus showing that COVID-19 infections are not limited to the respiratory system, but also appear in the kidneys, pancreas, small intestine and circulatory system²¹.

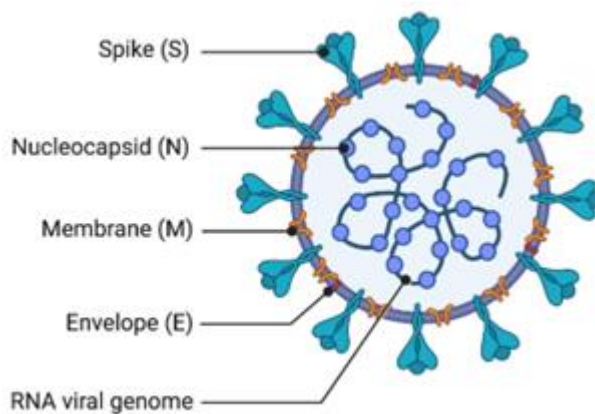


Figure 1. Structure of the SARS-CoV-2 virus²².

Coronaviruses are composed of four structural proteins known as the nucleocapsid protein (N), spike protein (S), envelope protein (E), membrane protein (M) and small membrane (SM) glycoprotein, as shown in **Figure 1**^{20, 22, 23}. The N protein forms the helical capsid structure, which houses the RNA genome which runs in the 5' – 3' direction²⁴. The nucleocapsid is encapsulated in a lipid envelope, which consists of the S, E and M proteins. The E, M and SM proteins are involved in virus assembly. The S proteins function in virus entry and host cell recognition^{23, 25}. The S proteins form large protrusions on the surface of the virus and are comprised of three sections: the large ectodomain, the transmembrane domain and the intracellular region. It is a clove-shaped trimer with three S1 heads and a trimeric S2 stalk. The S1 protein binds to the host receptor human ACE2 (hACE2) through the receptor binding domain and is activated proteolytically by proteases, which causes viral invasion of

the host cells. This is done when S2 fuses the viral and host membranes, releasing the viral genome into the host cell^{23, 26}.

During COVID-19 viral infections, the host proteases cleave the S protein into the receptor binding subunit S1 and the membrane fusion unit S2. The S1 subunit binds to sugar receptors and hACE2 on the surface of the host cell. The S2 subunit, the membrane binding portion, then undergoes conformational changes which results in a post-fusion state where the three pairs of repeating heptad regions in the trimeric S2 form a six-helix bundle. The now exposed hydrophobic fusion regions then insert into the host membrane and the viral and host membranes then become fused. The S proteins are primed by transmembrane protease 2 (TMPRSS2) which is essential for entry of SARS-CoV-2 coronavirus. Wang et al. described the clathrin- and caveolae-independent endocytic pathways for SARS-CoV viruses' cellular entry²⁹, which has been shown to also be used for cellular entry of SARS-CoV-2 viruses^{20, 26-29}. Despite various reports examining the mechanism of entry of SARS-CoV-2 viruses into cells, other than injecting its viral genome into such cells, at the time of writing this thesis, very little is known about how this virus undergoes replication and assembly.

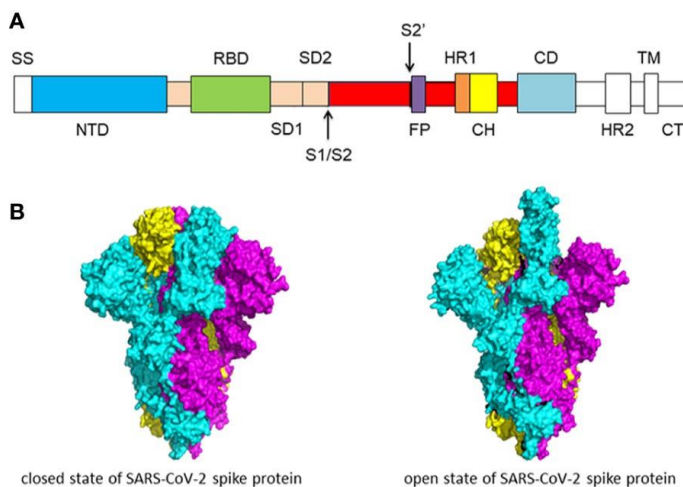


Figure 2. (A) Schematic of the primary structure of the SARS-CoV-2 spike protein, where the single sequence (SS), N-terminal domain (NTD), the receptor binding domain (RBD), subdomain 1 (SD1), subdomain 2 (SD2), the S1/S2 protease cleavage site, S2' protease cleavage site, the fusion peptide (FP), heptad repeat 1 (HR1), central helix (CH), connector domain (CD), heptad repeat 2 (HR2), the transmembrane domain TM and the cytoplasmic tail (CT) are indicated. (B) Cryo-EM structures of the spike protein in the closed state (left) and open state (right)³⁰.

Intrinsically disordered proteins (IDPs) and intrinsically disordered regions (IDRs) play a considerable role in a wide variety of biological functions, such as

DNO/RNA binding, protein binding and in facilitating access to binding sites. RNA – protein recognition requires RNA and protein conformational changes which is facilitated by the disordered residues. These disordered regions are necessary for other important viral processes, such as in transcription, translation and in cellular signalling. Coronaviruses can be categorised and is useful for identifying the life cycle and pathogenicity of the pathogen³¹. There are three segments of IDRs in SARS-CoV-2 nucleocapsid proteins, which connects the serine rich N-terminal domain (NTD) and C-terminal domain (CTD). The IDR that flanks the CTD plays a role in dimer association in SARS-CoV-2. In SARS-CoV-2, the spike protein is activated by host cell enzymes, such as trypsin, cathepsin L, furin and TMPRSS2, where a unique amino acid pattern (RARR) is present at the S1/S2 junction. This exposed disordered region flanking the CTD is cleaved by furin and is responsible for effective transmission. A number of missing residues in the monomeric structure have been observed, which obtain a stable conformation upon binding with the hACE2 receptor, termed as a disorder-to-order transition (DOT). These allow for a better shape complementary to the receptor and for spike protein and hACE2 affinity, thus is necessary to facilitating the binding of the spike protein to the hACE2 receptor^{20, 32}.

SARS-CoV-2 can be transmitted in two ways: by direct means through droplet and human-to-human transmission, and indirect contact by contaminated objects and airborne contamination. The misuse of personal protective equipment (PPE) has been shown to be a source of airborne infections. The person-to-person spread of SARS-CoV-2 occurs mainly through the dispersion of respiratory droplets, such as when a patient coughs, sneezes, talks or even sings. Typically, droplets do not spread farther than six feet and remain suspended in the air for a limited time³³. SARS-CoV-2 remains active and contagious in droplets for up to three hours. Van Doremalen et al has shown that SARS-CoV-2 can survive for up to 2 days on stainless steel and up to 3 days on plastic^{34, 35}. COVID-19 transmission can be avoided by taking various precautions. These involve the use of PPE, such as by wearing masks and gloves and the disposal of contaminated or used PPE after use, the appropriate use of disinfectants on surfaces and hands, and physical distancing of over 6 feet (2 meters) to remain out of range of the spread of contaminated droplets³³⁻³⁶.

1.2.2. Symptoms and Long-Term Effects

Like other coronaviruses, SARS-CoV-2 affects the respiratory system, causing disease and affecting respiratory health. There are various symptoms associated with COVID-19 infections which include fever, cough and shortness of breath, which typically appear 4 – 7 days, with a maximum incubation period 14 days after exposure to the virus. The severity of infections can vary from mild to severe, with some people being asymptomatic. Most people present with mild flu-like symptoms, while ~20 % of patients develop severe infections, which include pneumonia, respiratory failure and in some cases, death. Various other symptoms have been reported, which include tiredness, a runny nose, sore throat, headache, diarrhoea, vomiting and the loss of sense taste and/or smell. It has been identified by Salian et al that COVID-19 can be spread through droplets ranging from 0.6 – 100 μm in diameter, and the number of droplets has a proportional increase with respect to coughing rate³⁵. These droplets can also be generated in patients who are pre-symptomatic or asymptomatic through normal breathing and speech. A severe innate immune response and a sustained rise of systemic cytokine levels has been associated with COVID-19 infections, and as a result, the body's immune response has been used to drive and predict patient mortality and severity of the disease. Interleukin-1 β , interleukin-2, interleukin-2 receptor, interleukin-4, interleukin-10, interleukin-18, interferon- γ , C-reactive protein, granulocyte colony-stimulating factor, CXCL10, monocyte chemoattractant protein 1, macrophage inflammatory protein 1- α , and tumour necrosis factor- α have all been identified as mediators, when elevated, which can indicate the severity of COVID-19 infections. Patients can also display T-cell exhaustion with lower lymphocyte counts. Systemic inflammation can result in cognitive decline and neurodegenerative diseases, which raises concern that COVID-19 survivors may experience the development of neurodegenerative conditions in years to come³⁶⁻⁴⁰.

Long-term effects of COVID-19 infections have been reported to include a high risk for subsequent development of neurological disease, such as Alzheimer's disease. The increased cytokine levels can be used to predict hippocampal atrophy in patients that suffer severe sepsis and considering this effect, acute respiratory distress syndrome (ARDS) is the most frequent severe clinical presentation. ARDS along with chronic ventilation can result in the cognitive decline and executive dysfunction can persist for weeks or months after discharge from hospital. Despite this, Helms et al did

not find the direct presence of SARS-CoV-2 in cerebrospinal fluid, however the long-term effects of a cytokine storm may still contribute to neurodegenerative conditions developing in the future^{40, 41}.

1.2.3. Therapeutic Agents Effective in COVID-19 Treatment

In terms of treatment, several drugs have been identified to have a significant impact on COVID-19 treatment. Within the first year Remdesivir, an antiviral drug, and monoclonal antibodies, such as bamlanivimab, and the combined use of casirivimab and imdevimab were approved for the treatment of the COVID-19 disease⁴². However, although it has been shown to be a good antiviral agent, according to Ansems et al, Remdesivir has been shown to have no overall effect in alleviating symptoms during COVID-19 treatment⁴³. The combination of the two monoclonal antibodies bamlanivimab and etesevimab, was shown by Dougan et al to be effective in the early treatment of COVID-19 infections, overall, drastically decreasing the 28-day mortality rate⁴⁴. Other monoclonal antibodies such as the combination of casirivimab and imdevimab were also shown to be effective therapeutics used in the treatment of COVID-19, but were shown by Ganesh et al. to be less effective than treatment with either bamlanivimab alone or with a combination of bamlanivimab and etesevimab⁴⁵. Pandolfi et al showed that paracetamol (acetaminophen) was effective in reducing inflammation and fever in COVID-19 patients, however is not recommended for elderly patients as it can either increase or reduce the consumption of glutathione (GSH), which could potentially exacerbate symptoms, and thus increase risk factors associated with the infection⁴⁶. Ibuprofen was also investigated in the treatment of COVID-19. A study by Rinott et al investigated this drug as a treatment for COVID-19 among a wide variety of patients and when the statistics were compared, it clearly was shown that ibuprofen was greatly beneficial in the treatment of COVID-19⁴⁷. Age, gender, patients with underlying conditions, whether patients admitted to hospital, respiratory symptoms patients displayed and observed clinical outcomes, such as whether supplemental oxygen, mechanical ventilation, admission to the intensive care unit (ICU) and death, were used to compare and analyse results. Despite being very effective for the most part, the comparison of the clinical outcomes showed that the percentage of patients in each case who received and did not receive ibuprofen treatment were all within 1 % of each other, indicating that ibuprofen was ineffective in severe cases and most beneficial in less severe cases⁴⁷.

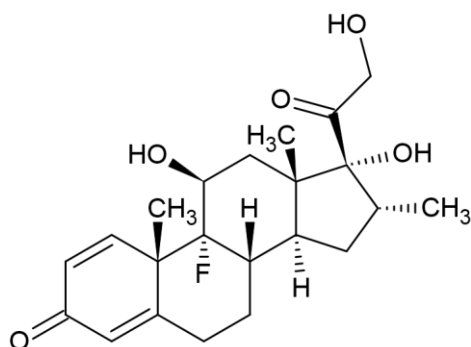
Dexamethasone (DEX) has been shown in multiple studies to be a very effective treatment for COVID-19 infections due to its effectiveness in high-grade inflammatory disorders and glioblastoma, which contributes to its activity in COVID-19 treatment. It is also a good candidate for COVID-19 treatment and the nanoformulation of DEX may help to sustain the anti-inflammatory and anti-oedema drug activity after patients have recovered from COVID-19 infections⁴⁸⁻⁵⁰. N-acetyl-L-cysteine (NAC) has been used in clinical practice in the treatments of critically ill patients suffering from sepsis and in recent times, to both prevent infection and treat patients with COVID-19⁷. It was selected as a treatment for this disease as it has antioxidant, anti-inflammatory and anti-immune-modulating effects which is beneficial in the treatment of SARS-CoV-2. It is also a glutathione (GSH) precursor, which is an important antioxidant produced in cells. In cells infected with SARS-CoV-2, glutathione is used up faster than it can be recycled, so NAC is an important drug in the treatment of COVID-19 as it helps to replenish GSH levels in cells^{7, 51, 52}.

With consideration of the effectiveness and importance of DEX and NAC in the treatment of COVID-19, these therapeutic agents were selected for electroanalysis to further develop the very limited understanding of the electrochemical behaviour of these molecules and to develop novel sensors for these molecules with high sensitivities.

1.3.0. Dexamethasone

Dexamethasone (DEX) (structure in **Structure 1.**) is a useful synthetic glucocorticosteroid that has many applications as a therapeutic agent, which includes the treatment of acute exacerbation of multiple sclerosis, allergies, cerebral oedema, inflammation, and shock. It has also been shown to alleviate the symptoms of atopic and contact dermatitis⁵³. Paediatric asthma patients who were administered DEX also benefitted from this drug, with no patients experiencing a relapse in symptoms or nausea and vomiting⁵⁴. DEX is also a good candidate for the treatment of bacterial meningitis according to de Gans et al, where 8 % of patients who received the drug had an unfavourable outcome compared to those with a placebo (11 %). Despite this article's aim being focussed on the treatment of bacterial meningitis (*Neisseria meningitidis*), DEX treatment in other infections such as *Streptococcus pneumoniae* were also examined, showing that DEX was also very, if not more effective as a treatment for *S. pneumoniae* infections than bacterial meningitis⁵⁵. Mohammed et al

also investigated DEX treatment for *Varicella pneumonia*, which causes chickenpox in children and pneumonia in adults. Their study demonstrated DEX's effectiveness which was clearly observed in severe cases where the duration of time spent in hospital because of the infection decreased with DEX and acyclovir treatment when compared to a placebo group who were only administered acyclovir. The faster decline in the concentrations of C-reactive protein (CRP) and interleukin-6 (IL-6) was also observed, further demonstrating the potent anti-inflammatory and immunosuppressive properties of DEX⁵⁶.



Structure 1. Chemical structure of dexamethasone (DEX)

1.3.1. Dexamethasone Treatment in COVID-19 Patients

More recently, DEX has been shown to be beneficial in the treatment of patients with COVID-19 infections due to its anti-inflammatory properties⁵⁰. DEX is effective as this compound mimics the actions of anti-inflammatory compounds produced by the body. In terms of the treatment of COVID-19 infections, DEX is 25 times more potent than other glucocorticosteroids such as hydrocortisone and prednisone⁵⁷, which is an important reason on why DEX has been shown to be effective in the treatment of COVID-19 patients. DEX is also stronger than nonsteroidal anti-inflammatory drugs (NSAIDs), such as aspirin and ibuprofen. DEX is a drug with anti-inflammatory and immunosuppressive properties, while the latter only block the vascular stage of inflammation^{50, 58}.

DEX has been shown to have a significant effect in patients hospitalised with severe COVID-19 infections, where the 28-day mortality rate among patients receiving invasive mechanical ventilation or oxygen alone decreased in patients administered 6 mg DEX once daily, compared to those receiving usual treatment⁵, further highlighting DEX's effectiveness in the treatment of SARS-CoV-2 infections.

1.3.2. Dexamethasone Mechanism of Action

DEX works by inhibiting the pro-inflammatory gene which codes for chemokines, cytokines, cell adhesion molecules (CAMs). Several mechanisms of action have been demonstrated for DEX. These include the direct alteration of membrane fusion, alterations of membrane fluidity, induction of protein inhibitors of phospholipase A₂ activity, alteration of membrane of polymorphonuclear (PMN), alteration of membrane lipids and direct inhibition of chemotactic peptide receptor number and function^{50, 59}.

In the body DEX acts in the body in several ways. DEX suppresses the migration of neutrophils and decreases the proliferation of lymphocyte colonies. In doing so, the capillary membranes become less permeable accompanied by higher vitamin A concentrations in the serum. Prostaglandin and the cytokines IL-1, IL-12, IL-18, tumour necrosis factors (TNFs), interferon gamma (IF- γ) and granulocyte-macrophage colony-stimulating factors become inhibited, thus reducing inflammation⁶⁰. Since COVID-19 infections cause a hyperinflammatory state in the body and the broad anti-inflammatory activity of DEX indicates its effectiveness in treating hyperinflammation caused by COVID-19⁵³.

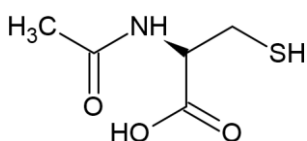
Addition of pharmacologic DEX doses to C2C12 murine myoblast cells has been shown to inhibit cell proliferation and protein synthase processes, which in turn, reduce myoblast differentiation and myotube fusion. At similar concentrations, DEX increases the production of the calcium binding transmembrane protein, dysferlin, which increases the production of myogenic differentiation, increasing myogenic fusion. Sustained administration of DEX has shown that the improved myogenic proliferation and differentiation, indicating that the forced production in skeletal muscle units (SMU) and blebbing was slower, indicating cell death when in comparison to without DEX administration⁶¹.

1.3.3. Dexamethasone quantitation

DEX has been quantified using various methods. The first of which is high performance liquid chromatography (LC-MS) in dried blood samples⁶². Other methods have described the use of UV spectrophotometric methods, proteomics based on liquid chromatography-high resolution tandem mass spectrometry⁶³⁻⁶⁷. These studies explored DEX quantitation in a variety of systems, from blood samples to pharmaceutical formulations, to tissue samples, for DEX alone and in combination with other drugs such as Remdesivir, each with reasonable sensitivities and selectivity for DEX. A niche array of DEX electrochemical sensors have been developed, utilising various electrodes and modifiers, such as carbon nanomaterials (CNMs), metal nanoparticles and amalgam films to name a few, to optimize DEX electrochemical response. An in-depth insight into DEX electrochemical sensors will be expanded upon in the introduction to Chapter 2.

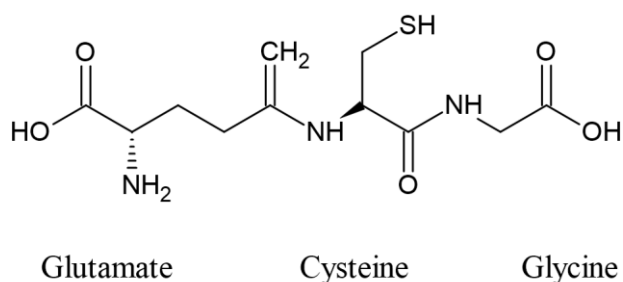
1.4.0. N-acetyl-L-cysteine

N-acetyl-L-cysteine (NAC) (**Structure 2.**) is a safe and inexpensive therapeutic agent that has been commercially available for a long time⁶⁸. NAC has been used to treat various diseases including cancer, cardiovascular diseases, human immunodeficiency virus (HIV) infections, acetaminophen-induced liver toxicity and metal toxicity⁶⁹. It is not found in natural sources, however it is a precursor to cysteine (Cys), which is found in many foods, such as chicken, turkey, garlic, yogurt and eggs. It is a well-tolerated mucolytic drug that moderates clinging mucous secretions and enhances glutathione transferase activity. Deacetylation of NAC occurs in the liver and small intestine during oral administration, resulting in the production of Cys, thus the bioavailability of NAC is decreased to between 4 – 10 %. The α -protected nitrogen contains an acetyl group. The acetyl group can be removed in most tissues by cleaving the acetyl group thus producing L-Cys⁷⁰. It is a useful therapeutic as it promotes detoxification and acts directly as a scavenger for free radicals in cells and blood serum, thus showing that it is a powerful antioxidant⁷⁰⁻⁷².



Structure 2. Chemical structure of N-acetyl-L-cysteine (NAC)

The key to the antioxidant power of NAC is that it is a glutathione (GSH) precursor, a naturally occurring antioxidising agent^{73, 74}. Upon deacetylation, the resulting L-Cys is used to promote glutathione biosynthesis, thus glutathione replenishment mediates all intracellular effects of NAC. Free L-Cys readily oxidises to the corresponding disulfide, cystine, thereby forming the cysteine/cystine redox couple⁷⁵. Considering antioxidant defences, GSH is the principle intracellular non-protein thiol that plays an important role in preserving the intracellular redox state, through its actions as a non-enzymatic reducing agent⁷⁶. GSH is a tripeptide consisting of a glutamate, cysteine and glycine residues (**Structure 3**)⁷⁶. In cells, two ATP-dependant processes are exploited for the synthesis of GSH. Firstly, γ -glutamylcysteine (γ -EC) is produced through the dimerisation of L-glutamate and L-cysteine. This reaction is catalysed by γ -glutamylcysteine synthase (γ -ECS). The second reaction involves the addition of glycine to γ -EC at the C-terminal end, which is catalysed by glutathione synthase (GS)^{75, 77, 78}.



Structure 3. Chemical structure of glutathione (GSH), showing the position of its amino acid components.

1.4.1. N-acetyl-L-cysteine Treatment in COVID-19 Patients

NAC has been shown to be beneficial in the treatment of patients suffering from COVID-19 due to being a precursor to GSH. As discussed, COVID-19 can cause severe inflammation, resulting in a cytokine storm and oxidative stress imbalance. The resulting oxidative stress imbalance results in a significant elevation in glutathione reductase (GR) in the blood serum, which leads to rapid depletion of GSH from cells. This effect was more prominently observed in severe COVID-19 cases and in ICU patients. With consideration to NAC being a GSH precursor, it was employed as a therapeutic to help restore and reduce the depletion of GSH in blood serum and in cells. NAC's relatively low toxicity and wide safety margin led it to being a good candidate to treat COVID-19 infections, where all patients administered NAC showed

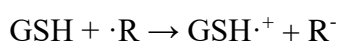
a significant decrease in the severity of symptoms, and on the whole, their conditions improved^{7,79}.

1.4.2. N-acetyl-L-cysteine Mechanism of Action

As discussed, NAC is used in cells as a precursor to GSH in cells⁷. In cells the acetyl group is cleaved, resulting in L-Cys⁷⁰. This L-Cys produced, in the case of severe oxidative stress caused by COVID-19, is then used to restore GSH levels in cells. Although GSH is recycled in cells, upon infection with SARS-CoV-2 this process increases, however, in severe cases this cannot match the amount of GSH required by cells to combat the infection. Therefore, GSH synthesis is required and carried out through the polymerization of L-glutamate, L-cysteine and glycine, catalysed by γ -ECS and GS as described above^{75,77,78}.

The mechanism of action of GSH has been proposed that H transfer from GSH to C radicals appears to be the mechanism of protection of GSH. It has also been postulated that the \cdot OH radical and GSH reaction occurs in addition to the sulphur-centred radical formed by either electron transfer or H removal from GSH. Two mechanisms have been shown to accurately depict GSH activity in cells for the removal of free radicals and thus, the relief of oxidative stress. The first of these involves a single electron transfer reaction (SET), and the second involves a H transfer reaction (HT), as depicted below:^{80,81}

SET:



HT:



It has been shown that these processes are important in the scavenging and elimination of free radicals in cells, thus helping to alleviate oxidative stress⁸¹⁻⁸³. Oxidative stress in biological systems is caused by free radicals, such as the superoxide anion radical ($\text{O}_2\cdot^-$), hydroxyl radical (\cdot OH) and reactive chlorine/bromine species, or nonradical species, such as hydrogen peroxide (H_2O_2), hypochlorite (OCl^-) and nitrites (NO_2^-), which can cause DNA and RNA mutations, metal ion interactions, alterations to protein processing, folding and trafficking and lipid oxidation to name a few⁸⁴. GSH helps to combat oxidative stress through scavenging for these reactive oxygen species

(ROS)⁸⁵. The effect of hyperbaric oxygen therapy on oxidative stress has been studied previously, and despite GSH levels remaining relatively unchanged, an improvement in C-reactive protein levels was observed which led to an overall reduction in inflammation⁸⁶. With consideration of the importance of GSH in the alleviation of oxidative stress in cells, it further confirms the effectiveness of NAC as a useful and effective therapeutic agent in the treatment of such diseases as COVID-19. Furthermore, it has been shown that upon cleavage of the acetyl group, L-Cys uptake by cells is much more efficient than that of GSH alone, for which little to no evidence has been shown for its uptake into cells, thus validating NAC as a useful therapeutic agent^{87, 88}.

1.4.3. N-acetyl-L-cysteine Quantitation

Few studies have been published regarding NAC quantitation, however, NAC has been quantified previously with high-performance liquid chromatography (HPLC)^{89, 90}. However o-phthaldialdehyde/N-acetyl-L-cysteine reagent has been used to amplify the response of protamine in UV-vis quantitative studies⁹¹. Various electrochemical studies quantifying NAC have been published, using gold electrodes and gold modified electrodes, exploiting the gold-thiol interactions for the electrooxidation of NAC. These will be described in more detail in the introduction to Chapter 3.

1.5.0. Nanomaterials of Interest

Nanomaterials refer to a material comprising of particles or constituents on the nanoscale, i.e., $X \times 10^{-9}$ units, for example 1 nanometre (nm) is equivalent to 1×10^{-9} meters (m). Nanomaterials are usually considered if the material has at least one external dimension within 1 – 100 nm⁹². Nanomaterials have numerous applications ranging from the purification of water containing contaminants such as toxic metal ions (e.g., Pb), greenhouse gases, organic and inorganic solutes, bacteria, viruses, pollutant quantification and cleaner production⁹³, to cancer imaging and therapy⁹⁴, to energy storage and conversion⁹⁵. More relevant to this project, carbon nanomaterials and metal nanoparticles have been exploited for their use in electrochemical sensors⁹⁶.

Nanomaterials can be categorised in various ways. Firstly, they can be categorised by their dimensionality, referring to their overall shape and structure. Secondly, nanomaterials can be classified by their composition⁹⁷. Nanomaterials can

vary greatly in shape and size, such as in carbon nanomaterials, where they can vary greatly in shape and dimensionality, such as carbon nanotubes, fullerenes (such as C₆₀) and graphene nanofibers to name a few⁹⁸. Alternatively, nanomaterials can also be categorised according to their composition, i.e., what they are made from, such as Pb, Pt, Au, and Cu, to name a few examples. These can also be differentiated further by dividing them into subcategories based off their morphology⁹⁷. These will be discussed in more detail throughout this section.

1.5.1. Carbon nanomaterials

Carbon nanomaterials (CNMs), as mentioned above, have a wide array of functions from sensing to imaging, to energy storage^{93, 95}. CNMs have a very broad range of morphologies which includes graphene sheets, carbon dots, nanodiamonds, single walled carbon nanotubes (SWCNTs), multi-walled carbon nanotubes (MWCNTs), fullerenes (such as C₆₀) and more recently carbon nano-onions (CNOs)⁹⁹⁻¹⁰¹, as shown in **Figure 3**. In terms of electrochemistry, CNMs have interesting properties, such as high capacitances which allows them to be used to effectively store energy in electrochemical batteries and capacitors¹⁰². CNMs, such as fullerenes have been used effectively in various electrochemical sensors for the detection of cancer relevant biomolecules¹⁰³. Similarly, magnetic multi-walled carbon nanotubes (MMWCNTs) have been used in the development of a ciprofloxacin electrochemical sensor¹⁰⁴. Investigations into sensors incorporating the use of CNOs has shown promising results due to the CNO's excellent resistance against bio-fouling and electrode stability compared to graphite nanoflakes (GNFs) and glassy carbon electrodes (GCEs)¹⁰⁵. CNOs are the newest carbon analogue and are particularly relevant to this research project and are discussed in greater detail below.

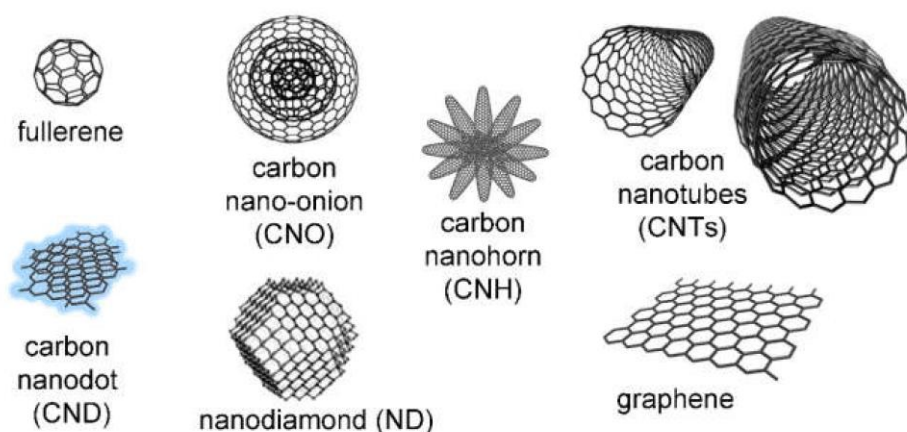


Figure 3. Chemical structures of various types of carbon nanomaterials¹⁰⁶.

1.5.2. Carbon Nano-onions

Carbon nano-onions (CNOs) are a new emerging class of carbon nanomaterials. They are concentric multi-layered fullerenes with typically a hollow core. Each concentric graphitic shell is composed of a network of localised sp^2 hybridised C atoms, which gives rise to interesting properties, such as their high capacitances¹⁰². CNOs are typically composed of 4 – 6 concentric quasi-spherical and polyhedral shaped graphitic shells approximately 0.335 nm apart, and measure between 4 – 6 nm in diameter¹⁰⁷.

CNOs can be synthesised in numerous ways, such as through the combustion of white and thin cotton, through a methane cracking method and through the thermal annealing of nanodiamond powders, of which the latter was used for the CNOs used in this project, outlined in **Figure 4**^{100, 108-110}. CNOs typically have high capacitance values. This has been reported to be attributed to the pore size of the carbon network, where the capacitance has been reported to be greater in nanomaterials with a smaller pore diameter. Due to the decreased surface area accessible to ions in solution the capacitance of the CNM increases¹¹¹. Furthermore, during their synthesis, they can be doped with heteroatoms such as boron (B), sulphur (S)^{102, 112-114}. Heteroatom doping can have a significant impact on their properties. S-doped-CNOs typically are less conductive than undoped-CNOs, hence increasing their super-capacitive properties. This can be attributed to defects in the graphitic shells caused by the S dopant, where defects and edges containing sp^3 C atoms reduces the overall electrical conductivity, which, in the case of an electrochemical sensor, alters the device performance¹¹⁵. Similarly, N-doped-CNOs contain pseudocapacitive sites at pyrrolic and pyridinic

sites in the structure, however, quaternary-N and nitrous oxide are responsible for the higher electrical conductivity of N-doped CNOs¹¹⁶⁻¹¹⁸. The N-active sites have been shown to have the ability to facilitate surface redox reactions. The positive charge on quaternary N and pyridinic N-oxide groups act as electron donors, thus attracting protons and/or compounds with positively charged functional groups, thus facilitating redox reactions involving nitrogen or neighbouring functional groups. This then has a beneficial impact on improving the electrochemical performance of N-doped-CNO supercapacitors¹¹⁹. Boron atoms contain three valence electrons which, along with their similar size to carbon atoms, allows them to be easily incorporated into a carbon matrix. B-doped CNOs have been shown to have an increase ability to catalyse oxygen reduction reactions (ORR)¹²⁰. Little has been reported about the electrochemical behaviour of B-doped-CNOs, however, like with other CNOs, a high capacitance was also observed upon B doping¹¹³. An overall increase in the capacitance has been reported upon heteroatom doping. This has been attributed to the increased porosity of the CNO surface and the surface defects in the carbon network induced upon boron and/or nitrogen doping^{121, 122}.

CNOs can also be modified through the covalent addition of functional groups, such as carboxylic acid groups, onto the CNO surface resulting in their oxidised forms (oxi-CNOs)¹²³. These have been used previously as a linker for the attachment of polymers and other molecules, such as drugs where CNOs are exploited as a mechanism for drug delivery, onto the CNO surface¹⁰⁰. The presence of carboxylic acid groups on the CNO surface has a significant impact on the capacitance. The capacitance significantly increases with the presence of these carboxylic acid groups due to the faradaic current that arises from these electroactive groups and enhanced surface areas through the opening and breakage of the graphitic layers of the CNOs¹²⁴. With consideration of this effect, the capacitance of oxidised heteroatom-doped CNOs, such as oxi-S-doped, oxi-N-doped, oxi-B doped and oxi-BN-doped CNOs, is expected to be greater than that of undoped oxi-CNOs, due to the combined effects of the heteroatom dopants and carboxylic acid functional groups altering the structure of the graphitic layers through the incorporated surface defects and through breakage and opening of the graphitic layers. A HR-TEM image of CNOs and a structural diagram, shown in **Figure 5**, shows the spherical and layered structure of CNOs^{121, 122, 124, 125}.

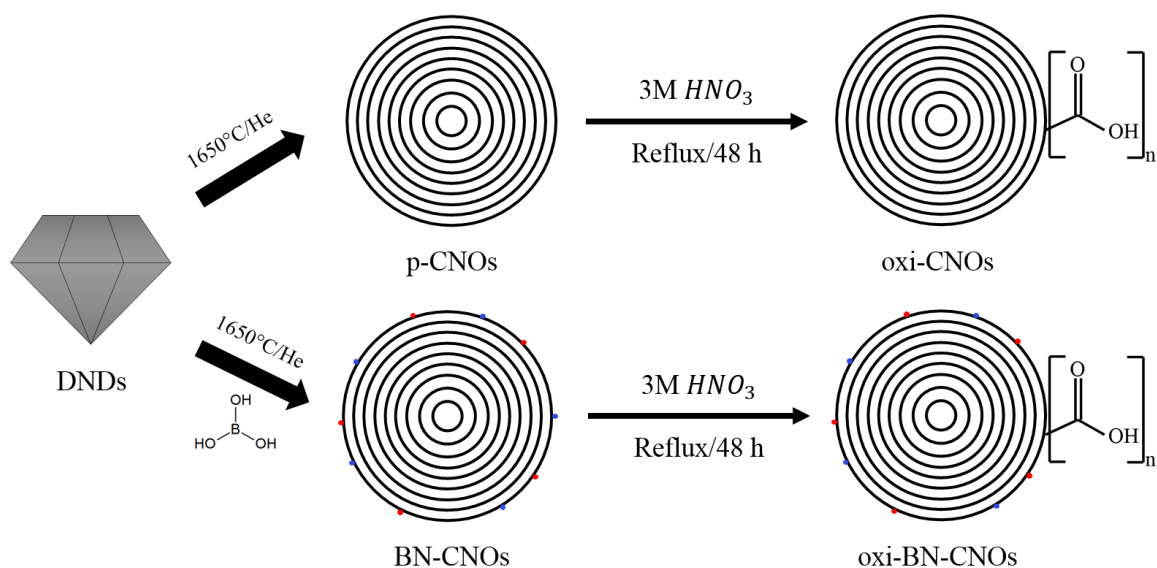


Figure 4. p-CNO and BN-doped-CNO synthesis through the thermal annealing of detonation nanodiamonds, with acid treatment in 3 M nitric acid yielding , oxi-CNOs and oxi-BN-doped-CNOs.

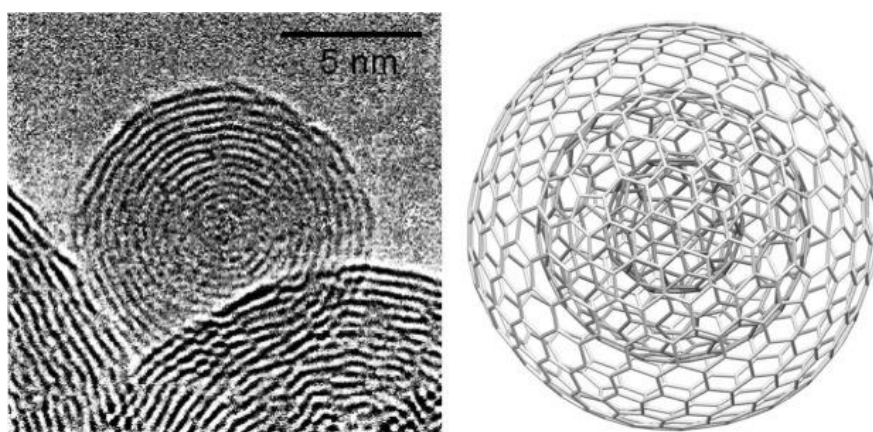


Figure 5. HR-TEM image of carbon nano-onions (left) with their structure (right) shown¹²⁵.

1.5.3. Metal Nanostructures

Metal nanostructures are another category of nanomaterials which have a wide range of applications throughout chemistry. They can be categorised further based on their composition and morphology⁹⁷. Their morphological categorisation includes the nanostructure's size, shape and structure¹²⁶. Metal nanostructures can exist in many forms, such as nanoparticles (NPs)¹²⁷, microparticles (MPs)¹²⁸, nano stars¹²⁹, nano urchins¹³⁰ and films¹³¹, to name a few. Common metals used in metal nanostructure fabrication include copper (Cu), gold (Au), platinum (Pt), nickel (Ni), silver (Ag), palladium (Pd), titanium (Ti) and iron (Fe) because of their non-toxic and catalytic activity¹³². They can be composed of these metals in their pure form or their oxides,

hydroxides, sulphides, phosphates, fluorides, and chlorides¹³³. These metal nanostructures have various applications in chemistry, such as their use on electronic devices, catalysis reactions, sensing, in energy conversion and storage, near infrared photothermal therapy and in surface enhanced Raman scattering¹²⁶. Metal nanostructures have also been used as electrode modifiers in electrochemical sensors for the detection and quantitation of pollutants, toxic chemicals and compounds, and for the analysis of drugs in biological samples, water samples or pharmaceutical formulations^{11, 12, 134}.

1.5.4. Metal Nanoparticles, Microparticles and Films

In this project, microparticles (MPs), metal films and nanoparticles (NPs) have been exploited for the electrochemical determination of dexamethasone (DEX) and N-acetyl-L-cysteine (NAC), with the aim to achieve sensors with high sensitivities for each drug, with electroanalysis of these drugs extracted from pharmaceutical samples. Silver nanoparticles (AgNPs), for example, are some of the most well developed and applicable nanoparticles, due to their relatively inexpensive cost. They have unique and useful chemical properties that make them useful candidates for catalytic, optical, and synthetic applications. They have been used in combination with other metals for the detection of Cd, Cr, Cu, Hg and Sb¹³⁵.

Firstly, electrochemically synthesised copper microparticles (CuMPs) were exploited for the electrochemical determination of DEX. MPs refer to particles between 1 – 1000 μm in diameter, while nanoparticles are typically within 1 – 100 nm in diameter^{92, 128}. Metal MPs and NPs have interesting electrochemical behaviour with excellent electrical conductivity which can be exploited to increase the anodic and/or cathodic electrochemical redox processes associated with the corresponding analytes¹³². Typically, metal nanoparticles have low capacitances due to the high conductivity of the metallic components, however, when combined with semiconducting materials, such as with layers of sulphur atoms in a trigonal prismatic (or antiprismatic) lattice, the capacitance increases stepwise with increasing semiconductor layers. Immobilisation of metal NPs or MPs on such heterostructures has been shown to enhance the photoelectric properties for an improved optoelectronic application¹³⁶. In terms of electroanalysis, metal NPs are attractive candidates as electrode modifiers because of their high electroactive surface areas, which can thus lead to a better electroanalytical performance¹¹. Typically, when examined using

cyclic voltammetry, metal NP and MP modified electrodes display anodic and cathodic waves associated with the electrochemical oxidation and reduction reactions of the metal(s) which the particles are composed of. The magnitude of these signals has the potential to be exploited as the analytical focus of the electrochemical sensor when considering how an analyte of interest can depress the anodic or cathodic metal faradaic response in response to increasing analyte concentration. This has been carried out by Pino et al for the dual detection of phenolic compounds and pesticides¹⁰. These anodic and cathodic metal faradaic responses can be used to gain information on the electrochemical behaviour and surface coverages of the particles at the electrode surfaces¹³⁷. An important consideration when using metal particle-based electrochemical sensors is their stability. While they are stable upon potential cycling, the use of an incompatible background electrolyte can be detrimental to metal particles at the electrode surface, as upon potential cycling, the chloride ions in solution interact with the positively charged metals allowing them to dissolve into solution, thus destroying the metal particles¹³⁸. For example, the use of chlorinated solvents will degrade Cu and Au modified electrodes. Recently, the use of metal films has been explored for the detection of metals such as Cu, Ni, Co, Cr, and a wide array of heavy metals¹³⁹⁻¹⁴¹. Metal film modified electrodes can be characterised and used in similar manners to how metal NPs and MPs can be used in electroanalysis, however, few studies have reported on the use of metal film modified electrodes used for the electroanalysis of organic compounds. This consideration will be applied to this project, where an electrodeposited Cu film will be explored to achieve a highly sensitive sensor for the detection of DEX.

1.5.5. Metal Nanostructure Formation

Metal nanostructures can be made in numerous ways. These include the reduction of Au³⁺ with NaBH₄ which is stabilised with thiols to ensure the production of highly stable particles with a well-controlled and narrow size distribution in the nm range. Au particles have also been synthesised through the spontaneous reduction of Ag⁺ ions in solution in the presence of hydroxyl groups in basic solution. The reduction of Ag⁺ can also be carried out in basic and air-saturated conditions of 2-propanol, resulting in the formation of colloids¹⁴². Copper nanoparticles, for example have been synthesised previously using a variety of methods. Firstly, a reduction method can be used using a variety of reducing agents, such as hydrazine, ascorbic

acid, hypophosphite or sodium borohydride and polyol, which result in uniformly sized and morphological CuNPs. Other methods include a microemulsion method, where two immiscible liquids are used as a thermodynamically stable emulsion to produce CuNPs with a diameter between 3 – 13 nm. A photochemical method can also be used to rapidly produce CuNPs with the aid of a reducing agent. The thermal decomposition of copper salts can also be used to produce CuNPs, however the particle sizes can vary from 3.5 – 40 nm in diameter. Lastly, the electrochemical reduction of Cu can be carried out to electrodeposit CuNPs directly onto an electrode surface¹⁴³, the process which was used in this project. Electrochemical methods involve the use of a copper salt, such as copper acetate or copper sulphate, in a background electrolyte that allows the copper to remain in solution. The case of the two copper salts mentioned, a sodium acetate buffer or 0.1 M H₂SO₄ would make suitable candidates for CuNP electrodeposition¹⁴⁴. This is also a requirement for all metal NP electrosynthesis. Various methods have been investigated for the electrosynthesis of metal NPs which all involve the electrochemical reduction of Mⁿ⁺ → M⁰ at the electrode surface, where M is the metal undergoing electroreduction and n denotes the oxidation state of the metal ions in solution. The most common electrodeposition methods include electrodeposition via cyclic voltammetry¹⁴⁵ and via potentiostatic methods¹⁴⁴. Various potentiostatic electrodeposition methods have been explored, the first being a single pulse potentiostatic method for the electrodeposition of CuNPs from 50 mM CuSO₄ in 0.1 M NaClO₄, where one pulse was applied at -1.2 V vs Ag/AgCl for 20 minutes¹⁴⁶. A second method for the electrodeposition of metal nanoparticles involves the use of a triple pulse potentiostatic method. In this method, lead nanoparticles (PbNPs) were electrochemically synthesised by employing a perturbation pulse (E₁) to remove adsorbed ions from the electrode surface, a seeding pulse (E₂) to seed Pb nuclei at the electrode surface, and finally, a growth pulse was applied to grow PbNPs from the seeded nuclei, as electroreduction of Pb occurs more readily at the more conductive Pb nuclei¹⁴⁷. Finally, a third method of metal nanoparticle synthesis involved a multi-potentiostatic pulse sequence, for the electrosynthesis of gold nanoparticles (AuNPs). A perturbation pulse (E₁) was also utilised here followed by a seeding pulse (E₂) to seed the Au nuclei. Alternating anodic and cathodic pulses were used to systematically grow the AuNPs at the electrode surface, resulting in a uniform distribution of uniformly sized AuNPs¹¹. A variation of the single pulse method was used for the electrodeposition of a copper film at a glassy

carbon electrode (GCE) surface in Chapter 2 of this project, where a perturbation pulse was added to ensure the GCE was free from residual copper before film electrosynthesis. The triple pulse electrodeposition method for PbNPs was adapted for the purpose of CuMP synthesis in Chapter 2. Finally, the multi-potentiostatic pulse method for the electrosynthesis of AuNPs was applied in Chapter 3 for the AuNP electrodeposition at an oxi-BN-doped CNO modified GCE. Each of these methods will be discussed in more detail in their corresponding chapters.

1.6.0. Electrochemical sensors

Firstly, electrochemical sensors exploit the use of 2 – 3 electrode systems, as shown in **Figure 6**, with a working electrode and auxiliary electrode, and in the case of a 3 electrode system, a reference electrode¹⁴⁸. The auxiliary (counter) electrode functions as an electron sink, where a pathway is provided for current to flow in the electrochemical cell without a significant current being passed through the reference electrode¹⁴⁹. The auxiliary electrode material should be selected with consideration such that electrochemical products formed at the auxiliary electrode do not interfere with those formed at the working electrode. For this reason typically a Pt wire electrode is used due to its electrochemical inertness¹⁵⁰. The role of the reference electrode is to involve a benchmark for measuring and controlling the potential of the working electrode by utilising a constant potential at low current densities. The reference electrode does not pass any current, thus does not interfere with measurements obtained at the working electrode¹⁵¹. Common reference electrodes employed in electrochemical devices include Ag/AgCl reference electrodes¹⁵², calomel reference electrodes¹⁵³, hydrogen reference electrodes¹⁵⁴, double junction reference electrodes¹⁵⁵ and liquid junction reference electrodes¹⁵⁶. Finally, the working electrode refers to the electrode used in an electrochemical system where the reaction of interest occurs. Typically, working electrodes are made from chemically stable materials that can facilitate electron transfer reactions and have a well-known morphology and surface area. Common working electrodes employed in electroanalytical devices include glassy carbon electrodes (GCEs), platinum electrodes (PtE) and gold electrodes (AuE), which can be macroelectrodes, microelectrodes or polished disc electrodes¹⁵⁷. Other electrodes can be in the form of pastes (carbon paste electrodes¹⁵⁸), inks in the form of screen printed electrodes¹⁵⁹ or as an amalgam¹⁶⁰, such as a silver paste amalgam electrode¹⁶¹. The potential of the

working electrode is monitored with respect to the reference electrode, where the current is passed between the working and auxiliary electrodes. Although, the current response is only monitored at the working electrode¹⁵¹.

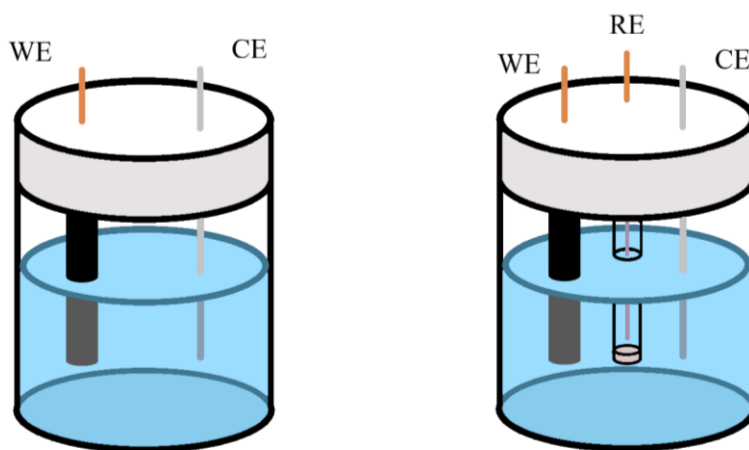


Figure 6. Schematic of two-electrode (left) and three-electrode (right) systems, indicating the positions of the working electrode (WE), auxiliary (counter) electrode (CE) and reference electrode (RE).

1.6.1. Categories of Electrochemical Sensors

Electrochemical sensors can be categorised based on the types of measurements carried out, including potentiometric, conductometric and amperometric/voltametric sensors. Electrochemical sensors produce digital signals that, upon analysis, can give information about the electrode used, analyte detected and to gain information about electron transfer processes occurring at the electrode surface¹⁶².

Potentiometric ion sensors or ion selective sensors can be categorised by their small size, portability, and their low cost, which makes them desirable candidates for commercial and practical use. These sensors are based on membranes containing neutral or charged carriers and have been used for the determination of a wide variety of organic and inorganic compounds. Outputs from these sensors are measured with respect to changes of the membrane potential. The electric potential (E_M) in classical models is represented as the sum of the boundary potential (E_{BP}) at the sample/ion-sensitive membrane boundary and by the diffusion potential inside the membrane (E_D), while a constant (C) is added to account for the potential at the internal contact.

In the classical modelling of these sensors, two approaches can be considered when carrying out electrochemical measurements, the first approach accounts for the internal diffusion potential (the phase-boundary-potential model) while the other approach disregards it (the total-membrane-potential approach)¹⁶³.

Conductometric sensors on the other hand are involved in the measurement of conductivity at a series of applied frequencies. These sensors rely on the changes in conductivity of a film or the bulk material. These sensors, however, are relatively non-selective, however, this platform has become a more viable method of electroanalysis through the modification of electrode surfaces and development of improved instrumentation. These sensors do not require reference electrodes, so their low cost and simplicity make them attractive electrode candidates¹⁶⁴.

Finally, amperometric sensors are named so due to the amperometric measurements made through recording the flow of electrical current in electrochemical cells at an applied potential. Voltammetric sensors, on the other hand, are made when the potential difference scanned across an electrochemical cell, from one pre-set potential to another. The cell current is then recorded as a function of the applied potential (E_{app}). The instrumentation requires controlled-potential equipment, and the electrochemical cell consists of a 2 – 3 electrode system immersed in the electrolyte solution. A background electrolyte is required to decrease solution resistance, eliminate electro-migratory effects and maintain constant ionic strength. The working electrode utilised has a profound influence on the performance of the sensor, where metals and various forms of carbon have been exploited to better suit the application of the sensor. The development of sensors applied in voltammetric measurements is an ever-evolving front, with developments incorporating the use of microelectrodes and microelectrode arrays. Chemically modified sensors, such as biosensors, carbon nanostructure modified and metal nanoparticle modified electrodes, are constantly under development with the aim to improve the overall sensor's performance, and their industrial and clinical applications are becoming of particular interest in recent years¹⁶⁴.

1.6.2. Electrochemical and Analytical Techniques Applied

Throughout this project various electrochemical and analytical techniques were employed for the electrochemical synthesis of Cu nanostructure and AuNPs at a

GCE surface for the accurate and reproducible quantitation of DEX and NAC. These techniques involved the use of cyclic voltammetry for DEX quantitation at bare and Cu modified electrodes, and for the electrochemical characterisation of p-CNOs, BN-doped-CNOs, oxi-CNOS and oxi-BN-doped CNOs, chronoamperometry for the electrodeposition of CuMPs, CuFs and AuNPs at bare and oxi-BN-doped CNO modified GCEs, chronocoulometry for NAC quantitative studies and electrochemical impedance spectroscopy for a further electrochemical characterization of the CuMPs, CuF, AuNPs and AuNP@oxi-BN-doped CNO modified GCEs. Scanning electron microscopy was utilised to visualise and determine the size distributions and morphologies of the CuMP/GCE, CuF/GCE, AuNP/GCE and the AuNP@oxi-BN-doped CNO/GCE.

1.6.2.1. Cyclic Voltammetry

Firstly, cyclic voltammetry (CV) refers to the most versatile and applicable electrochemical technique, which involves the cycling of the electrode potential back and forth between two fixed points. The electrodes are immersed in an unstirred solution, where the resulting current is measured. The working electrode's potential is controlled by measurement against a reference electrode, such as a saturated calomel electrode or a silver/silver chloride (Ag/AgCl) reference electrode. The controlled potential across the working and reference electrodes is considered an excitation signal. This is a linear potential scan with a triangular waveform, as shown in **Figure 7 (A)**, where the potential is swept between two values at either extreme of the CV, known as the switching potentials. As per **Figure 7 (A)** and **(B)**, the voltammogram is firstly scanned in the negative direction from 0.6 V to -0.2 V vs Ag/AgCl, where the direction is reversed, causing the potential to scan back positively. This is carried out at a particular scan rate (volts per unit time), in this case the potential is scanned at a scan rate of 100 mV s^{-1} , or 0.1 V s^{-1} . This can be determined from the slope of the plot of time vs potential in **Figure 7 (A)**. It is noteworthy that CV can be carried out over multiple cycles, as indicated by the red, purple, and blue double headed arrows in **Figure 7 (A)**. A voltammogram is obtained when the current is measured during a potential scan in either direction at the working electrode. This current is the response signal to the potential excitation response. It displays current (I (A)) or current density (J (A cm⁻²)) (y-axis) against potential (x-axis). **Figure 7 (B)** shows the typical cyclic voltammogram of a 5 mM $[\text{Fe}(\text{CN})_6]^{3/4-}$ redox probe in 0.1 M KCl at an unmodified

GCE. As shown in **Figure 7 (A)**, the potential is initially scanned in the negative direction, and when the potential is sufficient to reduce $[\text{Fe}(\text{CN})_6]^{3-}$ to $[\text{Fe}(\text{CN})_6]^{4-}$, a cathodic current signal is observed, in this case at 0.127 V. The same principle applies in the forward direction, where an anodic signal is observed at 0.283 V, where $[\text{Fe}(\text{CN})_6]^{4-}$ is oxidised to $[\text{Fe}(\text{CN})_6]^{3-}$. When the potential is sufficiently strong to reduce a compound, the cathodic current rapidly rises until the concentration of $[\text{Fe}(\text{CN})_6]^{3-}$ is diminished substantially, which causes the current to peak. A decay in the current is then observed as $[\text{Fe}(\text{CN})_6]^{3-}$ ions in the solution surrounding the electrode become depleted due to its electroreduction to $[\text{Fe}(\text{CN})_6]^{4-}$. The scan direction is then switched to the positive direction at -0.2 V for the reverse scan. Here the potential is significantly negative for the reduction of $[\text{Fe}(\text{CN})_6]^{3-}$ so the cathodic current continues despite being scanned in the positive direction. Similarly, when the potential is scanned in the positive direction, the potential becomes strong enough to cause the oxidation of $[\text{Fe}(\text{CN})_6]^{4-}$ to $[\text{Fe}(\text{CN})_6]^{3-}$, resulting in the electrooxidation process, which causes anodic current. Similar to the electroreduction process, the concentration of $[\text{Fe}(\text{CN})_6]^{4-}$ ions at the GCE surface become significantly diminished, causing the current to peak, followed by a decay in the current values. CV is a technique capable of the rapid generation of new oxidation states in the forward scan while proving its fate in the reverse direction, which is an important aspect when studying the voltammetry of coupled reactions¹⁶⁵.

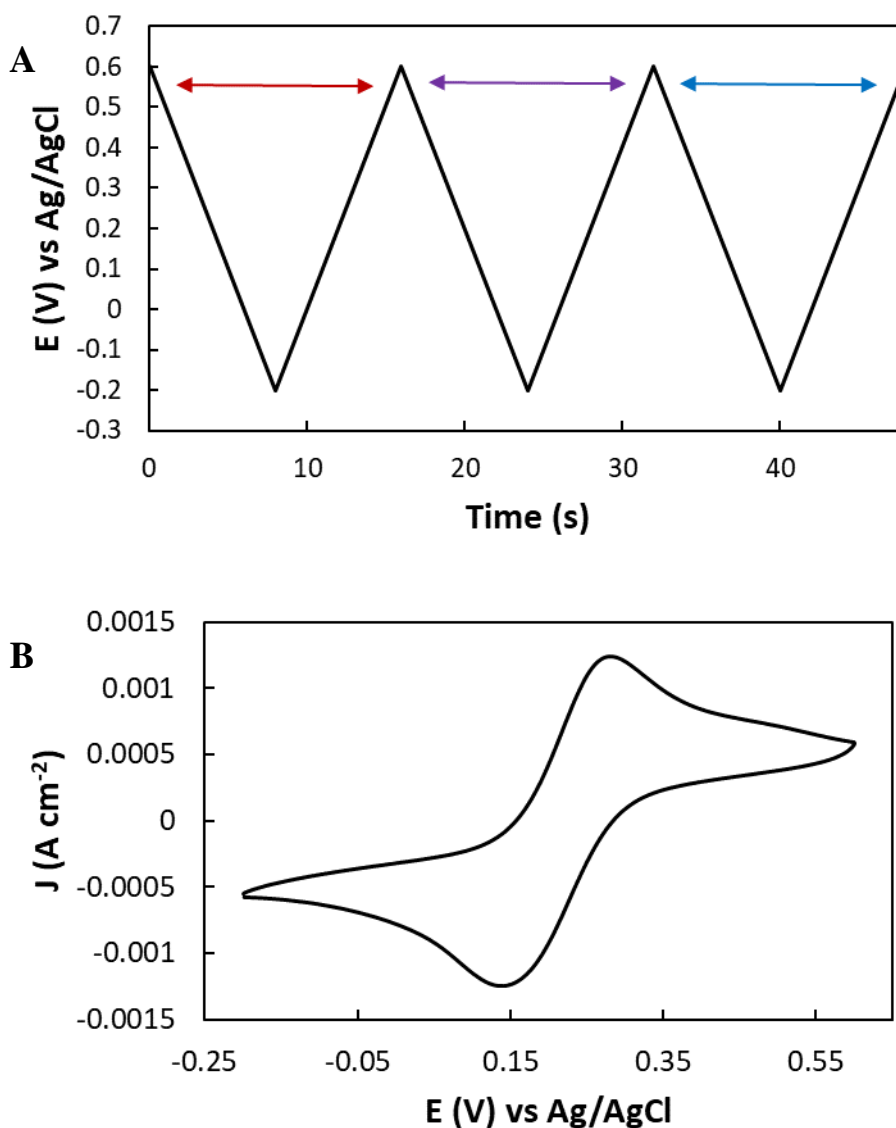


Figure 7. Plots of (A) time vs potential for cycle 1 – 3 (red, purple, and blue arrows) and (B) potential vs current density of the third cycle of the cyclic voltammogram of 5 mM $[\text{Fe}(\text{CN})_6]^{3/4+}$ in 0.1 M KCl at the bare GCE from -0.2 – 0.6 V vs Ag/AgCl at 100 mV s⁻¹.

1.6.2.2. Chronoamperometry and Chronocoulometry

Chronoamperometry (CA) refers to an electrochemical technique where a potential step is applied within a very short, ideally instantaneous, time to an electrode immersed or in contact with an electrolytic system containing a dissolved redox system, where measurements taken result in the flow of electrical current. This can be caused by a change in the composition of the electrolyte at the interface, which is particularly relevant to the concentration of species which make up the redox system. The current measured is initially very large due to being limited by the resistance of

the electrolyte. Part of the current is also used in recharging of the electrochemical double layer. The current then decreases rapidly as the mass transfer of ions from the bulk solution becomes the current limiting factor, where none of the consumed species' flow at the electrode surface. The current is controlled by the concentration profile of the consumed species, where the current profile extends deeper into the electrolyte solution with time. As the profile extends deeper, the slope decreases as a function of time along with the current supported by diffusion flow, resulting in the mathematical relationship defined as the Cottrell equation:¹⁶⁶

$$i = \frac{nFAC_0\sqrt{D}}{\sqrt{\pi t}} \dots\dots\dots(1)$$

where i is current, n is the number of electrons transferred, F is Faraday's constant, A is the electrode surface area, C_0 is concentration, D is the diffusion coefficient, and t is time.

Similarly, in chronocoulometric (CC) experiments, the potential of a working electrode is fixed at a value where the electrochemical reaction is only limited by diffusion, which can also be described using the Cottrell equation:

$$Q = \frac{2nFAC_0\sqrt{D}\sqrt{t}}{\sqrt{\pi}} \dots\dots\dots(2)$$

where Q is charge, n is the number of electrons transferred, F is Faraday's constant, A is the electrode surface area, C_0 is concentration, D is the diffusion coefficient, and t is time. In addition to the charge, the charge Q_{DL} is required to charge the electrochemical double layer from the value which corresponds to the initial electrode potential to the potential set by the step and charge required to convert species present on the electrode during the step, i.e., Q_0 , must be considered. Both Q_{DL} and Q_0 are independent of time and thus can easily be obtained from the Cottrell equation (2) by considering $t = 0$ s. the resulting value is then subtracted. Considering equation 2, CC has a number of applications, such as in determining diffusion coefficients (D), the electrochemical surface area (A) of a particular electrode, and analyte concentrations. In this thesis, CC will be employed in chapter 3 to determine NAC sample concentrations. This method seems equivalent to CA, however important considerations must be taken into account during CC applications. This involves the consideration that charge increases during the experiment, so only charge values significantly far from the application of the potential step can be evaluated as these

values are unaffected by the behaviour of the transient setup, such as distortions. Integration of CC has a smoothing effect, where noise on the response is averaged. These considerations are advantageous over CA measurements as, in addition to the ability to determine the Q_{DL} and Q_0 , these effects are not applicable to CA¹⁶⁶.

1.6.2.3. Electrochemical Impedance Spectroscopy

Electrochemical impedance spectroscopy (EIS) refers to an electrochemical technique that can be used to gain access and information about the kinetic characteristics of electrochemical systems, such as rate constants, diffusion coefficients, capacitances and resistance in a single experiment. However, this technique is restricted to the description of the behaviour of a system which lies in the linear range of electrochemical excitation. These measurements can be contrasted with other methods with non-linear properties, such as CV. EIS measurements require linear behaviour with a potential excitation below 25 mV at room temperature, where the potential dependency of charge-transfer reactions can be approximated as linear. EIS involves a variable-load experimental method and the linear transformation of time-domain signals and responses to frequency domains, with the calculation of the relevant impedance values, described as a complex quotient divided by current, thus the impedance calculation involves results of time-domain excitation at fixed frequencies. Its behaviour over this fixed range of frequencies gives rise to the impedance spectrum, which leads to EIS.¹⁶⁷

The simplest relationship between voltage and current is Ohm's Law, where resistance is independent of both current and voltage. This can be found by applying constant current while measuring the voltage across a resistor, however energy dissipative and storage elements are present in the system. Dependence on I and V cannot directly be expressed using Ohm's Law due to the dependence on time and the potential-current relationship requires a differential equation. Observing the system under variable voltage and current conditions allow the parameter values for the capacitance (C) and conductor length (L) to be determined, making the system more complex. An indirect method of applying Ohm's Law can be used in time-dependant systems due to how all linear differential equations can be transformed into the Laplace-domain, where they are transformed into ordinary equations in terms of complex frequency variables, $s = Re + I$, where $I = \sqrt{-1}$, and ω is the circular frequency¹⁶⁷.

The expression, ($Z_R(s) = R$, $Z_L(s) = sL$, and $Z_C = 1/sC$) can be used to derive the impedance of complex circuits, where the combination of impedances in a circuit follows the same set of rules that apply to combination resistors. Considering this, the equations can be defined directly in the Laplace domain, instead of forming a complex differential equation and then applying the Laplace transformation, thus, impedances add up, and in the case of parallel elements and admittances Y , which are defined as $Y(s) = 1/Z(s)$, also add up¹⁶⁷.

1.6.2.4. Scanning Electron Microscopy

In general, microscopy can be categorised under two main headings: optical microscopy (OM) and scanning electron microscopy (SEM). OM has been used for the last two hundred years, where simple devices were employed with vary limited capabilities. There are numerous differences between OM and SEM which encompasses differences in their properties and features. Firstly, the main difference between OM and SEM is that light is used in OM to view samples directly, while SEM depends on electron emission to view samples. Simple OM uses one lens to view samples, while compound OM utilises two lenses. Typically, OM have the ability to view samples anywhere from $400 - 1000 \times$ the original size of the sample. On the other hand, SEM can reach much higher magnifications of up to $300,000 \times$ the original size, which greatly dwarfs the magnification of OM devices. Both living cells and solid materials can be examined via OM, but few small organic compounds are visible and must be in the solid state. Greyscale images are produced in far more detail via SEM. Images produced from OM however, show the true colours of the samples analysed¹⁶⁸.

SEM works at much higher magnifications up to $300,000 \times$ the original size and can be used as an effective method to analyse organic and inorganic compounds on an nanometre (nm) to micrometre (μm) scale. Some modern SEM can view samples up to $1,000,000 \times$ their original size. SEM works in accordance with Energy Dispersive X-ray-Spectroscopy (EDS) to provide qualitative and semi-quantitative results regarding the composition of the sample in question. Both SEM and EDS, when used in unison have the capability to obtain fundamental information on the composition and morphologies of scanned materials¹⁶⁸.

Analysis is carried out on using SEM equipment, which consists of an electron gun, which is the source used to generate high energy electrons, a column to transport the electrons produced through two or more electromagnetic lenses, a deflection system, an electron detector and a chamber for the sample. A computer system with a screen is then used to display the scanned images. The electron beam is also controlled from the computer system. The device that houses samples contains a pressure system, which in turn allows wet or samples with minimal preparation be viewed. In some instruments, these samples can have a diameter of up to 200 mm and be up to 80 mm tall. As mentioned, SEM analysis is carried out through the application of a beam of high-energy electrons in the range of 100 – 30,000 eV, usually generated through a thermal source. Since the spot size generated from the electron gun is too large for the generation of a sharp image, the SEM is equipped with various lenses to compress the spot and focus the electron beam on the sample. Typically, the spot size is less than 10 nm in diameter, where the focused electrons passed through the final lens interact with the specimen and have the ability to penetrate up to 1 μm deep. These generate signals, and thus, an image is produced. The image generated is formed in a point-by-point manner, which is dependent on the movement of the scan coils which causes movement of the electron beam. The beam typically moves in straight lines to discrete locations until a rectangular pattern of parallel lines is produced at the specimen's surface. This is dependent on the magnification required, i.e. if a higher magnification is required the beam is deflected over a smaller area on the sample. The distance of the final lens from the sample has a direct impact on the magnification. An electron detector is used to detect the high energy electrons emitted from the scanned sample, thus generating the SEM image. Secondary electrons (SE) and backscattered electrons (BSE) are also used in the production of such images, where both are collected in the case of when a positive voltage is applied to the collector screen. On the other hand, only BSE are collected in the case when a negative voltage is applied to the screen. A Scintillator detector is used to collect both SE and BSE¹⁶⁸.

SEM is a technique widely used in both physical chemistry and electrochemistry. In physical chemistry it has been used to investigate the morphology of various nanomaterials, such as carbon nanotubes¹⁶⁹, carbon nano-onions¹¹³ and silica nanoparticles¹⁷⁰ to name a few. Similarly, in electrochemistry SEM is used to investigate the morphology of an electrode surface and/or modifications applied to its

surface such as electrochemical film electrodes¹⁷¹, metal nanoparticle modified electrodes¹⁷² and graphene network modified electrodes¹⁷³ to name some examples. In this project high resolution scanning electron microscopy (HR-SEM) has been exploited to further characterise and analyse the surface morphology of the CuMP and CuF modified GCEs in Chapter 2, and AuNP and AuNP@oxi-BN-doped CNO modified GCEs in Chapter 3.

From considering the effectiveness of DEX and NAC in the treatment of COVID-19 infections and the relatively few reports on their electrochemical quantitation, these drugs were selected for electroanalysis with the overarching aim to develop sensors that can be used to quantitatively analyse these drugs in pharmaceutical formulations. The sensors that will be developed will incorporate the use of various nanomaterials and will be investigated under a variety of conditions to gain a detailed understanding about their electrochemical behaviour, and their effects on their respective analytes.

1.7.0. References

1. Bui, M.; Chou, W. C.; Shorb, J.; Yoon, Y. C., Electrochemistry Basics. In *Analytical Chemistry*, LibreTexts, Ed. LibreTexts: LibreTexts, 2021.
2. Abreuña, H. D.; Kiya, Y.; Henderson, J. C., Batteries and electrochemical capacitors. *Physics Today* **2008**, *61* (12), 43-47.
3. Lucia, U., Overview on fuel cells. *Renewable and Sustainable Energy Reviews* **2014**, *30*, 164-169.
4. Guth, U.; Vonau, W.; Zosel, J., Recent developments in electrochemical sensor application and technology—a review. *Measurement Science and Technology* **2009**, *20* (4), 1-14.
5. Horby, P.; Lim, W. S.; Emberson, J. R.; Mafham, M.; Bell, J. L.; Linsell, L.; Staplin, N.; Brightling, C.; Ustianowski, A.; Elmahi, E.; Prudon, B.; Green, C.; Felton, T.; Chadwick, D.; Rege, K.; Fegan, C.; Chappell, L. C.; Faust, S. N.; Jaki, T.; Jeffery, K.; Montgomery, A.; Rowan, K.; Juszczak, E.; Baillie, J. K.; Haynes, R.; Landray, M. J., Dexamethasone in Hospitalized Patients with Covid-19. *N Engl J Med* **2021**, *384* (8), 693-704.
6. Munch, M. W.; Granholm, A.; Myatra, S. N.; Vijayaraghavan, B.; Cronhjort, M.; Wahlin, R. R.; Jakob, S. M.; Cioccarri, L.; Kjaer, M. N.; Vesterlund, G. K.; Meyhoff, T. S.; Helleberg, M.; Moller, M. H.; Benfield, T.; Venkatesh, B.; Hammond, N.; Micallef, S.; Bassi, A.; John, O.; Jha, V.; Kristiansen, K. T.; Ulrik, C. S.; Jorgensen, V. L.; Smitt, M.; Bestle, M. H.; Andreassen, A. S.; Poulsen, L. M.; Rasmussen, B. S.; Brochner, A. C.; Strom, T.; Moller, A.; Khan, M. S.; Padmanaban, A.; Divatia, J. V.; Saseedharan, S.; Borawake, K.; Kapadia, F.; Dixit, S.; Chawla, R.; Shukla, U.; Amin, P.; Chew, M. S.; Gluud, C.; Lange, T.; Perner, A., Higher vs lower doses of dexamethasone in patients with COVID-19 and severe hypoxia (COVID STEROID 2) trial: Protocol and statistical analysis plan. *Acta Anaesthesiol Scand* **2021**, *65* (6), 834-845.
7. De Flora, S.; Balansky, R.; La Maestra, S., Rationale for the use of N-acetylcysteine in both prevention and adjuvant therapy of COVID-19. *FASEB J* **2020**, *34* (10), 13185-13193.
8. Matuszewski, W. a. T.; M., Graphite Paste-based Enzymatic Glucose Electrode for Flow Injection Analysis. *Analyst* **1988**, *113* (5), 735-738.

9. Zhao, C.; Shao, C.; Li, M.; Jiao, K., Flow-injection analysis of glucose without enzyme based on electrocatalytic oxidation of glucose at a nickel electrode. *Talanta* **2007**, *71* (4), 1769-1773.
10. Pino, F.; Mayorga-Martinez, C. C.; Merkoçi, A., High-performance sensor based on copper oxide nanoparticles for dual detection of phenolic compounds and a pesticide. *Electrochemistry Communications* **2016**, *71*, 33-37.
11. Guin, S. K.; Pillai, J. S.; Ambolikar, A. S.; Saha, A.; Aggarwal, S. K., Template-free electrosynthesis of gold nanoparticles of controlled size dispersion for the determination of lead at ultratrace levels. *RSC Advances* **2013**, *3* (39).
12. Guin, S. K.; Parvathi, K.; Ambolikar, A. S.; Pillai, J. S.; Maity, D. K.; Kannan, S.; Aggarwal, S. K., An insight into the electrocatalysis of uranyl sulphate on gold nanoparticles modified glassy carbon electrode. *Electrochimica Acta* **2015**, *154*, 413-420.
13. Kilele, J. C.; Chokkareddy, R.; Rono, N.; Redhi, G. G., A novel electrochemical sensor for selective determination of theophylline in pharmaceutical formulations. *Journal of the Taiwan Institute of Chemical Engineers* **2020**, *111*, 228-238.
14. Qian, L.; Durairaj, S.; Prins, S.; Chen, A., Nanomaterial-based electrochemical sensors and biosensors for the detection of pharmaceutical compounds. *Biosens Bioelectron* **2021**, *175*, 112836.
15. Buledi, J. A.; Shah, Z.-u.-H.; Mallah, A.; Solangi, A. R., Current Perspective and Developments in Electrochemical Sensors Modified with Nanomaterials for Environmental and Pharmaceutical Analysis. *Current Analytical Chemistry* **2022**, *18* (1), 102-115.
16. Ciotti, M.; Ciccozzi, M.; Terrinoni, A.; Jiang, W. C.; Wang, C.; Bernardini, S., The COVID-19 pandemic. *Critical Reviews in Clinical Laboratory Sciences* **2020**, *57* (6), 365–388.
17. Pokhrel, S.; Chhetri, R., A Literature Review on Impact of COVID-19 Pandemic on Teaching and Learning. *Higher Education for the Future* **2021**, *8* (1), 133–141.
18. Allen, D. W., Covid-19 Lockdown Cost/Benefits: A Critical Assessment of the Literature. *International Journal of the Economics of Business* **2022**, *29* (1), 1-32.
19. Rawal, V.; Kumar, M.; Verma, A.; Pais, J., COVID-19 Lockdown

Impact on Agriculture and Rural Economy. *Social Scientist* **2020**, *48* (3/6 (562-565)), 67-82.

20. Yesudhas, D.; Srivastava, A.; Gromiha, M. M., COVID-19 outbreak: history, mechanism, transmission, structural studies and therapeutics. *Infection* **2021**, *49* (2), 199-213.

21. Liu, J.; Li, Y.; Liu, Q.; Yao, Q.; Wang, X.; Zhang, H.; Chen, R.; Ren, L.; Min, J.; Deng, F.; Yan, B.; Liu, L.; Hu, Z.; Wang, M.; Zhou, Y., SARS-CoV-2 cell tropism and multiorgan infection. *Cell Discov* **2021**, *7* (1), 17.

22. Hasoksuz, M.; Kilic, S.; Sarac, F., Coronaviruses and SARS-COV-2. *Turk J Med Sci* **2020**, *50* (SI-1), 549-556.

23. Velavan, T. P.; Meyer, C. G., The COVID-19 epidemic. *Trop Med Int Health* **2020**, *25* (3), 278-280.

24. Vasireddy, D.; Vanaparthi, R.; Mohan, G.; Malayala, S. V.; Atluri, P., Review of COVID-19 Variants and COVID-19 Vaccine Efficacy: What the Clinician Should Know? *J Clin Med Res* **2021**, *13* (6), 317-325.

25. Li, F., Structure, Function, and Evolution of Coronavirus Spike Proteins. *Annu Rev Virol* **2016**, *3* (1), 237-261.

26. Navabshan, I.; Sakthivel, B.; Pandiyan, R.; Antoniraj, M. G.; Dharmaraj, S.; Ashokkumar, V.; Khoo, K. S.; Chew, K. W.; Sugumaran, A.; Show, P. L., Computational Lock and Key and Dynamic Trajectory Analysis of Natural Biophors Against COVID-19 Spike Protein to Identify Effective Lead Molecules. *Mol Biotechnol* **2021**, *63* (10), 898-908.

27. Hofmann, H.; Pohlmann, S., Cellular entry of the SARS coronavirus. *Trends Microbiol* **2004**, *12* (10), 466-72.

28. Gralinski, L. E.; Menachery, V. D., Return of the Coronavirus: 2019-nCoV. *Viruses* **2020**, *12* (2).

29. Wang, H.; Yang, P.; Liu, K.; Guo, F.; Zhang, Y.; Zhang, G.; Jiang, C., SARS coronavirus entry into host cells through a novel clathrin- and caveolae-independent endocytic pathway. *Cell Res* **2008**, *18* (2), 290-301.

30. Wang, M. Y.; Zhao, R.; Gao, L. J.; Gao, X. F.; Wang, D. P.; Cao, J. M., SARS-CoV-2: Structure, Biology, and Structure-Based Therapeutics Development. *Front Cell Infect Microbiol* **2020**, *10*, 587269.

31. Tenchov, R.; Zhou, Q. A., Intrinsically Disordered Proteins: Perspective on COVID-19 Infection and Drug Discovery. *ACS Infect Dis* **2022**, *8* (3), 422-432.

32. Giri, R.; Bhardwaj, T.; Shegane, M.; Gehi, B. R.; Kumar, P.; Gadhave, K.; Oldfield, C. J.; Uversky, V. N., Understanding COVID-19 via comparative analysis of dark proteomes of SARS-CoV-2, human SARS and bat SARS-like coronaviruses. *Cell Mol Life Sci* **2021**, *78* (4), 1655-1688.
33. Lotfi, M.; Hamblin, M. R.; Rezaei, N., COVID-19: Transmission, prevention, and potential therapeutic opportunities. *Clin Chim Acta* **2020**, *508*, 254-266.
34. van Doremalen, N.; Bushmaker, T.; Morris, D. H.; Holbrook, M. G.; Gamble, A.; Williamson, B. N.; Tamin, A.; Harcourt, J. L.; Thornburg, N. J.; Gerber, S. I.; Lloyd-Smith, J. O.; de Wit, E.; Munster, V. J., Aerosol and Surface Stability of SARS-CoV-2 as Compared with SARS-CoV-1. *New England Journal of Medicine* **2020**, *382* (16), 1564-1567.
35. Galbadage, T.; Peterson, B. M.; Gunasekera, R. S., Does COVID-19 Spread Through Droplets Alone? *Front Public Health* **2020**, *8*, 163.
36. Sheikhi, K.; Shirzadfar, H.; Sheikhi, M., A Review on Novel Coronavirus(Covid-19): Symptoms, Transmission and Diagnosis Tests. *Research in Infectious Diseases and Tropical Medicine* **2020**, *2* (1), 1-8.
37. Salian, V. S.; Wright, J. A.; Vedell, P. T.; Nair, S.; Li, C.; Kandimalla, M.; Tang, X.; Carmona Porquera, E. M.; Kalari, K. R.; Kandimalla, K. K., COVID-19 Transmission, Current Treatment, and Future Therapeutic Strategies. *Mol Pharm* **2021**, *18* (3), 754-771.
38. Duguid, J. P., The Numbers and the Sites of Origin of the Droplets Expelled During Expiratory Activities. *Edinburgh Medical Journal* **1945**, *52* (22), 385-401.
39. Zayas, G.; Chiang, M. C.; Wong, E.; MacDonald, F.; Lange, C. F.; Senthilselvan, A.; King, M., Cough aerosol in healthy participants: fundamental knowledge to optimize droplet-spread infectious respiratory disease management. *BMC Pulmonary Medicine* **2012**, *12* (1), 11.
40. Heneka, M. T.; Golenbock, D.; Latz, E.; Morgan, D.; Brown, R., Immediate and long-term consequences of COVID-19 infections for the development of neurological disease. *Alzheimers Res Ther* **2020**, *12* (1), 69.
41. Helms, J.; Kremer, S.; Merdji, H.; Clere-Jehl, R.; Schenck, M.; Kummerlen, C.; Collange, O.; Boulay, C.; Fafi-Kremer, S.; Ohana, M.; Anheim, M.; Meziani, F., Neurologic Features in Severe SARS-CoV-2 Infection. *New England Journal of Medicine* **2020**, *382* (23), 2268-2270.

42. Wang, C.; Wang, Z.; Wang, G.; Lau, J. Y. N.; Zhang, K.; Li, W., COVID-19 in early 2021: current status and looking forward. *Signal Transduction and Targeted Therapy* **2021**, *6* (114), 1-14.
43. Ansems, K.; Grundeis, F.; Dahms, K.; Mikolajewska, A.; Thieme, V.; Piechotta, V.; Metzendorf, M. I.; Stegemann, M.; Benstoem, C.; Fichtner, F., Remdesivir for the treatment of COVID-19. *Cochrane Database of Systematic Reviews* **2021**, *8*, 1-94.
44. Dougan, M.; Nirula, A.; Azizad, M.; Mocherla, B.; Gottlieb, R. L.; Chen, P.; Hebert, C.; Perry, R.; Boscia, J.; Heller, B.; Morris, J.; Crystal, C.; Igbinalolor, A.; Huhn, G.; Cardona, J.; Shawa, I.; Kumar, P.; Adams, A. C.; Van Naarden, J.; Custer, K. L.; Durante, M.; Oakley, G.; Schade, A. E.; Holzer, T. R.; Ebert, P. J.; Higgs, R. E.; Kallewaard, N. L.; Sabo, J.; Patel, D. R.; Dabora, M. C.; Klekotka, P.; Shen, L.; Skovronsky, D. M.; Investigators, B.-. Bamlanivimab plus Etesevimab in Mild or Moderate Covid-19. *N Engl J Med* **2021**, *385* (15), 1382-1392.
45. Ganesh, R.; Philpot, L. M.; Bierle, D. M.; Anderson, R. J.; Arndt, L. L.; Arndt, R. F.; Culbertson, T. L.; Destro Borgen, M. J.; Hanson, S. N.; Kennedy, B. D.; Kottke, B. B.; Larsen, J. J.; Ramar, P.; Rosedahl, J. K.; Seville, M. T.; Speicher, L. L.; Tulledge-Scheitel, S. M.; Wilker, C. G.; Razonable, R. R., Real-World Clinical Outcomes of Bamlanivimab and Casirivimab-Imdevimab Among High-Risk Patients With Mild to Moderate Coronavirus Disease 2019. *J Infect Dis* **2021**, *224* (8), 1278-1286.
46. Pandolfi, S.; Simonetti, V.; Ricevuti, G.; Chirumbolo, S., Paracetamol in the home treatment of early COVID-19 symptoms: A possible foe rather than a friend for elderly patients? *J Med Virol* **2021**, *93* (10), 5704-5706.
47. Rinott, E.; Kozer, E.; Shapira, Y.; Bar-Haim, A.; Youngster, I., Ibuprofen use and clinical outcomes in COVID-19 patients. *Clin Microbiol Infect* **2020**, *26* (9), 1259 e5-1259 e7.
48. Lammers, T.; Sofias, A. M.; van der Meel, R.; Schiffelers, R.; Storm, G.; Tacke, F.; Koschmieder, S.; Brümmendorf, T. H.; Kiessling, F.; Metselaar, J. M., Dexamethasone nanomedicines for COVID-19. *Nature Nanotechnology* **2020**, *15* (8), 622-624.
49. Johnson, R. M.; Vinetz, J. M., Dexamethasone in the management of covid - 19. *BMJ* **2020**, *370*, m2648.

50. Ahmed, M. H.; Hassan, A., Dexamethasone for the Treatment of Coronavirus Disease (COVID-19): a Review. *SN Compr Clin Med* **2020**, *2* (12), 2637-2646.
51. Shi, Z.; Puyo, C. A., N-Acetylcysteine to Combat COVID-19: An Evidence Review. *Ther Clin Risk Manag* **2020**, *16*, 1047-1055.
52. Assimakopoulos, S. F.; Aretha, D.; Komninos, D.; Dimitropoulou, D.; Lagadinou, M.; Leonidou, L.; Oikonomou, I.; Mouzaki, A.; Marangos, M., N-acetylcysteine reduces the risk for mechanical ventilation and mortality in patients with COVID-19 pneumonia: a two-center retrospective cohort study. *Infect Dis (Lond)* **2021**, *53* (11), 847-854.
53. Johnson, D. B.; Lopez, M. J.; Kelley, B., Dexamethasone. *StatPearls* **2022**.
54. Keeney, G. E.; Gray, M. P.; Morrison, A. K.; Levas, M. N.; Kessler, E. A.; Hill, G. D.; Gorelick, M. H.; Jackson, J. L., Dexamethasone for Acute Asthma Exacerbations in Children: A Meta-analysis. *Pediatrics* **2014**, *133* (3), 493-499.
55. De Gans, J.; Van De BEEK, D., Dexamethasone in Adults with Bacterial Meningitis. *The New England Journal of Medicine* **2002**, *347* (20), 1549-1556.
56. Saraya, M. A.; Amal, A. E.-A. I., Dexamethasone as adjunctive therapy for treatment of varicella pneumonia. *Egyptian Journal of Chest Diseases and Tuberculosis* **2012**, *61* (3), 9-13.
57. Meikle, A. W.; Tyler, F. H., Potency and duration of action of glucocorticoids. Effects of hydrocortisone, prednisone and dexamethasone on human pituitary-adrenal function. *The American Journal of Medicine* **1977**, *63* (2), 200-207.
58. Becker, D. E., Basic and Clinical Pharmacology of Glucocorticosteroids. *Anesthesia Progress* **2013**, *60* (1), 25-32.
59. Coates, T. D.; Wolach, B.; Tzeng, D. Y.; Higgins, C.; Baehner, R. L.; Boxer, L. A., The mechanism of action of the antiinflammatory agents dexamethasone and Auranofin in human polymorphonuclear leukocytes. *Blood* **1983**, *62* (5), 1070-1077.
60. Johnson, D. B.; Lopez, M. J.; Kelley, B., *Dexamethasone*. StatPearls Publishing, Treasure Island (FL): 2021.
61. Larson, A. A.; Syverud, B. C.; Florida, S. E.; Rodriguez, B. L.; Pantelic, M. N.; Larkin, L. M., Effects of Dexamethasone Dose and Timing on Tissue-Engineered Skeletal Muscle Units. *Cells Tissues Organs* **2018**, *205* (4), 197-207.
62. Patel, P.; Tanna, S.; Mulla, H.; Kairamkonda, V.; Pandya, H.; Lawson, G., Dexamethasone quantification in dried blood spot samples using LC-MS: The

potential for application to neonatal pharmacokinetic studies. *J Chromatogr B Analyt Technol Biomed Life Sci* **2010**, 878 (31), 3277-82.

63. Friedrich, R. B.; Ravello, A.; Cichota, L. C.; Rolim, C. M. B.; Beck, R. C. R., Validation of a simple and rapid UV spectrophotometric method for dexamethasone assay in tablets. *Química Nova* **2009**, 32 (4).

64. Stella, R.; Bovo, D.; Mastrorilli, E.; Pezzolato, M.; Bozzetta, E.; Biancotto, G., Anabolic treatments in bovines: quantification of plasma protein markers of dexamethasone administration. *PROTEOMICS* **2021**, 21 (16), 2000238.

65. Van den hauwe, O.; Perez, J. C.; Claereboudt, J.; Peteghem, C. V., Simultaneous determination of betamethasone and dexamethasone residues in bovine liver by liquid chromatography/tandem mass spectrometry. *Rapid Communications in Mass Spectrometry* **2001**, 15 (11), 857-861.

66. Samtani, M. N.; Jusko, W. J., Quantification of dexamethasone and corticosterone in rat biofluids and fetal tissue using highly sensitive analytical methods: assay validation and application to a pharmacokinetic study. *Biomedical Chromatography* **2007**, 21 (6), 585-597.

67. Reckers, A.; Wu, A. H. B.; Ong, C. M.; Gandhi, M.; Metcalfe, J.; Gerona, R., A combined assay for quantifying remdesivir and its metabolite, along with dexamethasone, in serum. *J Antimicrob Chemother* **2021**, 76 (7), 1865-1873.

68. Youssef, G.; Ali, M. A.; Alaa, N.; Makin, B.; Waly, M.; AbouSetta, A., N-acetyl-cysteine in anovulatory women: the impact of postcoital test. *Middle East Fertility Society Journal* **2006**, 11 (2), 109–112.

69. Zafarullaha, M.; Li, M. Q.; Sylvester, J.; Ahmadb, M., Molecular mechanisms of N-acetylcysteine action. *Cellular and Molecular Life Sciences* **2003**, 60, 6-20.

70. Dilger, R. N.; Baker, D. H., Oral N-acetyl-l-cysteine is a safe and effective precursor of cysteine1. *Journal of Animal Science* **2007**, 85 (7), 1712-1718.

71. Mokhtari, V.; Afsharian, P.; Shahhoseini, M.; Kalantar, S. M.; Moini, A., A Review on Various Uses of N-Acetyl Cysteine. *Cell Journal* **2016**, 19 (1), 11-17.

72. De Vries, N.; De Flora, S., N-acetyl-l-cysteine. *Journal of Cellular Biochemistry* **1993**, 53 (S17F), 270-277.

73. Elgindy, E. A.; El-Huseiny, A. M.; Mostafa, M. I.; Gaballah, A. M.; Ahmed, T. A., N-acetyl cysteine: could it be an effective adjuvant therapy in ICSI cycles? A preliminary study. *Reprod Biomed Online* **2010**, 20 (6), 789-96.

74. Gaucher, C.; Boudier, A.; Bonetti, J.; Clarot, I.; Leroy, P.; Parent, M., Glutathione: Antioxidant Properties Dedicated to Nanotechnologies. *Antioxidants (Basel)* **2018**, *7* (5), 1-21.
75. McBean, G. J., Cysteine, Glutathione, and Thiol Redox Balance in Astrocytes. *Antioxidants (Basel)* **2017**, *6* (3), 1-13.
76. Arranz, L.; Fernandez, C.; Rodriguez, A.; Ribera, J. M.; De la Fuente, M., The glutathione precursor N-acetylcysteine improves immune function in postmenopausal women. *Free Radic Biol Med* **2008**, *45* (9), 1252-62.
77. Noctor, G.; Arisi, G. G. M.; Jouanin, L.; Kunert, K. J.; Rennenberg, H.; Foyer, C. H., Glutathione: biosynthesis, metabolism and relationship to stress tolerance explored in transformed plants. *Journal of Experimental Botany* **1998**, *49* (321), 623–647.
78. Meister, A., Glutathione Biosynthesis and Its Inhibition. In *Methods in Enzymology*, Academic Press, 1995; Vol. 252, pp 26-30.
79. Borgohain, R.; Yang, J.; Selegue, J. P.; Kim, D. Y., Controlled synthesis, efficient purification, and electrochemical characterization of arc-discharge carbon nano-onions. *Carbon* **2014**, *66*, 272-284.
80. Dodd Mooz, E.; Meister, A., Tripeptide (Glutathione) Synthetase. Purification, Properties, and Mechanism of Action. *Biochemistry* **1967**, *6* (6), 1722-1734.
81. Galano, A.; Alvarez-Idaboy, J. R., Glutathione: mechanism and kinetics of its non-enzymatic defense action against free radicals. *RSC Advances* **2011**, *1* (9).
82. Leopoldini, M.; Russo, N.; Toscano, M., The molecular basis of working mechanism of natural polyphenolic antioxidants. *Food Chemistry* **2011**, *125* (2), 288-306.
83. Galano, A.; Francisco-Marquez, M., Peroxyl-Radical-Scavenging Activity of Garlic: 2-Propenesulfenic Acid versus Allicin. *Journal of Physical Chemistry B*. **2009**, *113* (49), 16077–16081.
84. Sies, H.; Berndt, C.; Jones, D. P., Oxidative Stress. *Annu Rev Biochem* **2017**, *86*, 715-748.
85. Thom, S. R., Oxidative stress is fundamental to hyperbaric oxygen therapy. *J Appl Physiol (1985)* **2009**, *106* (3), 988-95.
86. Rossignol, D. A.; Rossignol, L. W.; James, S. J.; Melnyk, S.; Mumper, E., The effects of hyperbaric oxygen therapy on oxidative stress, inflammation, and

- symptoms in children with autism: an open-label pilot study. *BMC Pediatr* **2007**, *7*, 36.
87. Issels, R. D.; Nagele, A.; Eckert, K.-G.; Willmanns, W., Promotion of cystine uptake and its utilization for glutathione biosynthesis induced by cysteamine and N-acetylcysteine. *Biochemical Pharmacology* **1988**, *37* (5), 881-888.
88. Anderson, M. E.; Powrie, F.; Puri, R. N.; Meister, A., Glutathione monoethyl ester: Preparation, uptake by tissues, and conversion to glutathione. *Archives of Biochemistry and Biophysics* **1985**, *239* (2), 538-548.
89. Ploemen, J. H. T. M.; Van Schanke, A.; Van Ommen, B.; Van Bladeren, P. J., Reversible Conjugation of Ethacrynic Acid with Glutathione and Human Glutathione S-Transferase PI-1. *Cancer Research* **1994**, *54*, 915-919.
90. Wu, W.; Goldstein, G.; Adams, C.; Matthews, R. H.; Ercal, N., Separation and quantification of N-acetyl-L-cysteine and N-acetyl-cysteine-amide by HPLC with fluorescence detection. *Biomedical Chromatography* **2006**, *20* (5), 415-422.
91. Lochmann, D.; Stadlhofer, S.; Weyermann, J.; Zimmer, A., New protamine quantification method in microtiter plates using o-phthaldialdehyde/N-acetyl-L-cysteine reagent. *Int J Pharm* **2004**, *283* (1-2), 11-7.
92. Peralta-Videa, J. R.; Zhao, L.; Lopez-Moreno, M. L.; de la Rosa, G.; Hong, J.; Gardea-Torresdey, J. L., Nanomaterials and the environment: a review for the biennium 2008-2010. *J Hazard Mater* **2011**, *186* (1), 1-15.
93. Khin, M. M.; Nair, A. S.; Babu, V. J.; Murugan, R.; Ramakrishna, S., A review on nanomaterials for environmental remediation. *Energy & Environmental Science* **2012**, *5* (8).
94. Barreto, J. A.; O'Malley, W.; Kubeil, M.; Graham, B.; Stephan, H.; Spiccia, L., Nanomaterials: Applications in Cancer Imaging and Therapy. *Advanced Materials* **2011**, *23* (12), H18-H40.
95. Feng, H. P.; Tang, L.; Zeng, G. M.; Zhou, Y.; Deng, Y. C.; Ren, X.; Song, B.; Liang, C.; Wei, M. Y.; Yu, J. F., Core-shell nanomaterials: Applications in energy storage and conversion. *Adv Colloid Interface Sci* **2019**, *267*, 26-46.
96. Chen, A.; Chatterjee, S., Nanomaterials based electrochemical sensors for biomedical applications. *Chem Soc Rev* **2013**, *42* (12), 5425-38.

97. Van de Voorde, M.; Tulinski, M.; Jurczyk, M., Engineered Nanomaterials: a Discussion of the Major Categories of Nanomaterials. In *Metrology and Standardization of Nanotechnology*, 2017; pp 49-74.
98. Dai, L.; Chang, D. W.; Baek, J.-B.; Lu, W., Carbon Nanomaterials for Advanced Energy Conversion and Storage. *Small* **2012**, 8 (8), 1130-1166.
99. Hong, G.; Diao, S.; Antaris, A. L.; Dai, H., Carbon Nanomaterials for Biological Imaging and Nanomedicinal Therapy. *Chem Rev* **2015**, 115 (19), 10816-906.
100. Bartelmeß, J.; Giordani, S., Carbon nano-onions (multi-layer fullerenes): chemistry and applications. *Beilstein J Nanotechnol* **2014**, 5, 1980-98.
101. Yang, C.; Denno, M. E.; Pyakurel, P.; Venton, B. J., Recent trends in carbon nanomaterial-based electrochemical sensors for biomolecules: A review. *Anal Chim Acta* **2015**, 887, 17-37.
102. Abbas, Q.; Raza, R.; Shabbir, I.; Olabi, A. G., Heteroatom doped high porosity carbon nanomaterials as electrodes for energy storage in electrochemical capacitors: A review. *Journal of Science: Advanced Materials and Devices* **2019**, 4 (3), 341-352.
103. Yang, Y.; Yang, X.; Yang, Y.; Yuan, Q., Aptamer-functionalized carbon nanomaterials electrochemical sensors for detecting cancer relevant biomolecules. *Carbon* **2018**, 129, 380-395.
104. Bagheri, H.; Khoshsafar, H.; Amidi, S.; Hosseinzadeh Ardakani, Y., Fabrication of an electrochemical sensor based on magnetic multi-walled carbon nanotubes for the determination of ciprofloxacin. *Analytical Methods* **2016**, 8 (16), 3383-3390.
105. Yang, J.; Zhang, Y.; Kim, D. Y., Electrochemical sensing performance of nanodiamond-derived carbon nano-onions: Comparison with multiwalled carbon nanotubes, graphite nanoflakes, and glassy carbon. *Carbon* **2016**, 98, 74-82.
106. Adorinni, S.; Rozhin, P.; Marchesan, S., Smart Hydrogels Meet Carbon Nanomaterials for New Frontiers in Medicine. *Biomedicines* **2021**, 9 (5), 570.
107. Mykhailiv, O.; Zubyk, H.; Plonska-Brzezinska, M. E., Carbon nano-onions: Unique carbon nanostructures with fascinating properties and their potential applications. *Inorganica Chimica Acta* **2017**, 468, 49-66.
108. Yang, J.; Kim, S. H.; Kwak, S. K.; Song, H. K., Curvature-Induced Metal-Support Interaction of an Islands-by-Islands Composite of Platinum Catalyst and

Carbon Nano-onion for Durable Oxygen Reduction. *ACS Appl Mater Interfaces* **2017**, *9* (28), 23302-23308.

109. Suryawanshi, S. R.; Kaware, V.; Chakravarty, D.; Walke, P. S.; More, M. A.; Joshi, K.; Rout, C. S.; Late, D. J., Pt-nanoparticle functionalized carbon nano-onions for ultra-high energy supercapacitors and enhanced field emission behaviour. *RSC Advances* **2015**, *5* (99), 80990-80997.

110. Lu, H.; Eggers, P. K.; Gibson, C. T.; Duan, X.; Lamb, R. N.; Raston, C. L.; Chua, H. T., Facile synthesis of electrochemically active Pt nanoparticle decorated carbon nano onions. *New Journal of Chemistry* **2015**, *39* (2), 915-920.

111. Chmiola, J.; Yushin, G.; Gogotsi, Y.; Portet, C.; Simon, P.; Taberna, P. L., Anomalous Increase in Carbon Capacitance at Pore Sizes Less than 1 Nanometer. *American Association for the Advancement of Science* **2006**, *313* (5794), 1760-1763.

112. Thomas, M. P.; Wanninayake, N.; De Alwis Goonatilleke, M.; Kim, D. Y.; Guiton, B. S., Direct imaging of heteroatom dopants in catalytic carbon nano-onions. *Nanoscale* **2020**, *12* (10), 6144-6152.

113. Mykhailiv, O.; Brzezinski, K.; Sulikowski, B.; Olejniczak, Z.; Gras, M.; Lota, G.; Molina-Ontoria, A.; Jakubczyk, M.; Echegoyen, L.; Plonska-Brzezinska, M. E., Boron-Doped Polygonal Carbon Nano-Onions: Synthesis and Applications in Electrochemical Energy Storage. *Chemistry* **2017**, *23* (29), 7132-7141.

114. Camisasca, A.; Sacco, A.; Brescia, R.; Giordani, S., Boron/Nitrogen-Codoped Carbon Nano-Onion Electrocatalysts for the Oxygen Reduction Reaction. *ACS Applied Nano Materials* **2018**, *1* (10), 5763-5773.

115. Mohapatra, D.; Dhakal, G.; Sayed, M. S.; Subramanya, B.; Shim, J. J.; Parida, S., Sulfur Doping: Unique Strategy To Improve the Supercapacitive Performance of Carbon Nano-onions. *ACS Appl Mater Interfaces* **2019**, *11* (8), 8040-8050.

116. Paraknowitsch, J. P.; Thomas, A., Doping carbons beyond nitrogen: an overview of advanced heteroatom doped carbons with boron, sulphur and phosphorus for energy applications. *Energy & Environmental Science* **2013**, *6* (10).

117. Mohapatra, D.; Muhammad, O.; Sayed, M. S.; Parida, S.; Shim, J.-J., In situ nitrogen-doped carbon nano-onions for ultrahigh-rate asymmetric supercapacitor. *Electrochimica Acta* **2020**, *331*.

118. Pallavolu, M. R.; Gaddam, N.; Banerjee, A. N.; Nallapureddy, R. R.; Joo, S. W., Superior energy-power performance of N-doped carbon nano-onions-based

asymmetric and symmetric supercapacitor devices. *International Journal of Energy Research* **2021**, *46* (2), 1234-1249.

119. Han, L.-N.; Wei, X.; Zhu, Q.-C.; Xu, S.-M.; Wang, K.-X.; Chen, J.-S., Nitrogen-doped carbon nets with micro/mesoporous structures as electrodes for high-performance supercapacitors. *Journal of Materials Chemistry A* **2016**, *4* (42), 16698-16705.

120. Goclon, J., Manipulation of structural and electronic properties of B-doped carbon nano-onions based on DFT modelling. *Applied Surface Science* **2020**, 532.

121. Mutuma, B. K.; Matsoso, B. J.; Momodu, D.; Oyedotun, K. O.; Coville, N. J.; Manyala, N., Deciphering the Structural, Textural, and Electrochemical Properties of Activated BN-Doped Spherical Carbons. *Nanomaterials (Basel)* **2019**, *9* (3).

122. Takagi, K.; Natsui, K.; Watanabe, T.; Einaga, Y., Increasing the Electric Double-Layer Capacitance in Boron-Doped Diamond Electrodes. *ChemElectroChem* **2019**, *6* (6), 1683-1687.

123. Bartelmess, J.; Quinn, S. J.; Giordani, S., Carbon nanomaterials: multi-functional agents for biomedical fluorescence and Raman imaging. *Chem Soc Rev* **2015**, *44* (14), 4672-98.

124. Liu, Y.; Kim, D. Y., Enhancement of Capacitance by Electrochemical Oxidation of Nanodiamond Derived Carbon Nano-Onions. *Electrochimica Acta* **2014**, *139*, 82-87.

125. Camisasca, A.; Giordani, S., Carbon nano-onions in biomedical applications: Promising theranostic agents. *Inorganica Chimica Acta* **2017**, *468*, 67-76.

126. Fan, Z.; Huang, X.; Tan, C.; Zhang, H., Thin metal nanostructures: synthesis, properties and applications. *Chem Sci* **2015**, *6* (1), 95-111.

127. Rao, C. N. R.; Kulkarni, G. U.; Thomas, P. J.; Edwards, P. P., Metal nanoparticles and their assemblies. *Chemical Society Reviews* **2000**, *29*, 27-35.

128. Veerapandian, S.; Jang, W.; Seol, J. B.; Wang, H.; Kong, M.; Thiyagarajan, K.; Kwak, J.; Park, G.; Lee, G.; Suh, W.; You, I.; Kilic, M. E.; Giri, A.; Beccai, L.; Soon, A.; Jeong, U., Hydrogen-doped viscoplastic liquid metal microparticles for stretchable printed metal lines. *Nat Mater* **2021**, *20* (4), 533-540.

129. Chirumamilla, M.; Gopalakrishnan, A.; Toma, A.; Proietti Zaccaria, R.; Krahn, R., Plasmon resonance tuning in metal nanostars for surface enhanced Raman scattering. *Nanotechnology* **2014**, *25* (23), 235303.

130. Xu, F.; Shang, W.; Ma, G.; Zhu, Y.; Wu, M., Metal organic framework wrapped gold nanourchin assembled on filter membrane for fast and sensitive SERS analysis. *Sensors and Actuators B: Chemical* **2021**, 326.
131. Abeles, B.; Sheng, P.; Coutts, M. D.; Arie, Y., Structural and electrical properties of granular metal films. *Advances in Physics* **1975**, 24 (3), 407-461.
132. Lu, Y.; Liang, X.; Niyungeko, C.; Zhou, J.; Xu, J.; Tian, G., A review of the identification and detection of heavy metal ions in the environment by voltammetry. *Talanta* **2018**, 178, 324-338.
133. Piñón-Segundo, E.; Mendoza-Muñoz, N.; Quintanar-Guerrero, D., Nanoparticles as Dental Drug-Delivery Systems. In *Nanobiomaterials in Clinical Dentistry*, 2013; pp 475-495.
134. Male, K. B.; Hrapovic, S.; Liu, Y.; Wang, D.; Luong, J. H. T., Electrochemical detection of carbohydrates using copper nanoparticles and carbon nanotubes. *Analytica Chimica Acta* **2004**, 516 (1-2), 35-41.
135. Sawan, S.; Maalouf, R.; Errachid, A.; Jaffrezic-Renault, N., Metal and metal oxide nanoparticles in the voltammetric detection of heavy metals: A review. *TrAC Trends in Analytical Chemistry* **2020**, 131.
136. Sreeprasad, T. S.; Nguyen, P.; Kim, N.; Berry, V., Controlled, defect-guided, metal-nanoparticle incorporation onto MoS₂ via chemical and microwave routes: electrical, thermal, and structural properties. *Nano Lett* **2013**, 13 (9), 4434-41.
137. Prodromidis, M. I.; Florou, A. B.; Tzouwara-Karayanni, S. M.; Karayannis, M. I., The Importance of Surface Coverage in the Electrochemical Study of Chemically Modified Electrodes. *Electroanalysis* **2000**, 12 (18), 1498-1501.
138. Lee, K. J.; McCarthy, B. D.; Dempsey, J. L., On decomposition, degradation, and voltammetric deviation: the electrochemist's field guide to identifying precatalyst transformation. *Chem Soc Rev* **2019**, 48 (11), 2927-2945.
139. Jovanovski, V.; Xhanari, K.; Finsgar, M., Editorial: Recent advances of metal-film electrodes for trace electrochemical analysis. *Front Chem* **2022**, 10, 973672.
140. Heitzmann, M.; Bucher, C.; Moutet, J.-C.; Pereira, E.; Rivas, B. L.; Royal, G.; Saint-Aman, E., Complexation of poly(pyrrole-EDTA like) film modified electrodes: Application to metal cations electroanalysis. *Electrochimica Acta* **2007**, 52 (9), 3082-3087.

141. March, G.; Nguyen, T. D.; Piro, B., Modified electrodes used for electrochemical detection of metal ions in environmental analysis. *Biosensors (Basel)* **2015**, 5 (2), 241-75.
142. Siegel, J.; Kvítek, O.; Ulbrich, P.; Kolská, Z.; Slepíčka, P.; Švorčík, V., Progressive approach for metal nanoparticle synthesis. *Materials Letters* **2012**, 89, 47-50.
143. Khodashenas, B.; Ghorbani, H. R., Synthesis of copper nanoparticles : An overview of the various methods. *Korean Journal of Chemical Engineering* **2014**, 31 (7), 1105-1109.
144. Nikolić, N. D.; Popov, K. I.; Pavlović, L. J.; Pavlović, M. G., Morphologies of copper deposits obtained by the electrodeposition at high overpotentials. *Surface and Coatings Technology* **2006**, 201 (3-4), 560-566.
145. Tarolla, N. E.; Voci, S.; Reyes-Morales, J.; Pendergast, A. D.; Dick, J. E., Electrodeposition of ligand-free copper nanoparticles from aqueous nanodroplets. *Journal of Materials Chemistry A* **2021**, 9 (35), 20048-20057.
146. Zhou, X. J.; Harmer, A. J.; Heinig, N. F.; Leung, K. T., Parametric Study on Electrochemical Deposition of Copper Nanoparticles on an Ultrathin Polypyrrole Film Deposited on a Gold Film Electrode. *Langmuir* **2004**, 20 (12), 5109-5113.
147. Guin, S. K.; Sharma, H. S.; Aggarwal, S. K., Electrosynthesis of lead nanoparticles on template free gold surface by potentiostatic triple pulse technique. *Electrochimica Acta* **2010**, 55 (3), 1245-1257.
148. Beach, R. D.; Conlan, R. W.; Godwin, M. C.; Moussy, F., Towards a Miniature Implantable In Vivo Telemetry Monitoring System Dynamically Configurable as a Potentiostat or Galvanostat for Two- and Three-Electrode Biosensors. *IEEE Transactions on Instrumentation and Measurement* **2005**, 54 (1), 61-72.
149. Cho, K. H.; Lee, S.-M.; Choi, K. C., Wall Voltage and Priming Effect Due to Auxiliary Electrode in AC PDP With Auxiliary Electrode. *IEEE Transactions on Plasma Science* **2007**, 35 (5), 1567-1573.
150. Janata, J., *Principles of Chemical Sensors*. 2 ed.; Springer Science + Business Media: Springer Science + Business Media, 2009; p 1-388.
151. Kissinger, P. T.; Heineman, W. R., *Laboratory Techniques in Electroanalytical Chemistry*. 2 ed.; Marcel Dekker, Inc.: 1996.

152. East, G. A.; del Valle, M. A., Easy-to-Make Ag/AgCl Reference Electrode. *Journal of Chemical Education* **2000**, *77* (1), 97.
153. Vitello, J. D.; Pistone, D.; Cormier, A. D., A problem associated with the use of a calomel reference electrode in an ISE analytical system. *Scandinavian Journal of Clinical and Laboratory Investigation* **1996**, *56* (sup224), 165-171.
154. Küver, A.; Vogel, I.; Vielstich, W., Distinct performance evaluation of a direct methanol SPE fuel cell. A new method using a dynamic hydrogen reference electrode. *Journal of Power Sources* **1994**, *52* (1), 77-80.
155. Coetzee, J. F.; Gardner, C. W. Jr.; Teflon Double-Junction Reference Electrode for Use in Organic Solvents. *Analytical Chemistry* **1982**, *54* (14), 2625-2626.
156. Dohner, R. E.; Wegmann, D.; Morf, W. E.; Simon, W., Reference Electrode with Free-Flowing Free-Diffusion Liquid Junction. *Analytical Chemistry* **1986**, *58* (6), 2586-2589.
157. Horwood, C., Ionic liquids as electrolytes for electrochemistry. In *Ionic Liquids in Analytical Chemistry*, 2022; pp 329-342.
158. Švancara, I.; Walcarius, A.; Kalcher, K.; Vytřas, K., Carbon paste electrodes in the new millennium. *Open Chemistry* **2009**, *7* (4), 598-656.
159. Wang, J.; Tian, B.; Nascimento, V. B.; Agnes, L., Performance of screen-printed carbon electrodes fabricated from different carbon inks. *Electrochimica Acta* **1998**, *43* (23), 3459-3465.
160. Mikkelsen, Ø.; Schrøder, K. H., Amalgam Electrodes for Electroanalysis. *Electroanalysis* **2003**, *15* (8), 679-687.
161. Yosypchuk, B.; Šestáková, I., Working Electrodes from Amalgam Paste for Electrochemical Measurements. *Electroanalysis* **2008**, *20* (4), 426-433.
162. Shetti, N. P.; Nayak, D. S.; Reddy, K. R.; Aminabhvi, T. M., Graphene–Clay-Based Hybrid Nanostructures for Electrochemical Sensors and Biosensors. In *Graphene-Based Electrochemical Sensors for Biomolecules*, 2019; pp 235-274.
163. Bobacka, J.; Ivaska, A.; Lewenstam, A., Potentiometric Ion Sensors. *Chemical Reviews* **2008**, *108* (2), 329-351.
164. Stradiotto, N. R.; Yamanaka, H.; Zanoni, M. V. B., Electrochemical Sensors: A Powerful Tool in Analytical Chemistry. *Journal of the Brazilian chemistry Society* **2003**, *14* (2), 159-173.

165. Kissinger, P. T.; Heineman, W. R., Cyclic Voltammetry. *Journal of Chemical Education* **1983**, *60* (9), 702-706.
166. Holze, R., *Experimental Electrochemistry A Laboratory Textbook*. 2 ed.; Wiley-VCH: Wiley-VCH, 2019; p 290.
167. Barsukov, Y.; Macdonlad, J. R., Electrochemical Impedance Spectroscopy. In *Characterization of Materials*, E.N. Kaufmann (Ed.): 2012; Vol. 2, pp 1-17.
168. Mohammed, A.; Abdullah, A. In *Scanning Electron Microscopy (SEM): A Review*, International Conference on Hydraulics, Pneumatics, Sealing Elements, Tools, Precision Mechanics, Specific Electronic Equipment & Mechatronics, Romania, Romania, 2019.
169. Bonard, J. M.; Dean, K. A.; Coll, B. F.; Klinke, C., Field emission of individual carbon nanotubes in the scanning electron microscope. *Phys Rev Lett* **2002**, *89* (19), 197602.
170. Buhr, E.; Senftleben, N.; Klein, T.; Bergmann, D.; Gnieser, D.; Frase, C. G.; Bosse, H., Characterization of nanoparticles by scanning electron microscopy in transmission mode. *Measurement Science and Technology* **2009**, *20* (8).
171. Mathebe, N. G.; Morrin, A.; Iwuoha, E. I., Electrochemistry and scanning electron microscopy of polyaniline/peroxidase-based biosensor. *Talanta* **2004**, *64* (1), 115-20.
172. Guin, S. K.; Knittel, P.; Daboss, S.; Breusow, A.; Kranz, C., Template- and Additive-free Electrosynthesis and Characterization of Spherical Gold Nanoparticles on Hydrophobic Conducting Polydimethylsiloxane. *Chem Asian J* **2017**, *12* (13), 1615-1624.
173. Zhang, D.; Wang, G.; Yuan, Y.; Li, Y.; Jiang, S.; Wang, Y.; Ye, K.; Cao, D.; Yan, P.; Cheng, K., Three-dimensional functionalized graphene networks modified Ni foam based gold electrode for sodium borohydride electrooxidation. *International Journal of Hydrogen Energy* **2016**, *41* (27), 11593-11598.

**Chapter 2: Electrochemical
Determination of Dexamethasone at
Unmodified and Copper Modified
Glassy Carbon Electrodes**

Table of Contents

2.1.0. Introduction	68
2.2.0. Experimental	71
2.2.1. Materials and reagents.....	71
2.2.2. Instrumentation.....	71
2.2.3. Procedures	71
2.2.3.1. Dexamethasone standards preparation	71
2.2.3.2. Redox studies and electroanalysis of dexamethasone	71
2.2.3.3. Copper particle electrodeposition.....	72
2.2.3.4. Non-aqueous sample preparation from an anti-inflammatory cream	73
2.2.3.5. Aqueous sample preparation from a solid dose form	73
2.3.0. Results and Discussion	73
2.3.1. Dexamethasone electrochemical investigations at an unmodified glassy carbon electrode	73
2.3.2. Electrosynthesis of copper particles via double and triple potentiostatic pulse method	82
2.3.4. Electrochemical Impedance Spectroscopy	93
2.3.5. Surface characterisation of copper particles formed using both double and triple potentiostatic pulse method	99
2.3.6. Dexamethasone electroanalysis at the copper dispersed surface formed using the double potentiostatic pulse Method I	102
2.3.5. Electroanalysis of dexamethasone extracted from pharmaceutical samples.	111
2.4.0. Conclusions	115
2.5.0. References	116

2.1.0. Introduction

Dexamethasone (DEX) is a synthetic glucocorticosteroid which is known for its potent anti-inflammatory effects. It has been reported to be effective in the reduction of cerebral oedema and for the treatment of acute exacerbation of multiple sclerosis, allergies, inflammation, and shock. It has also been used as a preoperative drug in the prophylaxis of postoperative nausea and vomiting^{1,2}. Recently, amidst the COVID-19 pandemic, it has been shown that DEX is an effective steroidal candidate for the treatment of patients suffering from COVID-19 infections due to its anti-inflammatory properties³. The effectiveness of DEX in the treatment of COVID-19 was demonstrated in a study by the Recovery Collaborative Group, where the 28-day mortality rate was lowered in patients hospitalised with severe infections and among those receiving mechanical ventilation upon DEX administration⁴.

From these studies focusing on DEX's effectiveness in treating severe COVID-19 infections, this drug has been looked at with great interest, however, only limited quantitative studies on this drug have been published. UV/Vis and high-performance chromatography, such as LC-MS, have been reported as standard methods for DEX quantitation⁵⁻⁸ and fewer reports on the electroanalysis of DEX have been published as a complementary approach. Previous work on the electrochemical quantitation of DEX have employed graphene modified GCEs in PBS (pH 7.25)¹, Fe₃O₄/PANI-Cu^{II} microsphere modified carbon ionic liquid electrodes in KH₂PO₄ (pH 2.0)⁹, paper based analytical devices^{10, 11}, and a hanging mercury drop electrode in Britton-Robinson buffer (pH 2.0)^{12, 13}.

The need for drugs associated with more than one active component in the same formulation presents a challenge in developing robust methodologies with short time to result¹² and electrochemical sensors can rise to combat such challenges. The medication can also be misused as a sports doping agent⁹ and is of concern in relation to adulteration of medicines¹¹ and as a suspected endocrine disruptor with associated environmental concerns¹³.

Investigation of the redox properties of such drugs also enables an insight into their *in vivo* metabolic fates and pharmacological activity¹². Oliveira et al reported the reduction of DEX using hanging mercury drop electrodes (HMDE) using cyclic voltammetry and square wave adsorptive voltammetry with two peaks associated with

the reduction of ketone groups at C3 and C20, which result in the dimerisation of two DEX molecules at C3 forming pinacol, a vicinal alcohol, while reduction at C20 results in a compound with a hydroxyl group. The resulting reduction products formed favour the adsorption on the HMDE and when deployed in the analysis of raw natural waters^{12, 13}. The electrochemical determination of DEX at different types of graphene modified electrodes has also been examined¹ with the structural defects and edges resulting in the increase in catalytic activity and DEX response in high capacity buffer (phosphate buffered saline). The potential shifted linearly with respect to electrolyte pH over the range 3-8.5 with slope of 61 mV/pH suggesting equal numbers of protons and electrons involved in the reduction process. It was evident that at higher pH's that the DEX response decreased, confirming that protons are required for the electroreduction process to occur. A sensor based on Fe₃O₄/polyaniline-Cu(II) modified carbon ionic liquid electrode was applied for the sensitive determination of DEX in real samples⁹ where the Fe₃O₄/PANI-Cu(II) microsphere accelerated electron transfer for oxidation of dexamethasone. In another report, a graphene oxide/hematite composite electrode enabled examination of a DEX oxidation response over the range 0.1-10 μM with LOD 0.046 μM ¹⁰. An electrochemical paper based analytical device for dual steroid (dexamethasone and prednisolone) was designed¹¹ for quantification of adulterated steroids in herbal medicines, where the sensor relied on separation (due to partition coefficient differences through the silica gel coated paper fluidic) and detection using differential pulse voltammetry in a 3D printed device over the range 10 – 500 $\mu\text{g ml}^{-1}$ in Britton Robinson buffer pH 4 containing 1.0 M KCl with LOD 3.59 $\mu\text{g mL}^{-1}$.

Most studies with the exception of Fatahi et al⁹ exploited the DEX cathodic signal in terms of quantitation in acidic electrolyte solutions. Therefore, to expand upon the previous work carried out regarding the electrochemical quantitation of DEX, a dual evaluation of DEX is presented here which exploits anodic and cathodic redox processes in both non-aqueous and aqueous media, respectively, with consideration for the increasing interest in this therapeutic agent. In order to achieve a highly sensitive sensor, the use of metal nanoparticles were explored due to their effectiveness in detecting compounds and metal pollutants¹⁴⁻¹⁶. Electrosynthesis is an efficient method for the preparation of metal particles on an electrode surface realising uniformity of shape and structure^{17, 18}. Particle size dispersion of gold nanoparticles

has been reported via template free electrosynthesis¹⁹ with the hemispherical gold nanoparticles demonstrating excellent electrocatalytic activity in the absence of surface stabilising agent with a multiple potentiostatic pulse strategy leading to high density of particles on glassy carbon electrodes. Control of particle size, crystal structure and shape of the metal nanoparticle are important and can be achieved by judicious choice of nucleation vs growth competition during formation¹⁸. Template free electrochemically synthesised copper particles were proposed in this work as a novel potential electrode modifier for the electroanalysis of DEX and both aqueous and non-aqueous electrochemical quantitation was realised in pharmaceutical formulations at modified and unmodified electrodes respectively. The work represents, to the best of our knowledge, the first such report of non-aqueous electrochemical investigation of this corticosteroid being compatible with hydrophobic cream formulation extraction and quantitation.

Copper and its oxides are attractive, due to their electrocatalytic properties and have the advantages of low production cost, high stability and good electrical properties²⁰. Low cost copper particles have been explored as working surfaces for CO₂ reduction (electrochemical reduction of CO₂ to ECO₂R) to value added commodity chemicals (methanol, ethanol, formic acid) exploiting high specific surface areas with access to substrates, while nanostructures can control product selectivity^{21, 22}.

The aim here was to exploit copper nano/micro clusters formed by a template free dual and triple pulse potentiostatic method to be used for DEX quantitation in an alkaline electrolytic system, where varying the electrodeposited nuclei and pulse parameters were employed to achieve the maximum DEX electrochemical response. Various morphologies, such as spheres, flowers and star-like microstructures were realised depending on the electrodeposition approach and electrode used. Subsequent DEX investigations examined possible interactions between DEX functional groups and the Cu nanostructure modified GCE, relating to the adsorption of DEX to the nanostructures and reduction of the adsorbed reduction product, where the novel secondary signal was the analytical focus of these investigations.

2.2.0. Experimental

2.2.1. Materials and reagents

Copper acetate monohydrate [$\text{Cu}(\text{CH}_3\text{COO})_2 \cdot \text{H}_2\text{O}$] (98 %) (Sigma-Aldrich), lithium perchlorate [LiClO_4] (98 %) (Merck), sodium acetate [CH_3COONa] (99 %) (Sigma-Aldrich), potassium chloride [KCl] (99 %) (Sigma-Aldrich), glacial acetic acid [CH_3COOH] (99 %) (Sigma-Aldrich), sodium hydroxide [NaOH] (96 %) (Sigma-Aldrich), dexamethasone [$\text{C}_{22}\text{H}_{29}\text{FO}_5$] (98 %) (Sigma-Aldrich), ethanol absolute [$\text{C}_2\text{H}_5\text{OH}$] (99.8 %) (Sigma-Aldrich), methanol [CH_3OH] (99.9 %) (Sigma-Aldrich), Cortopin 1% w/w hydrocortisone cream (Pinewood Healthcare), sucrose [$\text{C}_{12}\text{H}_{22}\text{O}_{11}$] (99.5 %) (Sigma-Aldrich), magnesium stearate [$[\text{CH}_3(\text{CH}_2)_{16}\text{CO}_2]_2\text{Mg}$] (Merck).

2.2.2. Instrumentation

Electrochemical investigations were carried out using a three-electrode cell, using a glassy carbon electrode (GCE) as the working electrode, a platinum wire as the auxiliary and Ag/AgCl (saturated KCl) was used as the reference electrode. Measurements were made using a Solartron SI2187 Electrochemical Interface and a CHI Instruments 600E Potentiostat/Galvanostat. Materials and reagents were weighed out using a Sartorius LA230S analytical balance, and a VWR ultrasonic cleaner model USC100T was used as required. Screen printed electrodes used were Metrohm DropSens (11L carbon e) (Aux.: C; Ref.: Ag/AgCl). The scanning electron microscopy was performed on a FEI (Thermo) Helios G4 CX Dual Beam SEM-FIB with Oxford Instruments EDS.

2.2.3. Procedures

2.2.3.1. Dexamethasone standards preparation

A dexamethasone standard solution was prepared in 0.1 M LiClO_4 in methanol (solubility $16.625 \text{ mg mL}^{-1}$). Dexamethasone was also prepared in alkaline media 0.1 M NaOH (pH 13) with methanol added at a ratio of 3:7. Solutions were stored in the refrigerator prior to use.

2.2.3.2. Redox studies and electroanalysis of dexamethasone

Electroanalysis was carried out via cyclic voltammetry at 100 mV s^{-1} , examining the behaviour over the potential range 1.5 to -1.8 V. Prior to each experiment, high purity N_2 gas was passed through the solution for 10 min to deaerate the supporting

electrolyte. In the case of the non-aqueous electrochemistry, anodic scans over the range -1.8 to 1.5 V vs Ag|Ag⁺ were performed while aqueous studies focused on the cathodic region from -0.05 to -1.8 V vs. Ag/AgCl at both bare and modified electrodes. All measurements were made in triplicate. Electrochemical Impedance Spectroscopy involved both faradaic and non-faradaic experiments with E = 0.2176 and -0.177 V respectively, amplitude 5 mV and frequency range 0.01-100,000 Hz in a 5 mM Fe²⁺/Fe³⁺ redox probe.

2.2.3.3. Copper particle electrodeposition

Firstly, the GCE electrode surface was polished in a figure of eight pattern on a polishing pad with a 1- μ m monocrystalline diamond suspension for 1 minute and was rinsed with a jet of deionised water (DI). The electrode was then sonicated for 30 s in DI and dried under high purity N₂ gas flow. The electrode was modified with copper using two approaches. The precursor solution was 10 mM copper acetate in 0.1 M sodium acetate buffer (pH 4.5) which comprised of a mixture of 0.1 M sodium acetate and 0.1 M acetic acid, and the pulse potentials were chosen from a voltammogram of this quiescent solution.

- (I) Potentiostatic dual-pulse Method I from 10 mM copper acetate in 0.1 M sodium acetate buffer (pH 4.5), where a perturbation pulse was applied initially at 0.7 V for 5 s to remove any adsorbed copper ions from the GCE surface followed by the growth pulse at -0.47 V for 60 s, which allowed for copper nucleation and growth. Following electrodeposition, the Cu surface was then examined in 0.1 M NaOH, resulting in two oxidation and two reduction metal processes reflecting Cu/Cu₂O and Cu₂O/CuO/Cu(OH)₂.
- (II) Potentiostatic triple pulse Method II from 10 mM copper acetate in 0.1 M sodium acetate buffer (pH 4.5), where optimised conditions included a perturbation pulse applied initially at 0.7 V for 5 s (this leads to a depletion region with removal of Cu²⁺ (aq) adsorbed ions), followed by a seeding (nucleation) pulse at -0.47 V for 5 ms and lastly a growth pulse at -0.265 V for 50 s (diffusion of Cu²⁺ (aq) ions from bulk solution towards the seeded nuclei).

2.2.3.4. Non-aqueous sample preparation from an anti-inflammatory cream

Four cream samples were prepared by spiking an anti-inflammatory commercially available cream (Cortopin 1 % w/w hydrocortisone cream) with 0.0 %, 0.25 %, 0.35 % and 0.5 % w/w dexamethasone. Each sample was stirred vigorously in 5 mL of methanol for 2 hours before refrigeration overnight. Samples were then filtered via gravity filtration and the residue was rinsed with cold methanol. The sample was then concentrated into 2 mL methanol and was refrigerated overnight. A second gravity filtration was carried out where the samples were filtered into 10 mL volumetric flasks containing 0.106 g LiClO₄ and made up to the mark with methanol resulting in 0.1 M LiClO₄.

2.2.3.5. Aqueous sample preparation from a solid dose form

Four 100 mg tablet samples containing 0.0, 2.0, 4.0, 6.0, 10.0 & 15.0 mg DEX were formulated and prepared in house. Each tablet contained 5 mg magnesium stearate and powdered sucrose was added until each tablet weighed 100 mg in total. The four mixtures were mixed thoroughly in a Mortar and Pestle such that all components were distributed homogeneously. The samples were transferred to a disc shaped mould (1.3 cm in diameter) and 10 tonnes of pressure was then applied to each tablet sample for 15 minutes using a hydraulic press, where the tablet mixtures were compressed into a solid disc. Following this process each tablet was ground to a powder and placed into a vial. Methanol was added and each mixture was stirred at a high speed for 1 hr to extract the DEX. The samples were then filtered and washed 3 times with 1.0 mL methanol. The methanol was evaporated such that 1.0 mL of the sample remained. 1.0 mL methanol was added followed by 2.0 mL 0.1 M NaOH with subsequent mixing. The sample was then filtered into a volumetric flask. The vial was firstly rinsed with 2.0 mL of 1:1 methanol: 0.1 M NaOH and finally with 1.0 mL 0.1 M NaOH before the sample was made up to the graduation mark with 0.1 M NaOH.

2.3.0. Results and Discussion

2.3.1. Dexamethasone electrochemical investigations at an unmodified glassy carbon electrode

Firstly, the voltametric behaviour of 1.0 mM dexamethasone (DEX) was examined in methanol with 0.1 M LiClO₄ as supporting electrolyte. Electrochemical studies were initially carried out at the bare glassy carbon electrode (GCE) over the

potential range $-1.8 - 1.5$ V vs Ag/Ag^+ . Upon examining the voltammogram in **Figure 1**, a weak reduction signal was observed at -1.3 V vs Ag/Ag^+ (II) and a strong oxidation wave was present at 1.3 V vs Ag/Ag^+ (I). The oxidation wave was the analytical focus in subsequent electrochemical investigations in methanol, where electrooxidation occurs at C11, depicted in **Scheme 1**. The cathodic wave at -1.5 V was attributed to the electrolyte/oxygen interference present in the background. The cyclic and acyclic ketone at C3 and C20 respectively are thought to be likely sites for DEX reduction¹² with potential for dimerisation at the C3 position (see chemical structure as insert **Figure 1**).

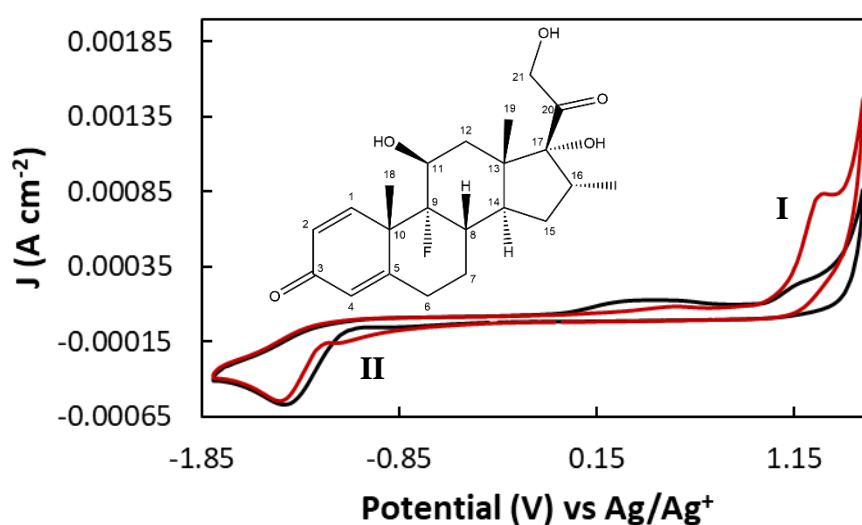
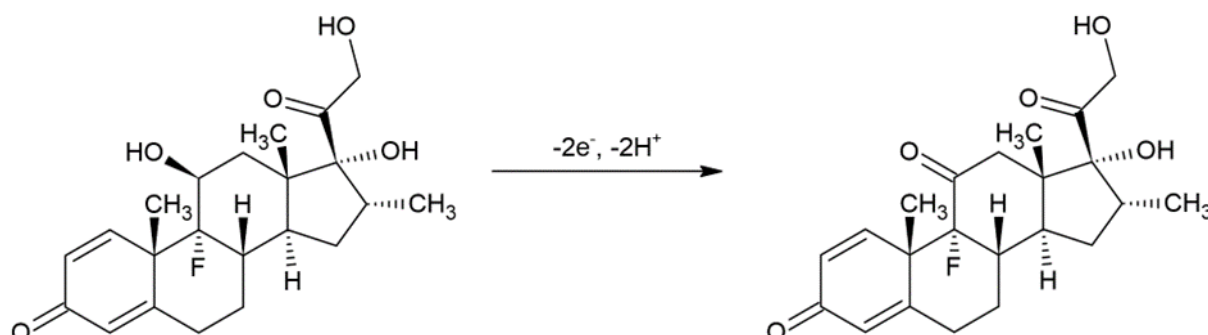


Figure 1. Voltammetry of a deaerated solution of 1 mM DEX in 0.1 M LiClO_4 in MeOH (black) vs the electrolyte background (red) at a bare GCE from -1.8 V to 1.5 V at 100 mV s^{-1} . A clear oxidation peak can be seen at 1.3 V (I) with weak reduction at -1.3 V (II) vs Ag/Ag^+ .



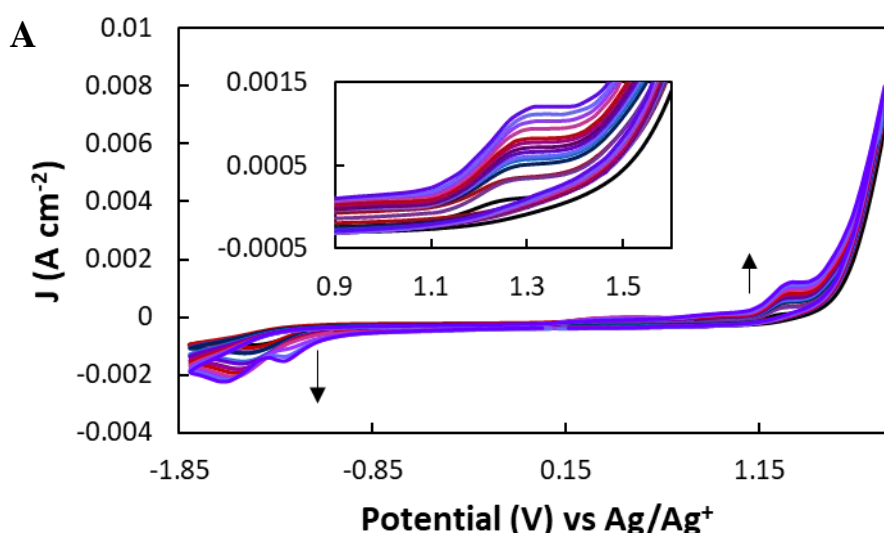
Scheme 1. Depicting the electrooxidation of DEX occurring at the C11 alcohol group, resulting in the formation of a ketone group at this position.

A scan rate study of 1 mM DEX was then carried out at the bare GCE over a wider potential range, from -1.8 – 1.8 V vs Ag/AgCl, to examine the influence of scan rate on both current and peak potential (**Figure 2 (A)**). The anodic peak was monitored ($E_p = 1.3$ V vs. Ag/Ag⁺), and the peak current clearly increased as the scan rate was increased from 10 – 200 mV s⁻¹, where a linear relationship was observed with respect to the square root of the scan rate (**Figure 2 (B)**), which demonstrated the diffusion controlled nature of electrochemically irreversible oxidation process, with equation $I_{p(a)} = 3 \times 10^{-3} v^{1/2} - 1.24 \times 10^{-4}$ ($r^2=0.990$). The anodic peak showed a dependence on scan rate and a cathodic shift was observed with scan rate increasing from 10 – 200 mV s⁻¹. A plot of log J (current density) vs log n was linear with slope 0.56 confirming the diffusion-controlled process (**Figure 2 (C)**).

$$i_p = 2.99 \times 10^5 \times n \times \sqrt{\alpha n_a} \times A \times C \times \sqrt{D} \times \sqrt{v} \dots \dots \dots (1)$$

$$E_p - E_{p(\frac{1}{2})} = \frac{1.857 \times R \times T}{\alpha n_a \times F} \dots \dots \dots (2)$$

where α is the transfer co-efficient, n is the number of electrons in the rate determining step, D_0 is the diffusion co-efficient, v is scan rate, $E_{p(1/2)}$ is the potential where current is half the peak value. Taking E_p and $E_{p1/2}$ as 1.3 and 1.2 V respectively, αn_a was estimated at 0.47.



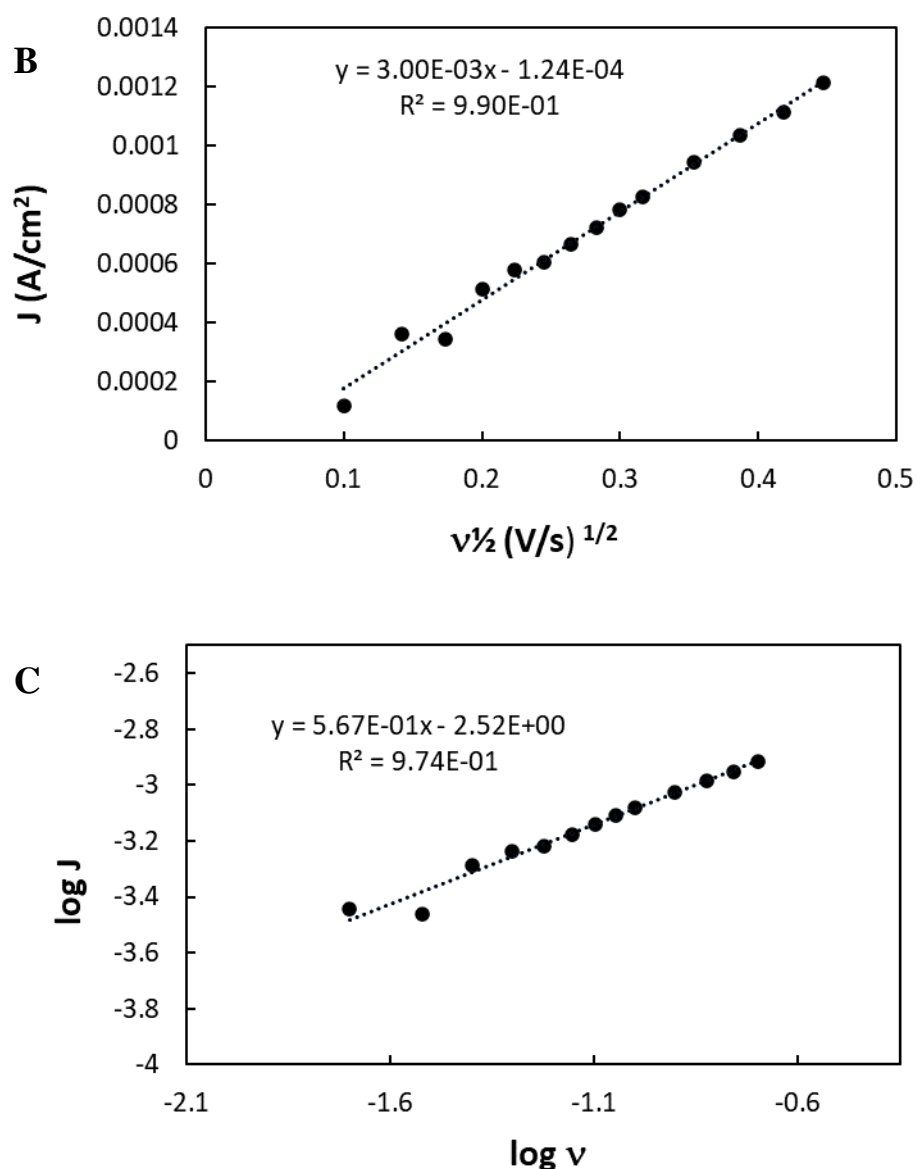


Figure 2(A) Overlaid voltammograms of 1 mM dexamethasone in 0.1 M LiClO₄ in methanol at the bare GCE, from -1.8 V to 1.8 V at scan rate 10-200 mV s⁻¹. **(B)** Graph showing the square root of scan rate vs current density for the oxidation peak of 1 mM dexamethasone in (A). **(C)** Graph showing $\log J$ vs $\log v$ resulting in a linear plot with slope 0.567, confirming the process was diffusion controlled.

A DEX calibration curve was then generated by cyclic voltammetry resulting in sensitivity of $5.42 \times 10^2 \pm 2.88 \mu A cm^{-2} mM^{-1}$ and over the range 0.83 – 3.07 mM with $r^2 = 0.998$ ($n=3$) based on the oxidation process at 1.3 V vs Ag/Ag⁺ (I) in methanol/0.1 M LiClO₄ (**Figure 3 (A) and (B)**). The peak at 0.5 V represented an unknown process evident in this solvent /electrolyte system and did not respond linearly to DEX additions. This process was only observed when the potential was swept to the lower cathodic limit, however the low cathodic limit was required in order to observe a strong anodic DEX response observed at 1.3 V. From examining DEX at

a higher cathodic limit, the signal at 1.3 V became far less defined, and thus was unsuitable to be used in DEX quantitation.

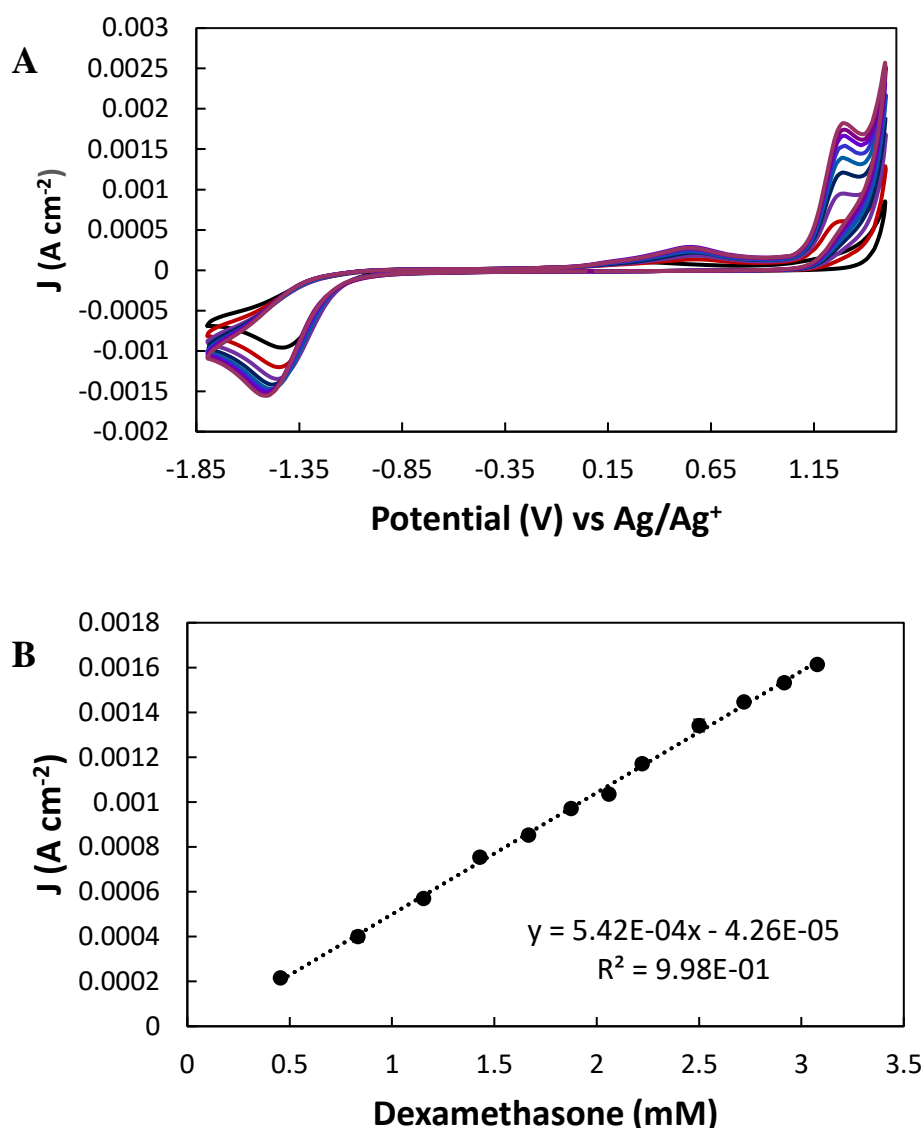


Figure 3 (A) Voltammetry of DEX (0.45 -3.07 mM) in 0.1 M LiClO₄ / MeOH with the background electrolyte (black) (degassed by bubbling with N₂) at a bare GCE from -1.8 V to 1.5 V at 100 mV s⁻¹. (B) Calibration curve showing linear relationship between dexamethasone concentration and anodic current density with sensitivity $5.42 \times 10^2 \mu\text{A cm}^{-2} \text{mM}^{-1}$ over the range examined. (n=3)

Prior electroanalysis of DEX employed an acidic aqueous environment demonstrating the proton dependant nature of the reduction process at position C20^{12, 13} (Scheme 2). Dexamethasone reduction was compared under acidic (0.1 M sodium acetate buffer at pH 4.45) and basic (0.1 M NaOH at pH 13) conditions in Figure 4 (A) and (B), although the DEX reduction signal was found to be shifted more negative under basic conditions. Despite this cathodic shift, the peak observed in the alkaline

solution was visibly sharper in appearance and 1.44-fold larger than that observed in the 0.1 M sodium acetate buffer. Resonance effects at C3 may stabilise this site relative to C20, the latter of which may be responsible for this process, as verified by Oliviera et al using quantum chemical studies¹² on reduction of the conjugated and unconjugated ketone groups. **Figure 4 (A)** shows the aqueous voltammetry of 1 mM DEX in alkaline conditions relative to background supporting electrolyte (0.1 M NaOH, pH 13) with peak current for the cathodic process at $1.3 \times 10^{-4} \text{ A cm}^{-2}$ ($E_p = -1.54 \text{ V}$) relative to $8.98 \times 10^{-5} \text{ A cm}^{-2}$ ($E_p = -1.23 \text{ V}$) for 0.1 M sodium acetate buffer (30:70 methanol: buffer ratio) as shown in **Figure 4 (B)**. Considering the cathodic DEX signals observed in both electrolyte solutions, electrochemical investigations were carried out in the alkaline electrolyte environment as this medium also favoured visualisation of the copper nanostructured oxide redox processes, thus presenting the optimum conditions.

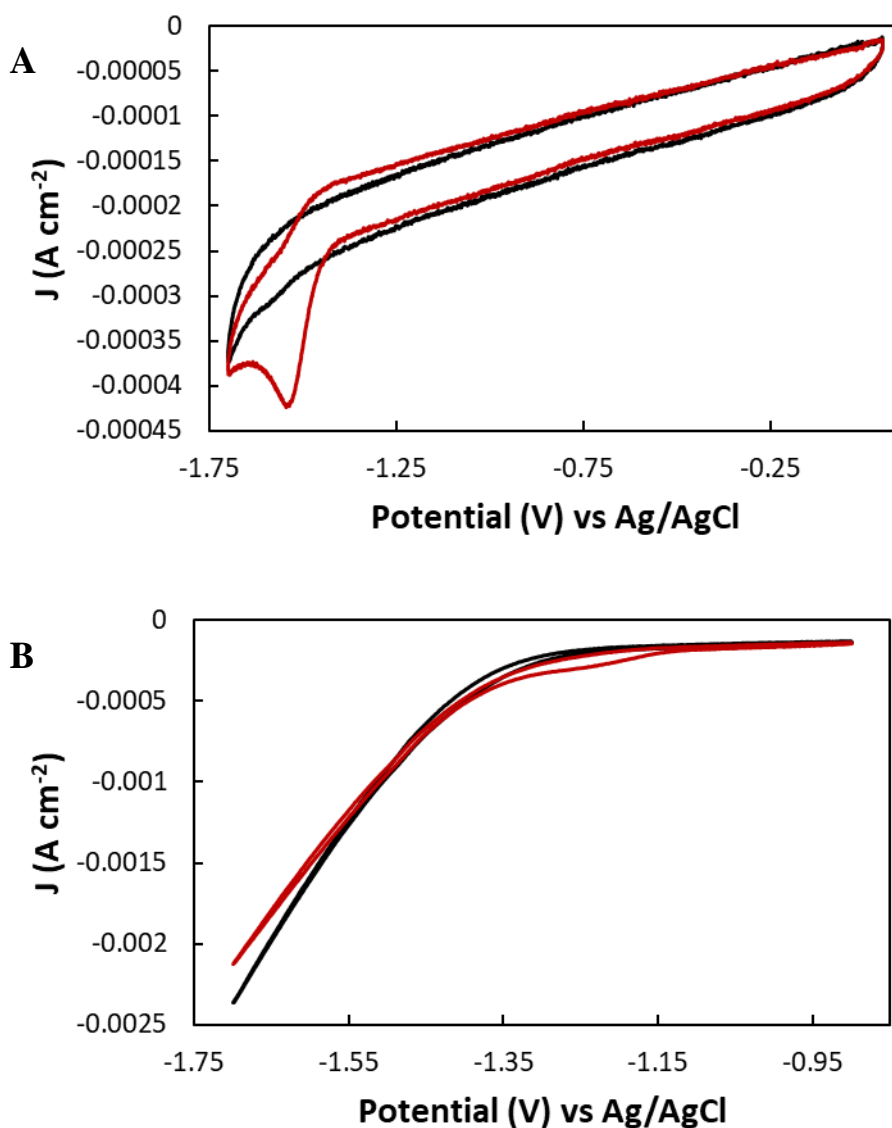
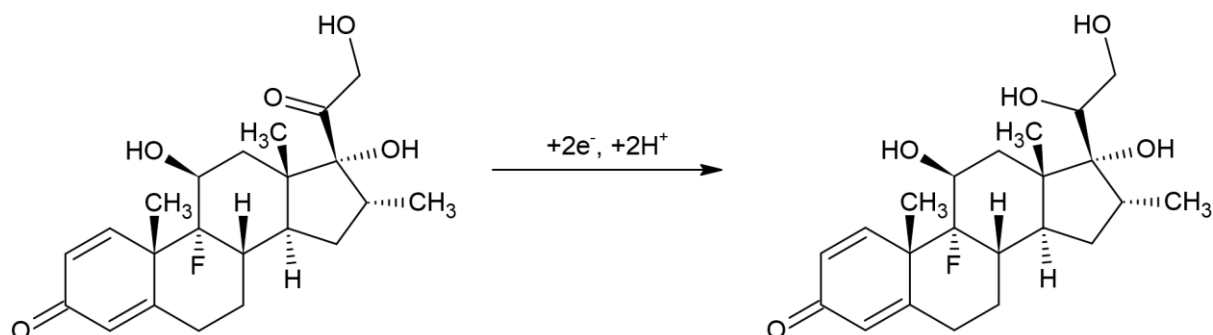
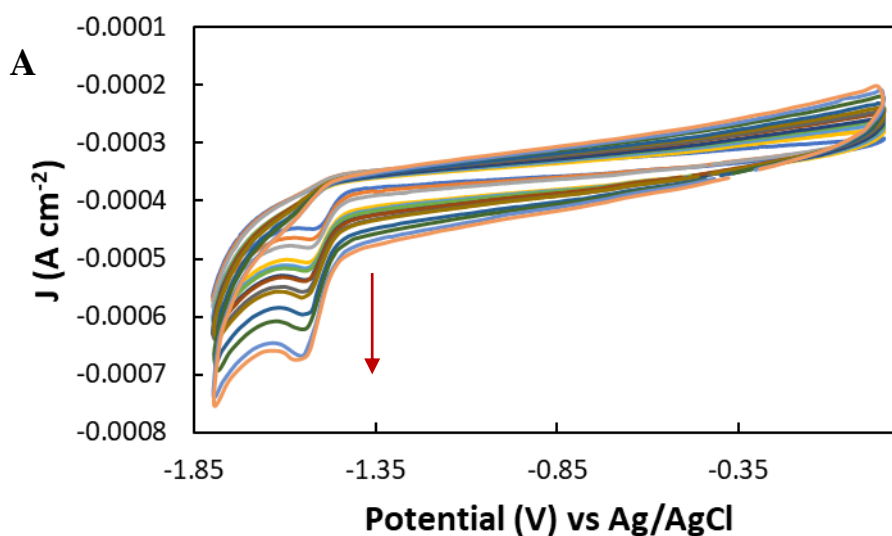


Figure 4 (A) Voltammery of 1 mM DEX in 0.1 M NaOH (red) supporting electrolyte (black) at 100 mV s^{-1} . (B) Voltammery of 1 mM dexamethasone (red) in 0.1 M sodium acetate buffer pH 4.45 (black) at 100 mVs^{-1} .



Scheme 2. Depicting the electroreduction of DEX at the C20 ketone group, resulting in the formation of an alcohol group.

A scan rate study followed (**Figure 5**) using 1 mM DEX in 0.1 M NaOH over the range 10 – 200 mV s⁻¹, which indicated that the electrochemically irreversible reduction process demonstrated mixed diffusion-adsorption controlled behaviour over this range while E_p was constant with respect to scan rate. A calibration was then performed by CV (**Figure 6**) in 0.1 M NaOH resulting in a sensitivity of 276 ± 0.14 μA cm⁻² mM⁻¹ over the range 0.0781 – 5.0 mM with r² = 0.90 (n=3), with LOD = 342 ± 0.0017 μM and LOQ = 2,285 ± 0.012 μM.



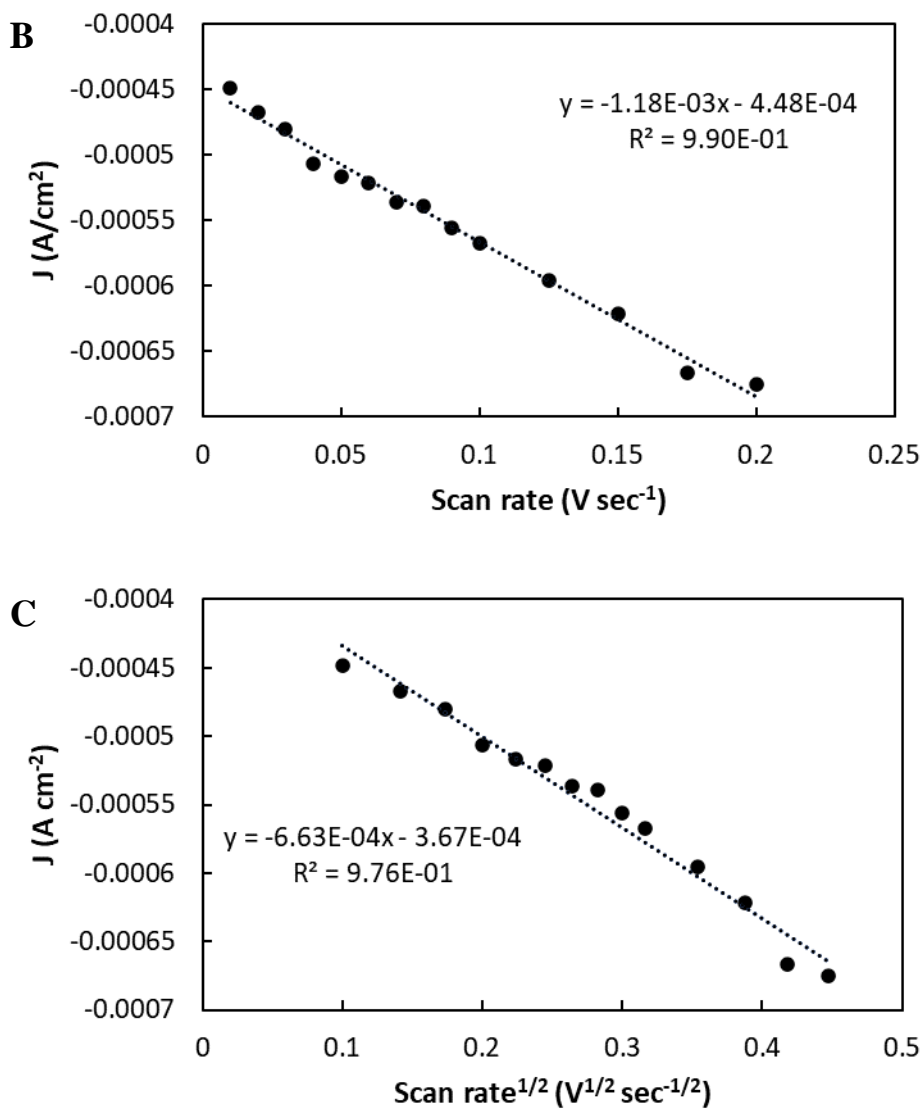


Figure 5 (A) Overlaid voltammograms for degassed 1 mM dexamethasone in 0.1 M NaOH (pH 13.0) from -0.05 V to 1.8 V over scan rates 10 – 200 mV s⁻¹. (B) Graph showing the scan rate vs current density for the reduction of 1 mM dexamethasone with dependence up to 50 mV s⁻¹. (C) Graph showing the square root of scan rate vs current density for the reduction of 1 mM dexamethasone.

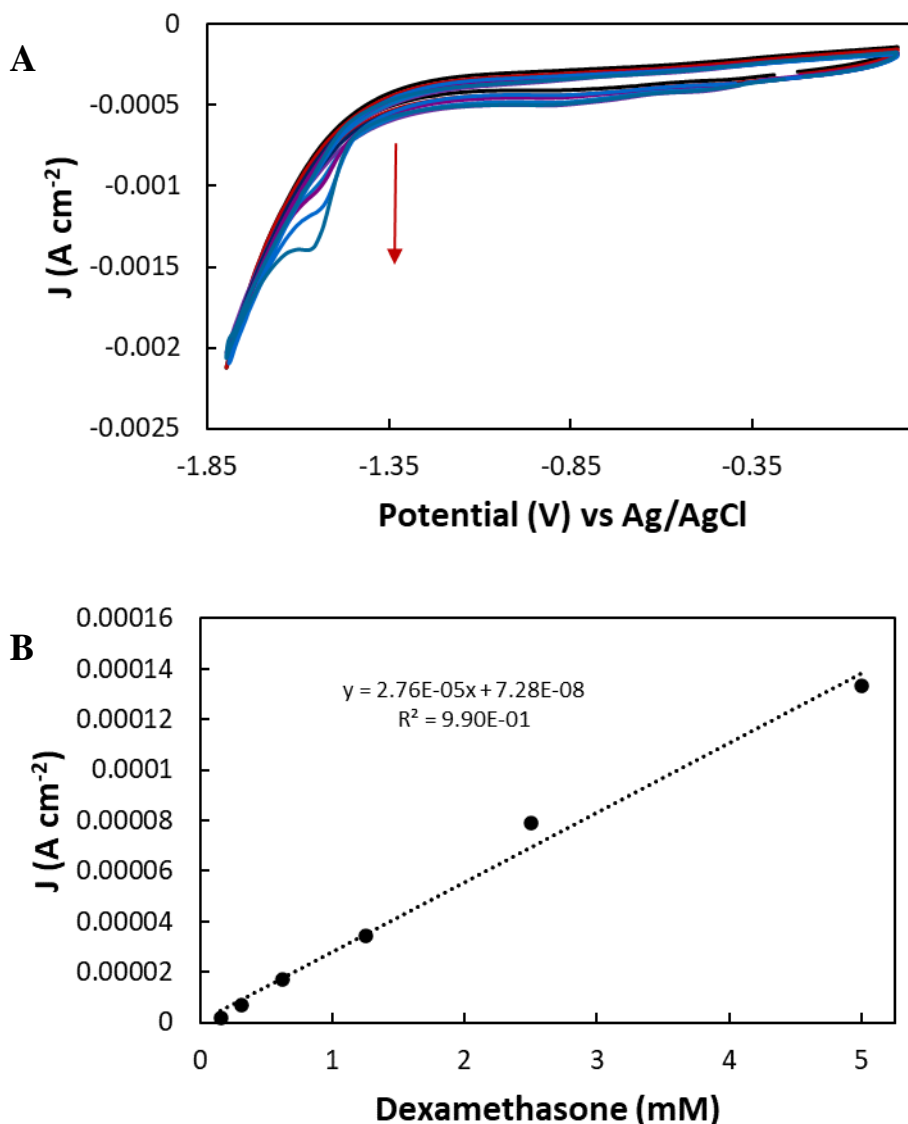


Figure 6 (A) Calibration of DEX at GCE in 0.1 M NaOH pH 13 (deaerated), over the range 0.0781 – 5.0 mM DEX with potential range 0.05 – -1.8 V at 100 mV s⁻¹. **(B)** Corresponding calibration curve resulting in a sensitivity of 2.76×10^{-5} A mM⁻¹ (n=3).

2.3.2. Electrosynthesis of copper particles via double and triple potentiostatic pulse method

Copper was deposited using two approaches, each of which were examined with respect to their influence on the DEX analytical signal. In the first (Method I) a dual pulse potentiostatic method as described in section 2.3.2. was employed where potentials were selected based on the voltammetry of a 10 mM copper acetate in 0.1 M sodium acetate buffer solution (pH 4.5), which resulted in the formation of a copper film formed at the GCE surface (CuF/GCE) (**Figure 7 (A)** and **Figure 8 (b)**). Application of perturbation pulse potential E_1 removes adsorbed Cu²⁺ ions resulting

in a depletion region at the GCE surface. A subsequent nucleation pulse was used to seed the particles with subsequent growth of the copper nuclei via diffusion, with the aim to achieve controllable homogeneous Cu particle growth. Optimisation of the pulse duration was based on the constant potential amperometric trace of a solution of 10 mM copper acetate as shown in **Figure 7 (B)** where the system changed from a potential where no reaction occurred to a steady-state reaction controlled by the rate of mass transfer of cupric ions to the electrode surface. The potential was stepped from the open circuit potential to set values from -0.06 – -0.47 V, with investigation of the time passed until appearance of the current maxima as the selected pulse potential was made more negative (**Figure 7 (B)**). From the series of potentiostatic current transients shown was observed that the features include the rapid decrease in current representing charging of the double layer, followed by a rising current due to new phase growth of nuclei on the surface which was followed by coalescing diffusion fields giving rise to a current maximum followed by planar diffusion decay²³. From this series of experiments, the hemispherical diffusion regions were determined and selected for use in the electrosynthesis of the Cu particles in Method II as outlined below, while linear diffusion of Cu²⁺ to the GCE surface was exploited in Method I, which resulted in the formation of a Cu film.

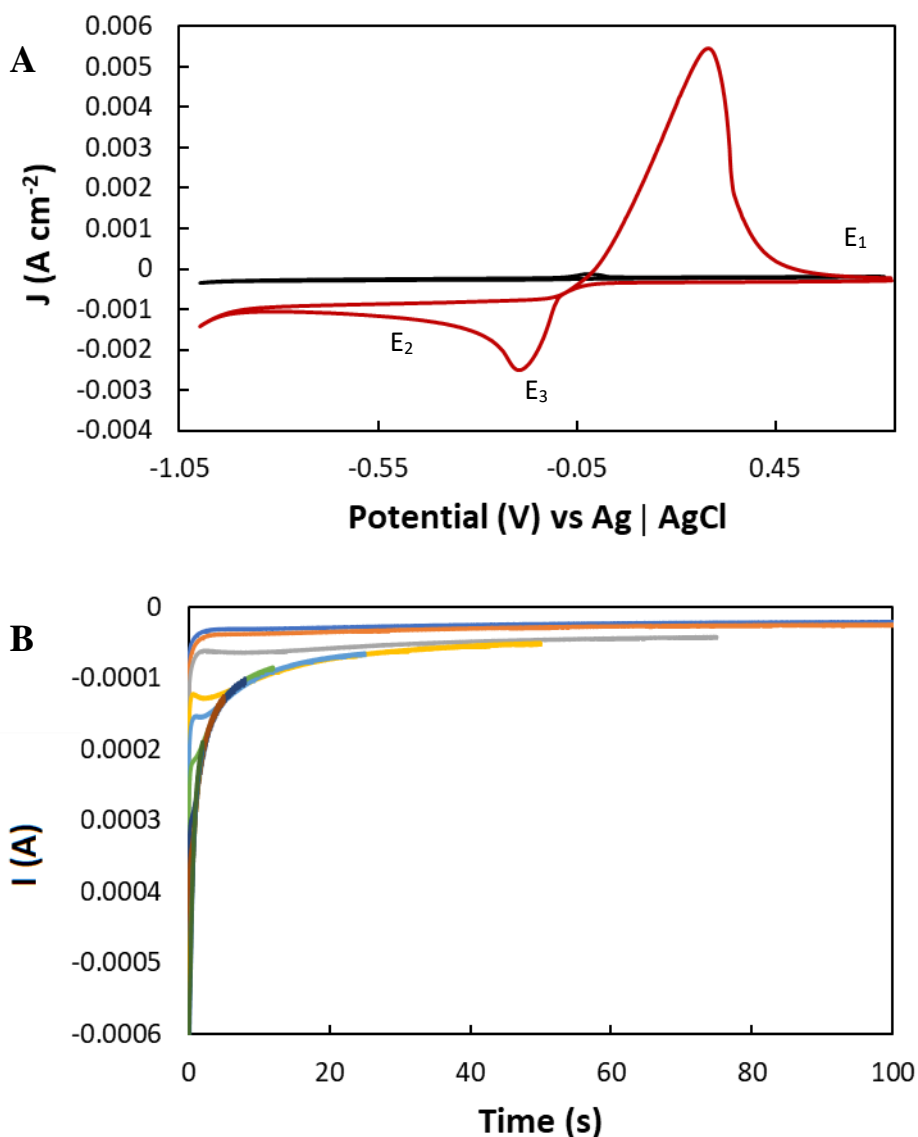
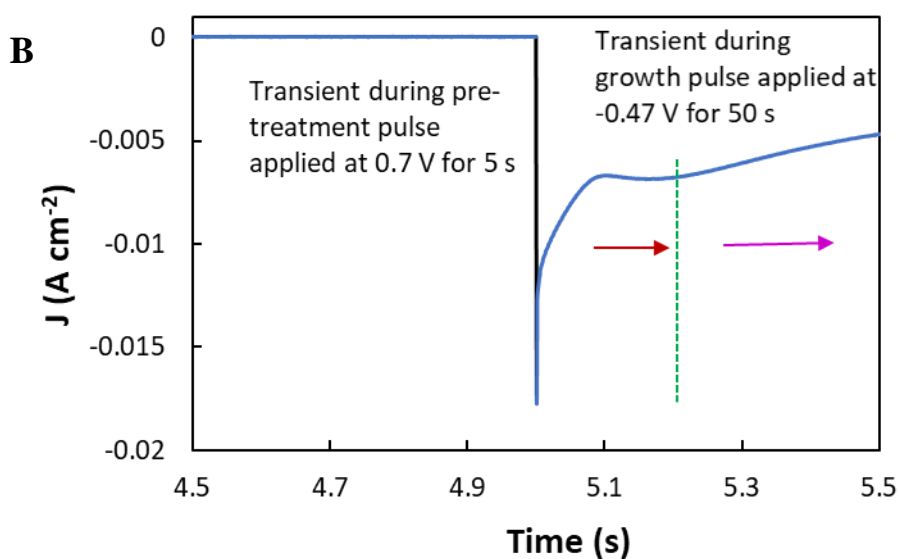
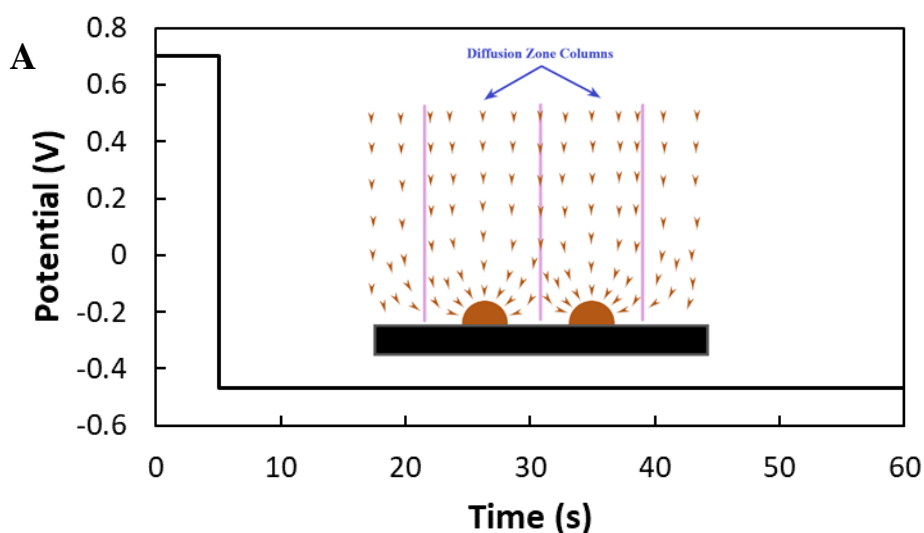


Figure 7 (A) Voltammetry of 10 mM $\text{Cu}(\text{Ac})_2$ in 0.1 sodium acetate buffer (pH 4.5, deaerated) at the bare GCE from -1.2 V to 0.7 V at 20 mV s^{-1} , with pulse potentials $E_1 = 0.7 \text{ V}$, $E_2 = -0.47 \text{ V}$ and $E_3 = -0.265 \text{ V}$ labelled. **(B)** Chronoamperometry trace of 10 mM $\text{Cu}(\text{Ac})_2$ from -0.06 V to -0.47 V with current-time display to be used for the selection of the nucleation and growth pulses for Cu particle deposition in Methods I and II.

Method I (dual pulse potentiostatic deposition of copper nanostructures)

The first perturbation pulse ($E_1 = 0.7 \text{ V}$) removed adsorbed Cu^{2+} ions, was followed by a growth pulse ($E_2 = -0.47 \text{ V}$) for 50 s (**Figure 8 (A)**) allowing linear diffusion to the copper particles to occur. In this case a nucleation pulse was not employed (see Method II below). The region during the growth pulse following the red arrow to the green line (**Figure 8 (B)**) indicates where hemispherical diffusion occurs, resulting in the formation of copper nanoparticles. After this current maxima,

the hemispherical diffusion regions overlap which allows linear diffusion to occur (current decay with respect to $t^{-1/2}$) resulting in the formation of branched copper structures with the redox features evident in **Figure 8 (C)** and detailed below. The $E_{1/2}$ for the more anodic $\text{Cu}^+ \rightarrow \text{Cu}^{2+}$ process was -0.177 V , while the sharp reduction process at -0.664 V reflected reduction of Cu^+ to Cu^0 which matches those processes identified in the literature for similar deposition methodologies²⁴⁻²⁶.



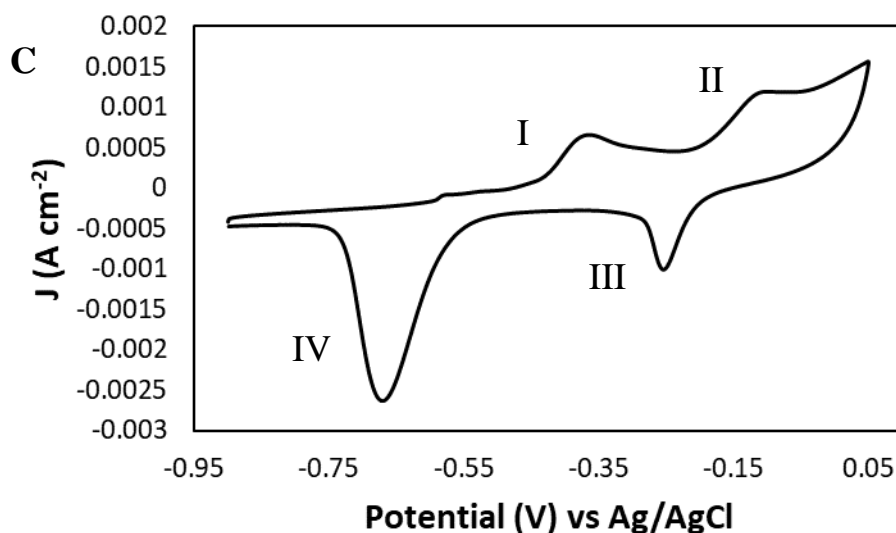
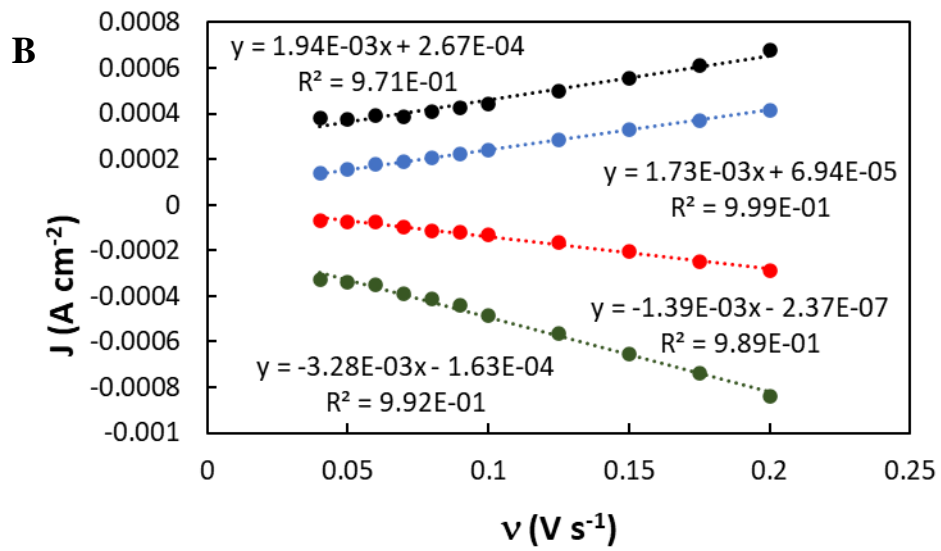
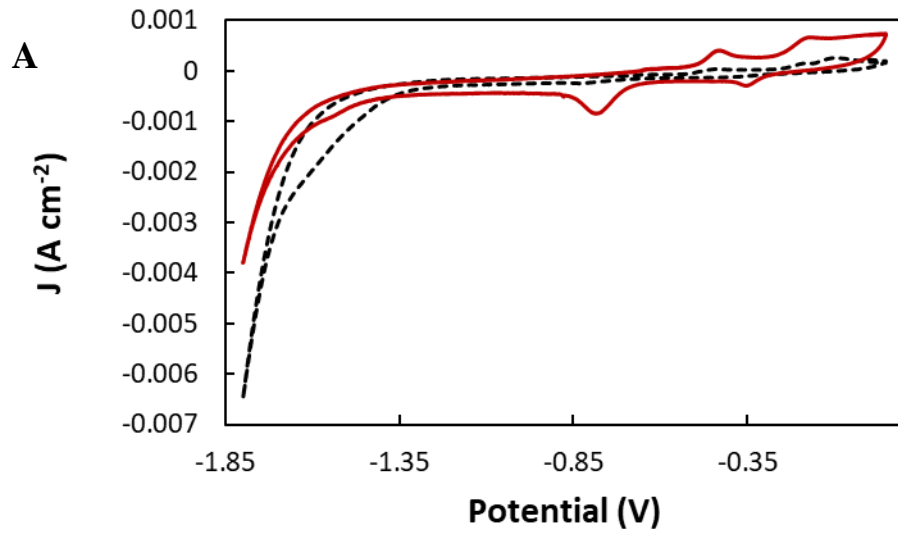


Figure 8 (A) Potential-time input signal where the reduction potential was varied from -0.08 V to -0.55 V over the timescale 100 to 5 s with schematic showing the growth of the CuNPs through radial diffusion (B) Chronoamperometry of 10 mM Cu(Ac)₂ where the electrode was initially pre-treated, followed by the application of the growth pulse. (C) Voltammetry of the Cu modified GCE in 0.1 M NaOH from -0.9 – 0.05 V at 100 mV s⁻¹.

The Cu film realised using Method 1 electrosynthesis at a GCE was examined in 0.1 M NaOH from -1.8 – 0.05 V at 100 mV s⁻¹, where two oxidation and two reduction peaks were observed labelled I – IV. A scan rate study followed over the range 10 – 200 mV s⁻¹ (**Figure 9 (A)**) which allowed the surface coverage value to be calculated as $3.492 - 2.065 \times 10^{-9}$ mol cm⁻². The E_p values were independent of scan rate in all cases. **Table 1** assigns the redox processes and gives surface coverage values as estimated from the slope of the linear I_p vs n plots (**Figure 9 (B)**).

Method I was evaluated with respect to influence on the DEX quantitative signal with **Table 2**, summarising the conditions examined resulting in method B1 being optimum, justifying the conditions selected above (see corresponding data shown in **Figure 8 (C)**).



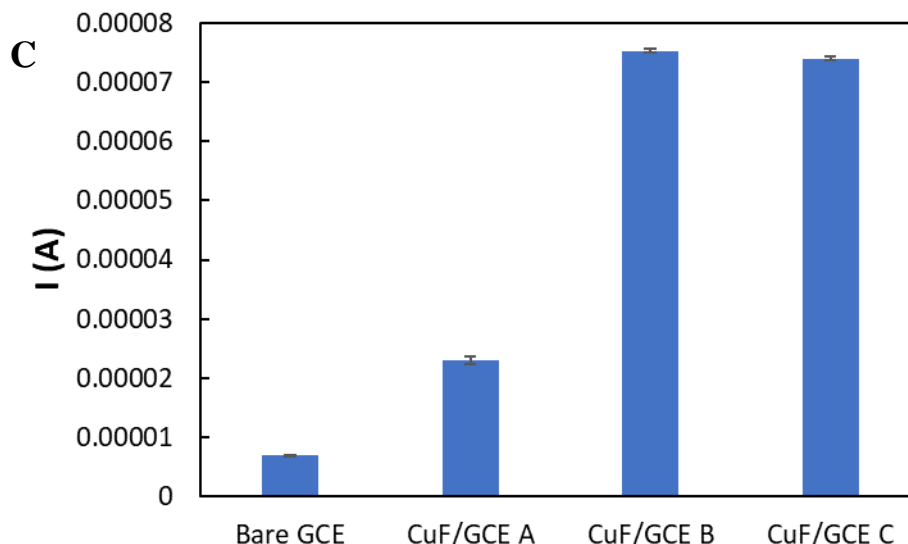


Figure 9 (A) Voltammetry of the Cu film in 0.1 M NaOH from -1.0 – 0.05 V from 10 – 200 mV s⁻¹ (first (dashed) and last (red) curves shown). (B) Graph of current density vs scan rate for each peak I – IV (black, blue, red, green respectively), from which the surface coverage was calculated to lie within the range $\Gamma = 1.480 - 3.492 \times 10^{-9}$ mol cm⁻². (C) DEX (1 mM) response for E₁ and E₂ pulse conditions outlined in **Table 2**.

Table 1. Assignment of redox processes and surface coverage for copper electrochemistry.

Peak no.	Assigned redox process	E _p (V)	Surface coverage (Γ) (mol cm ⁻²)
I	Cu/Cu ₂ O Cu/Cu ¹⁺	-0.402	1.842×10^{-9}
II	Cu ₂ O → CuO and Cu(OH) ₂ Cu ¹⁺ /Cu ²⁺	-0.182	2.065×10^{-9}
III	Reduction to Cu ₂ O CuO → Cu ₂ O	-0.342	1.480×10^{-9}
IV	Reduction of CuO/Cu ₂ O surface oxides to Cu metal Cu ¹⁺ → Cu ⁰ Cu ²⁺ → Cu ⁰	-0.773	3.492×10^{-9}

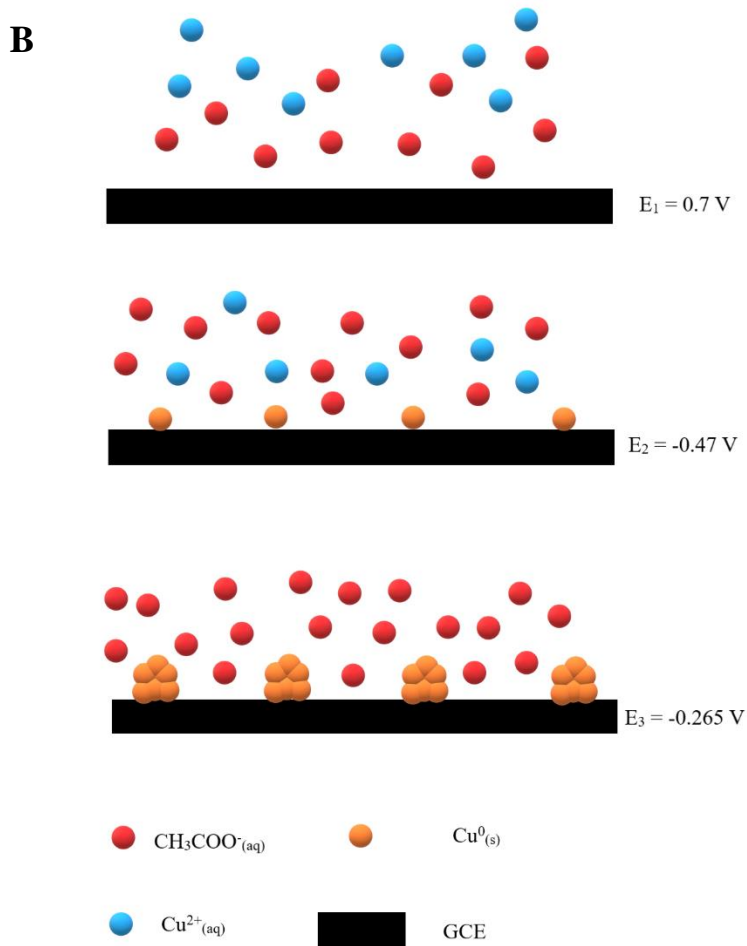
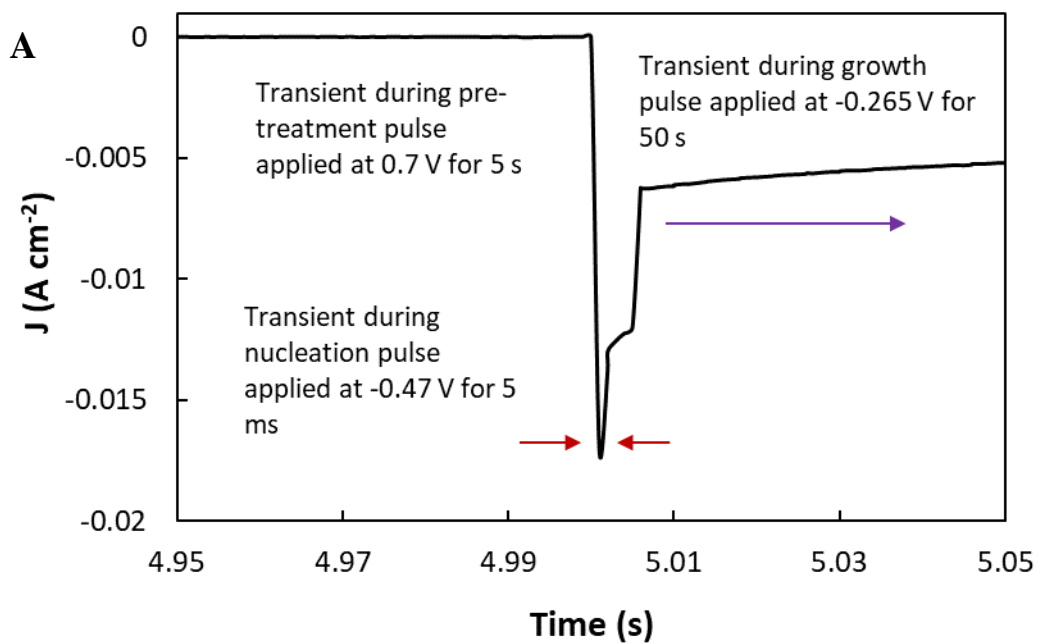
Table 2. Method I dual pulse optimisation of copper deposition conditions with corresponding effect on DEX (1 mM) response for peak at -1.34 V (see **Figure 8 (C)**).

	Step 1 (E ₁)		Step 2 (E ₂)	
	Potential (V)	Time (s)	Potential (V)	Time (s)
A1	0.7	5	-0.315	5
B1	0.7	5	-0.47	50
C1	0.7	5	-0.47	60

Method II (triple pulse potentiostatic deposition of copper nanostructures)

This method was adapted from Guin *et al*¹⁸ for Pb nanoparticle deposition onto Au surfaces. The first step forms metal adatoms (nucleation) followed by growth via subsequent phase formation. The energy of the Cu-carbon interaction is greater than that of Cu-Cu growth and the 2D copper nuclei led to a compact layer which was more positive than the bulk deposition potential, followed by 3D islands on the predeposited monolayer (verified by CV deposition data with the E_p value shifting from -0.63 V (cycle 1) to -0.42 V (subsequent cycles) – data not shown. The potential of the nucleation step (E₂ = -0.47 V) was selected from the diffusion limiting region of the copper acetate voltammogram (**Figure 7 (A)**) in order to achieve a good rate of nucleation. The third pulse step (E₃ = -0.265 V) maintained the homogeneous growth of Cu nuclei while simultaneously preventing the progressive nucleation at the carbon surface. The seeding pulse (E₂) used was for a duration of 5 ms for rapid electrodeposition of Cu nuclei while the following growth pulse (E₃) facilitated the slow growth of the Cu particles from the seeded Cu nuclei over a sufficient time period (50 s). **Figure 10 (A) and (B)** shows the current profile during the three-step process.

Electrosynthesis of optimised CuNPs resulted in two oxidation processes at E_(a) = -0.1 V and -0.4 V vs. Ag/AgCl and two reduction processes at E_(c) = -0.35 V and -0.8 V vs. Ag/AgCl respectively. **Figure 10 (C)** gives the comparison of the voltammograms arising from Method I and II with the former resulting in higher current density due to the larger particles achieved. A scan rate study realised linear current density (*J*) vs. *v* plots, which resulting in surface coverage values in the range 1.69 – 6.323 x 10⁻⁴ mol cm⁻² (**Figure 10 (D)**).



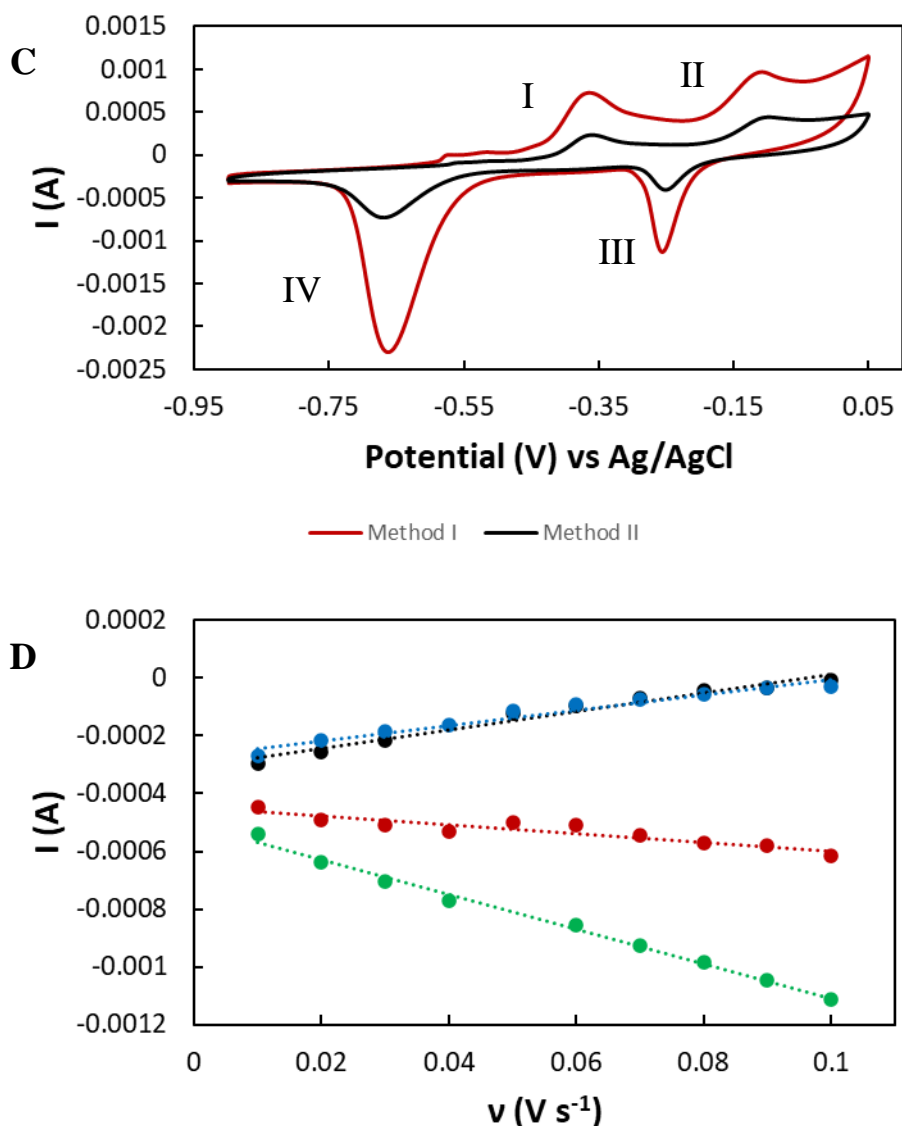


Figure 10 (A) Optimised three step electrodeposition of copper nanoparticles (CuNPs) ($E_1 = 0.7$ V for 5 s, $E_2 = -0.47$ V for 5 ms and $E_3 = -0.265$ for 50 s) (B) Schematic illustrating CuMP electrodeposition onto a GCE surface via the triple pulse potentiostatic method (Method II). (C) Overlaid Voltammetry of the CuMPs formed from Method II (black curve) vs those formed from Method I (red curve) in 0.1 M NaOH from 0.05 V to -1.8 V at 100 mV s^{-1} , where peaks I – IV are associated with copper electrochemistry. (D) Scan rate study J vs n plots for the copper processes I – IV (black, blue, red, green respectively), using Method II.

Table 3. and **Figure 11** below show the optimisation of the triple pulse method II on the DEX response with the influence of the growth pulse duration being most significant with optimum time of 50 s at -0.265 V vs. Ag/AgCl. E_1 was kept constant throughout the investigation. By varying E_2 and E_3 , a wide variety of electrodeposition parameters were tested monitoring the 1 mM DEX response at -1.34 V (see **Figure 11**). The effect of the nucleation pulse was first investigated with -0.47 V being found

as the optimum potential followed by the effect of the growth pulse (E_3). The E_3 pulse potential selected was -0.265 V, and the pulse duration was investigated with the best response when the electrodeposition was allowed to run until the peak maximum was reached at 50 s (parameters in **Table 3** below).

Table 3. Various CuNP electrodeposition parameters which were screened with 1.0 mM dexamethasone to identify the optimum method. The parameters that were changed are highlighted in red.

	Step 1 (E_1)		Step 2 (E_2)		Step 3 (E_3)	
Deposition method	Potential (V)	Time (s)	Potential (V)	Time (s)	Potential (V)	Time (s)
A	0.7	5	-0.47	0.005	-0.315	2
B	0.7	5	-0.5	0.005	-0.315	2
C	0.7	5	-0.55	0.005	-0.315	2
D	0.7	5	-0.6	0.005	-0.315	2
E	0.7	5	-0.65	0.005	-0.315	2
F	0.7	5	-0.47	0.002	-0.315	2
G	0.7	5	-0.47	0.005	-0.265	30
H	0.7	5	-0.47	0.005	-0.265	5
I	0.7	5	-0.47	0.005	-0.265	50
J	0.7	5	-0.47	0.005	-0.265	10

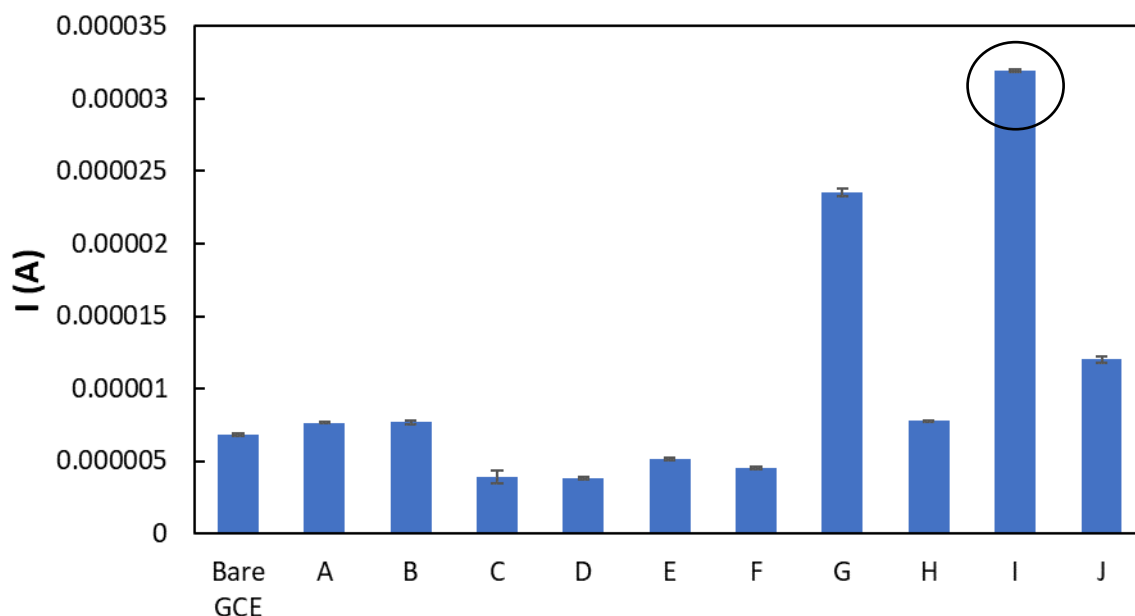


Figure 11. Bar chart monitoring the DEX cathodic response at the bare and each CuMP modified GCE.

2.3.4. Electrochemical Impedance Spectroscopy

Firstly, an anionic redox probe which comprised of 5mM $[\text{Fe}(\text{CN})_6]^{3/4-}$ redox probe in 0.1 M NaOH was used to further characterise the CuF/GCE and CuMP/GCE. The voltammogram of the redox probe in **Figure 12 (B)** displayed similar effects at each Cu modified GCEs, where the peak separation drastically decreased in the presence of Cu when compared to the voltammetry of the bare GCE, thus demonstrating that the electron transfer process was much easier at the Cu modified GCEs. The $[\text{Fe}(\text{CN})_6]^{3/4-}$ anodic and cathodic peaks were also more prominent at the CuF/GCE and CuMP/GCE, further indicating that the presence of Cu on the electrode surface increased the accessibility of the surface.

Electrochemical impedance spectroscopy (EIS) followed using both non-faradaic and faradaic impedance (**Figure 12**). EIS was employed in order to examine nanoparticle modified surfaces to achieve a better understanding of electron transfer between electrolyte and the surface²⁵. Non-faradaic experiments with an applied potential of -0.177 V resulted in a trend with respect to the higher frequency region representing charge transfer resistance in the following sequence: Bare GCE > CuF (I) > CuMP (II) (**Figure 12 (A)**) providing evidence that the smaller particles deposited using Method II increased charge transfer surface properties. **Figure 12 (B)** shows the redox probe $\text{Fe}^{2+/3+}$ process at bare and modified copper surfaces with

dramatic change in peak-to-peak separation relative to the bare GCE. Nyquist and Bode plots for faradaic EIS (in equimolar $[\text{Fe}(\text{CN})_6]^{4-/3-}$, 5 mM redox probe) are shown in **Figure 12 (C)** with corresponding data in **Table 4**. The corresponding capacitances of the GCE CuF/GCE and CuMP/GCE were calculated as 1.087×10^{-6} , 1.746×10^{-6} and 1.356×10^{-6} , respectively, where the smaller capacitance of the CuMPs confirmed the smaller quantity of Cu at the GCE surface which was in line with the surface coverage calculated from the scan rate studies.

In the case of the faradaic studies the Nyquist plots in **Figure 12(C)** show straight lines representing the diffusion limiting step in the low frequency region while a semicircle appears in the high frequencies domain indicating electron transfer limiting steps for the copper modified surface being lower than that at the bare GCE in the case of materials prepared using Method I and Method II (see **Table 4** for corresponding simulation data). From examining the Bode plots of the bare GCE and CuMP/GCE (**Figure 12**), the stability of each electrode was demonstrated. The Gain Margin of the CuMP/GCE and CuF/GCE were calculated as 1.993 Db and 1.811 Db respectively (2.961 Db for the bare GCE), thus the positive values demonstrate the electrochemical stability of both electrodes.

The Gain Margin was calculated by:

$$GM = 0 - G \text{ dB} \dots\dots\dots(1)$$

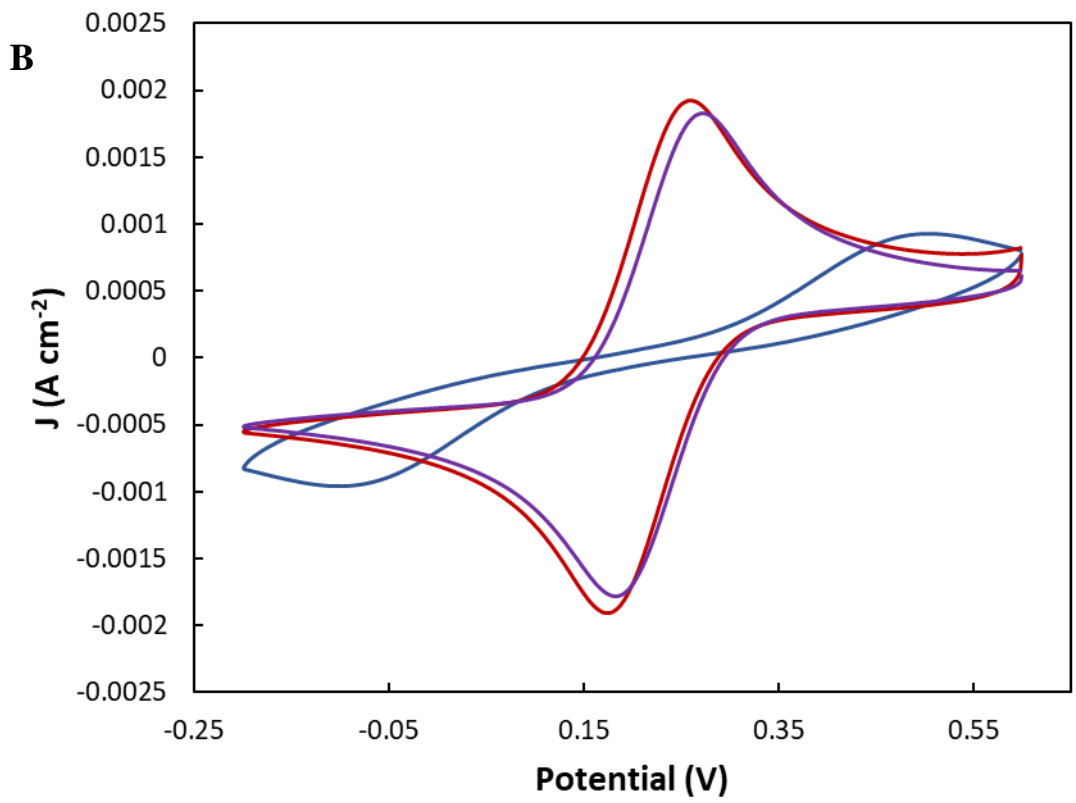
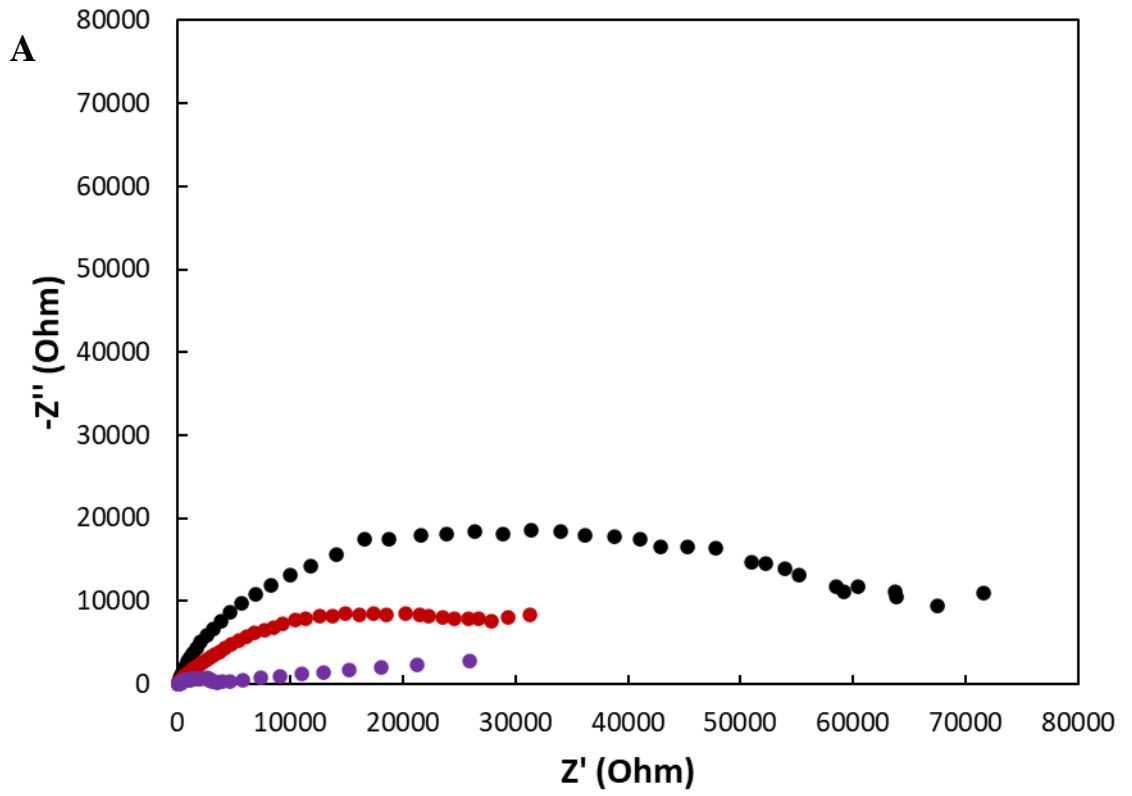
where GM is the Gain Margin and G is the gain.

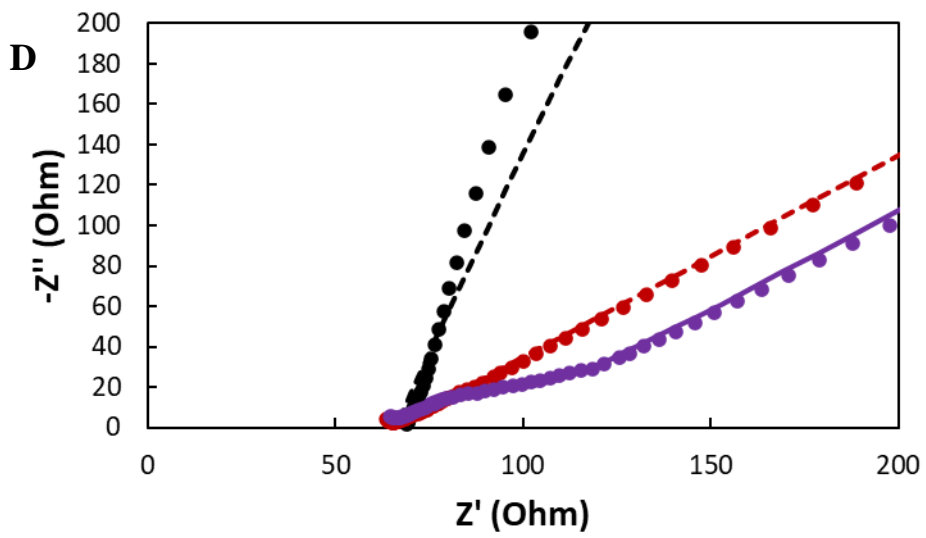
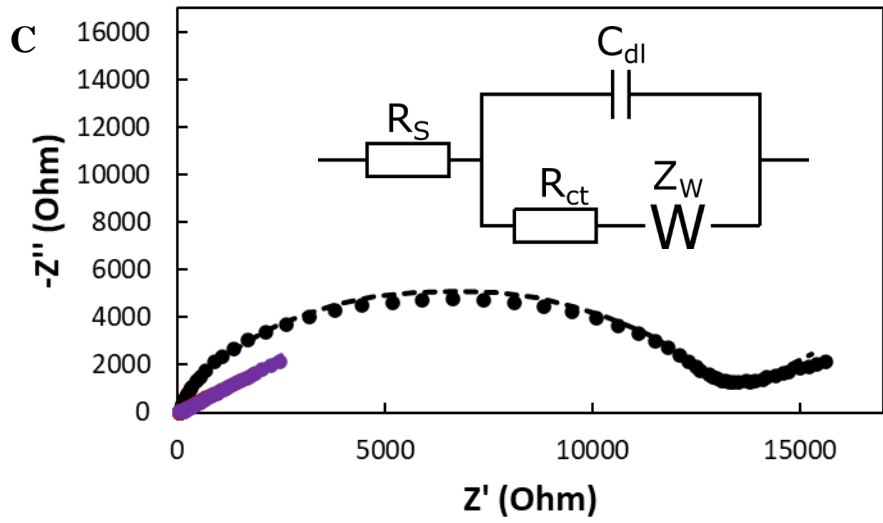
The Bode plots also gave useful information on confirming the resistance of each GCE analysed. From examining the Bode plot in **Figure 12 (F)**, maximum phase was determined as -72.7° , and -5.3° and -11.2° for the bare GCE, CuF/GCE and CuMP/GCE, respectively. This give information on the behaviour of each electrode, where -90° is equivalent to an ideal capacitor and 45° is equivalent to a pseudo-capacitor. Angles measured at 45° indicating a high ionic permeability, thus showing that it is a poor insulator²⁷. With consideration for the phase angle, the results confirm that the presence of Cu at the GCE surface increases the ionic permeability of each modified electrode and show that the Cu modifications improves the conductivity of the GCE in comparison to the bare GCE. The curve for the bare GCE occurs at a larger phase angle at lower frequencies, which suggests lower ionic permeability and therefore greater insulating properties for each of the Cu modified GCEs, where the

curve occurs at a lower phase angle and at higher frequencies. The slope of the Bode magnitude plot (**Figure 12 (E)**) can give an indication on the resistance and capacitance of the electrode in question, where a slope close to -1 represents an ideal capacitor and a slope close to 0 at higher frequencies indicates resistive behaviour, which could occur at a capacitive material. The slope of the bare GCE was calculated as -0.83, and at higher frequencies it was calculated as 0.0414, thus demonstrating the capacitive behaviour of the bare GCE. For the CuF/GCE, the slope was calculated to be -0.147, and -0.419 at higher frequencies, demonstrating the low capacitance of the CuF/GCE. Similarly, the slope of the CuMP/GCE was calculated as -0.14 and -0.44 at higher frequencies, also demonstrating the low capacitance of the CuF/GCE. These results support the highest capacitance of bare GCE followed by the CuF/GCE and CuMP/GCE.

Table 4. Showing the $\Delta E_p(V)$, $E_{1/2}(V)$ and $J_{p(a)}/J_{p(c)}$ of the bare GCE, CuF/GCE and CuMP/GCE.

	$\Delta E_p(V)$	$E_{1/2}(V)$	$J_{p(a)}/J_{p(c)}$
Bare GCE	0.659	0.2025	0.99
Method I	0.086	0.217	0.99
Method II	0.09	0.228	1.02





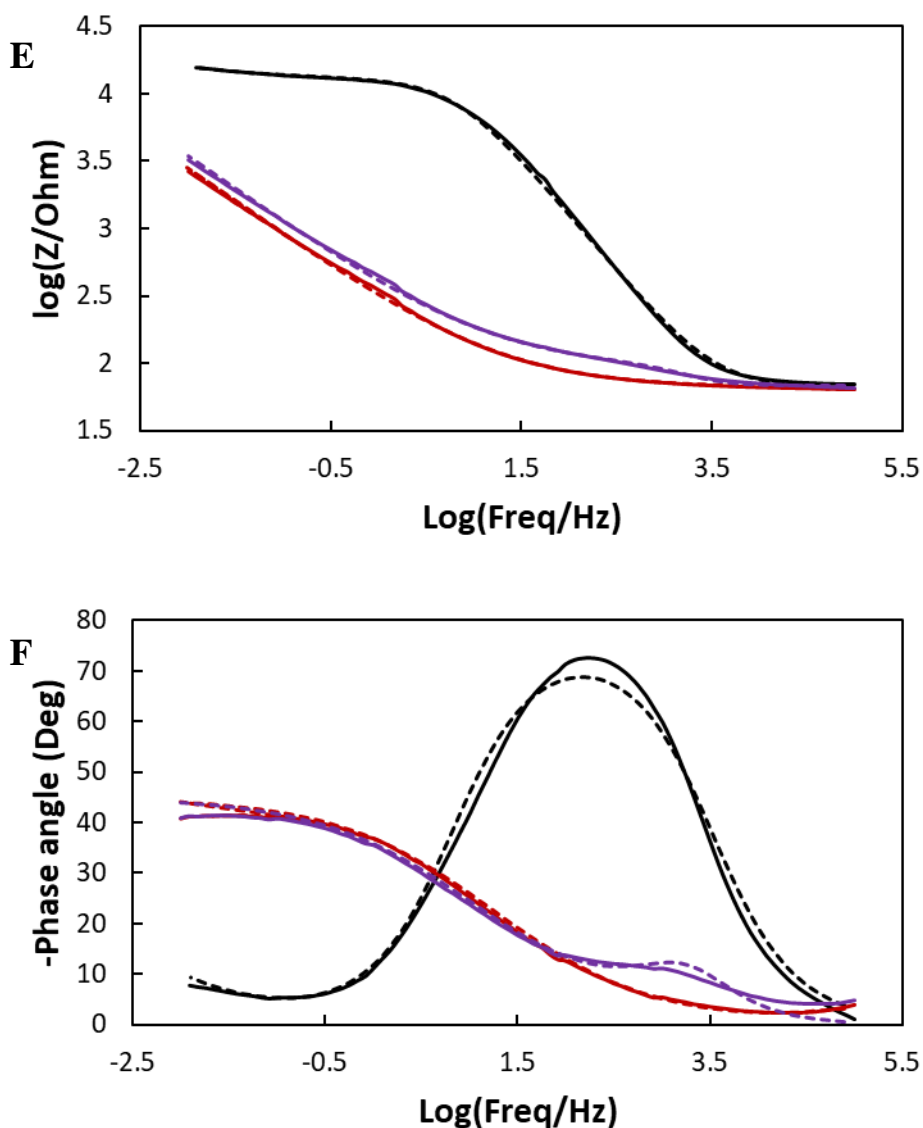


Figure 12. (A) Nyquist plots of the bare (black), Cu particles realised using Method I modified (red) and CuMPs formed using Method II (purple) GCEs in 0.1 M NaOH, with $E_{app} = -0.177$ V and frequency range 0.01 – 100,000 Hz at an amplitude of 5 mV (average of $n=2$). (B) Voltammetry of $[\text{Fe}(\text{CN})_6]^{3/4-}$ in 0.1 M NaOH at the bare (blue), Cu particle (Method I dual pulse method, red) modified and Cu particle (Method II – triple pulse method, purple) modified GCEs from -0.2 – 0.6 V at 100 mV sec^{-1} . (C) EIS of the bare GCE (black), Cu particle modified GCE (Method I, red) and the Cu particle modified GCE (Method II, blue) in 5 mM $[\text{Fe}(\text{CN})_6]^{-3/4}$ in 0.1 M NaOH with n from 0.01 – 100,000 Hz with an amplitude of 5 mV. $E = 0.202$ V, 0.217 V and 0.228 V for the bare GCE, Cu particles Method I and Cu particles Method II, respectively, with (D) a zoomed in view of the hemispherical regions of the CuF/GCE and CuMP/GCE. Bode plots of (E) the gain and (F) the negative phase angle vs \log_{10} of the frequency.

Table 5. Impedance data showing the R_s , R_{CT} , C_{dl} and Gain Margins (where applicable) for the bare, CuF/GCE and CuMP/GCE.

Non-faradaic impedance						
	Bare GCE		CuF/GCE		CuMP/GCE	
	Exp		Exp		Exp	
R_s (Ω)	98.66		101		104	
R_{CT} (Ω)	67369.2		3388.9		27773.9	
C_{dl}	1.087×10^{-6}		1.746×10^{-6}		1.356×10^{-6}	
Faradaic impedance						
	Bare GCE		CuF/GCE		CuMP/GCE	
	Exp	Sim	Exp	Sim	Exp	Sim
R_s (Ω)	65.2 ± 0.09	70.7 ± 0.13	65.6 ± 0.17	66.2 ± 0.09	66.3 ± 0.62	67.5 ± 0.15
R_{ct} (Ω)	13053 ± 186	11240 ± 144	6.0 ± 0.406	7.4 ± 0.822	20.7 ± 0.787	25.4 ± 3.348
C_{dl} (F)	$7.056 \pm 0.075 \times 10^{-7}$	$1.072 \pm 0.144 \times 10^{-6}$	$5.988 \pm 0.236 \times 10^{-6}$	$6.261 \pm 0.357 \times 10^{-6}$	$2.455 \pm 0.085 \times 10^{-6}$	$3.024 \pm 0.346 \times 10^{-6}$
Gain Margin (Db)	2.961 ± 0.022	2.950 ± 0.041	1.811 ± 0.034	1.818 ± 0.024	1.993 ± 0.052	1.974 ± 0.032
Phase Margin ($^\circ$)	55.9 ± 0.121	59.1 ± 0.32	0.2 ± 0.011	0.2 ± 0.009	-1.8 ± 0.021	-0.9 ± 0.012

(n=3)

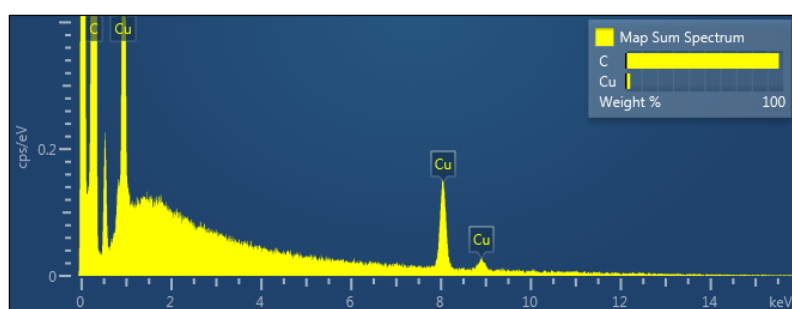
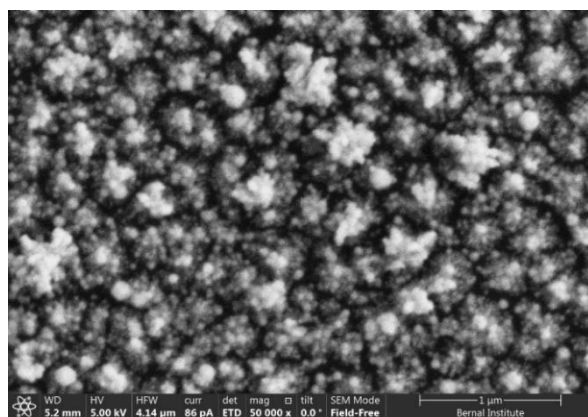
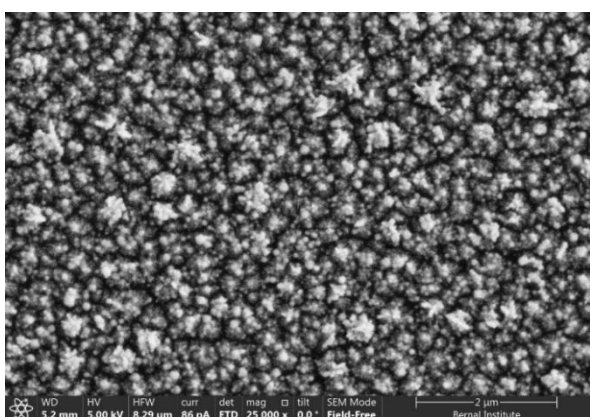
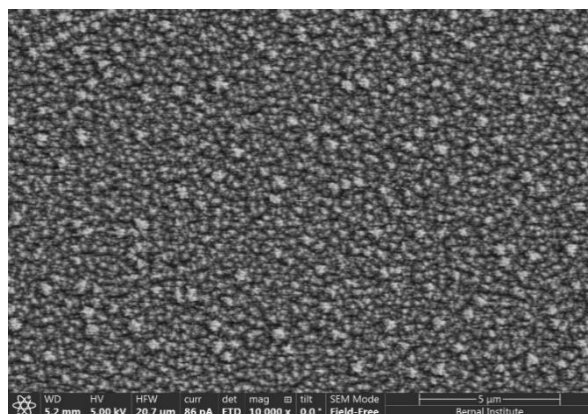
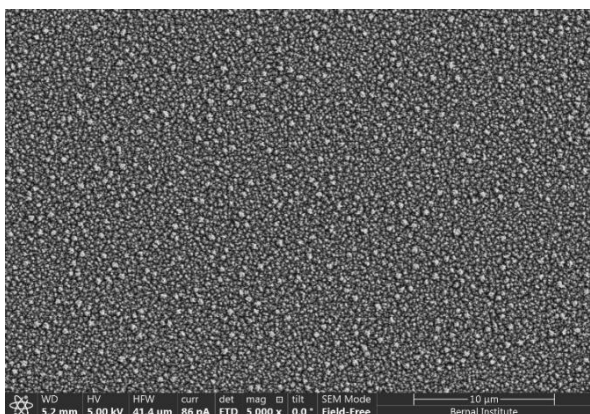
2.3.5. Surface characterisation of copper particles formed using both double and triple potentiostatic pulse method

HRSEM and EDS images shown in **Figure 13** below confirm the shape and distribution of the particles and EDS confirms the dominant surface copper content. The dual pulse deposition, shown in **Figure 13 (A)** resulted as expected in a uniformly heterogeneous copper surface where the conditions encouraged extensive particle growth. **Figure 12 (B)** shows the triple pulse sequence, which involved the more cathodic seed step allowed for nucleation with subsequent particle growth to 300 nm

and 600 nm (average $n = 718$) copper clusters (**Figure 14**) with some smaller particles, all of which appeared extremely well dispersed on the surface of the glassy carbon electrode.

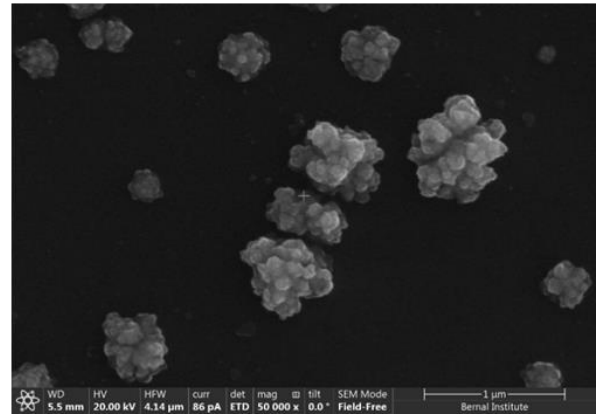
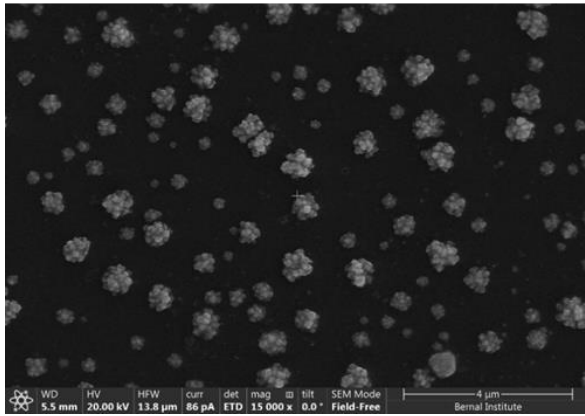
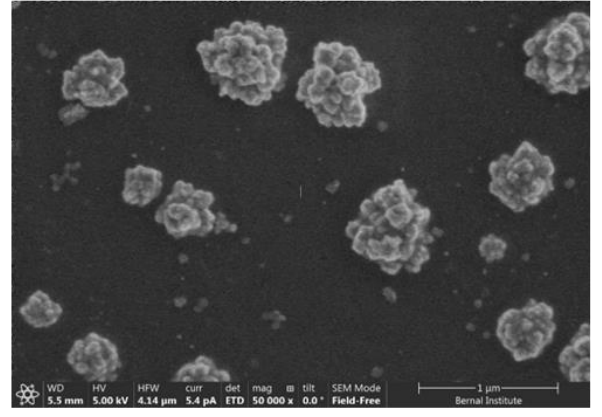
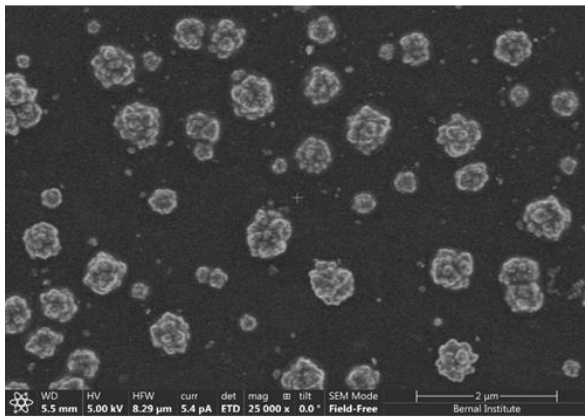
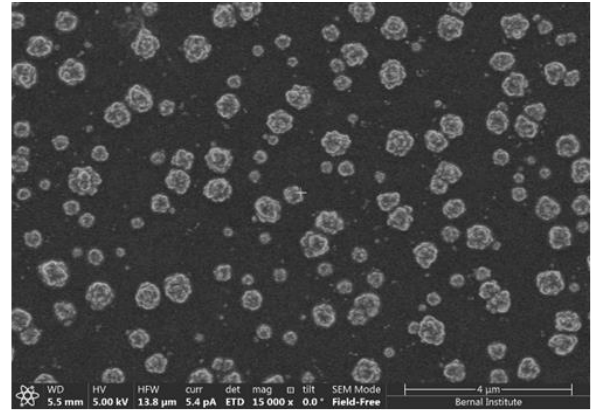
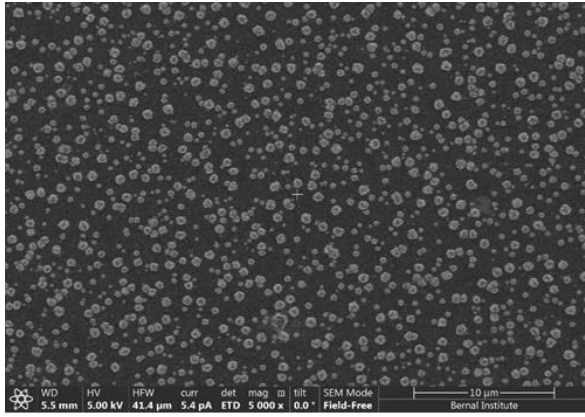
A

Method I dual pulse deposition



B

Method II triple pulse deposition



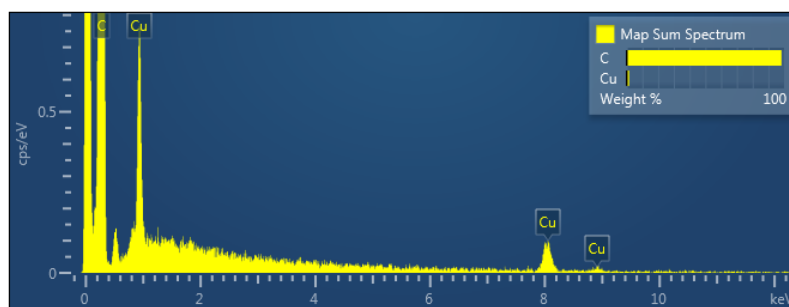


Figure 13. SEM image of the (A) Cu deposition at GCE (dual pulse potentiostatic electrodeposition) with EDS (B) Cu nanoclusters at GCE (triple pulse potentiostatic electrodeposition) with EDS providing confirmation of copper.

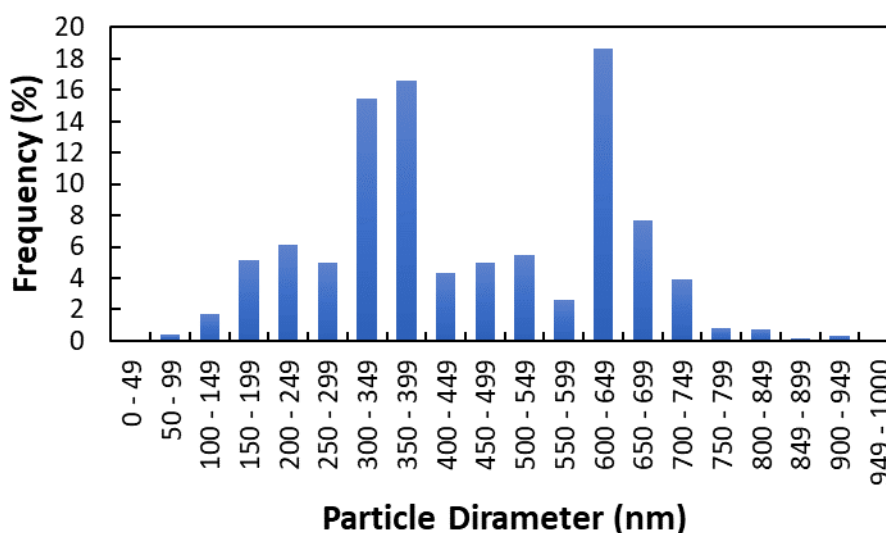


Figure 14. Particle size distribution of the CuMP modified GCE.

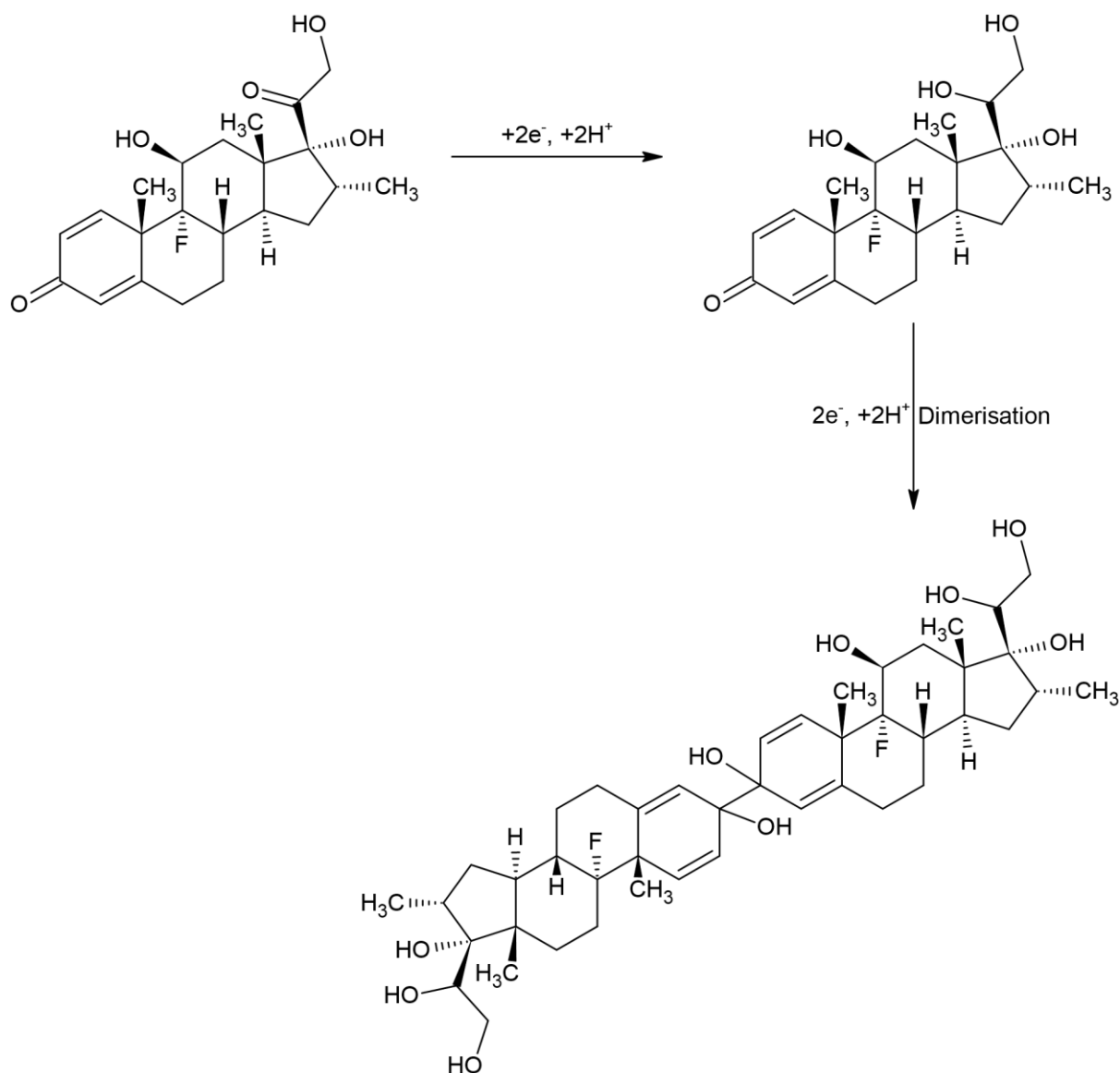
2.3.6. Dexamethasone electroanalysis at the copper dispersed surface formed using the double potentiostatic pulse Method I

In terms of electroanalysis, the electroactive surface area of the CuF/GCE and CuMP/GCE must be accounted for. This was done by firstly considering the area under the first Cu oxidation peak, i.e., peak I, giving the charge. This was then divided by the copper charge density factor for this peak, $352 \mu\text{C cm}^{-2}$. The area corresponding to the CuF/GCE and CuMP/GCE were calculated as $0.113 \pm 0.002 \text{ cm}^{-2}$ and $0.0896 \pm 0.002 \text{ cm}^{-2}$.

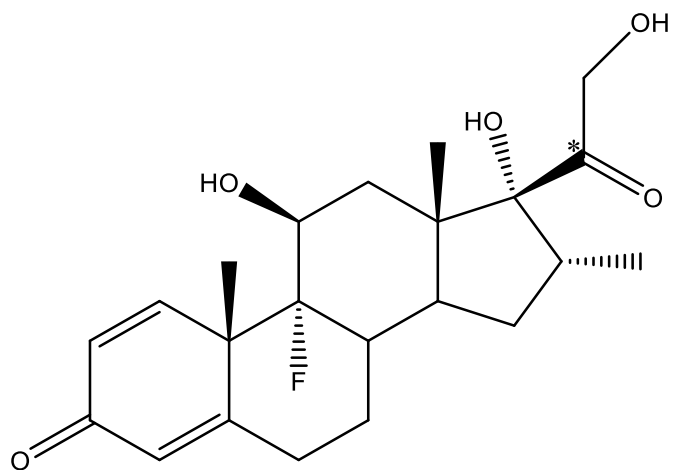
Figure 15 shows the DEX voltammetry at the copper modified electrode vs background electrolyte and results in two DEX cathodic peaks at -1.44 V and -1.33 V.

A marginal increase in the DEX reduction response was observed accompanied with a 125 mV anodic shift in response to the presence of copper on the GCE surface. Interestingly, a second DEX reduction signal was observed on the return cycle at -1.35 V at the copper modified GCE. This can be attributed to metal complexation with the first DEX reduction product. The adsorbed reduction product can then be reduced for a second time at C3, forming a DEX dimer in the form of a vicinal alcohol known as pinacol¹². A calibration was performed for 0.0781 – 5.0 mM DEX where peaks I and II were monitored simultaneously.

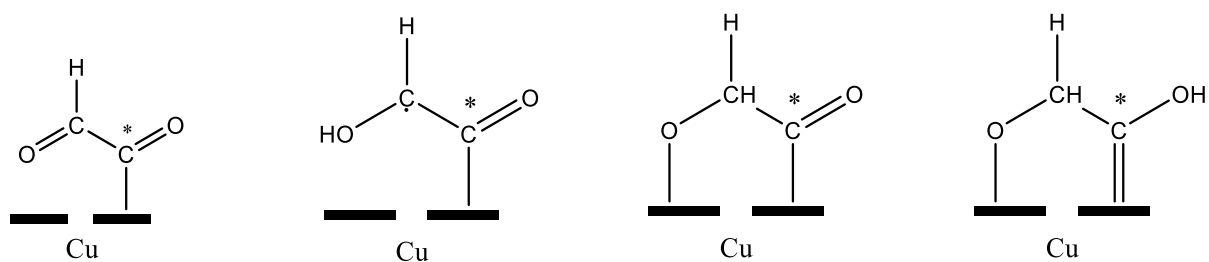
The DEX reduction signal (V) underwent a 150 mV anodic shift relative to the bare electrode (-1.37 V vs Ag/AgCl) at the copper modified surface with a second reduction signal (VI) observed at $E_p = -1.33$ V upon the return cycle – possibly due to surface copper interactions with the DEX reduction product, which is thought to involve the C3 ketone group as described previously by Oliveira et al^{28,29}, where upon undergoing electroreduction, results in the dimerisation of two DEX molecules at C3 (**Scheme 3**)¹². This peak (VI) (**Figure 15 and 16 (A)**) was responsive to DEX additions and not evident in the background scan nor in the absence of copper nanostructures. To interpret this process, we look to copper as being centre stage for the carbon dioxide reduction reaction as a means to reduce waste CO₂ by converting to fuels and chemical feedstocks^{28, 29}. GCE is commonly employed as a supporting electrode for nanoparticle catalysis and there may be overlapping Cu surface interactions in this instance with respect to the DEX carbonyl group at C20 (*, **Scheme 4**) being analogous to the reduction of surface adsorbed CO (formed from electroreduction of CO₂) to C₂ products according to the ethylene pathway³⁰. According to Garza *et al* reduction of CO to CHO is followed by reaction with CO to form COCHO which is tautomeric with the C-C bond formation being the rate determining step³⁰. Such adsorbed species may help explain this new reduction process on the reverse sweep with a possible site of interaction and overlapping tentative adsorbed products shown in **Scheme 4**.



Scheme 3. Depicting the two step DEX reduction process observed at the Cu modified GCEs, where in the first step, DEX undergoes electroreduction at the C20 ketone, producing an alcohol group. In the second reduction step, the C3 keytone group is reduced, resulting in a dimerisation of two adjacent DEX molecules.



Dexamethasone



Surface interaction at C20

Scheme 4. Depicting possible surface interactions between DEX and the Cu nanostructure modified GCEs at C20.

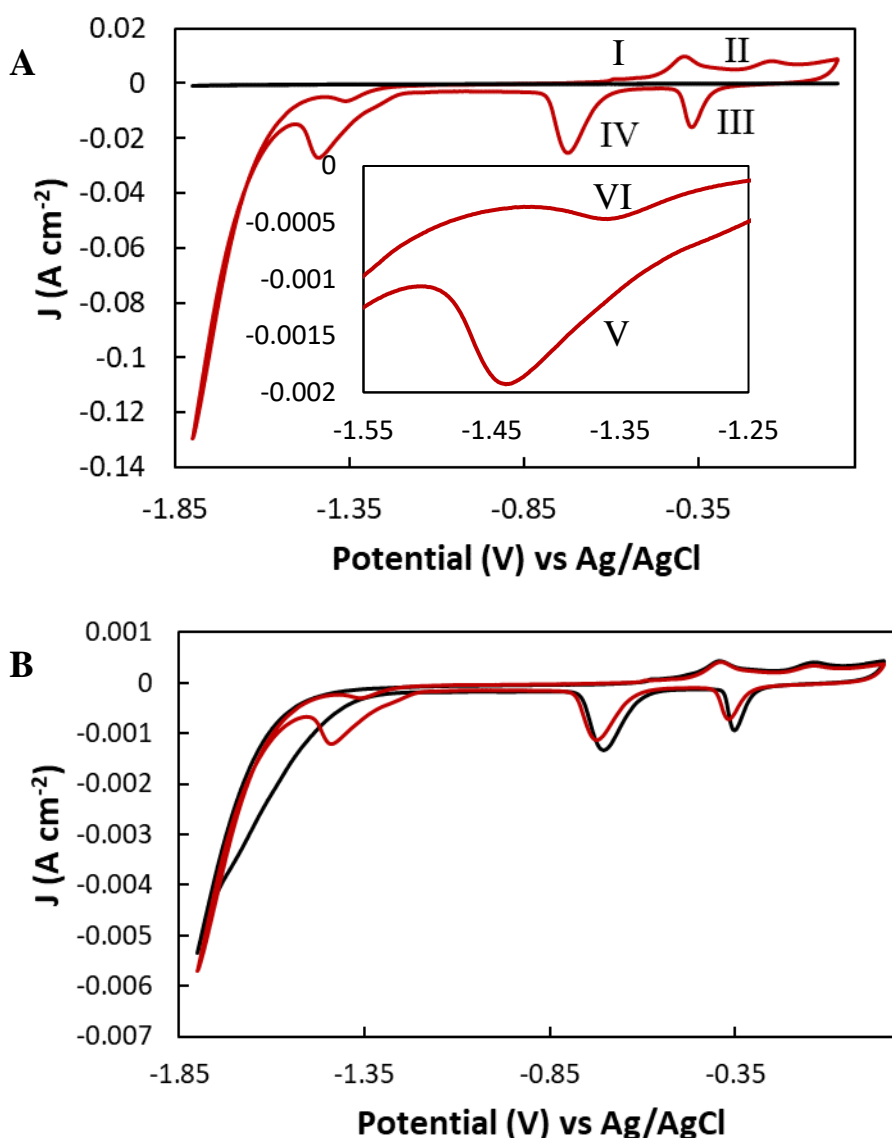
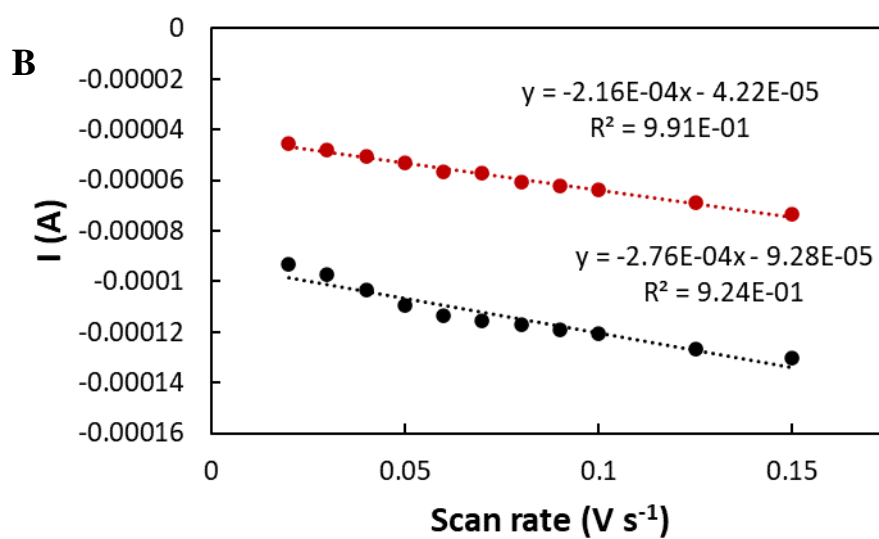
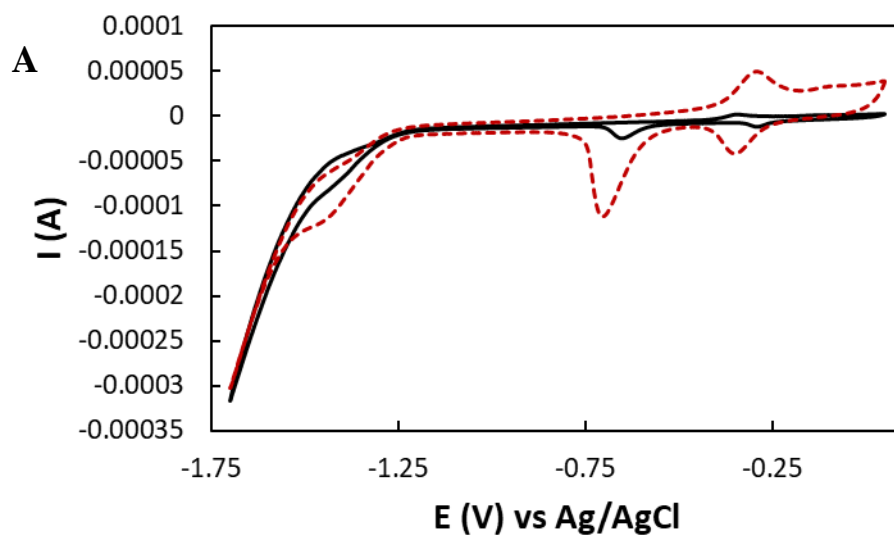


Figure 15. (A) Voltammetry of 1 mM dexamethasone at the bare (black) and Method I Cu particle (red) GCEs from -1.8 V to 0.05 V at 100 mV s^{-1} . (B) Voltammetry of 1 mM DEX (red) in 0.1 M NaOH (black) at the Cu particle modified GCE from -1.8 – 0.05 V at 100 mV s^{-1} .

From examining 1 mM DEX in 0.1 M NaOH at the CuF modified GCE at $20 - 200 \text{ mV s}^{-1}$ (**Figure 16 (A)**), a further insight into the electrochemical behaviour of DEX was obtained. From examining the plot of scan rate vs peak current in **Figure 16 (B)**, the electrochemical reduction process VI was linear with respect to increasing scan rate, indicating that this reduction process was surface controlled, while the reduction response associated with peak V was not linear in response to increasing scan rate. The plots of the peak current vs the square root of the scan rate for signals V and VI were both linear (**Figure 16 (C)**), thus determining the diffusion-controlled nature of the process V. These observations are in agreement with the proposed

electrochemical reduction process shown in **Scheme 4**. It was also observed that both electroreduction responses displayed a dependence on the scan rate, where a 0.059 V and 0.154 V cathodic shift was observed for responses V and VI respectively.



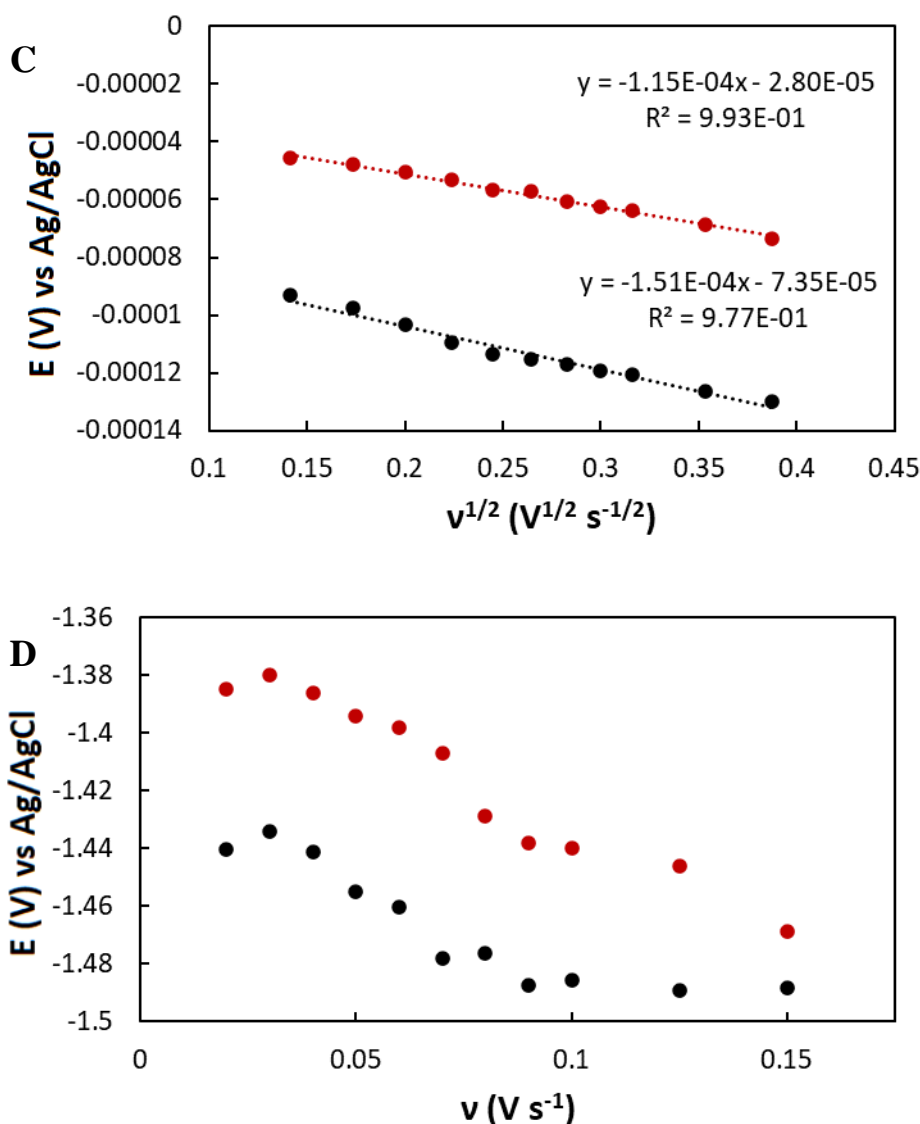
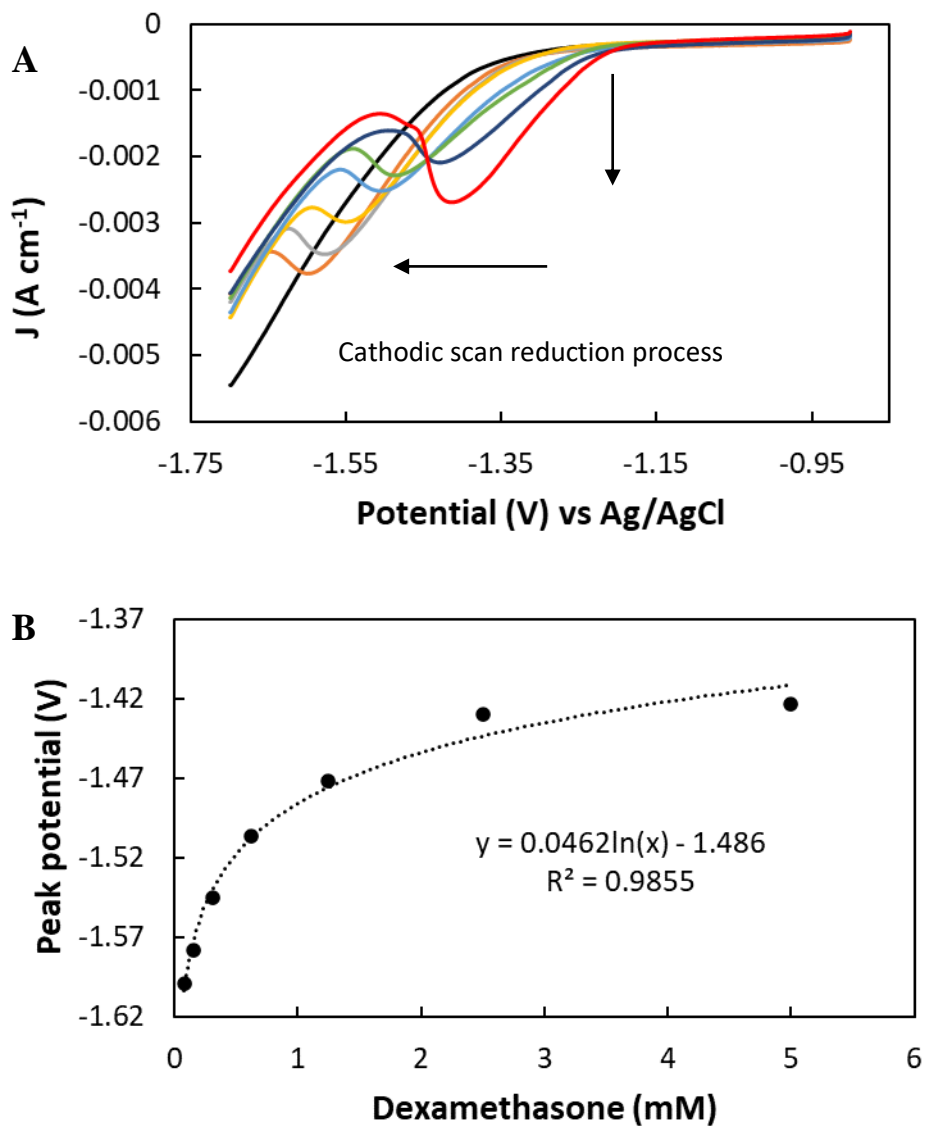


Figure 16 (A) Voltammetry of 1 mM DEX at the CuF modified GCE from -1.7 – 0.05 V at 20 – 150 mV s^{-1} (20 and 150 mV s^{-1} shown as the black line and red dashed line respectively). Plots of the (B) peak current vs v , (C) peak current vs $v^{1/2}$ and (D) peak potential vs v , where the signal V cathodic response shown in black and the signal VI cathodic response shown in red.

Due to the significant cathodic shift in this forward peak (peak V) (**Figure 17** (A) (B)), the reverse signal (peak VI) was utilised as quantitative response to DEX as there was no overall shift in peak potential with respect to increasing concentration (**Figure 17** (C)). The calibration resulted in a sensitivity of $2.0 \times 10^2 \mu\text{A cm}^{-2} \text{mM}^{-1}$ ($n = 3$) for the CuF/GCE, with $\text{LOD} = 28 \pm 0.45 \mu\text{M}$ and $\text{LOQ} = 95 \pm 1.5 \mu\text{M}$. The signals for the CuMP/GCE and bare GCE were quite lower than that of the CuF/GCE at $1.13 \times 10^2 \mu\text{A cm}^{-2} \text{mM}^{-1}$ and $2.78 \times 10^1 \mu\text{A cm}^{-2} \text{mM}^{-1}$ respectively (**Table 6**), thus

indicating the optimum electrode conditions for DEX quantitation. The LOD was calculated as $343 \pm 1.7 \mu\text{M}$ and LOQ was $2,285 \pm 11.5 \mu\text{M}$ for the bare GCE, indicating that the DEX could be detected at concentrations 12 times lower and quantified at concentrations 24 times lower at the CuF modified GCE than at the bare GCE.



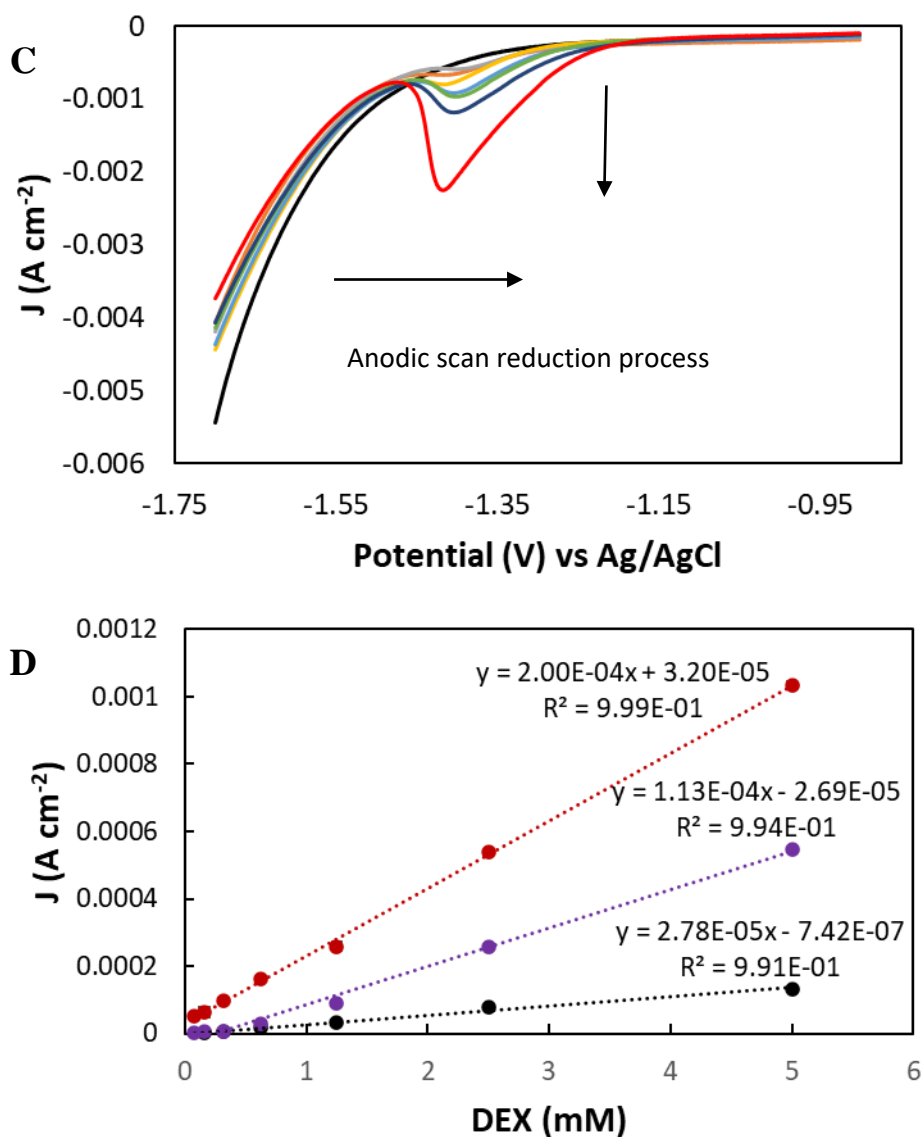


Figure 17 (A) CV of increasing dexamethasone 0.0781 – 5 mM in 0.1 M NaOH at the Method I modified GCE over the range 1.5 to -1.8 V in the forward direction monitoring peak V. (B) Corresponding plot of peak potential at -1.6 – -1.4 V vs concentration confirming the cathodic shift in the forward direction monitoring peak V with DEX additions. (C) CV of increasing dexamethasone 0.0781 – 5 mM in 0.1 M NaOH at the copper modified GCE over the range 1.5 to -1.8 V in the reverse direction monitoring peak VI with (D) Corresponding dexamethasone calibration curve with resulting sensitivities of $2.00 \times 10^2 \mu\text{A cm}^{-2} \text{mM}^{-1}$ peak V (red) and $1.13 \times 10^2 \mu\text{A cm}^{-2} \text{mM}^{-1}$ for the CuF/GCE and CuMP/GCE respectively (calibration at the bare GCE shown in orange with sensitivity $2.76 \times 10^1 \mu\text{A cm}^{-2} \text{mM}^{-1}$). (n = 3)

Table 6. Comparison of copper electrodeposited electrode response for Method I and II relative to the bare GCE response.

Electrodeposition method	Sensitivity @CuGCE (Reverse reduction wave at $E_p = -1.33$ V)	Sensitivity @Bare GCE ($E_p = -1.55$ V)
CuMP/GCE (Triple Pulse)	3.96×10^{-5} A cm ⁻² mM ⁻¹ (n = 3)	2.76×10^{-5} A mM ⁻¹ cm ⁻² (1.4-fold increase) (n = 3)
CuF/GCE (Dual Pulse)	9.61×10^{-5} A cm ⁻² mM ⁻¹ (n = 3)	2.76×10^{-5} A mM ⁻¹ cm ⁻² (3.5-fold increase) (n = 3)

2.3.5. Electroanalysis of dexamethasone extracted from pharmaceutical samples.

In order to put the non-aqueous and aqueous DEX quantitation to the test the steroid was recovered from (a) a commercial cream sample and (b) solid dose formulation prepared in house. Sample quantitation from spiked commercial hydrocortisone cream exploited the non-aqueous electroanalysis based on the anodic DEX wave at 1.3 V (see **Figure 18 (A)**) with the sample prepared according to the procedure in section 2.3.3. Corresponding recovery data is summarised in **Table 7 (A)** for triplicate replicates. **Figure 18 (B)** shows the DEX recovery from a tablet formulation prepared according to section 2.3.4 with recovery data (n=3) in **Table 7 (B)**.

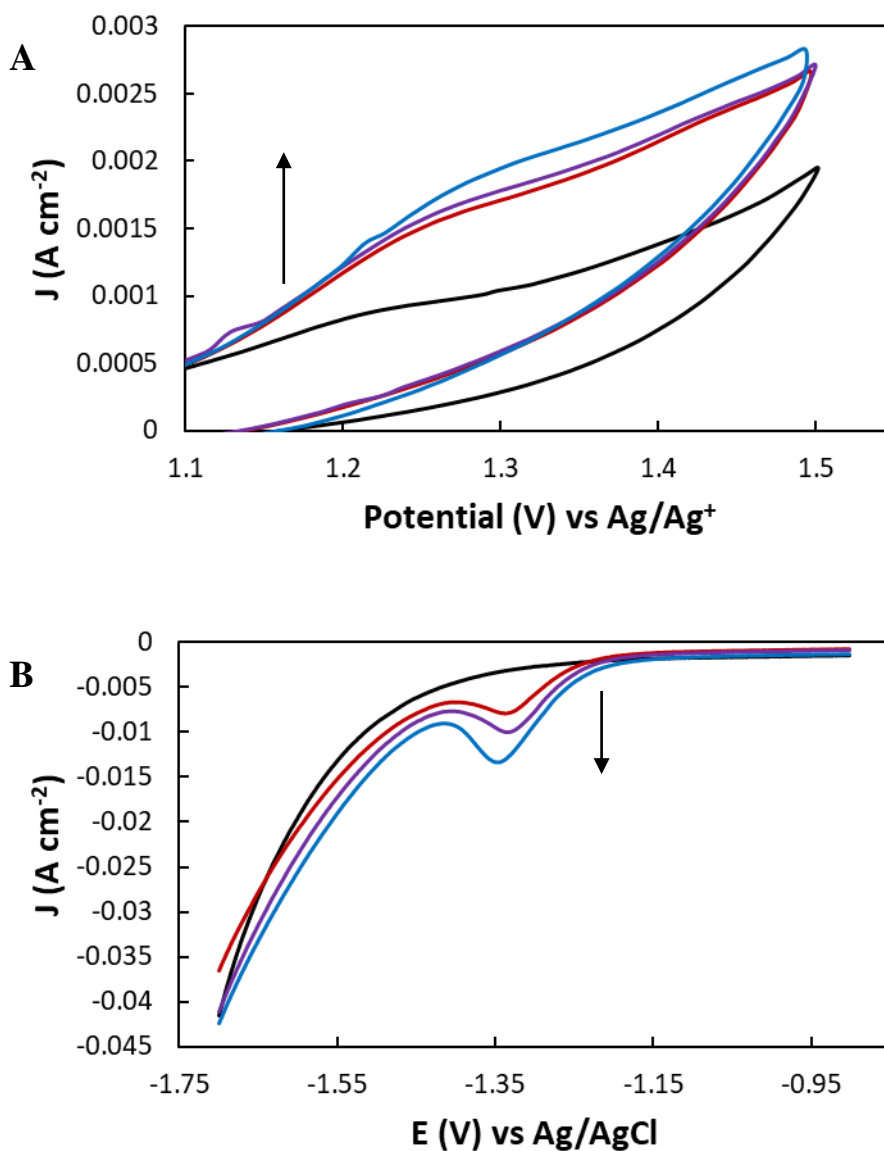


Figure 18 (A) Voltammetry of dexamethasone extracted from 1.0 g of 3 cream samples (0.0 % (black), 0.25 % (red), 0.35 % (purple) and 0.5 % (blue) w/w dexamethasone) in 0.1 M LiClO_4 in MeOH zoomed in on the anodic response. **(B)** Voltammetry of DEX extracted from the tablet samples containing 0 (black) 6 (red), 10 (purple) and 15 (blue) mg DEX (return sweep only shown).

The average % recovery for the cream extraction (0.25 – 0.5% DEX) based on the non-aqueous calibration and anodic signal realised 101.77 ± 2.54 % ($n=3$) recovery. The aqueous sensor was unsuitable for the spiked cream sample as some paraffin dissolved into methanol during the extraction process and formed a waxy solid upon evaporation of the solvent prior to addition of the aqueous electrolyte. Some of this solid was carried over to the aqueous solution despite being filtered into the volumetric flask used to prepare the analytical sample, thus having a significant impact on the accuracy of the sample recovery. The non-aqueous extraction was the most

suitable and 93.46 – 107.99 % DEX was recovered with a 0.14 – 6.33 % variance between each sample. The solid dose form (prepared in house with excipients sucrose and lubricant magnesium stearate) resulted in 84.64 ± 3.50 % for n=3 using the reverse adsorption peak associated with the DEX-Cu interaction at -1.3 V vs. Ag/AgCl. The aqueous sensor was suitable for the tablet extraction as there was no issue with unwanted electroactive or insoluble compounds, in this case the magnesium stearate, being carried over during both the methanol and 1:1 methanol: 0.1 M NaOH filtration steps. Due to the higher sensitivity and lower LOD and LOQ values, the CuF/GCE was utilised as it was the optimum DEX electrochemical sensor. In total, 77.46 – 87.91 % DEX was recovered with a 1.93 – 4.97 % variance between each sample.

Table 7 (A) Theoretical dexamethasone concentration extracted from 1.0 g of commercial hydrocortisone cream and reconstituted into 10 mL MeOH, the average sample concentrations measured and % recovery (n=3) **(B)** Displaying the theoretical concentration and signal, the average E_p and I_p values, variance, standard deviation, recovery, and percentage recovery for tablets containing 2 – 15 mg DEX.

(A) Cream extraction data				
				
Cream (% w/w DEX)	Theoretical concentration (mM)	DEX recovered (mM)	% Recovery	% Variance
0.25 %	0.637	0.685 ± 0.0434	107.46	6.321
0.35 %	0.892	0.926 ± 0.00131	103.86	0.142
0.5 %	1.217	1.197 ± 0.0141	93.99	1.178
(B) Tablet extraction data				
				
Tablet (mg DEX)	Theoretical concentration (mM)	DEX recovered (mM)	% Recovery	% Variance
6	1.529	1.25 ± 0.027	84.36	3.34
10	2.548	1.97 ± 0.098	79.56	5.72
15	3.822	3.36 ± 0.065	89.99	1.44

2.4.0. Conclusions

In conclusion, this work has advanced understanding of the electrochemistry of the therapeutic dexamethasone in a wide variety of conditions. Firstly, DEX was quantified in a non-aqueous system, which comprised of 0.1 M LiClO₄ in MeOH. A DEX oxidation response was observed at 1.3 V at the bare GCE and with the aid of a scan rate study, the diffusion-controlled nature of this oxidative process was demonstrated. The DEX oxidation was carried out over the range 0.83 – 3.07 mM, with sensitivity of $5.42 \times 10^2 \mu\text{A cm}^{-2} \text{mM}^{-1}$ and $R^2 = 0.998$. DEX was then studied at bare and Cu nanostructure modified GCEs under alkaline conditions (0.1 M NaOH). Dexamethasone quantitation was achieved over the range 0.0781 – 0.5 mM with sensitivity of $6.93 \times 10^{-5} \text{ A cm}^{-2} \text{mM}^{-1}$ at an unmodified electrode (reduction process monitored). Electrosynthesis of optimised CuF/GCE using a dual pulse potentiostatic approach was employed, which resulted in two oxidation processes at $E_{(a)} = -0.1 \text{ V}$ and $-0.4 \text{ V vs Ag/AgCl}$ and two reduction processes at $E_{(c)} = -0.35 \text{ V}$ and $-0.8 \text{ V vs Ag/AgCl}$ respectively, resulting in surface coverage values in the range $3.492 - 2.065 \times 10^{-9} \text{ mol cm}^{-2}$. Electrosynthesis of optimised CuMP/GCE using a triple pulse potentiostatic approach was also employed, which resulted in two oxidation processes resulting in surface coverage values in the range $1.69 - 6.32 \times 10^{-4} \text{ mol cm}^{-2}$. The Cu nanostructure modified GCEs resulted in an anodic shift in the DEX cathodic process accompanied by a second reduction process on the return cycle which was exploited as the analytical signal. Quantitation was carried out by CV over the range 0.0781 – 5 mM with sensitivities $2.00 \times 10^2 \mu\text{A cm}^{-2} \text{mM}^{-1}$ and $1.13 \times 10^2 \mu\text{A cm}^{-2} \text{mM}^{-1}$ for the CuF and CuMP modified GCEs respectively ($2.78 \times 10^1 \mu\text{A cm}^{-2} \text{mM}^{-1}$ for the bare GCE). Further work will extend the surface characterisation of the optimal electrodeposited CuMP followed by DPV and constant pulse methodologies with the view to examine co-analysis potential with respect to related and interfering molecules.

2.5.0. References

1. Alimohammadi, S.; Kiani, M. A.; Imani, M.; Rafii-Tabar, H.; Sasanpour, P., Electrochemical Determination of Dexamethasone by Graphene Modified Electrode: Experimental and Theoretical Investigations. *Sci Rep* **2019**, *9* (1), 11775.
2. Johnson, D. B.; Lopez, M. J.; Kelley, B., *Dexamethasone*. StatPearls Publishing, Treasure Island (FL): 2021.
3. Munch, M. W.; Granholm, A.; Myatra, S. N.; Vijayaraghavan, B.; Cronhjort, M.; Wahlin, R. R.; Jakob, S. M.; Cioccarri, L.; Kjaer, M. N.; Vesterlund, G. K.; Meyhoff, T. S.; Helleberg, M.; Moller, M. H.; Benfield, T.; Venkatesh, B.; Hammond, N.; Micallef, S.; Bassi, A.; John, O.; Jha, V.; Kristiansen, K. T.; Ulrik, C. S.; Jorgensen, V. L.; Smitt, M.; Bestle, M. H.; Andreasen, A. S.; Poulsen, L. M.; Rasmussen, B. S.; Brochner, A. C.; Strom, T.; Moller, A.; Khan, M. S.; Padmanaban, A.; Divatia, J. V.; Saseedharan, S.; Borawake, K.; Kapadia, F.; Dixit, S.; Chawla, R.; Shukla, U.; Amin, P.; Chew, M. S.; Gluud, C.; Lange, T.; Perner, A., Higher vs lower doses of dexamethasone in patients with COVID-19 and severe hypoxia (COVID STEROID 2) trial: Protocol and statistical analysis plan. *Acta Anaesthesiol Scand* **2021**, *65* (6), 834-845.
4. Horby, P.; Lim, W. S.; Emberson, J. R.; Mafham, M.; Bell, J. L.; Linsell, L.; Staplin, N.; Brightling, C.; Ustianowski, A.; Elmahi, E.; Prudon, B.; Green, C.; Felton, T.; Chadwick, D.; Rege, K.; Fegan, C.; Chappell, L. C.; Faust, S. N.; Jaki, T.; Jeffery, K.; Montgomery, A.; Rowan, K.; Juszczak, E.; Baillie, J. K.; Haynes, R.; Landray, M. J., Dexamethasone in Hospitalized Patients with Covid-19. *N Engl J Med* **2021**, *384* (8), 693-704.
5. Chen, Q.; Zielinski, D.; Chen, J.; Koski, A.; Werst, D.; Nowak, S., A validated, stability-indicating HPLC method for the determination of dexamethasone related substances on dexamethasone-coated drug-eluting stents. *J Pharm Biomed Anal* **2008**, *48* (3), 732-8.
6. Razuc, M. F.; Grünhut, M.; Garrido, M.; Fernández Band, B. S., Second order advantage applied to the spectrophotometric analysis of ciprofloxacin and dexamethasone in ophthalmic drops; automatic green method using on-line photodegradation. *Analytical Sciences: The International Journal of the Japan Society of Analytical Chemistry* **2014**, *30* (12), 1121-1127.

7. Xu, Q., Incorporating solid-phase extraction into compendial procedures for the determination of dexamethasone and impurities in low-dose drug products. *J Pharm Biomed Anal* **2019**, *175*, 112773.
8. Hegazy, M. A.; Lotfy, H. M.; Rezk, M. R.; Omran, Y. R., Novel spectrophotometric determination of chloramphenicol and dexamethasone in the presence of non labeled interfering substances using univariate methods and multivariate regression model updating. *Spectrochim Acta A Mol Biomol Spectrosc* **2015**, *140*, 600-13.
9. Fatahi, A.; Malakooti, R.; Shahlai, M., Electrocatalytic oxidation and determination of dexamethasone at an Fe₃O₄/PANI–CuII microsphere modified carbon ionic liquid electrode. *RSC Advances* **2017**, *7* (19), 11322-11330.
10. Mazloum-Ardakani, M.; Sadri, N.; Eslami, V., Detection of Dexamethasone Sodium Phosphate in Blood Plasma: Application of Hematite in Electrochemical Sensors. *Electroanalysis* **2020**, *32* (6), 1148-1154.
11. Primpray, V.; Chailapakul, O.; Tokeshi, M.; Rojanarata, T.; Laiwattanapaisal, W., A paper-based analytical device coupled with electrochemical detection for the determination of dexamethasone and prednisolone in adulterated traditional medicines. *Anal Chim Acta* **2019**, *1078*, 16-23.
12. Oliveira, T. M.; Ribeiro, F. W.; Soares, J. E.; de Lima-Neto, P.; Correia, A. N., Square-wave adsorptive voltammetry of dexamethasone: redox mechanism, kinetic properties, and electroanalytical determinations in multicomponent formulations. *Anal Biochem* **2011**, *413* (2), 148-56.
13. Oliveira, T. M. B. F.; Ribeiro, F. W. P.; do Nascimento, J. M.; Soares, J. E. S.; Freire, V. N.; Becker, H.; de Lima-Neto, P.; Correia, A. N., Direct Electrochemical Analysis of Dexamethasone Endocrine Disruptor in Raw Natural Waters. *Journal of the Brazilian Chemical Society* **2012**, *23* (1), 110-119.
14. Cioffi, N.; Colaianni, L.; Ieva, E.; Pilolli, R.; Ditaranto, N.; Angione, M. D.; Cotrone, S.; Buchholt, K.; Spetz, A. L.; Sabbatini, L.; Torsi, L., Electrosynthesis and characterization of gold nanoparticles for electronic capacitance sensing of pollutants. *Electrochimica Acta* **2011**, *56* (10), 3713-3720.
15. Guin, S. K.; Parvathi, K.; Ambolika, A. S.; Pillai, J. S.; Maity, D. K.; Kannan, S.; Aggarwal, S. K., An insight into the electrocatalysis of uranyl sulphate on gold nanoparticles modified glassy carbon electrode. *Electrochimica Acta* **2015**, *154*, 413-420.

16. Guin, S. K.; Pillai, J. S.; Ambolikar, A. S.; Saha, A.; Aggarwal, S. K., Template-free electrosynthesis of gold nanoparticles of controlled size dispersion for the determination of lead at ultratrace levels. *RSC Advances* **2013**, *3* (39).
17. Ambolikar, A. S.; Guin, S. K., Template-free Electrosynthesis of Platinum NanoCauliflowers for Catalysing Electron Transfer Reaction of Plutonium. **2020**, *32*, 2503 – 2510.
18. Guin, S. K.; Sharma, H. S.; Aggarwal, S. K., Electrosynthesis of lead nanoparticles on template free gold surface by potentiostatic triple pulse technique. *Electrochimica Acta* **2010**, *55* (3), 1245-1257.
19. Guin, S. K.; Knittel, P.; Daboss, S.; Breusow, A.; Kranz, C., Template- and Additive-free Electrosynthesis and Characterization of Spherical Gold Nanoparticles on Hydrophobic Conducting Polydimethylsiloxane. *Chem Asian J* **2017**, *12* (13), 1615-1624.
20. Moozarm Nia, P.; Woi, P. M.; Alias, Y., Facile one-step electrochemical deposition of copper nanoparticles and reduced graphene oxide as nonenzymatic hydrogen peroxide sensor. *Applied Surface Science* **2017**, *413*, 56-65.
21. Qiao, J.; Fan, M.; Fu, Y.; Bai, Z.; Ma, C.; Liu, Y.; Zhou, X. D., Highly-active copper oxide/copper electrocatalysts induced from hierarchical copper oxide nanospheres for carbon dioxide reduction reaction. *Electrochimica Acta* **2015**, *153*, 559-565.
22. Dongare, S.; Singh, N.; Bhunia, H., Electrocatalytic reduction of CO₂ to useful chemicals on copper nanoparticles. *Applied Surface Science* **2021**, 537.
23. Huang, L.; Lee, E.-S.; Kim, K.-B., Electrodeposition of monodisperse copper nanoparticles on highly oriented pyrolytic graphite electrode with modulation potential method. *Colloids and Surfaces A: Physicochemical and Engineering Aspects* **2005**, *262* (1-3), 125-131.
24. Mani, V.; Devasenathipathy, R.; Chen, S.-M.; Wang, S.-F.; Devi, P.; Tai, Y., Electrodeposition of copper nanoparticles using pectin scaffold at graphene nanosheets for electrochemical sensing of glucose and hydrogen peroxide. *Electrochimica Acta* **2015**, *176*, 804-810.
25. Yang, J.; Jiang, L. C.; Zhang, W. D.; Gunasekaran, S., A highly sensitive non-enzymatic glucose sensor based on a simple two-step electrodeposition of cupric oxide (CuO) nanoparticles onto multi-walled carbon nanotube arrays. *Talanta* **2010**, *82* (1), 25-33.

26. Teo, W. Z.; Ambrosi, A.; Pumera, M., Direct electrochemistry of copper oxide nanoparticles in alkaline media. *Electrochemistry Communications* **2013**, *28*, 51-53.
27. Laschuk, N. O.; Easton, E. B.; Zenkina, O. V., Reducing the resistance for the use of electrochemical impedance spectroscopy analysis in materials chemistry. *RSC Adv* **2021**, *11* (45), 27925-27936.
28. Vavra, J.; Shen, T.-H.; Stoian, D.; Tileli, V.; Buonsanti, R., Real-time Monitoring Reveals Dissolution/Redeposition Mechanism in Copper Nanocatalysts during the Initial Stages of the CO₂ Reduction Reaction. *Angewandte Chemie International Edition* **2021**, *60* (3), 1347-1354.
29. Chang, X.; Wang, T.; Zhao, Z.-J.; Yang, P.; Greeley, J.; Mu, R.; Zhang, G.; Gong, Z.; Luo, Z.; Chen, J.; Cui, Y.; Ozin, G. A.; Gong, J., Tuning Cu/Cu₂O Interfaces for the Reduction of Carbon Dioxide to Methanol in Aqueous Solutions. *Angewandte Chemie International Edition* **2018**, *57* (47), 15415-15419.
30. Garza, A. J.; Bell, A. T.; Head-Gordon, M., Mechanism of CO₂ Reduction at Copper Surfaces: Pathways to C₂ Products. *ACS Catalysis* **2018**, *8* (2), 1490-1499.

**Chapter 3: Electrochemical
Characterisation of Carbon Nano-
Onions and their Decoration with
Gold Nanoparticles for the
Electrochemical Determination of N-
Acetyl-L-Cysteine**

Table of Contents

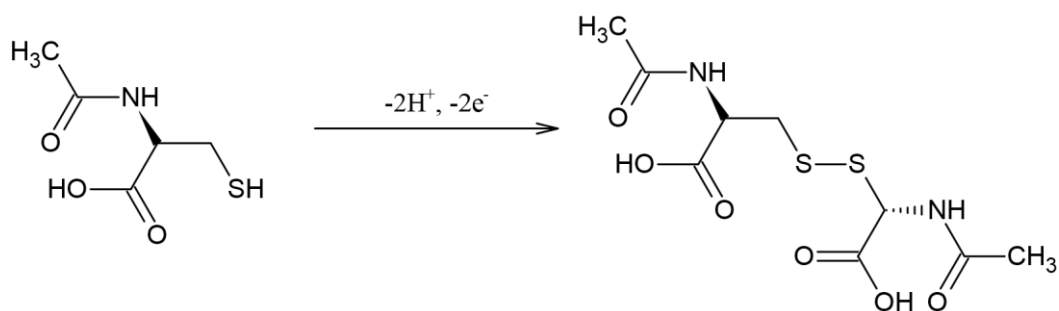
3.1.0. Introduction & Literature Review:	123
3.2.0. Experimental:	126
3.2.1. Materials and reagents	126
3.2.2. Instrumentation	126
3.2.3. Procedures	127
3.2.3.1. N-acetyl-L-cysteine preparation	127
3.2.3.2. Preparation of the working electrodes	127
3.2.3.3. Gold nanoparticle electrodeposition	127
3.2.3.4. Electrochemical characterisation of the gold nanoparticle modified glassy carbon electrode	128
3.2.3.5. Preparation of carbon nano-onion modified electrodes	129
3.2.3.6. Electrodeposition of the optimised gold nanoparticles at the oxi-BN-doped carbon nano-onions	129
3.2.3.7. N-acetyl-L-cysteine electrochemical testing at the optimum gold nanoparticle modified carbon nano onion surface	130
3.2.3.8. N-acetyl-L-cysteine recovery from a commercial formulation	130
3.3.0. Results and Discussion:	131
3.3.1. N-acetyl-L-cysteine electrochemical investigations at bare electrodes	131
3.3.2. Gold nanoparticle electrodeposition on glassy carbon electrodes using pulsed electrodeposition	136
3.3.3. Optimisation of the electrosynthesis conditions for gold nanoparticle deposition	142
3.3.4. Electrochemical characterisation of gold nanoparticles following optimisation based on N-acetyl-L-cysteine response	145
3.3.5. Surface analysis of the electrodeposited gold nanoparticles on glassy carbon electrodes	151
3.3.6. Electrochemical characterisation of carbon nano-onions on glassy carbon electrodes	154

3.3.7. Gold nanoparticle electrodeposition at the oxi-BN-doped carbon nano-onion modified electrode.....	168
3.3.8. Surface analysis of the electrodeposited gold nanoparticles on oxi-BN doped carbon nano-onion modified electrodes	182
3.3.9. Electrochemical determination of N-acetyl-L-cysteine at the AuNP@oxi-BN-doped CNO modified GCE	183
3.3.1.0. N-acetyl-L-cysteine sample analysis	191
3.4.0. Conclusions	194
3.5.0. References	195

3.1.0. Introduction & Literature review:

N-acetyl-L-cysteine (NAC) is a safe and inexpensive medication, not found in nature. It is a drug that has various uses and functions in biological systems. It promotes glutathione synthesis and promotes detoxification. NAC is a useful treatment of diseases that generate oxygen free radicals as it acts as a scavenger for free radicals¹. The key to the antioxidant power of NAC is that it is a glutathione precursor, a naturally occurring antioxidising agent^{2,3}. NAC is also a cysteine (Cys) precursor due to the α -protection of the nitrogen by an acetyl group. The acetyl group can be removed in most tissues by cleaving the acetyl group thus producing Cys⁴. This occurs when NAC penetrates cells. The resulting L-Cys can then be used to promote glutathione synthesis, thus all of NAC's intracellular effects are mediated by glutathione replenishment. Although glutathione is recycled in cells, this process increases but cannot match the amount of glutathione required during COVID-19 infections. Glutathione synthesis is then required, which increases enormously during infection. Oral administration of NAC is an effective way of increasing glutathione levels as it has better oral and topical bioavailability than glutathione. Therefore, NAC is a drug that is being examined in the treatment to COVID-19 infections⁵.

NAC has been characterised previously with the use of various electrochemical sensors. These studies determined NAC at a bare gold electrode (AuE)⁶, with the use of catechol as an electrochemical indicator at a carbon paste electrode (CPE)⁷, copper nitroprusside adsorbed on 3-aminopyrisisica modified carbon paste electrode⁸, copper oxide nanostructures on an ITO substrate⁹, cyclodextrin-carbon nanotube modified glassy carbon electrode¹⁰, multi-walled carbon nano tube and Nafion modified GCE¹¹, gold film modified carbon microelectrode¹², and an acetaminophen ruthenium oxide nanoparticle modified GCE¹³. In each case electrochemical studies of NAC were carried out at a variety of pH's (pH 3 – 8), where the highest NAC oxidative response was observed in acidic media at pH ~ 4.45. The use of a gold modified electrode, or an unmodified gold electrode was also shown to have the clearest response due to the interactions between the thiol group on NAC and the gold surface, where upon electrooxidation, the NAC becomes adsorbed to the gold surface through the sulphur atom. These sulphur atoms are in oxidation state I and then combine forming the dimer N,N'-diacetylcysteine (**Scheme 1**)⁶.



Scheme 1 Electrooxidation of N-acetyl-L-cysteine to disulfide N,N'-diacetylcystine

Gold nanoparticles (AuNPs) have a wide variety of applications in both the biological and chemical fields. In biology AuNPs have a wide variety of applications, such as in labelling, where they are a very useful contrasting agent due to their ability to absorb and scatter light. Similarly, they are also of importance in single particle tracking, where molecules and structures on the cell surface are labelled with AuNPs and their movement and the movement of receptors are monitored using photothermal imaging. They have also been used as a platform for the delivery of molecules into cells, such as genes, where the molecules are adsorbed to the AuNP surface and taken into cells through the recognition of specific ligands on the AuNP surface by receptors on the cell surface¹⁴. In synthetic chemistry, AuNPs can be used to make hydrophobically stabilised clusters, such as PEG-S capped supra-spherical supra-particle hosts which uptake and release hydrophobic organic guest molecules, such as bisphenol A. These structures can be used in the synthesis of polycarbonate plastics. The interstitial pores and voids between the hydrocarbon shells around the gold core result in a network of cavities that allow for the effective diffusion of guest molecules to the host domains used in polymer synthesis¹⁵. In electrochemistry, AuNPs have been used in a variety of sensors. These sensors have been used for the detection of uranyl sulphate, the determination of lead at ultra-trace levels and within biosensors incorporating enzymes such as glucose oxidase¹⁶⁻¹⁸. AuNPs can be synthesised using several methods, the first being through the reduction of gold hydrochlorate by citrate, the reduction of tetrachloroaurate using trisodium citrate and by the reduction of tetrachloroaurate using sodium borohydride¹⁹⁻²¹. Various electrochemical methods have also been employed to synthesise AuNPs directly onto an electrode surface. These methods involved galvanostatic modes, the electrolysis of AuCl in DMF using O₂ at the reducing agent and finally through the template-free multiple-potentiostatic pulse method of chloroauric acid in 0.1 M HCl^{17, 22, 23}. This multiple-potentiostatic

pulse method resulted in the highly controlled electrosynthesis of uniformly sized AuNPs, and therefore this method was exploited in this sensor design for NAC determination. To improve the NAC response further an underlying carbon nanomaterial (functionalised carbon nano onions (CNOs)) was examined. There have been various reports on the combination of CNOs with metallic nanomaterials such as platinum nanoparticles^(24-26,24-26,33) and here we propose the combination of AuNPs electrodeposited on electrodes modified with oxidized B and N doped CNOs, which has thus far not been reported to be the best of our knowledge.

CNOs are concentric multi-layered fullerenes which consist of several graphitic layers with the fullerene C₆₀ or larger at its centre²⁷. CNOs have localised π electrons in their spherical structure, caused by the peripheral defects in the spherical graphitic shells. They display interesting electrochemical behaviour, such as having a very high capacitance. This feature makes them a good material to be used in supercapacitors²⁸. The pseudo-rectangular shape of CNO cyclic voltammograms (CVs) is indicative of their double layer capacitive behaviour²⁹. CNOs have been used in various electrochemical sensors such as in the electrochemical determination of dopamine in the presence of uric and ascorbic acids, where CNOs were used in a composite with poly(diethylammonium chloride)³⁰.

CNOs can have altered compositions and structures. The first of these involves heteroatom doping, such as with B and N. These dopants are incorporated into their spherical graphitic layers upon CNO synthesis. These dopants have been reported to enhance their oxygen reduction reaction (ORR) activity³¹. It has been reported that pyramidal N-atoms can improve the overall capacitance of the nanomaterial and that quaternary N-atoms can help to improve their overall conductivity, thus improving their super capacitive ability through the N active sites, facilitating redox reactions with a preference for electrochemical reduction processes³². Boron can also influence electrochemical redox reactions favouring electroreduction processes by acting as an electron acceptor. B also has an influence on the improvement of the capacitance over their undoped counterparts through the introduction of defects in the graphitic layers and through the decrease in pore size^{33, 34}. The addition of carboxylic acid groups to the CNO surface, resulting in their oxidized forms (oxi-CNOs) can also have an impact on their redox reaction processes, favouring the reduction processes. The introduction

of defects on the oxi-CNO surface is accompanied by a larger electroactive surface area, and these factors in turn have a profound impact on improving their capacitances^{29, 35}.

In these investigations, the electrochemistry of NAC was investigated at GCEs and AuEs. Various CNOs (pristine CNOs (p-CNOs), BN-doped CNOs, oxidized CNOs (oxi-CNOs and oxi-BN doped CNOs) will be electrochemically characterised at a GCE surface using various electrochemical techniques. In this chapter, the electrochemical synthesis of uniformly sized AuNPs at GCE and oxi-BN-doped CNO modified surfaces was investigated as a potential electrode modifier to maximise the NAC electro-oxidative response.

3.2.0. Experimental:

3.2.1. Materials and reagents

N-acetyl-L-cysteine [$C_5H_9NO_3S$] (99 %) (Flurochem), sodium acetate [CH_3COONa] (99 %) (Sigma-Aldrich), glacial acetic acid [CH_3COOH] (Sigma-Aldrich), extra pure sulfuric acid solution in water [H_2SO_4] (96 %) (Sigma-Aldrich), potassium phosphate monobasic [KH_2PO_4] (99.5 %) (Sigma-Aldrich), potassium phosphate dibasic [K_2HPO_4] (99 %) (Sigma-Aldrich), sodium carbonate [Na_2CO_3] (99.5 %) (Sigma-Aldrich), 5 M hydrochloric acid solution in water [HCl] (Sigma-Aldrich), gold chloride [$HAuCl_4$] (99.4 %) (Sigma-Aldrich), pristine carbon nano-onions (p-CNOs), BN-doped carbon nano-onions (BN-doped CNOs), oxidized carbon nano-onions (oxi-CNOs), oxidized BN-doped carbon nano-onions (oxi-BN-doped CNOs), absolute ethanol [C_2H_5OH] (99.8 %) (Sigma-Aldrich), potassium chloride [KCl] (100.5 %) (Sigma-Aldrich), potassium ferricyanide [$K_3[Fe(CN)_6]$] (99 %) (Sigma-Aldrich), potassium hexacyanoferrate trihydrate [$K_4[Fe(CN)_6].3H_2O$] (99.5%) (Merck), hexaammineruthenium(II) chloride [$[Ru(NH_3)_6]Cl_2$] (99.9%) (Sigma-Aldrich), N-acetyl L-cysteine commercial sample (0.6 g per capsule) (Holland & Barratt).

3.2.2. Instrumentation

Electrochemical investigations were carried out using a three-electrode cell, with a glassy carbon electrode (GCE) and a gold electrode (AuE) as the working electrodes, a platinum wire as the auxiliary and an Ag/AgCl (saturated KCl) as the reference electrode. Measurements were made using a Solartron SI2187

Electrochemical Interface and a CHI Instruments 600E Potentiostat/Galvanostat. Materials and reagents were weighed out using a Sartorius LA230S analytical balance, and a VWR ultrasonic cleaner (model USC100T) was used for nanoparticle suspension and electrolyte/analyte dissolution. Screen printed electrodes used were Metrohm DropSens 11L screen printed carbon electrodes (Aux.: C; Ref.: Ag/AgCl). The scanning electron microscopy was performed by Dr. Vasily Lebedev on a FEI (Thermo) Helios G4 CX Dual Beam SEM-FIB with Oxford Instruments EDS.

3.2.3. Procedures

3.2.3.1. N-acetyl-L-cysteine preparation

N-acetyl-L-cysteine (NAC) standards were prepared (solubility 100 mg mL^{-1} in water) in a sodium acetate buffer (pH 4.45) which comprised of a mixture of 0.1 M sodium acetate and 0.1 M acetic acid, potassium phosphate buffer (pH 7.25) and sodium carbonate buffer (pH 10.35). 1 mM NAC standards were examined via cyclic voltammetry (CV) to identify the most appropriate working electrode and electrolyte for subsequent electroanalytical studies. 1 mM NAC was also investigated in 0.1 M H_2SO_4 (pH 0.7) via CV.

3.2.3.2. Preparation of the working electrodes

Firstly, the electrode surface was polished in a figure of eight pattern on a polishing pad with a $1 \mu\text{m}$ monocrystalline diamond suspension for 1 minute and rinsed with a jet of deionised water. The electrode was then sonicated in deionised water for 30 seconds. This process was repeated with both the GCE and AuE working electrodes.

3.2.3.3. Gold nanoparticle electrodeposition

A freshly polished glassy carbon electrode was modified with electrodeposited gold nanoparticles (AuNPs) of uniform size using a multi-pulse potentiostatic sequence. The AuNPs were deposited from a 1 mM HauCl_4 solution in 0.1 M HCl. As HauCl_4 is hygroscopic, deionised water was added to the dry HauCl_4 crystals (1 g mL^{-1} solution of HauCl_4) to ensure that the quantity of HauCl_4 was accurately known. Four potentials were selected from the cyclic voltammogram of 1 mM HauCl_4 in 0.1 M HCl and the conditions (pulse duration and amplitude) were optimised resulting in the template-free

electrosynthesis of AuNPs. The procedure involved a perturbation pulse at $E_0 = 0.92$ V for 10 s to remove gold ions adsorbed to the GCE surface. This was then followed by a nucleation pulse, where E_1 was selected at -0.13 V for 60 ms. An anodic pulse was then applied at $E_2 = 0.92$ V for 2.5 ms to remove excess gold at the GCE surface. Alternating growth ($E_m = 0.55$ V for 1 s: $m = 3, 5, 7, \dots, 1499$) and anodic pulses ($E_n = 0.92$ V for 5 ms: $n = 4, 6, 8, \dots, 1500$) followed in order to grow uniformly sized AuNPs from the seeded nuclei (see potential waveform sequence **Figure 1**). Each of the potentials and their corresponding pulse lengths were optimised in order to achieve conditions which resulted in the maximum NAC anodic signal.

3.2.3.4. Electrochemical characterisation of the gold nanoparticle modified glassy carbon electrode

Following the electrodeposition process, the AuNP modified GCE was gently washed by dipping in deionised water. The electrodes were then examined using CV in 0.1 M sodium acetate buffer (pH 4.45) supporting electrolyte, which resulted in an anodic process at 1.2 V and a cathodic process at 0.9 V. The surface coverage was estimated by monitoring these processes over scan rates 10 – 200 mV s^{-1} . A 5 mM $[\text{Fe}(\text{CN})_6]^{3/4-}$ redox probe in 0.1 M NaOH was used to gain further insight into the electron transfer processes. Electrochemical impedance spectroscopy (EIS) was also carried out in the same system by application of an AC sinusoidal voltage of 0.005V over the frequency range 0.01 – 100,000 Hz with an amplitude of 0.005 V. High resolution SEM images and EDS spectra were also obtained of the optimised AuNPs surface and particle size distribution investigated

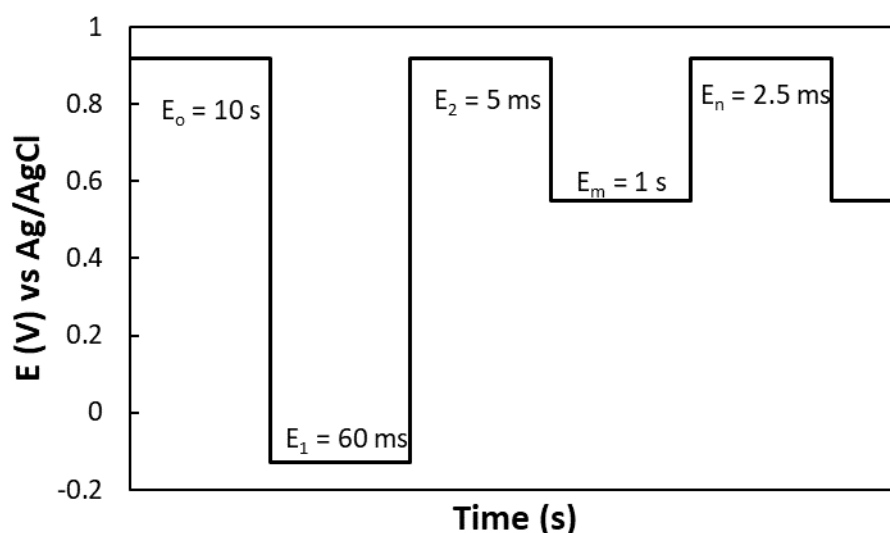


Figure 1. Schematic of the AuNP electrodeposition process with respect to pulse potential vs time.

3.2.3.5. Preparation of carbon nano-onion modified electrodes

A 1 mg mL^{-1} suspension of each of the carbon nano-onions (CNOs) (p-CNOs, oxi-CNOs, BN-doped CNOs and oxi-BN-doped CNOs) were prepared in absolute ethanol with vigorous sonication for 45 minutes to ensure well dispersed suspensions. The CNO suspensions were sonicated for a further 5 minutes immediately prior to use. A GCE was polished as described above, rinsed in ethanol and allowed to dry. $10\text{ }\mu\text{L}$ of the CNO suspension was drop-cast onto the GCE surface and the layer was dried using a heat lamp. The CNO modified GCE was examined by CV in 0.1 M KCl supporting electrolyte. Scan rate studies were carried out at each CNO modified GCE to allow capacitance and surface coverage estimations (faradaic responses were evident in the case of the oxi-CNOs and oxi-BN-doped CNOs). A $1\text{ mM } [\text{Fe}(\text{CN})_6]^{3/4-}$ anionic redox probe in 0.1 M KCl and a 1 mM hexaammineruthenium (II) chloride cationic redox probe were used to gain further insight into the electrochemical behaviour of each CNO modified surface.

3.2.3.6. Electrodeposition of the optimised gold nanoparticles at the oxi-BN-doped carbon nano-onions

The AuNPs@oxi-BN-CNOs were prepared using the optimised AuNP electrodeposition process as described above for GC electrodes. In order to optimise the dilutions of the oxi-BN-doped CNOs, 1 mg mL^{-1} , 0.1 mg mL^{-1} ,

0.05 mg mL⁻¹ and 0.02 mg mL⁻¹ suspensions were employed. Firstly, 10 µL of the oxi-BN-doped CNO suspension was drop cast onto a freshly polished and dried GCE surface and dried under a heat lamp. The AuNPs were then deposited electrochemically using the multi-pulse potentiostatic sequence. Following electrodeposition, the electrode surface was washed gently in deionised water and examined by running CVs of 1 and 10 mM NAC in 0.1 M H₂SO₄. This process was repeated for each dilution of the oxi-BN-doped CNOs. The optimum AuNPs@oxi-BN-doped CNO/GCE was then analysed by varying the scan rate and by performing electrochemical impedance spectroscopy together with SEM/EDS investigations.

3.2.3.7. N-acetyl-L-cysteine electrochemical testing at the optimum gold nanoparticle modified carbon nano onion surface

NAC standards were prepared in 0.1 M sodium acetate buffer (pH 4.45) and its electrochemical behaviour was examined at the AuNP@oxi-BN-doped CNO/GCE with scan rate studies and calibration using constant potential coulometry, where $E_{app} = 1.15$ V vs. Ag/AgCl with charge recorded for 5 s. This measurement was recorded in triplicate in 5 mL of the background electrolyte with 5 s quiet time between each measurement. Additions of 10 µL of 0.1 M NAC was added to the 5 mL of the background electrolyte with sequential additions over the range 0.2 – 2.53 mM NAC. The charge was measured at 4.5 s from the third measurement of each experiment. These calibrations studies were carried out in both 0.1 M H₂SO₄ and in 0.1 M sodium acetate buffer (pH 4.45), ultimately opting to utilise the sodium acetate buffer (pH 4.45) in the electroanalysis of NAC from a commercial formulation.

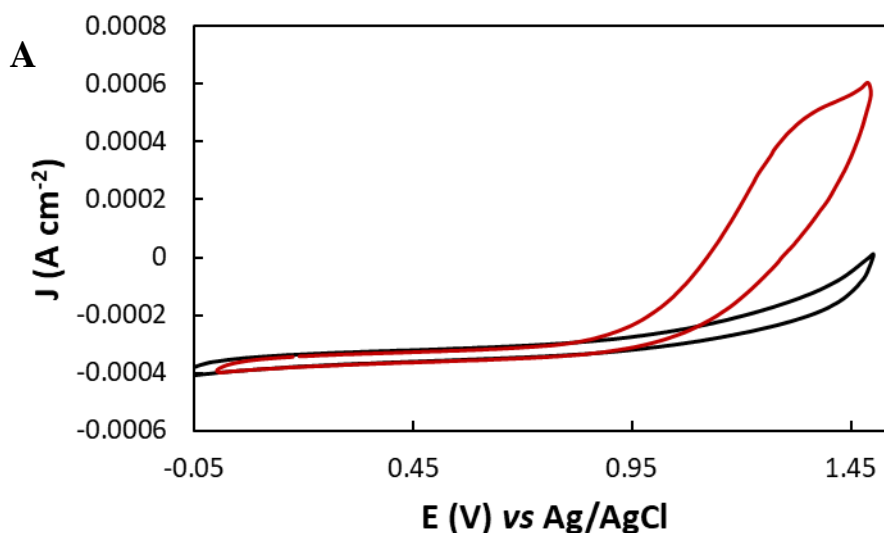
3.2.3.8. N-acetyl-L-cysteine recovery from a commercial formulation

An NAC commercial solid dose tablet containing 80 % w/w NAC was obtained and samples containing 1 mM and 2 mM NAC prepared by weighing out the calculated amount of the sample powder. It was then dissolved in 5 mL of the sodium acetate buffer (pH 4.45) and filtered into a 25 mL volumetric flask to remove insoluble excipients. 5 mL of the prepared sample was then measured, and standard addition performed via coulometry over the range 0.199 to 0.99 mM. The sample concentration and subsequent recovery was then estimated (n=3) by extrapolation using the linear data plots obtained.

3.3.0. Results and Discussion:

3.3.1. N-acetyl-L-cysteine electrochemical investigations at bare electrodes

Firstly, NAC was investigated via CV in an acidic medium due to the proton-dependant nature of the NAC electrooxidation process⁶, however, basic, and neutral pH's were also screened. The voltammetry of 1 mM NAC in 0.1 M sodium acetate buffer (pH 4.45) was initially studied at both bare glassy carbon electrodes (GCE) and bare gold electrodes (AuE). The voltammetry of NAC at the bare GCE, shown in **Figure 2 (A)**, clearly showed a strong oxidative response at 1.4 V vs Ag/AgCl. This signal was an ill-defined wave which took the shape of a shoulder with an unclear J_p max. However, in the case of the bare AuE (**Figure 2 (B)**), a clear NAC oxidative response was observed at 0.97 V vs Ag/AgCl. This response was clearly defined but overlapped with the Au response at 1.18 V vs Ag/AgCl.



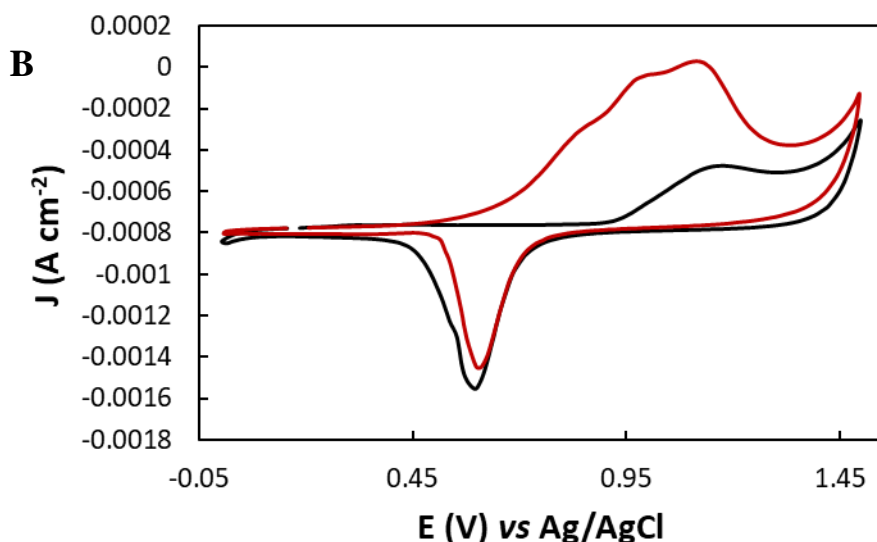
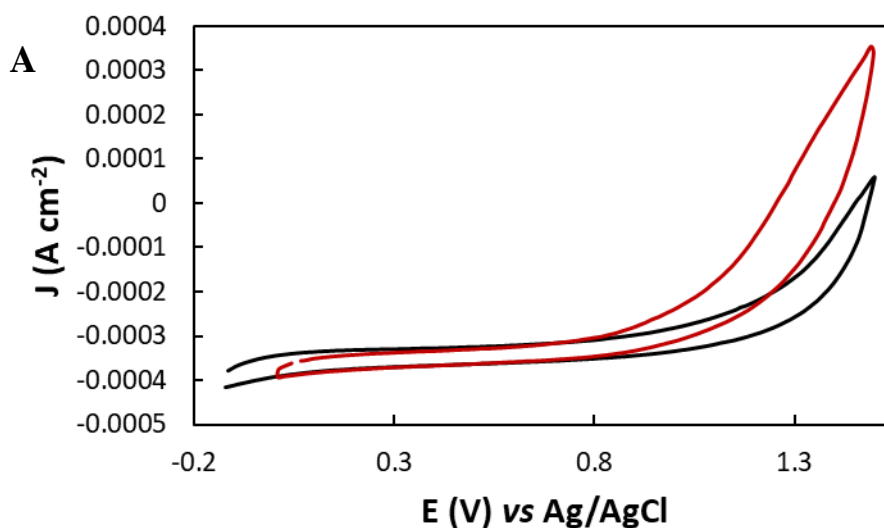


Figure 2. Voltammetry of 1 mM NAC (red curve) in 0.1 M sodium acetate buffer (pH 4.45) at the bare GCE (A) and bare AuE (B) from 0.0 – 1.5 V at 100 mV s^{-1} . Black curve represents background electrolyte voltammetry in each case.

The voltammetry of 1 mM NAC in a 0.1 M potassium phosphate buffer (pH 7.15) was then investigated at polished GCE and AuE (**Figure 3 (A) & (B)**). The resulting voltammograms were similar in general shape to the voltammograms of 1 mM NAC in 0.1 M sodium acetate buffer (pH 4.45), however, the NAC peak intensity in the potassium phosphate buffer obtained at the bare GCE and bare AuE was significantly lower than that obtained in the sodium acetate buffer.



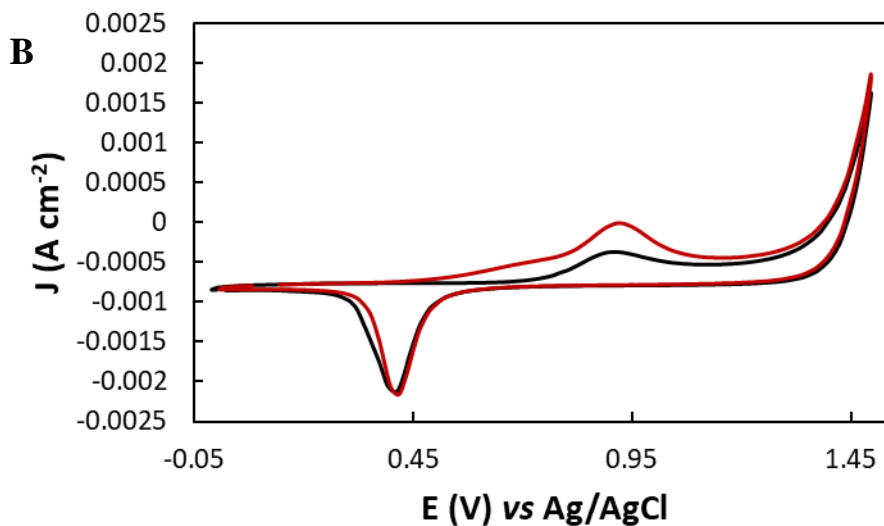
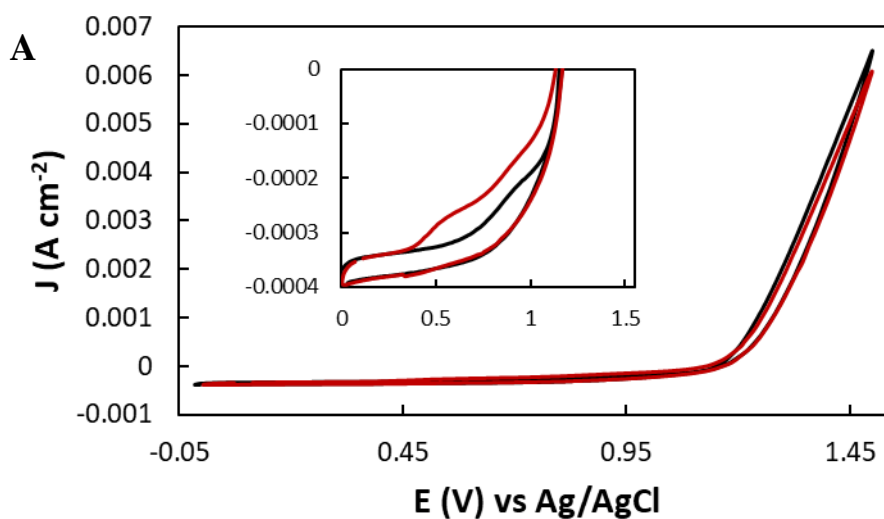


Figure 3. Voltammetry of 1 mM NAC in 0.1 M phosphate buffer (pH 7.15) at the bare GCE (**A**) and bare AuE (**B**) from 0.0 – 1.5 V at 100 mV s^{-1} .

Finally, the voltammetry of 1 mM NAC in a 0.1 M sodium carbonate buffer (pH 10.35) was then investigated at the bare GCE and AuE (**Figure 4 (A) & (B)**). This system resulted in the lowest NAC response at the bare AuE, where NAC was not detected. However, at the bare GCE, a small anodic shoulder was observed at 0.66 V vs Ag/AgCl (see insert).



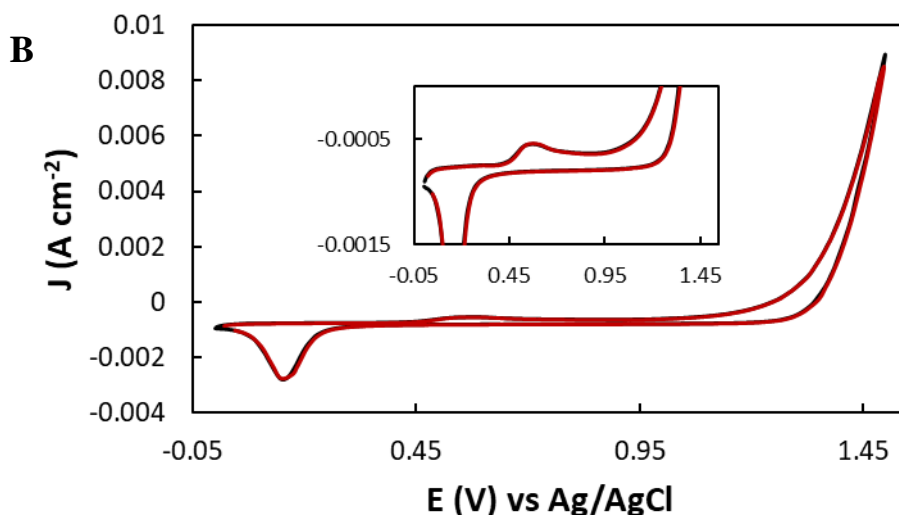


Figure 4. Voltammetry of 1 mM NAC in 0.1 M carbonate buffer (pH 10.35) at the bare GCE (A) and bare AuE (B) from 0.0 – 1.5 V at 100 mV s⁻¹.

In consideration of the three buffered electrolytes and pH range examined it was clearly observed that the acidic medium allowed the greatest NAC redox signal to be obtained, further supporting the proton-dependant nature of the electro-oxidation process, thus identifying the optimum conditions for NAC electroanalysis⁶. Once the optimum pH was identified, 1 mM NAC was studied by varying the scan rate. Firstly, this was carried out at the bare GCE (Figure 5 (A)), where the scan rate was varied from 20 – 200 mV s⁻¹. The NAC electro-oxidation response was present only at the voltammograms of 10 and 20 mV s⁻¹. This may have been due to the adsorptive nature of the NAC oxidation process¹².

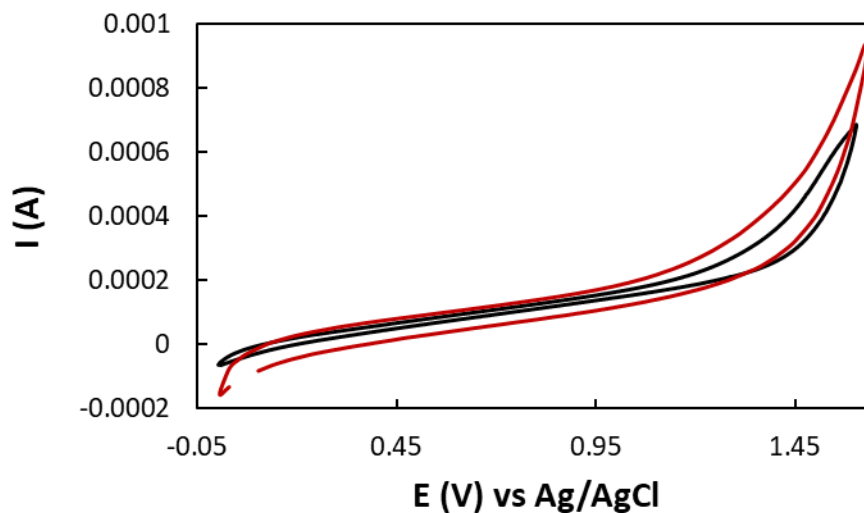


Figure 5. Voltammetry of 1 mM NAC in 0.1 M sodium acetate buffer (pH 4.45) at the bare GCE from 20 – 200 mV s^{-1} over the range 0 – 1.7 V vs Ag/AgCl (20 mV s^{-1} and 200 mV s^{-1} shown in red and black, respectively).

When the scan rate was varied from 10 – 200 mV s^{-1} at the bare AuE (**Figure 6 (A) & (B)**), a distinct oxidative peak was observed at 0.9 V vs Ag/AgCl. This signal was also scan rate dependant and increased linearly with respect to the scan rate, indicating that the oxidation process was adsorption controlled.

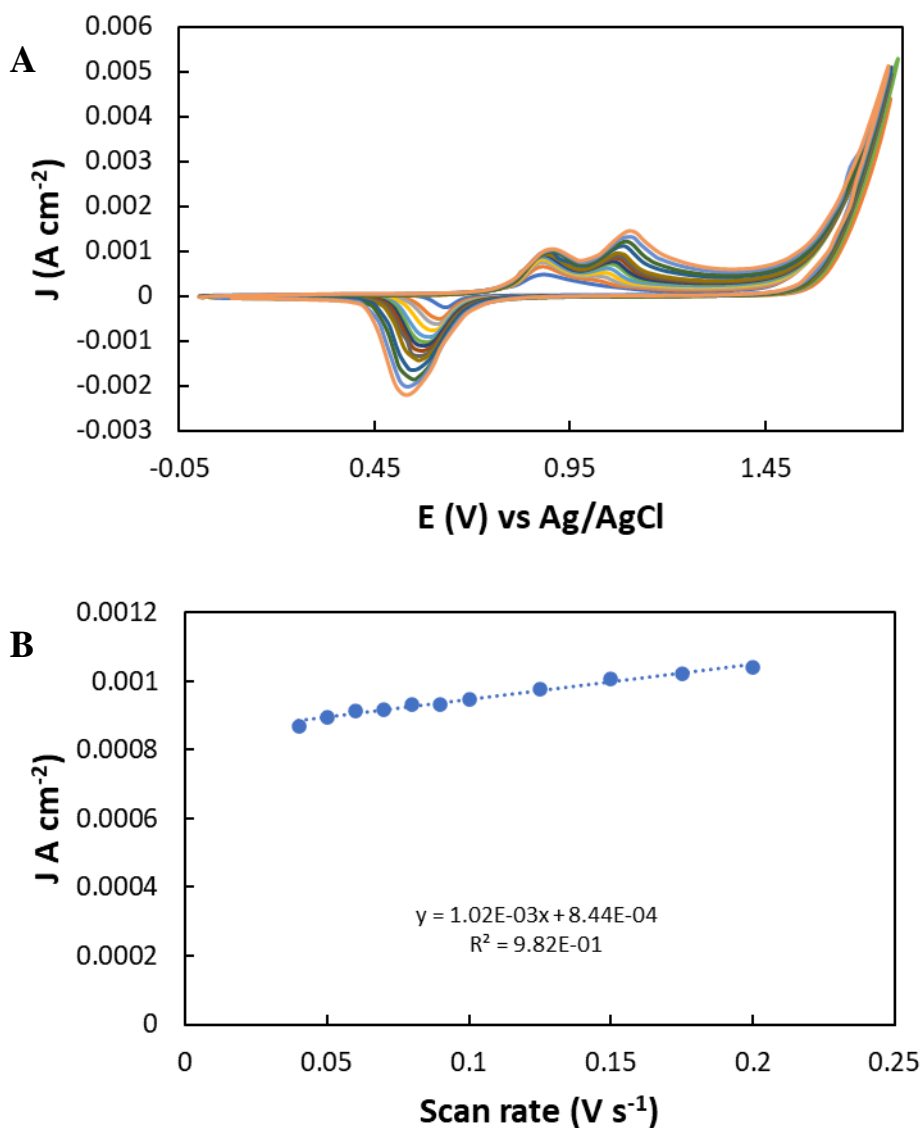


Figure 6 (A) Voltammetry of 1 mM NAC in 0.1 M sodium acetate buffer (pH 4.45) at the bare AuE from 10 – 200 mV s^{-1} over 0 – 1.7 V vs Ag/AgCl. **(B)** Corresponding plot of the scan rate vs current density of the NAC oxidative response from 40 – 200 mV s^{-1} .

3.3.2. Gold nanoparticle electrodeposition on glassy carbon electrodes using pulsed electrodeposition.

Electrosynthesis of gold nanoparticles (AuNPs) on GCEs followed the procedure outlined in section 3.3.3 with potentials selected based on the voltammetry of 1 mM HauCl_4 in 0.1 M HCl at the bare GCE. **Figure 7 (A)** shows the third cycle of the cyclic voltammogram of 1 mM HauCl_4 in 0.1 M HCl at the bare GCE at the scan rate of 100 mV s^{-1} . A single oxidation peak during the forward scan and reduction

peak during the reverse scan were observed at 1.074 V and 0.335 V respectively, which were attributed to the oxidation of Au⁰ to Au³⁺ and the reduction of Au³⁺ to Au⁰. From this CV, a set of potentials were selected to be used in the multi-pulse potentiostatic pulse sequence. The pulses used were a nucleation pulse (E₁), an anodic pulse (E₂) and alternating growth and anodic pulses (E_m and E_n). The multi-pulse potentiostatic sequence was used, as the process allows for the formation of uniformly sized AuNPs. This was achieved through the sequential electrodeposition and dissolution of gold from an electrode surface through the use of anodic and cathodic pulses.

Prior to the AuNP electrodeposition, a perturbation pulse was applied at 0.92 V for 10 s to oxidize and remove any residual gold on the GCE surface. The first cathodic pulse applied was the nucleation pulse. This was selected at a negative potential much lower than the Au reduction response to ensure and exploit the fast diffusion of Au³⁺ to the GCE surface. The applied pulse was short and fell within the hemispherical diffusion region of the chronoamperogram (discussed further below) to ensure the deposition of Au nuclei on the GCE surface act as nucleation points for subsequent gold growth. A short anodic pulse was then applied to remove subcritical nuclei and to allow the even distribution of AuNPs on the GCE surface.

Sequential growth (cathodic) and anodic pulses were applied to ensure the uniform growth of the AuNPs. A potential was selected at the Au reduction peak to facilitate the slow and controllable hemispherical diffusion of Au³⁺ ions to the GCE surface (**Figure 8 (A) – (C)**). A short anodic pulse was then applied to remove excess Au from the GCE surface and further nuclei seeded during these pulses.

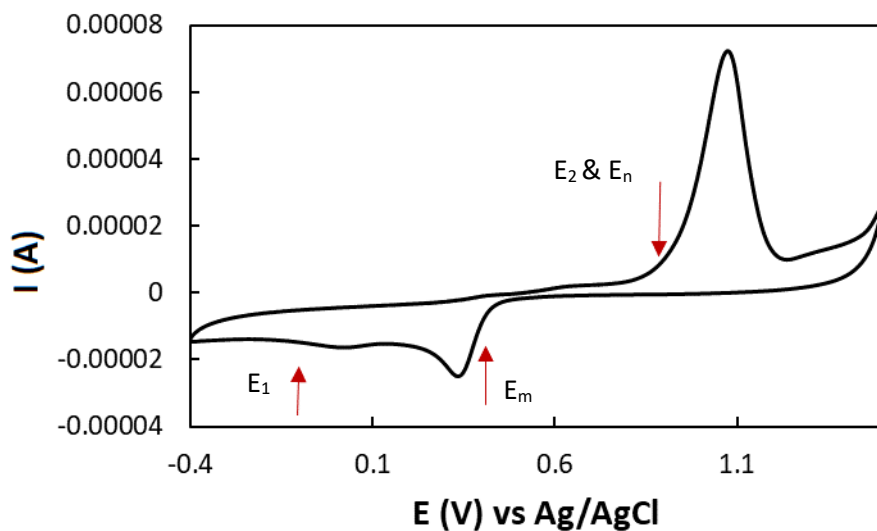
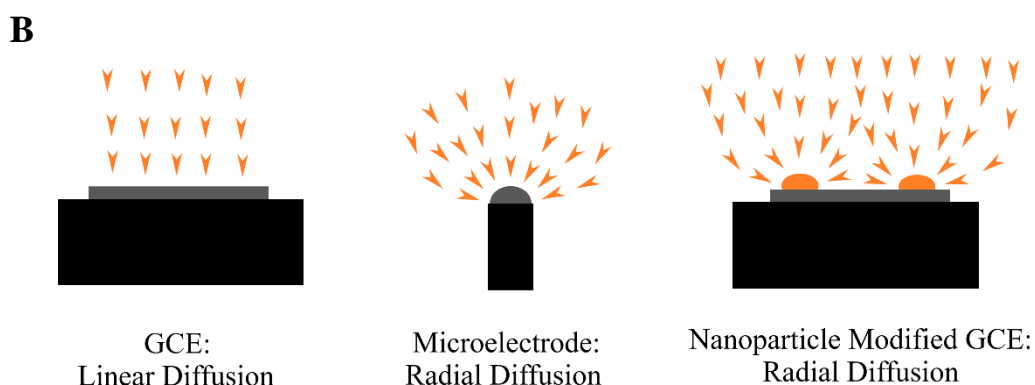
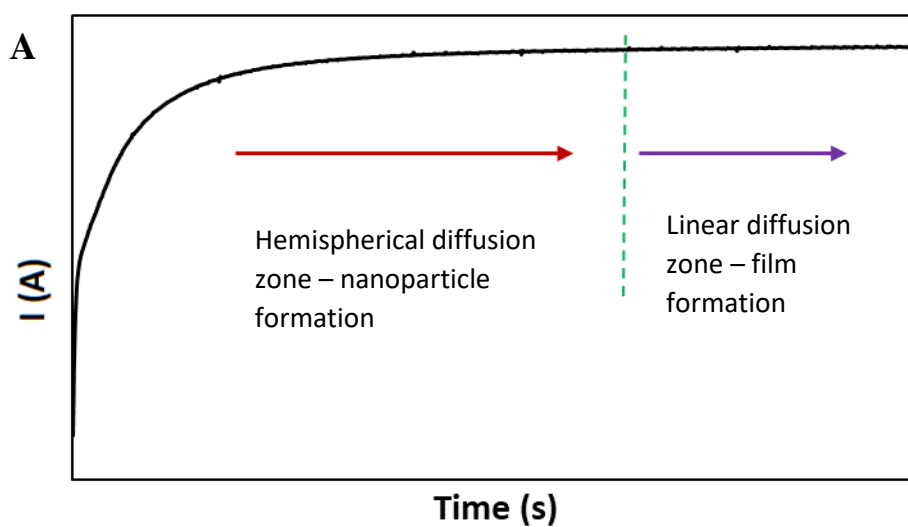


Figure 7. Voltammetry of 1 mM HAuCl_4 in 0.1 M HCl at the bare GCE from -0.4 – 1.5 V at 100 mV s^{-1} , with the electrodeposition pulse potentials indicated (red arrows).



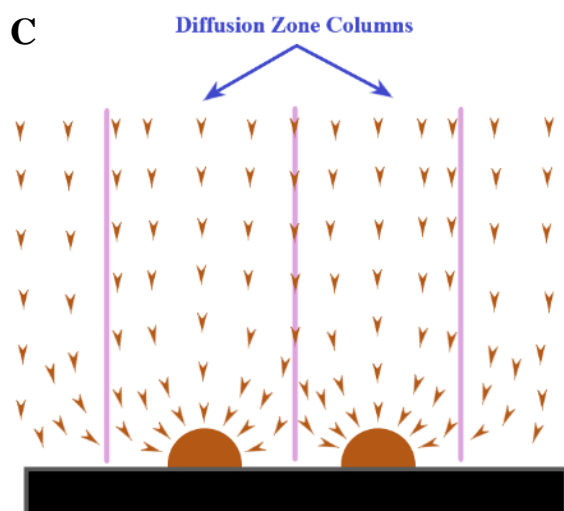
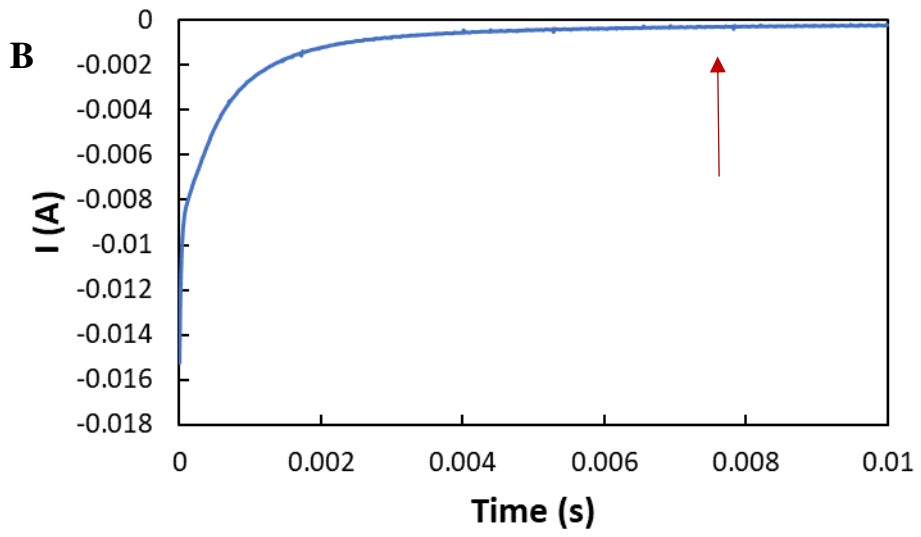
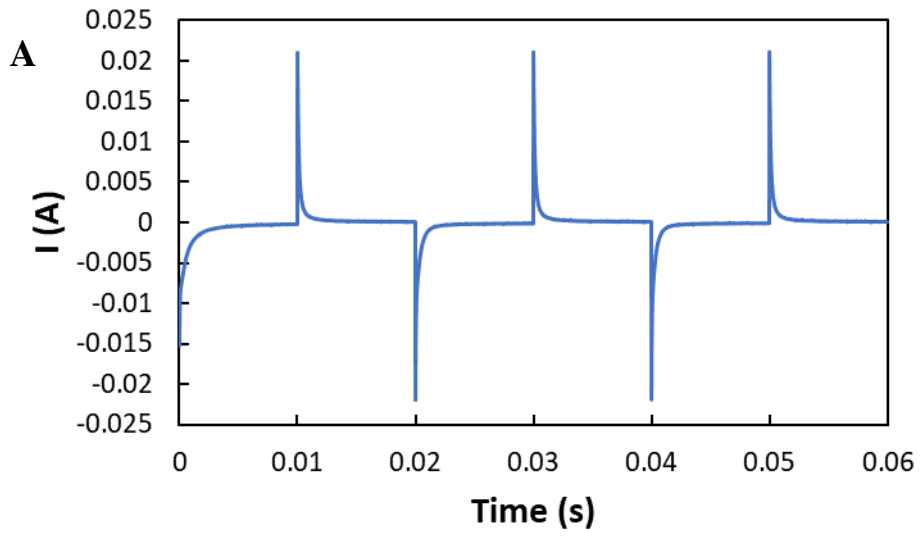


Figure 8 (A) Chronoamperometry of 1 mM HAuCl₄ at the bare GCE for $E_i = 0.8$ V, $E_c = -0.13$ V, $t_c = 0.01$ s (B) Schematic of illustrating linear vs hemispherical diffusion of Au³⁺ ions towards an unmodified GCE surface, a microelectrode surface and nanoparticle modified GCE surface (C) Schematic illustrating the hemispherical diffusion of Au³⁺ ions to the GCE surface via hemispherical diffusion zones around seeded Au nuclei.



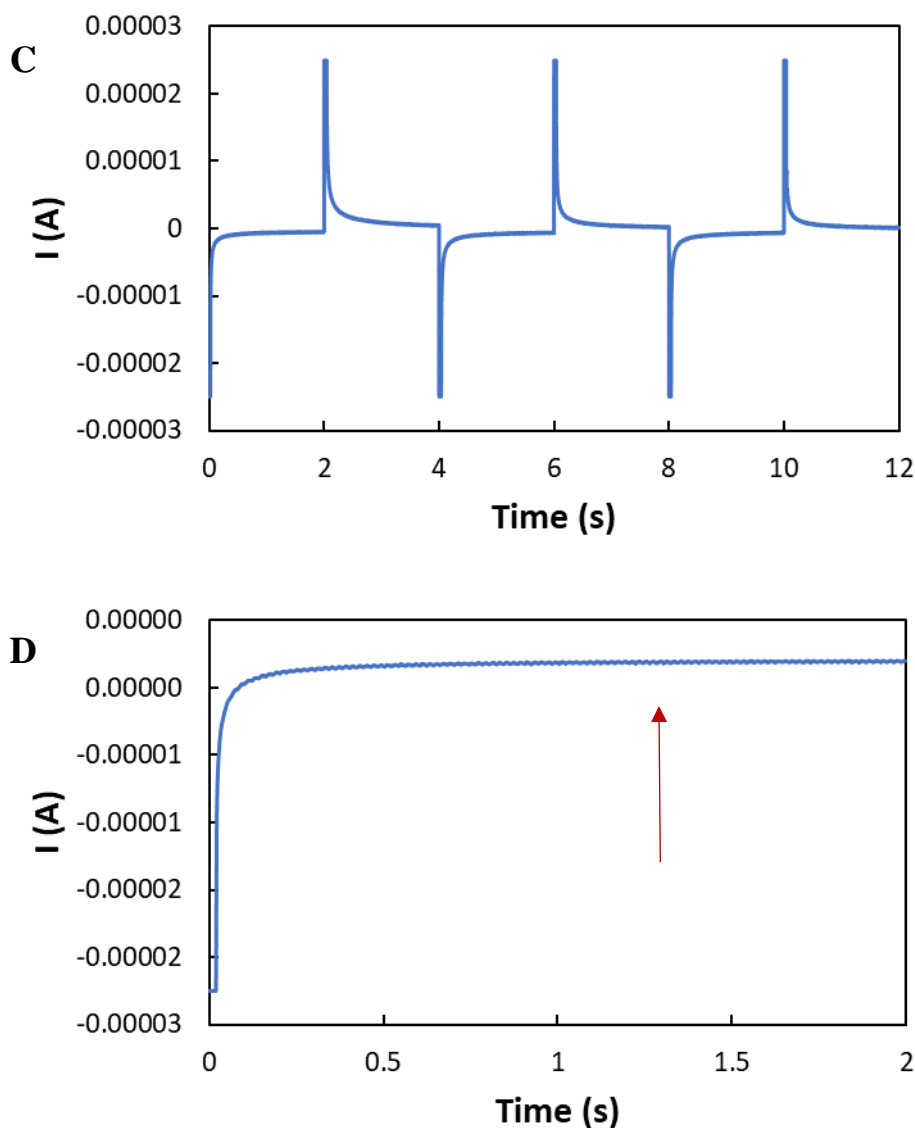


Figure 9 (A) Chronoamperometry of 1 mM HAuCl₄ at the bare GCE for 3 consecutive cycles where $E_i = 0.8$ V, $E_a = 0.92$ V, $E_c = -0.13$ V, $t_c = t_a = 0.01$ s. (B) Magnified image of the first cathodic transient of the first cycle. (C) Chronoamperometry of 1 mM HAuCl₄ at the bare GCE for 3 consecutive cycles where $E_i = 0.8$ V, $E_a = 0.92$ V, $E_c = 0.55$ V, $t_c = t_a = 2$ s. (D) Magnified image of the first cathodic transient of the first step.

Firstly, in **Figure 9 (B)**, chronoamperometry of 1 mM HAuCl₄ in 0.1 M HCl was carried out at the bare GCE for six consecutive steps with alternating cathodic pulses of -0.13 V and anodic pulses of 0.92 V, with a pulse width of 0.01 s for each. The anodic transient observed in the first step reached a plateau after 9 ms with a current transient at 50.33 μ s, however, this current transient rapidly decreased and disappeared in the third and fifth steps. Following transient from 0 – 9 ms in the first step until the plateau, the hemispherical diffusion region was identified which was

critical for the electrodeposition of uniformly sized AuNPs¹⁷. After this point the hemispherical diffusion zones overlapped and linear diffusion of Au³⁺ occurred resulting in the overlap of the electrodeposited Au particles on the GCE surface.

Figure 9 (C) shows the chronoamperometry of 1 mM HAuCl₄ in 0.1 M HCl at the bare GCE using alternating cathodic and anodic pulses over six steps. The cathodic pulses were applied at 0.55 V and the anodic pulses were applied at 0.92 V, with a pulse width of 2 s for each. From an examination of the first step, the first anodic pulse did not show a wave as observed in **Chapter 2, Figure 7 (B)** due to the slower diffusion of Au³⁺ ions to the GCE surface. The chronoamperogram of this experiment showed a rapid increase in current before reaching a plateau at 1.32 s at the current maximum, thus identifying the hemispherical diffusion zone between 0 and 1.32 s. The cathodic current here increased due to the presence of electrodeposited gold at the electrode surface. After the anodic step was carried out, a tiny amount of residual gold metal remained on the GCE surface. This trace amount of gold provided nucleation points for gold deposition in the subsequent cathodic step as Au³⁺ electrodeposition occurs more easily onto Au than depositing directly onto a GCE³⁶. Because of this, more gold is electrodeposited in each subsequent step, which in turn cause the stepwise current increase in the anodic steps.

From carrying out these experiments, the potentials to be used in the nucleation, growth and anodic pulses were selected as well as their initial corresponding pulse widths.

3.3.3. Optimisation of the electrosynthesis conditions for gold nanoparticle deposition

The electrodeposited AuNPs were optimised by sequentially changing the pulse parameters. The resulting AuNPs were then tested with 1 mM NAC with the aim to maximise the NAC anodic response. E₁, E₂ and E_n were kept constant while E_m was changed. The perturbation pulse (E₀) was also kept constant at 0.92 V for 10 s. The pulse width t₁ was kept constant throughout. E_m was changed with the aim of achieving greater AuNP particle size, by decreasing E_m, the rate of electrodeposition would increase, leading to larger nanoparticles. This however would lead to a less

controllable particle size and would be unfavourable. By investigating this, it was clearly observed that this did not increase the NAC oxidative response. By increasing the pulse width t_m , the resulting particles would be expected to be larger in size, and conversely, decreasing t_m would lead to smaller particles as less Au^{3+} would diffuse to the GCE surface. E_n was kept constant while t_n was altered. By increasing t_n the particle size would be expected to decrease as more Au would be re-oxidized and stripped from the electrode surface. Less Au was re-oxidized when t_n was decreased which would lead to a larger particle size. These parameters were examined as per **Table 1** and were tested by CV using 1 mM NAC in 0.1 M H_2SO_4 and compared to the bare GCE and AuE (macro electrodes). From comparing the NAC oxidative responses at each electrode, it was clearly determined that the AuNPs that resulted from method 2 gave the greatest NAC response, and thus these conditions were selected as the optimum AuNPs, as highlighted in **Table 2**.

Table 1. Electrodeposition parameters used for the optimisation of the gold nanoparticle deposition for NAC quantitation.

Method number	Pulse 1 (P ₁)	t ₁	Pulse 2 (P ₂)	t ₂	Pulse m (P _m)	t _m (m = 3, 5, 7 ..., 1499)	Pulse n (P _n)	t _n (n = 4, 6, 8, ..., 1500)
	Potential (V)	Time (s)	Potential (V)	Time (s)	Potential (V)	Time (s)	Potential (V)	Time (s)
1	-0.13	0.06	0.92	0.005	0.55	1	0.92	0.005
2	-0.13	0.06	0.92	0.005	0.55	1	0.92	0.0025
3	-0.13	0.06	0.92	0.005	0.55	1.5	0.92	0.0025
4	-0.13	0.065	0.92	0.005	0.55	1	0.92	0.0025
5	-0.13	0.06	0.92	0.005	0.39	1	0.92	0.005
6	-0.13	0.06	0.92	0.005	0.39	1	0.92	0.0025
7	-0.13	0.06	0.92	0.005	0.39	1.5	0.92	0.0025
8	-0.13	0.06	0.92	0.005	0.39	0.5	0.92	0.0025

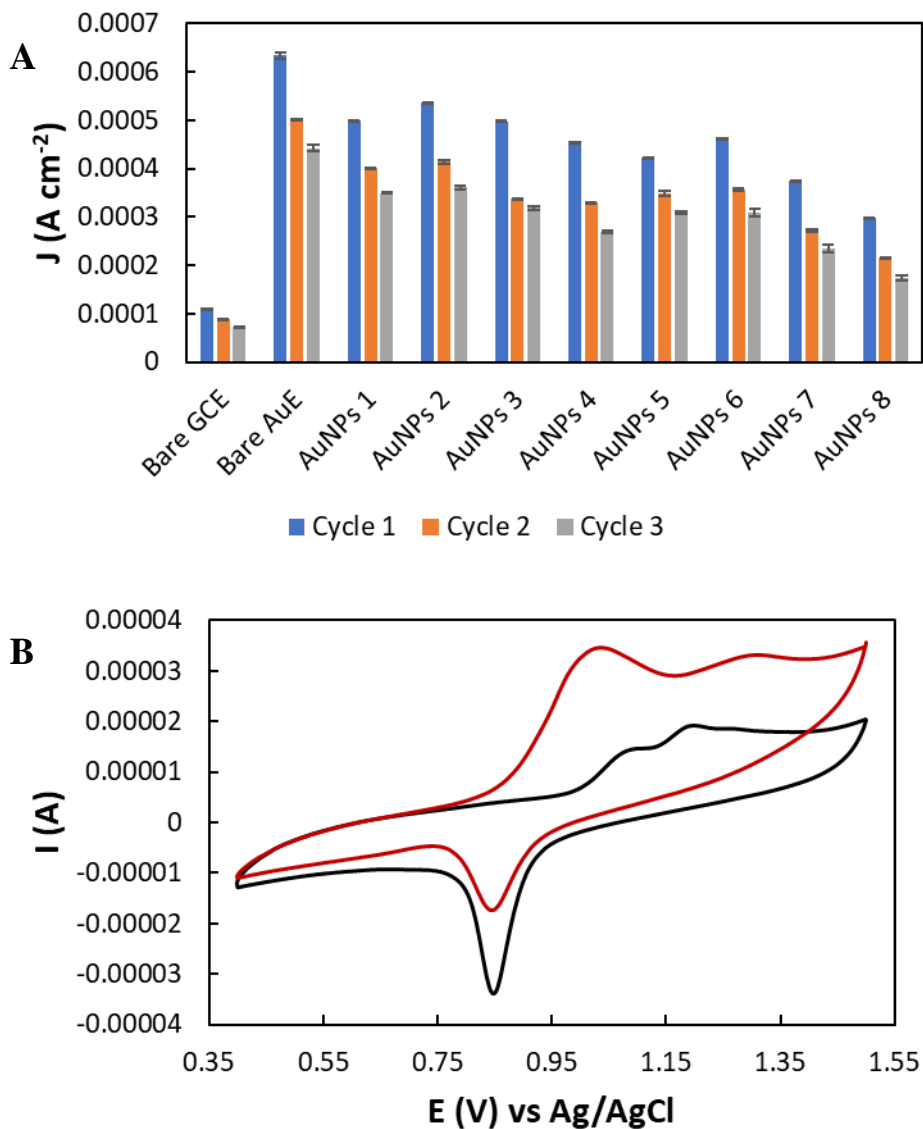


Figure 10 (A) Bar chart monitoring the NAC oxidative response at the bare GCE, AuE and each AuNP/GCE for conditions 1-8 as per **Table 1**. The optimum AuNP electrodeposition parameters were $P_1 = -0.13$ V for 60 ms, $P_2 = 0.92$ V for 5 ms, $P_m = 0.55$ V for 1 s and $P_n = 0.92$ V for 2.5 ms. **(B)** Voltammetry of 1 mM NAC (red) in 0.1 M H₂SO₄ (black) at the optimum AuNP/GCE from 0.4 – 1.5 V at 100 mV s⁻¹.

Figure 10 (A) shows the NAC oxidative response at each electrode used in cycles 1 through 3. The best NAC response was observed at the bare AuE, but this was followed by the AuNPs 2 (**Figure 10 (B)**). The lowest response was observed at the bare GCE.

Table 2. Summary of the optimised AuNP electrodeposition process.

Pulse	Potential (V)	Time (s)	Pulse #
Seed (Nucleation) pulse (P ₁)	E ₁ = -0.13 V	t ₁ = 0.06	1
Anodic pulse (P ₂)	E ₂ = 0.92 V	t ₂ = 0.005 s	2
Growth pulse (P _m)	E _m = 0.55 V	t _m = 1 s	3,5,7....1499
Anodic pulse (P _n)	E _n = 0.92 V	t _n = 0.0025 s	4,6,8....1500
Total number of pulses			1500

3.3.4. Electrochemical characterisation of gold nanoparticles following optimisation based on N-acetyl-L-cysteine response

The optimum AuNPs modified GCEs were then characterised using various electrochemical techniques. Firstly, a scan rate study was carried out over 0.4 – 1.5 V from 10 – 200 mV s⁻¹. Upon examination of the plot in **Figure 11 (B)**, it was clearly observed that both the oxidative and reductive processes were adsorption controlled, having a linear relationship with respect to scan rate. By monitoring the peak currents, the surface coverage values were estimated at $\Gamma = 4.459 \times 10^{-10}$ mol cm⁻² for the anodic response and $\Gamma = 4.923 \times 10^{-10}$ mol cm⁻² for the cathodic response. An anionic redox probe was then used to further characterise the AuNPs with the aid of 5 mM [Fe(CN)₆]^{3/4-} in 0.1 M NaOH. This type of investigation is usually carried out in 0.1 M KCl background electrolyte, however, the presence of Cl⁻ ions in solution was found to degrade the gold surface due to the high formation constant of [AuCl₄]⁻ which will in turn diffuse from the electrode surface and strip the Au from the electrode^{12, 37, 38}. This was not observed in the alkaline electrolyte and thus, was suitable to further study the electrochemical behaviour of the AuNP/GCE.

Based on the voltammogram in **Figure 11 (A)** it was clearly observed that the CV at the AuNP/GCE was vastly different from that at the bare GCE. At the bare GCE the $\Delta E_p =$ was 0.666 V, while at the AuNP/GCE the $\Delta E_p = 0.171$ V (**Table 3**). The substantial decrease in peak separation clearly shows that the barrier to electron

transfer has been significantly reduced and that the electron transfer process occurred quicker at that AuNP/GCE in comparison to the bare GCE³⁷.

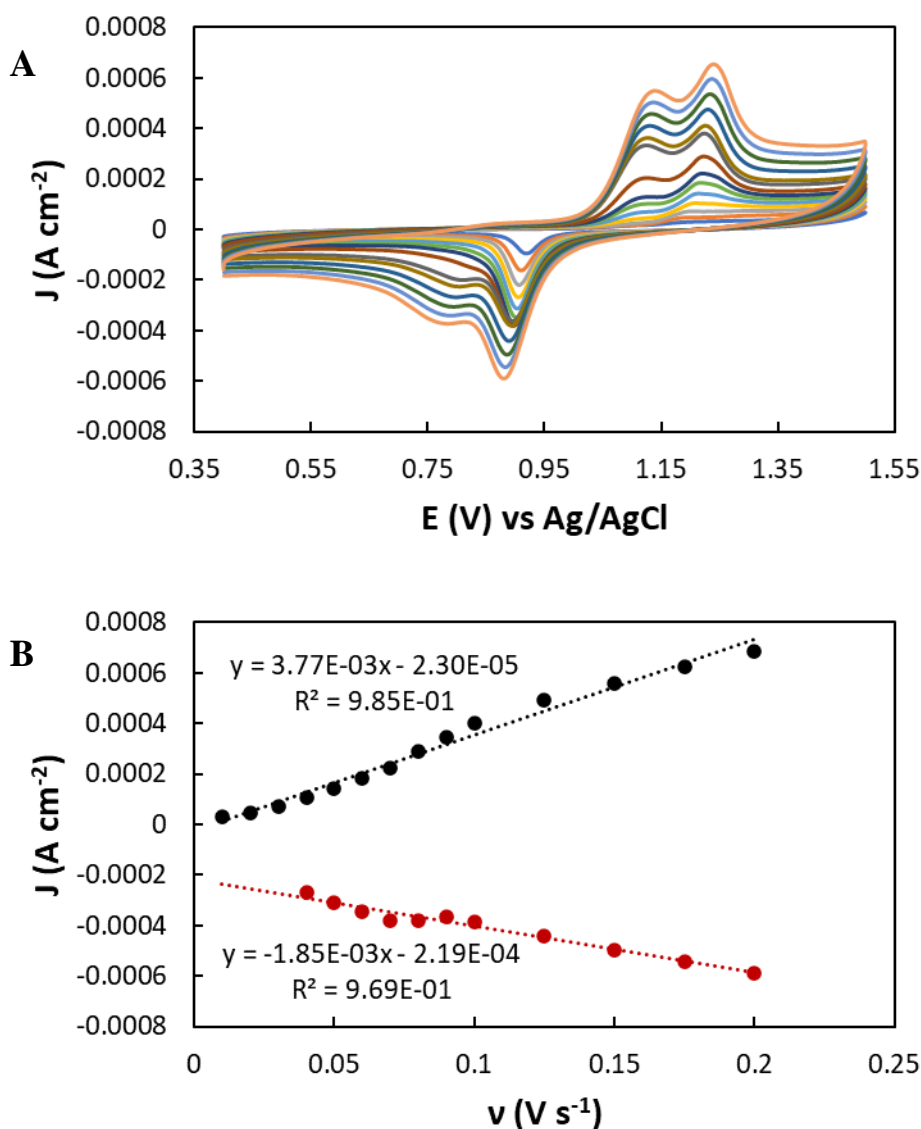
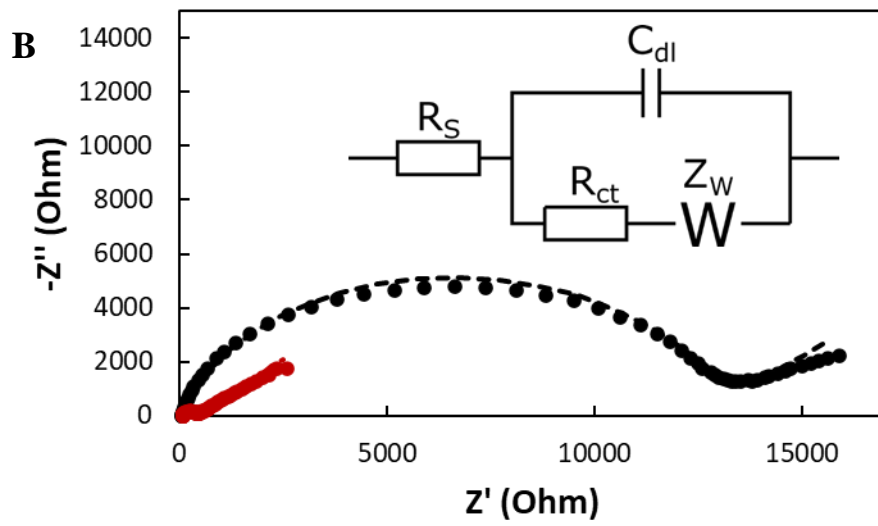
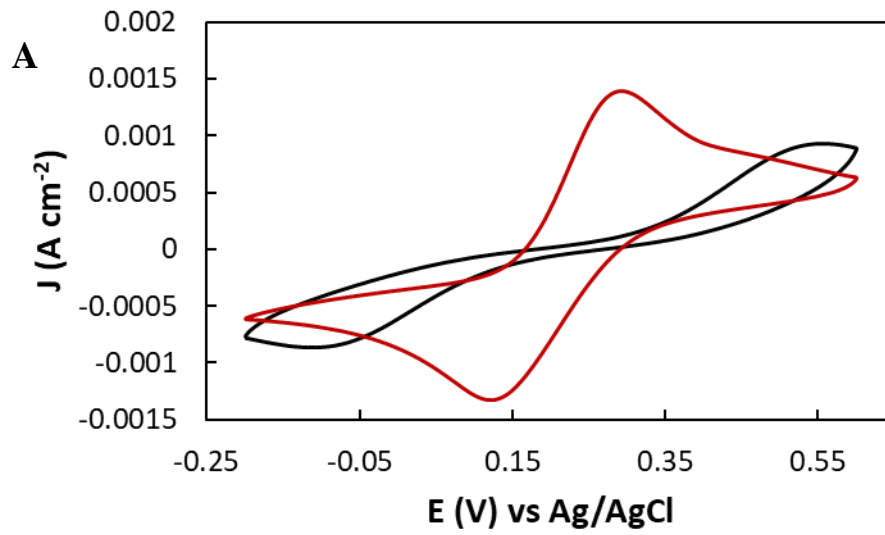


Figure 11 (A) Voltammetry of the AuNP/GCE from 0.4 – 1.5 V in 0.1 M H₂SO₄ from 10 – 200 mV s⁻¹. (B) Plot of the scan rate vs current density of the AuNP/GCE.

Electrochemical impedance spectroscopy (EIS) was also carried out in 5 mM [Fe(CN)₆]^{3/4-} in 0.1 M NaOH over 10 – 100,000 Hz (see section 3.3.5 for procedure). From these data, information regarding the initial resistance (R_s) and the charge transfer resistance (R_{ct}) can be obtained. The R_s was similar when comparing both electrodes, with the AuNP/GCE having the higher value, whereas the bare GCE had a significantly larger R_{ct} value as expected (Table 4.).



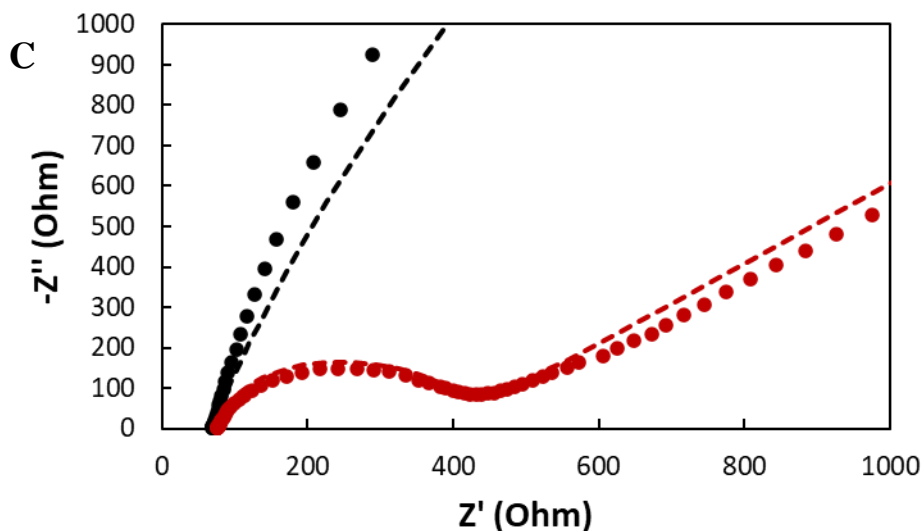


Figure 12 (A) Voltammetry of 5 mM $[\text{Fe}(\text{CN})_6]^{3/4-}$ in 0.1 M NaOH at the bare GCE (black) and AuNP/GCE (red) from -0.2 – 0.6 V at 100 mV s^{-1} . (B) Nyquist plot of the bare GCE (black) and the AuNP/GCE (red) in 5 mM $[\text{Fe}(\text{CN})_6]^{3/4-}$ in 0.1 M NaOH with n from 0.01 – 100,000 Hz with an amplitude of 5 mV. Simulated EIS data is shown by the dashed line. $E = 0.221 \text{ V}$ and 0.207 V for the bare and AuNP/GCEs, respectively. (C) Zoomed in image of the Nyquist plot highlighting the arc from the AuNP modified GCE with overlaid solid line representing simulation (Randles circuit data).

From examining the Bode plots of the bare GCE and AuNP/GCE (**Figure 13**), the stability of each electrode was demonstrated. The Gain Margin of the AuNP/GCE was calculated as 2.65 Db (2.961 Db for the bare GCE), thus the positive values demonstrate the stability of both electrodes. The Gain Margin was calculated by:

$$GM = 0 - G \text{ dB} \dots \dots \dots (1)$$

where GM is the Gain Margin and G is the gain.

The Bode plots also gave useful information on confirming the resistance of each GCE analysed. From examining the Bode plot in **Figure 12 (B)**, maximum phase was determined as -72.7° , and -38° for the bare GCE and AuNP/GCE, respectively. This gives information on the behaviour of each electrode, where -90° is equivalent to an ideal capacitor and 45° is equivalent to a pseudo-capacitor (**Table 4**). Angles measured at 45° indicates a high ionic permeability, thus showing that it is a poor insulator³⁹. With consideration for the phase angle, the results confirm that the presence of Au at the GCE surface increases the ionic permeability of each modified electrode and show that the Au modifications improves the conductivity of the GCE

in comparison to the bare GCE. The high phase angle indicates that the AuNP/GCE displays some capacitive properties, however conductive properties are more prominent. The curve for the bare GCE occurs at a larger phase angle at lower frequencies, which suggests lower ionic permeability and therefore greater insulating properties for the each of the Au modified GCEs, where the curve occurs at a lower phase angle and at higher frequencies.

The slope of the Bode magnitude plot (**Figure 12 (A)**) can give an indication on the resistance and capacitance of the electrode in question, where a slope close to -1 represents an ideal capacitor and a slope close to 0 at higher frequencies indicates resistive behaviour, which could occur at a capacitive material. The slope of the bare GCE was calculated as -0.83, and at higher frequencies it was calculated as 0.0414, thus demonstrating the capacitive behaviour of the bare GCE. For the AuNP/GCE, the slope was calculated to be -0.5, and -0.33 at higher frequencies, demonstrating the low capacitance of the CuF/GCE (**Table 4.**). These results support the highest capacitance of bare GCE followed by the AuNP/GCE.

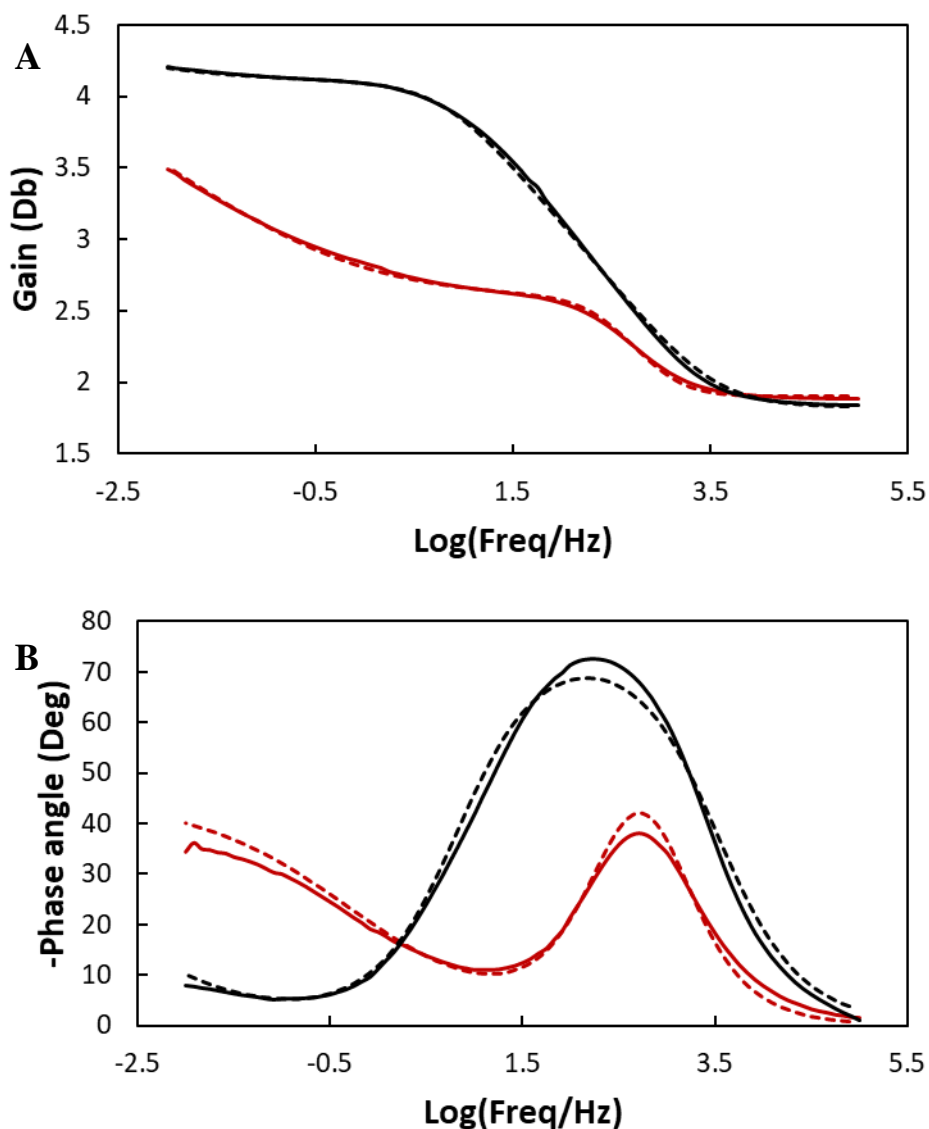


Figure 13. Corresponding experimental (solid lines) and simulated (dashed lines) Bode plots of the AuNP/GCE (red) and bare GCE (black) in 5 mM $[\text{Fe}(\text{CN})_6]^{3/4-}$ in 0.1 M NaOH with n from 0.01 – 100,000 Hz with an amplitude of 5 mV, where (A) shows the log of the frequency vs gain, and (B) shows the log of the frequency versus the phase angle.

Table 3. Comparison of the peak heights and potentials of 5 mM $[\text{Fe}(\text{CN})_6]^{3/4-}$ at the bare and AuNP/GCEs.

	$J_{p(a)}$ (A cm ⁻²)	$E_{p(a)}$ (V)	$J_{p(c)}$ (A cm ⁻²)	$E_{p(c)}$ (V)	ΔE_p (V)	$E_{p\ 1/2}$ (V)	$J_{p(a)}/J_{p(c)}$
Bare GCE	8.61×10^{-4}	0.554	7.89×10^{-4}	-0.112	0.666	0.221	1.09
AuNP/GCE	1.32×10^{-3}	0.292	1.17×10^{-3}	0.121	0.171	0.207	1.13

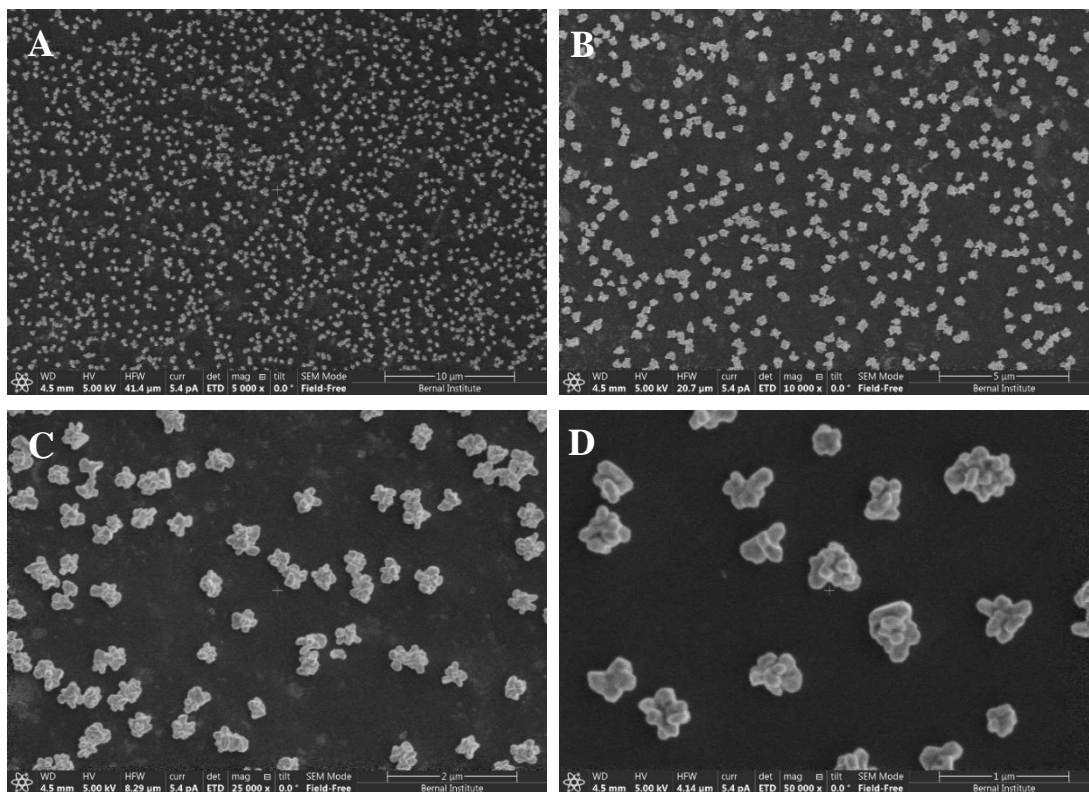
Table 4. Comparison of the R_s , R_{ct} , capacitances, Gain Margins and Phase Margins obtained from the EIS spectra for both simulated and experimental data obtained at the bare and AuNP/GCE.

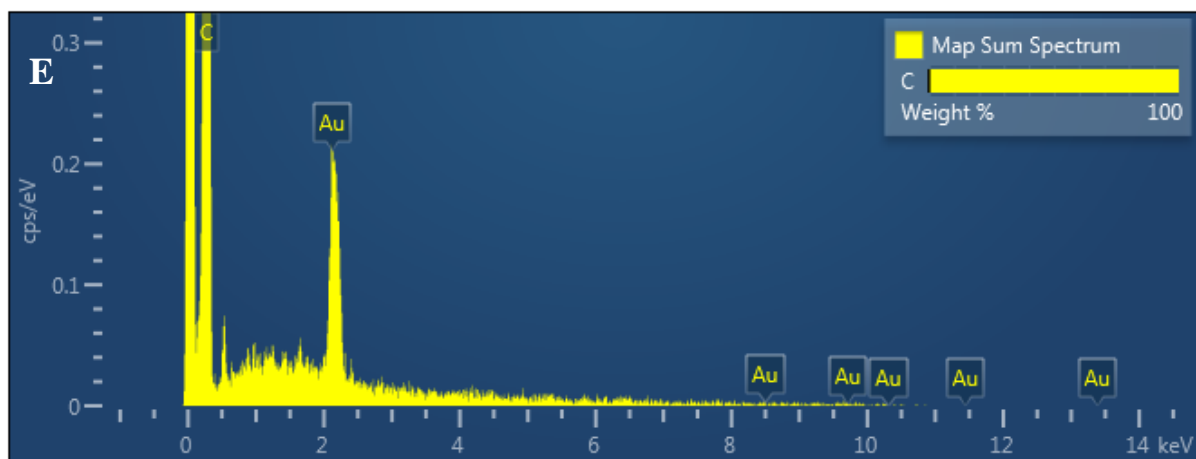
	Bare GCE		AuNP modified GCE	
	Experimental	Simulation	Experimental	Simulation
R_s (Ohm)	69.30 ± 0.66	67.30 ± 0.77	76.35 ± 0.2	79.71 ± 0.39
R_{ct} (Ohm)	13560.70 ± 389.8	13662.64 ± 391.97	365.75 ± 15.04	305.28 ± 16.08
Capacitance (F)	$7.56 \pm 0.24 \times 10^{-7}$	$6.33 \pm 0.25 \times 10^{-7}$	$1.55 \pm 0.212 \times 10^{-6}$	$2.21 \pm 0.212 \times 10^{-6}$
Gain Margin (Db)	2.96 ± 0.03	2.95 ± 0.04	2.65 ± 0.12	2.262 ± 0.21
Phase Margin (°)	55.9 ± 1.1	59.1 ± 1.5	26.6 ± 0.5	30.1 ± 0.7

3.3.5. Surface analysis of the electrodeposited gold nanoparticles on glassy carbon electrodes

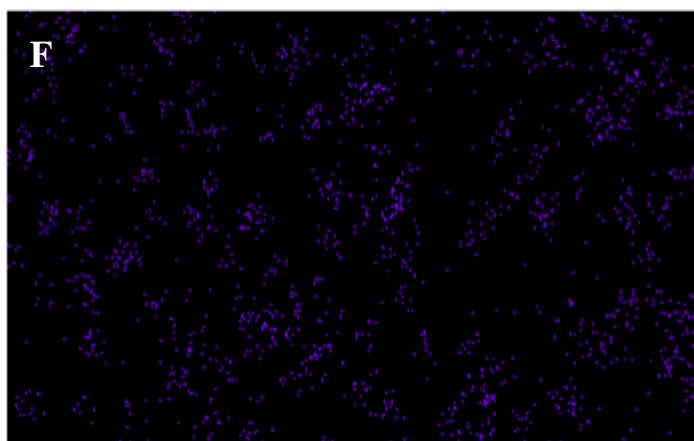
High resolution scanning electron microscopy (HR-SEM) was used to further characterise the AuNPs electrodeposited on the GCE surface. Images were taken between $5,000 - 10,000 \times$ magnification (**Figure 14 (A) – (D)**), where a high density of AuNPs were observed homogeneously distributed on the GCE surface. Upon examination of the AuNPs at higher magnification levels, the cluster-like particle shapes could be easily determined. The particle sizes were then estimated (sample size 435 particles) by measuring the diameter horizontally, diagonally from left to right and diagonally from right to left. The average of these three measurements was then obtained and gave the estimated particle size (**Figure 15**). Upon examination particles with a diameter of 300 – 319 nm accounted for 33 % of all particles followed by 320 – 339 nm (16.6 %) and 280 – 299 nm (7 %) indicating that the particle sizes were uniform across the GCE surface. Particles smaller than 279 nm were present and accounted for 12 % of the particle distribution while particles larger than 339 nm accounted for 30 % of the particle size distribution. Many of the larger particles

appeared to be formed from the overlap and aggregation of adjacent particles resulting in longer linear chain-like structures. The corresponding EDS spectrum and layered image only confirmed the presence of carbon and gold as expected, confirming that AuNPs were successfully electrodeposited onto a GCE surface.





Au M α 1



5 μ m

Figure 14. HR-SEM images of the electrodeposited AuNPs at the GCE surface at (A) 5,000 \times (B) 10,000 \times (C) 25,000 \times (D) 50,000 \times magnifications with the corresponding EDS (E) spectrum and (F) layered image.

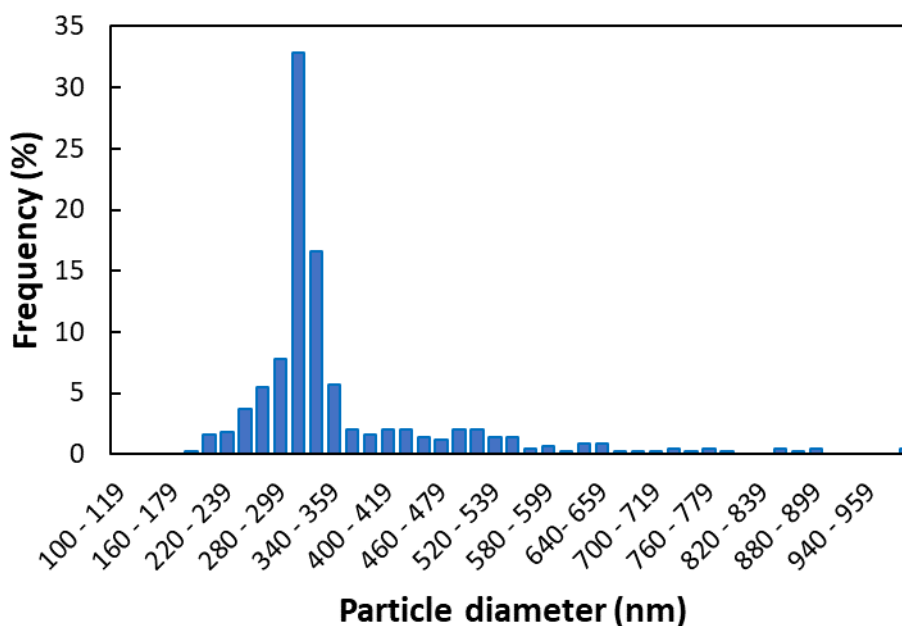


Figure 15. AuNP particle size distribution where particles between 300 – 319 nm accounted for 33 % of all particles followed by 320 – 339 nm (16.6 %) and 280 – 299 nm (7 %).

3.3.6. Electrochemical characterisation of carbon nano-onions on glassy carbon electrodes

The CNOs were applied to the freshly polished GCE by the drop-casting method as described in section 3, voltammetry of each CNO modified electrode was carried out in degassed 0.1 M KCl. Initially the CNOs were investigated over the potential range of -1.0 V to 1.0 V vs Ag/AgCl at 100 mV sec⁻¹ (**Figure 16 (A) – (D)**). It was clearly observed that each CNO layer exhibited high double layer capacitance as expected⁴⁰, and were stable after prolonged potential cycling (n = 50). The currents observed were in general much larger than that of the bare electrode reflecting the larger surface to volume ratio and active surface groups and features. These surface groups and features include the presence of carboxylic acid groups on the CNO surface, resulting in oxidized forms of CNOs (oxi-CNOs)³⁵ and the doping of the CNO nanostructure with heteroatoms (in this case B and N)⁴¹. The p-CNO and BN-doped CNOs exhibited the expected capacitive features, but an anodic and cathodic Faradaic

response was present in the case of both the oxi-CNOs and oxi-BN-doped CNOs, reflecting some redox activity due to the surface carbonyl/acidic functional groups.

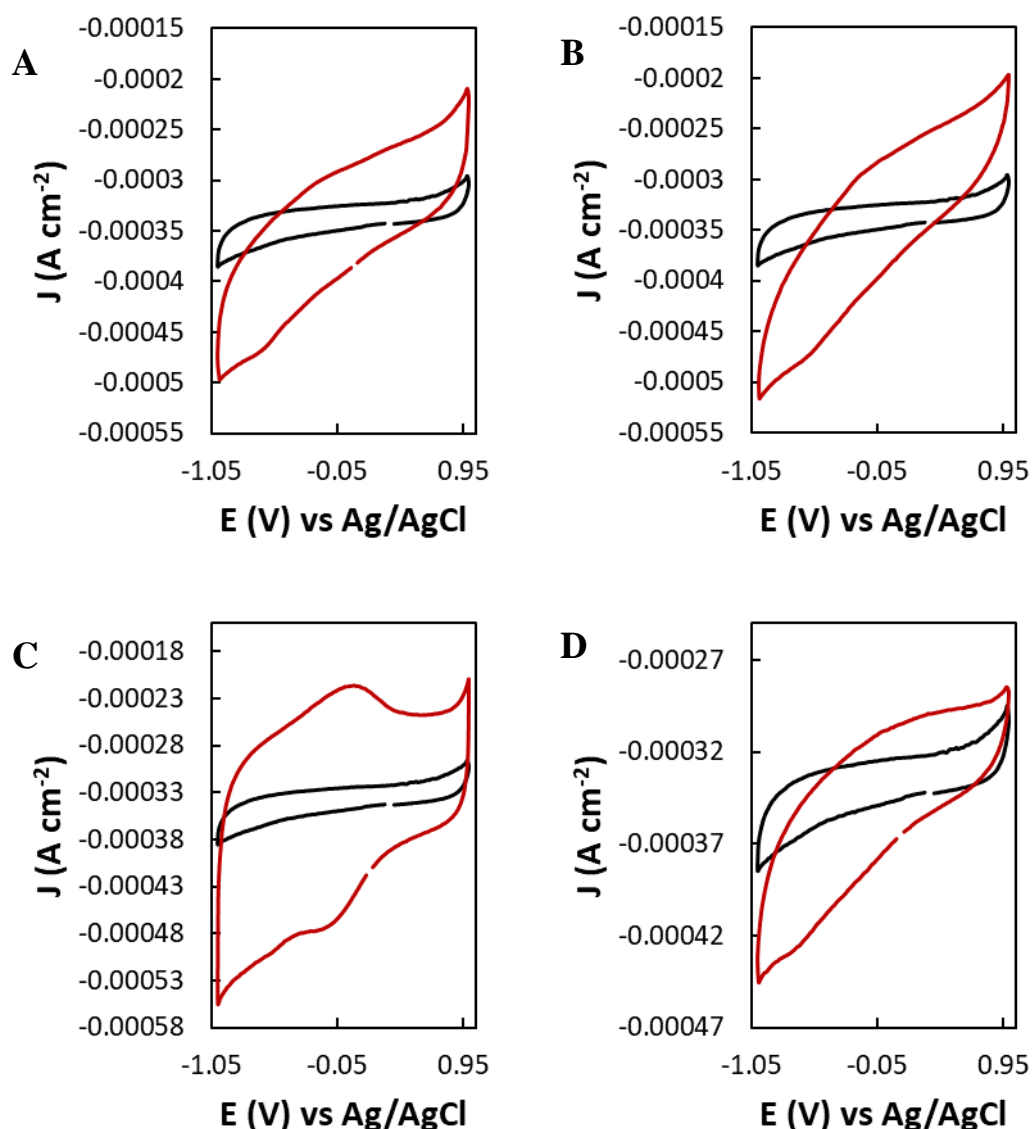


Figure 16. Voltammetry of 0.1 M KCl at the bare GCE (black) and at the **A)** p-CNO, **B)** BN-doped CNO, **C)** oxi-CNO and **D)** oxi-BN-doped CNO modified GCE with a $0.1416 \text{ mg cm}^{-2}$ surface loading (all CNO modified GCEs are shown as the red line) from -1.0 V to 1.0 V at 100 mV s^{-1} .

The effect of scan rate was then investigated for each of the CNOs, and the slope of the graphs of capacitive currents against the scan rate allowed specific capacitances for each modified electrode to be estimated via **Eq. 2** (**Figure 17** (A) – (F) and **Table 5**), where the oxi-CNOs had the highest and p-CNOs had the lowest capacitances as expected. The p-CNOs was a benchmark for comparison as neither

heteroatoms were doped into the nanostructure and the material was unfunctionalised. The p-CNOs still displayed a high capacitance and the pore size in a carbon network has a profound influence on the capacitance, where it has been reported that a smaller pore size in the carbon network of a nanomaterial will increase the capacitance due to the development of a surface area inaccessible to electrolytic ions in solution³⁴. It was clearly observed that the CNO capacitance increased when doped with B and N atoms. This has been attributed to the increased porosity of the CNO surface and by surface defects caused by the B and N centres^{42, 43}. The two oxidized CNOs (oxi-CNOs) on the other hand, were covalently modified with the introduction of carboxylic acid groups on their surface. These are interesting features as they can be used as a linker to attach polymers or other molecules to the CNO surface³⁵. These groups also have a significant effect in increasing the capacitance of the oxi-CNOs which has been attributed to the generation of faradaic current from these electroactive groups and from the enhanced surface area through the opening and breakage of the graphitic layers of the CNO⁴⁴. The capacitance of oxi-BN-doped CNOs, on the other hand, was expected to be greater than that of the oxi-CNOs due to the combined effect of the heteroatoms doped into the graphitic surface and the presence of the carboxylic acid groups, however the recorded value was lower than that of the oxi-CNOs. The capacitance was greater than that of the BN-doped CNOs indicating that the carboxylic acid groups had an effect but the functionalisation may have been carried out to a lesser degree due to the B and N doping, as this would decrease the number of possible functionalisation sites of the CNO surface.

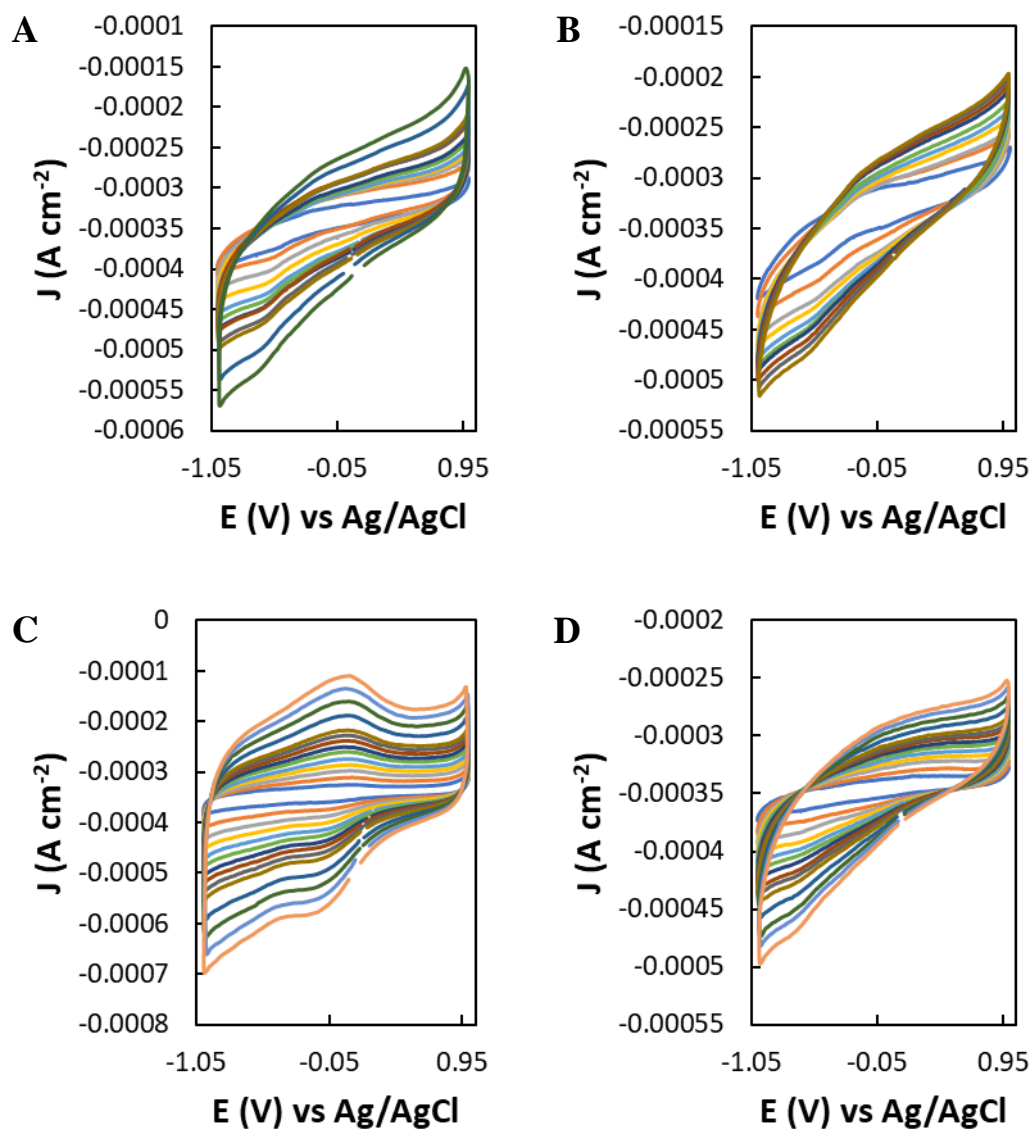
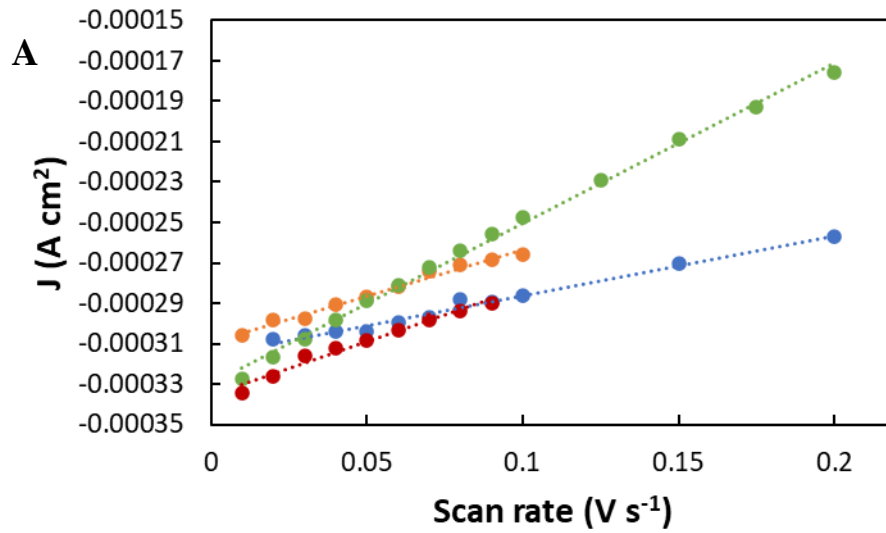


Figure 17. CV overlay of 0.1M KCl at the (A) p-CNO, (B) BN-doped CNO, (C) oxi-CNO and (D) oxi-BN-doped CNO modified GCE from -1.0V to 1.0V, vs Ag/AgCl over scan 10 – 100 mV sec^{-1} .

$$C_s = \frac{I}{vm} \dots \dots \dots (2)$$

where v = scan rate, m = mass of the CNOs (on the GCE surface in this case each GCE was loaded with 0.142 mg CNOs) and I is the current.



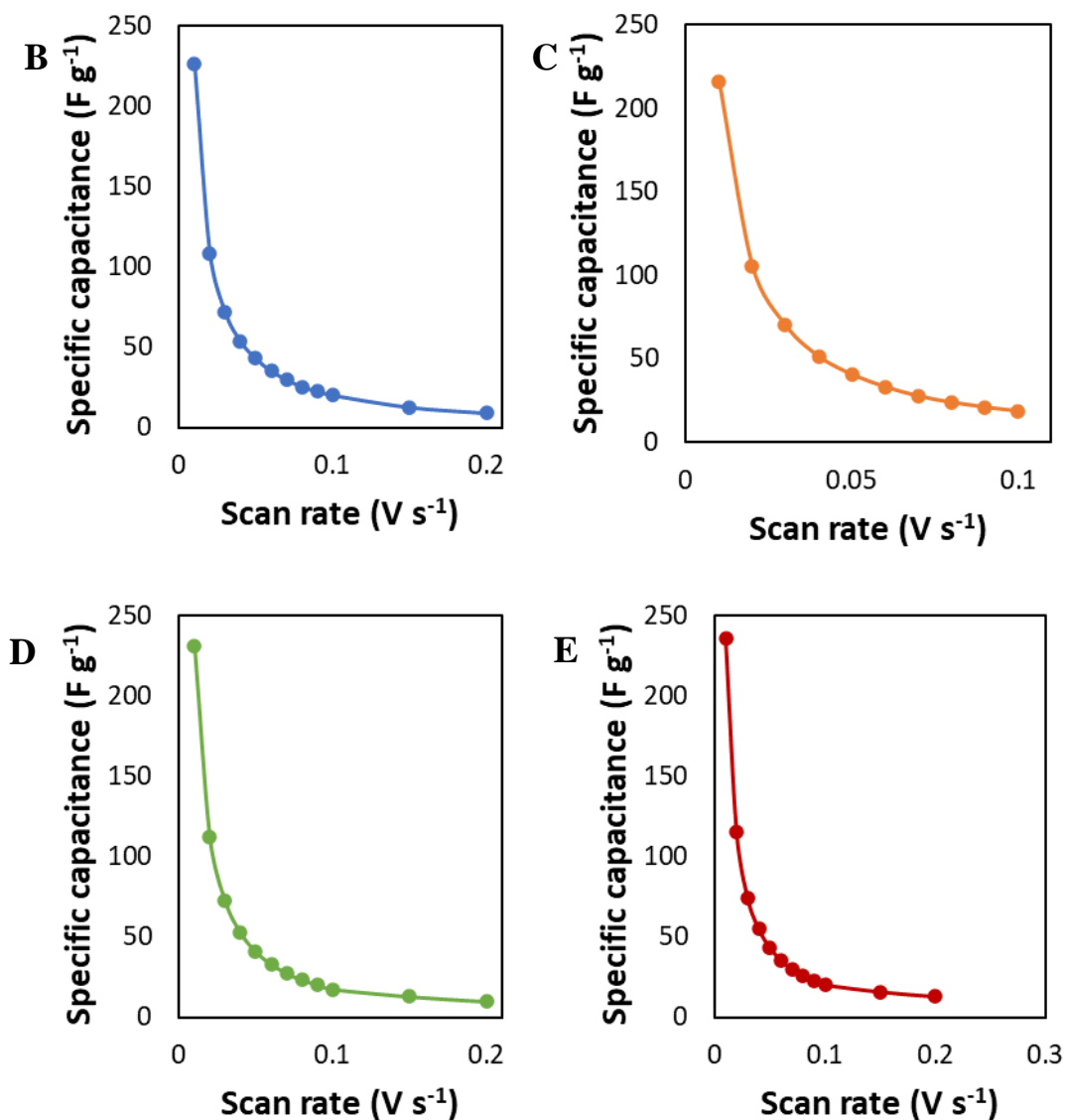
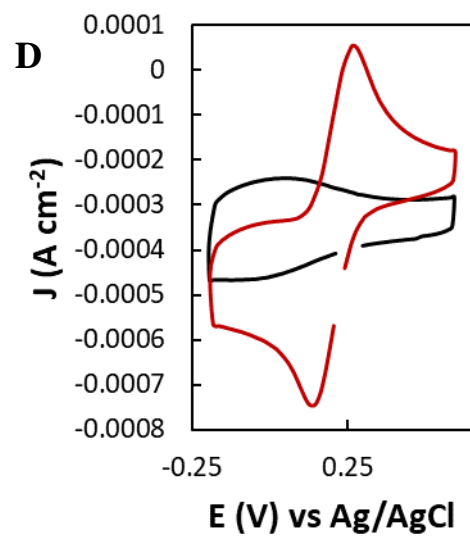
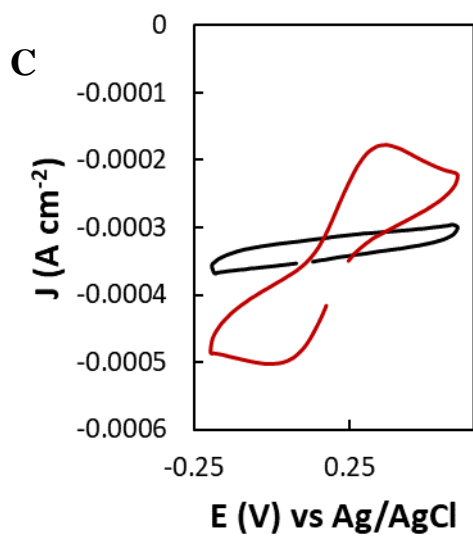
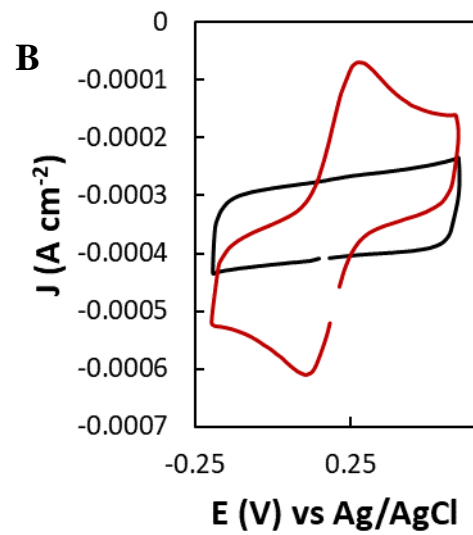
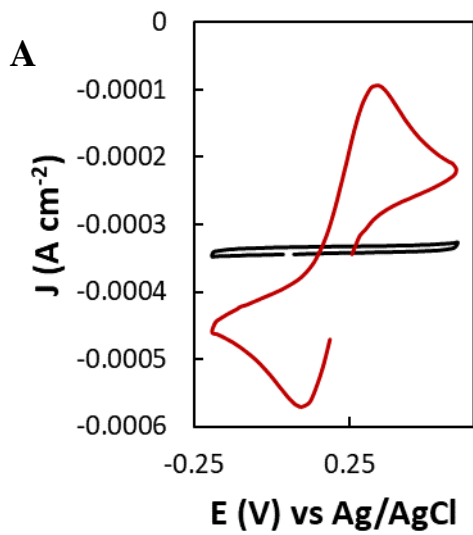


Figure 18 (A) Current density vs scan rate plots for the p-CNO (blue), BN-doped CNO (orange), oxi-CNO (green) and oxi-BN-doped CNO (red) modified GCEs (current measured at 0.5 V vs. Ag/AgCl), over a potential range of -1.0 – 1.0 V vs. Ag/AgCl from 10 – 200 mV s⁻¹ in 0.1 M KCl resulting in 5.28×10^{-4} F cm⁻². Specific capacitance measured as a function of scan rate with maximum at 10 mV s⁻¹ for the (B) p-CNOs, (C) BN-doped-CNOs, (D) oxi-CNOs and (E) oxi-BN-doped CNOs.

Table 5. Comparison of capacitances, electroactive surface areas and surface coverages for each of the CNOs, with the oxi-CNOs having the highest capacitance, greatest electroactive surface area and surface coverage calculated for the faradaic waves associated with oxi- functional groups.

	Capacitance (F cm ⁻²)	Specific capacitance (taken at 0.1 V) (F g ⁻¹)	Electroactive surface area (cm ²)	Surface coverage (mol cm ⁻²)
p-CNO/GCE	2.95×10^{-4}	2.08	0.195	N/A
BN-doped CNO/GCE	4.59×10^{-4}	3.24	0.190	N/A
oxi- CNO/GCE	7.97×10^{-4}	5.63	0.406	1.203 – 1.246 $\times 10^{-10}$
oxi-BN- doped CNO/GCE	5.28×10^{-4}	3.73	0.174	3.885 – 5.674 $\times 10^{-10}$

Anionic and cationic redox probes were employed to examine the surface characteristics of each CNO modified electrode. Firstly, a 1 mM $[\text{Fe}(\text{CN})_6]^{3/4-}$ anionic redox probe was investigated (**Figure 19 (A) – (D)**). The oxi-CNOs showed the largest peak values for the oxidation process, while the oxi-BN-doped CNOs showed the largest value for the reduction process while the BN-doped CNOs showed the smallest oxidation and reduction peak values. The p-CNOs and BN-doped CNOs showed no preference for either oxidation or reduction but the oxi-CNOs and oxi-BN-doped CNOs favoured the cathodic process (involving $[\text{Fe}(\text{CN})_6]^{3-}$) over that of the anodic one due to the presence of the negatively charged carboxylic groups on the oxi-CNO and oxi-BN-doped CNO surfaces.



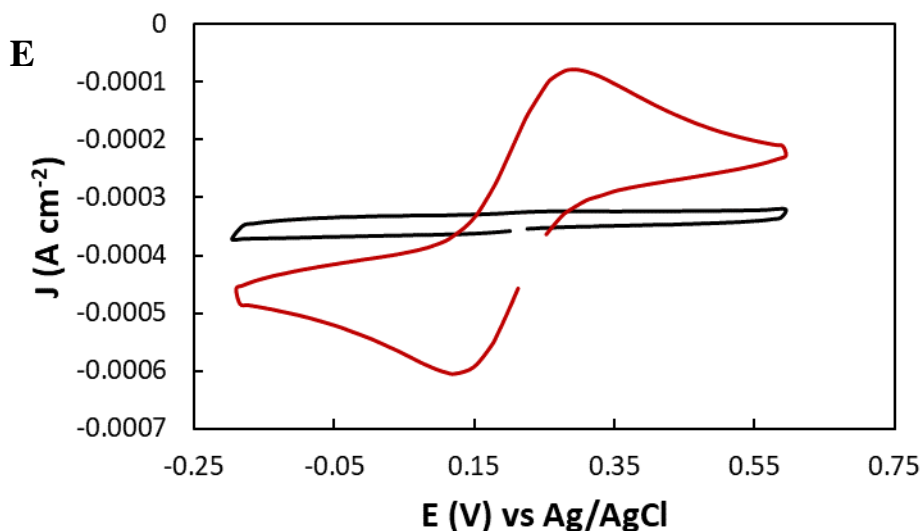


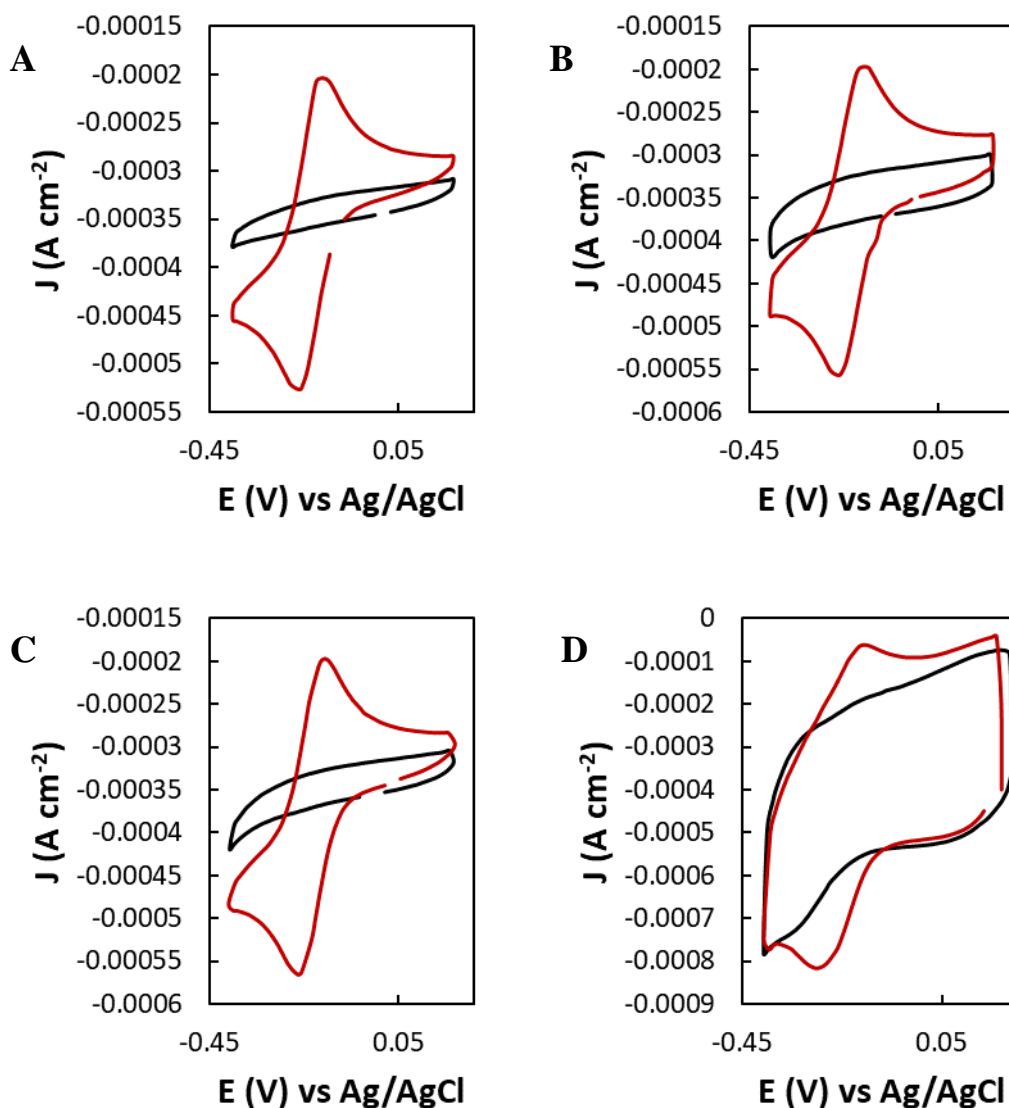
Figure 19. Cyclic Voltammetry at the (A) bare GCE, (B) p-CNO, (C) BN-doped CNO, (D) oxi-CNO and (E) oxi-BN-doped CNO modified GCEs relative to the background in 1 mM $[\text{Fe}(\text{CN})_6]^{3/4-}$ (red curves) in 0.1 M KCl at 100 mV s^{-1} (black curves).

Table 6. Comparison of the oxidation and reduction peak heights and potentials, ΔE_p values $E_{p1/2}$ values and J_p ratios of 1 mM $[\text{Fe}(\text{CN})_6]^{3/4-}$ at the bare and each of the CNO/GCEs.

	J_p (a) (A cm^{-2})	E_p (a) (V)	J_p (c) (A cm^{-2})	E_p (c) (V)	ΔE_p (V)	E_p $_{1/2}$ (V)	J_p (a)/ J_p (c)
Bare GCE	2.365×10^{-4}	0.325	2.265×10^{-4}	0.94	0.231	0.209	1.044
p-CNO/GCE	1.938×10^{-4}	0.275	1.976×10^{-4}	0.112	0.163	0.193	0.981
BN-doped CNO/GCE	1.41×10^{-4}	0.318	1.250×10^{-4}	0.0411	0.287	0.18	1.128
oxi-CNO/GCE	2.177×10^{-4}	0.275	3.175×10^{-4}	0.129	0.145	0.202	0.686
oxi-BN-doped CNO/GCE	2.475×10^{-4}	0.291	2.403×10^{-4}	0.122	0.169	0.207	0.956

Voltametric examination in a 1 mM $[\text{Ru}(\text{NH}_3)_6]^{2+}$ cationic probe followed (Figure 20 (A) – (D)). Conversely to the anionic redox probe, the oxi-BN-doped

CNOs showed the largest peak values for the oxidation process, while the oxi-CNOs showed the largest value for the reduction process. As per the anionic probe, the BN-doped CNOs showed the smallest oxidation and reduction peak values. The oxi-CNO and oxi-BN-doped CNO modified GCEs showed the largest peak separation ΔE_p , hindering electron transfer for the $\text{Ru}^{2+/3+}$ process while favouring the cathodic process in each case due to anionic functional groups facilitating electron transfer of the higher oxidation state of Ru^{3+} .



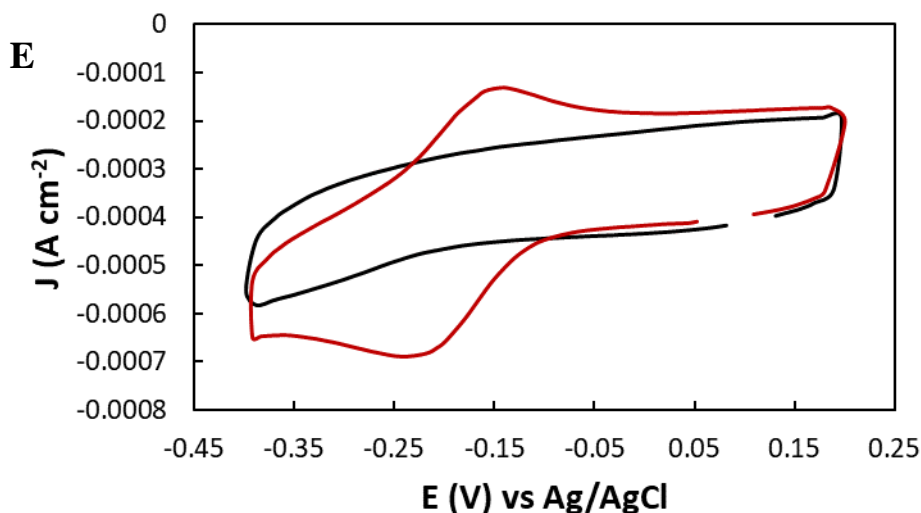


Figure 20. Cyclic Voltammetry at the (A) bare GCE, (B) p-CNO, (C) BN-doped CNO, (D) oxi-CNO and (E) oxi-BN-doped CNO modified GCEs (red curves) relative to the background (black curve) in presence of 1 mM $[\text{Ru}(\text{NH}_3)_6]^{2+}$ in 0.1 M KCl at 100 mV s^{-1} .

Table 7. Comparison of the oxidation and reduction peak heights and potentials, ΔE_p , $E_{p1/2}$ and J_p ratios of 1 mM $[\text{Ru}(\text{NH}_3)_6]^{2+}$ the bare and each of the CNO/GCEs. The bare GCE showed the largest peak oxidation value, whereas the oxi-BN-doped CNO/GCE gave the highest reduction signal. The oxi-CNO and oxi-BN-doped CNO/GCEs showed the largest peak separation.

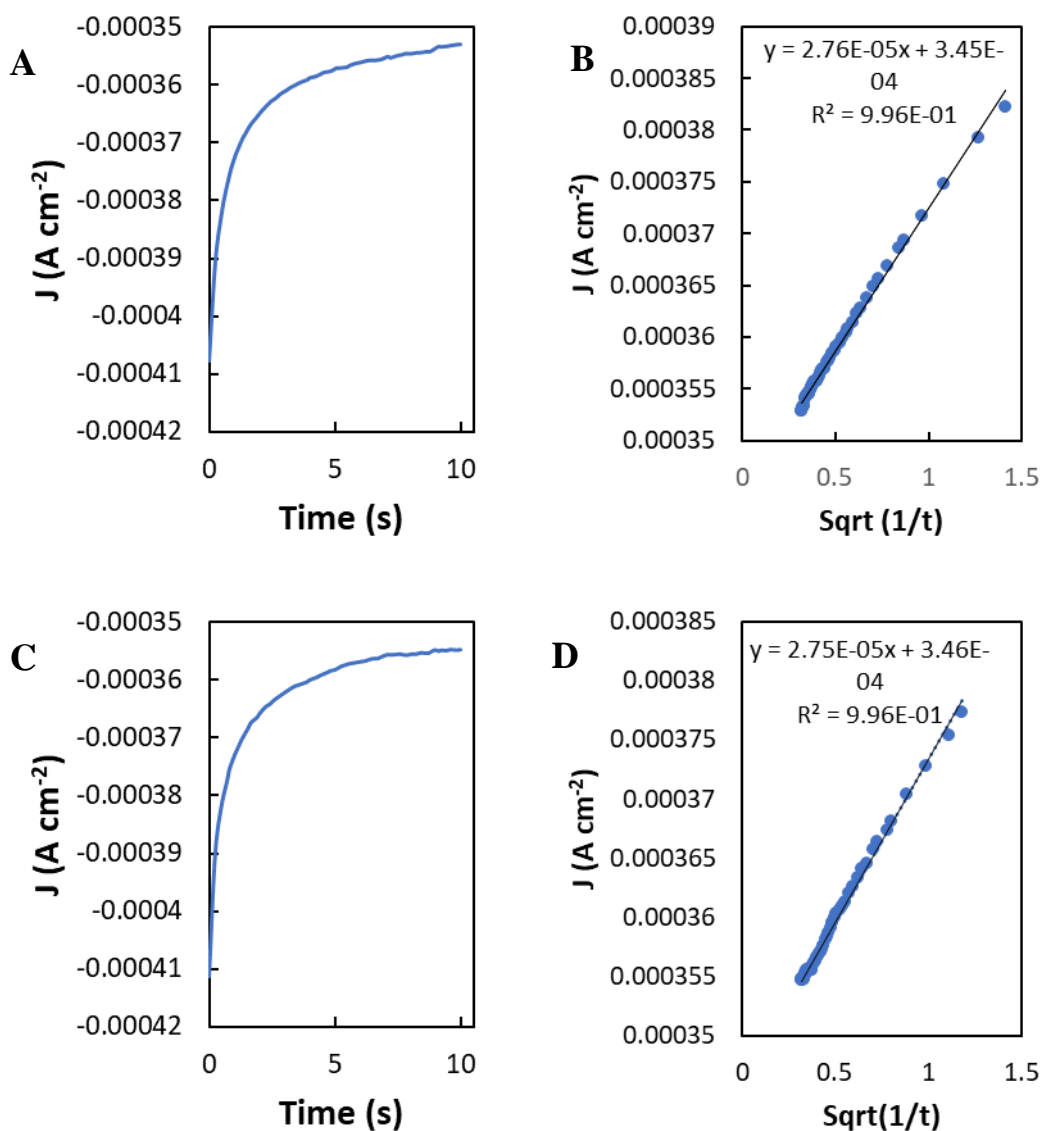
	$J_{p(a)}$ (A/cm^2)	$E_{p(a)}$ (V)	$J_{p(c)}$ (A/cm^2)	$E_{p(c)}$ (V)	ΔE_p (V)	$E_{p1/2}$	$J_{p(a)}/J_{p(c)}$
Bare GCE	1.706×10^{-4}	-0.149	1.660×10^{-4}	-0.211	0.063	-0.180	1.028
p-CNO/GCE	1.229×10^{-4}	-0.135	1.728×10^{-4}	-0.212	0.077	-0.173	0.711
oxi-CNO/GCE	1.295×10^{-4}	-0.149	1.830×10^{-4}	-0.260	0.112	-0.205	0.707
BN-doped CNO/GCE	1.295×10^{-4}	-0.148	1.877×10^{-4}	-0.214	0.066	-0.181	0.687
oxi-BN-doped CNO/GCE	1.260×10^{-4}	-0.149	1.977×10^{-4}	-0.243	0.093	-0.196	0.638

The electroactive surface area for the bare and each of the CNOs were obtained using chronoamperometry and were calculated using the Cottrell equation (3):

$$i = \frac{nFAC_0\sqrt{D}}{\sqrt{\pi t}} \dots\dots\dots(3)$$

Where i is current, n is the number of electrons transferred, F is Faraday's constant, A is the electrode surface area, C_0 is concentration, D is the diffusion coefficient and t is time. This was carried out using 1 mM [Ru(NH₃)₆].Cl₂, where the potential was held at -0.08 V vs. Ag/AgCl for 10 seconds. From these measurements, the currents were plotted against $\sqrt{1/t}$ resulting in linear Cottrell plots (**Figure 21 (A) – (H)**). Using the slope from the Cottrell plots and the Cottrell equation, the electroactive surface area values were calculated to be 0.195 ± 0.01 , 0.190 ± 0.01 , 0.406 ± 0.02 and 0.174 ± 0.01 cm² for the p-CNO, BN-doped CNO, oxi-CNO and oxi-BN-doped CNO modified GCEs, respectively (see **Table 5**). The wide variation in the electroactive surface area can be accounted for through the surface defects and modifications in the BN-doped and both oxidized forms of the CNOs. The p-CNO/GCE have the lowest surface area as expected as the pristine surface consists of a network structure of pure carbon. Fewer surface defects are present due to the absence of doped heteroatoms and carboxylic acid groups. Although the electroactive surface area of the BN-doped CNO/GCE is lower than the p-CNO/GCE, the electroactive surface area of the BN-doped CNO/GCE was expected to be greater than that of the p-CNO/GCE due to surface defects present in the network through B and N doping. However, the capacitive effects of the B and N atoms present may have a significant contribution to the decrease of the electroactive surface area. The oxi-CNO/GCE displayed the greatest electroactive surface area as expected due to the opening and breakage of the outer graphitic layer of the CNO surface. The electroactive carboxylic acid groups present on the oxi-CNO surface also contributes to the increased electroactive surface area. A combination of heteroatom doping and presence of carboxylic acid groups on the oxi-BN-doped CNO surface attributed to the increase in the electroactive surface area of the oxi-BN-doped CNO/GCE. The presence of the doped heteroatoms in the BN-doped CNO structure decreased the overall degree of CNO oxidation that they could undergo, resulting in fewer opening and breakage points on the outer shell, and thus, decreasing the number of carboxylic acid groups on the CNO surface attributing to the lower surface area than the oxi-CNO/ GCE. The greater electroactive surface area of the two oxidized species may

also be influenced by the hydrophilicity of each oxidized CNO caused by the presence of the carboxylic acid groups on the CNO surface.



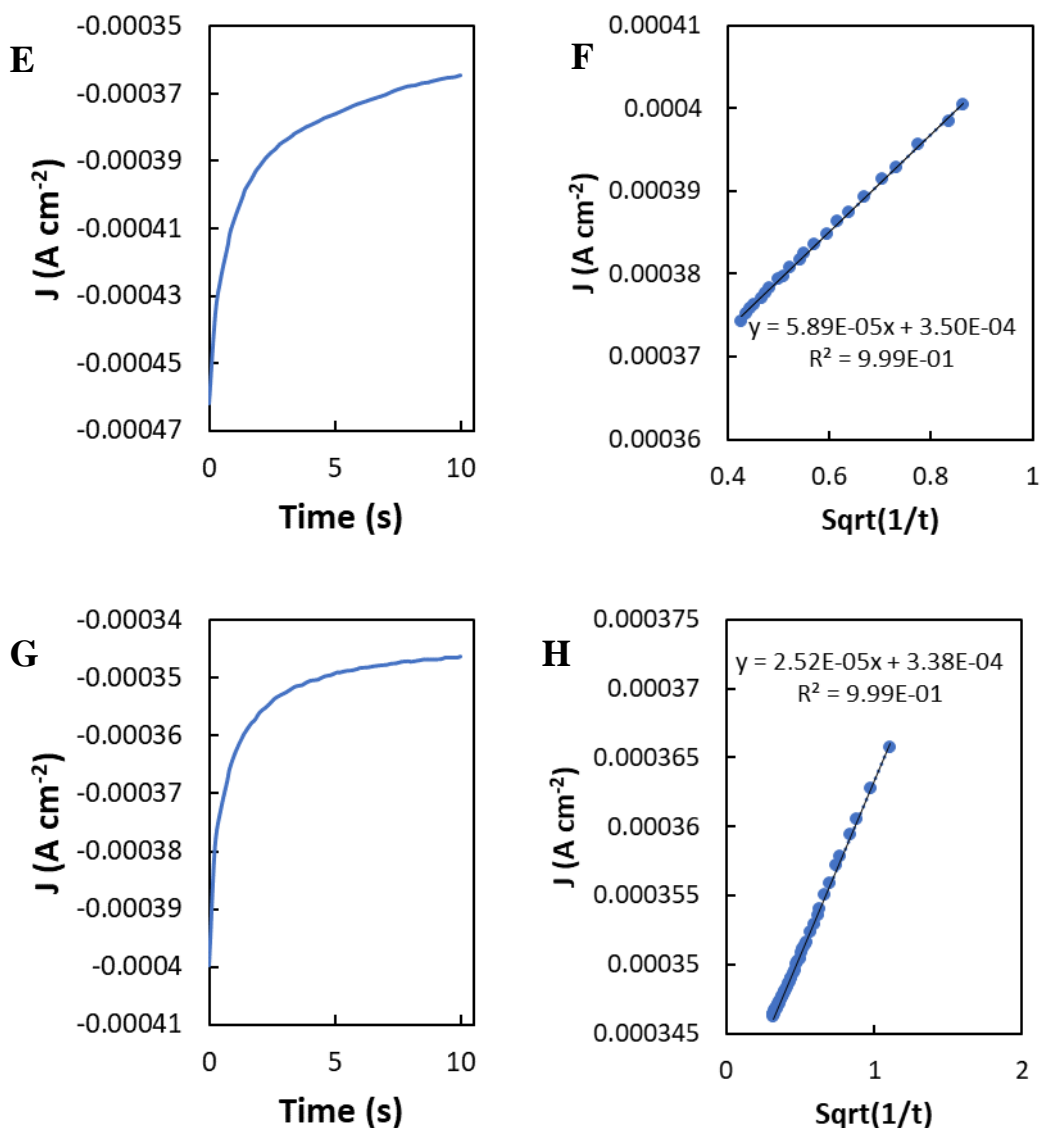


Figure 21. Chronoamperometry and corresponding Cottrell plots of the (A – B) p-CNO, (C – D) BN-doped CNO, (E – F) oxo-CNO and (G – H) oxo-BN-doped CNO/GCEs.

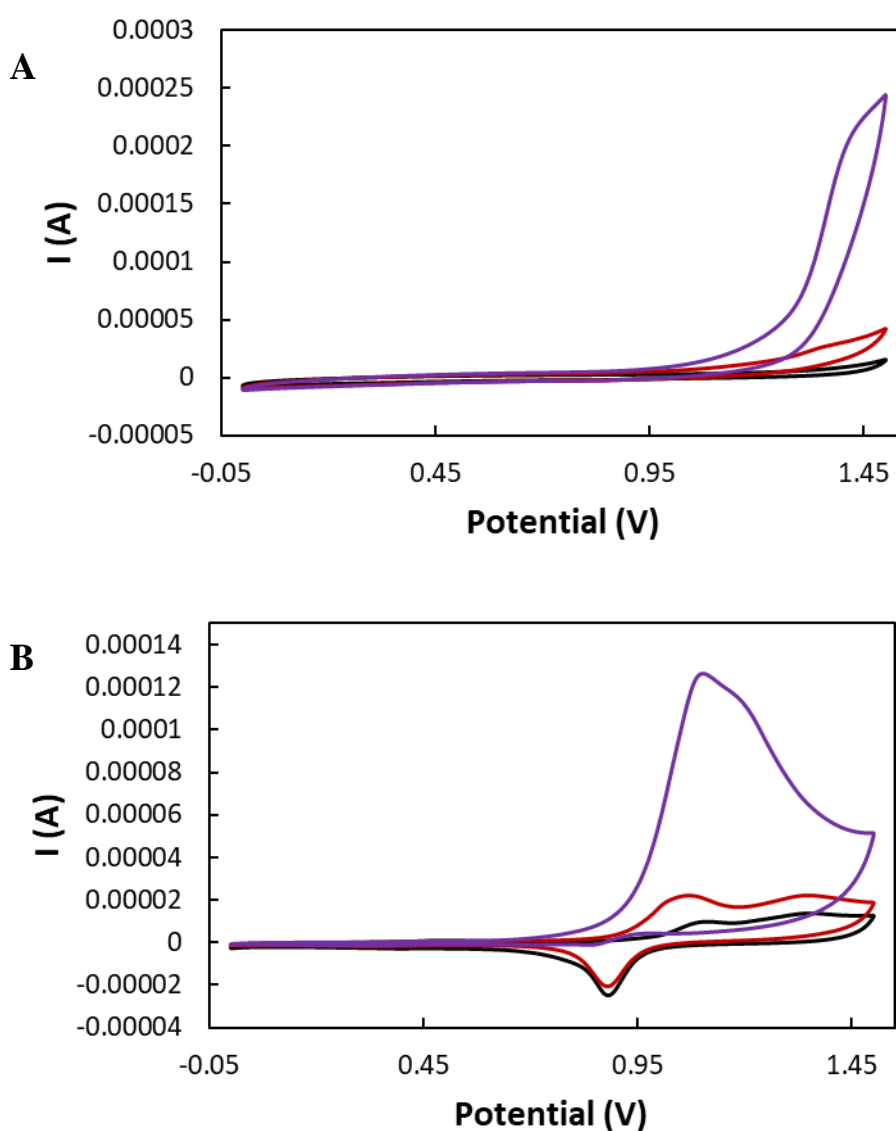
A practical issue arose regarding the 1 mg mL⁻¹ suspensions employed whereby upon standing, precipitation of the materials occurred over time, being particularly evident with the p-CNOs and BN-doped CNOs. Both the oxo-CNOs and oxo-BN-doped CNOs were more stable in EtOH due to the more polar nature of the surface functional groups which aided dispersion. In order to address this, various dilutions of the CNO of choice were made over 1/2, 1/5, 1/10 and 1/50 of the stock 1 mg mL⁻¹. Sonicating immediately prior to drop casting onto the electrode surface helped to maintain more controllable surface loadings.

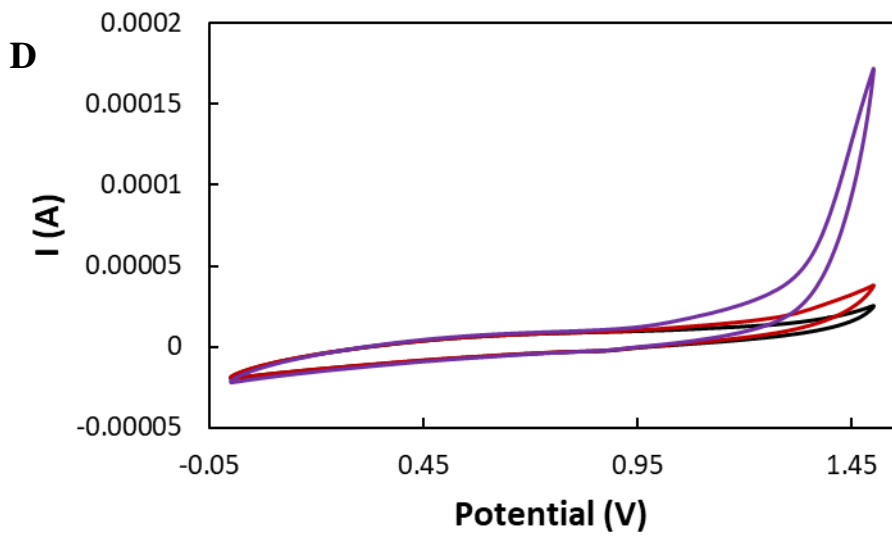
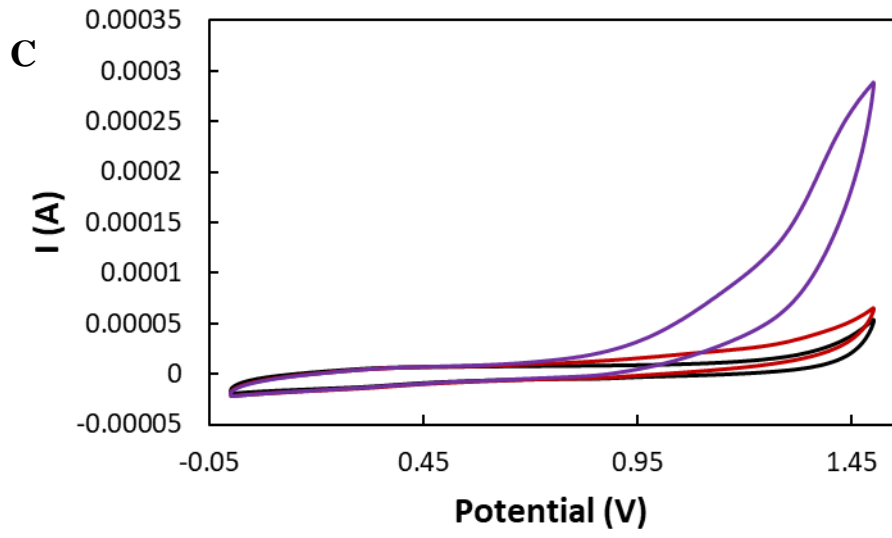
The polar functional groups which were introduced upon acid treatment (oxi and oxi-BN-doped CNOs) made these materials promising candidates for electrodeposition of metal particles. Prior work investigated the deposition of nanoparticles onto p-CNOs for durable oxygen reduction, ultra-high energy supercapacitors and enhanced field emission behaviour^{24, 25}. The CNOs used in previous studies were synthesised through the thermal annealing of nanodiamond powders, the combustion of white and thin cotton and through a methane cracking method^{24-26, 35}. The Pt nanoparticles (PtNPs) were applied to the resulting CNOs using various methods. Firstly, the PtNPs were mixed well with rather than dispersed onto the CNOs as both particles were of similar size. The PtNPs were then surrounded by the CNOs, physically isolating them from other PtNPs, resulting in the Pt/CNOs²⁴. Secondly, The CNOs were first activated with 2 M H₂SO₄ or 4 M HNO₃ at 120 °C followed by the treatment of the product with ethyleneglycol, deionized water and H₂PtCl₆ at 140 °C, giving rise to Pt-CNOs²⁵. The final Pt-CNO composites were prepared by initially activating the p-CNOs by refluxing overnight in HNO₃. The resulting oxi-CNOs were then washed with deionised water and dried in an oven at 120 °C. The composite was prepared by the addition of 0.5 – 15 µL of 0.1 M H₂PtCl₆ solution in H₂O into 0.5 mL of a 0.2 mg mL⁻¹ CNO suspension, ultrasonicated for 5 min and then aged at room temperature for 24 hours²⁶. From considering the prior work done using PtNPs on CNOs, a good foundation was laid down to apply the multi-potentiostatic pulse method to an oxi-BN-doped CNO/GCE, resulting in an AuNP@oxi-BN-CNO/GCE, to be used for the determination of NAC.

3.3.7. Gold nanoparticle electrodeposition at the oxi-BN-doped carbon nano-onion modified electrode

The oxi-BN-doped CNOs were selected for AuNP deposition as firstly they represent the most novel material and secondly, they exhibited favourable electron transfer properties arising from the anionic/cationic probe studies. A dilution series was performed to optimise loading with resulting 0.1, 0.05 and 0.02 mg mL⁻¹ suspensions. 10 µL of each CNO suspension was drop-cast onto a freshly polished GCE and tested via cyclic voltammetry with 1 mM and 10 mM NAC. These NAC samples were also tested using a bare GCE, bare AuE and a bare PtE (**Figure 22 (A)**)

– (F)). The NAC oxidation response was then compared (**Figure 23 (A) – (B)**), where the presence of the oxi-BN-doped CNOs did not increase the NAC oxidative response, but instead the NAC oxidative response decreased relative to the unmodified GCE. Interestingly, the signal decreased stepwise with decreasing oxi-BN-doped CNO concentration due to less active sites on the GCE surface provided by the CNOs. In order to investigate the influence of the AuNP on the modified GCE NAC signal, the pulse electroanalysis method optimised above was employed with the aim to maximise the NAC response.





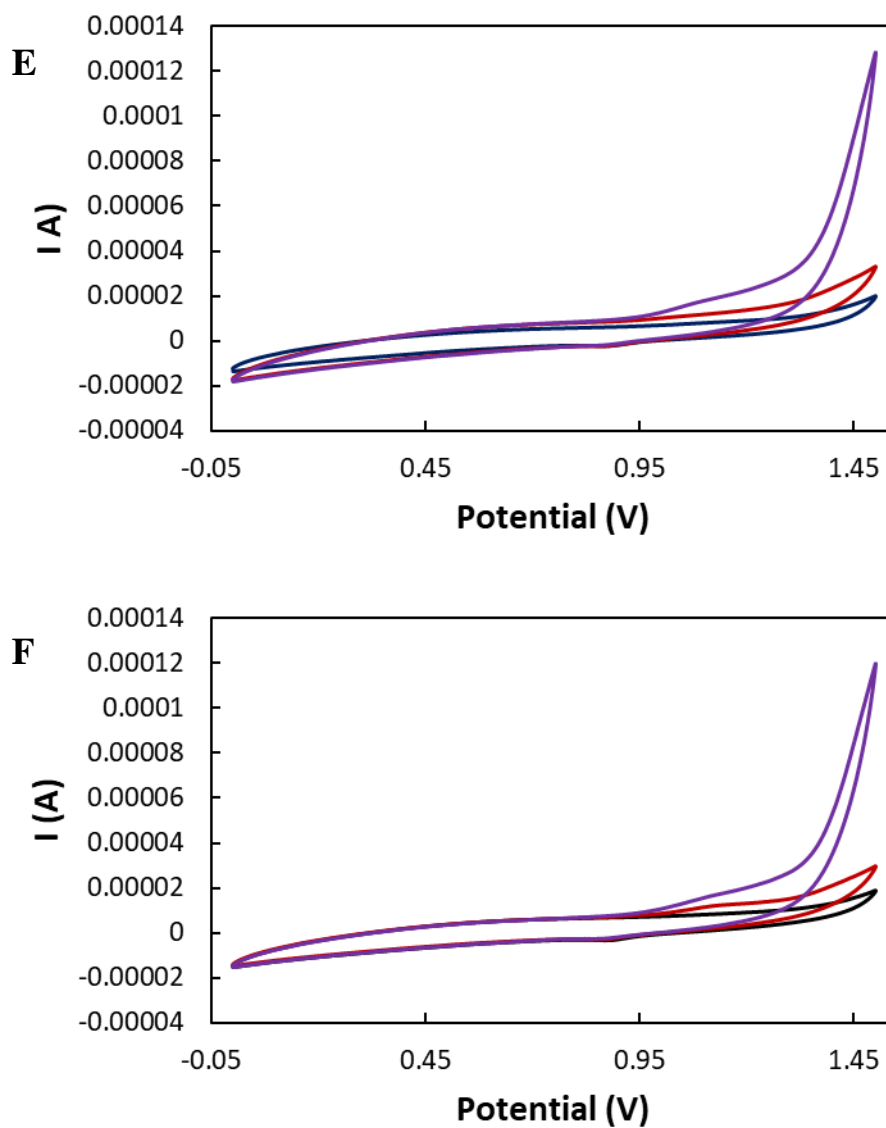


Figure 22. Voltammetry of 1 mM NAC (red) and 10 mM NAC (purple) in 0.1 M H₂SO₄ (black) at the bare (A) GCE, (B) bare AuE and GCEs modified with 10 μ L of (C) 1 mg mL⁻¹, (D) 0.1 mg mL⁻¹, (E) 0.05 mg mL⁻¹ and (F) 0.02 mg mL⁻¹ oxi-BN-doped CNOs from 0 – 1.4 V at 100 mV s⁻¹.

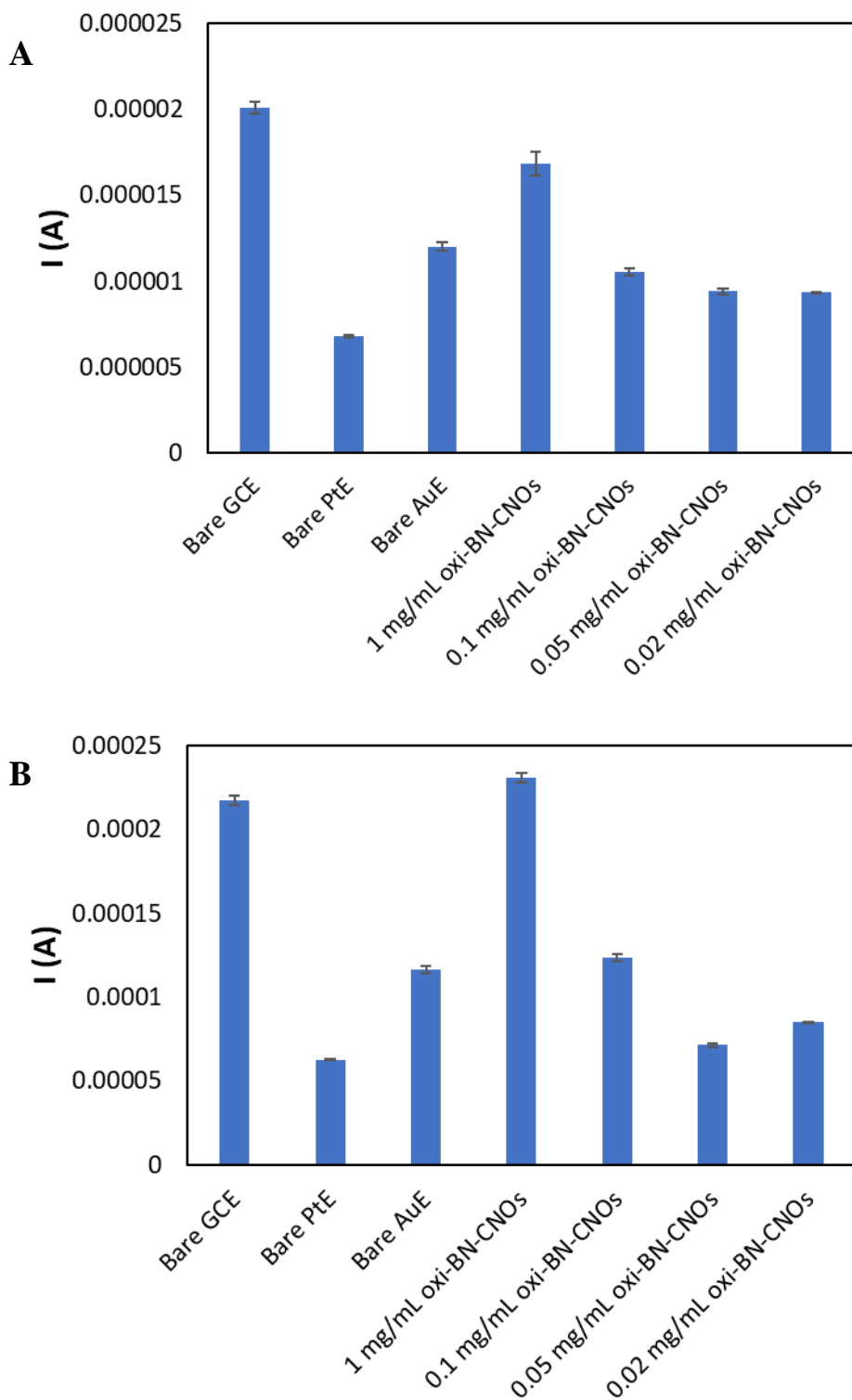
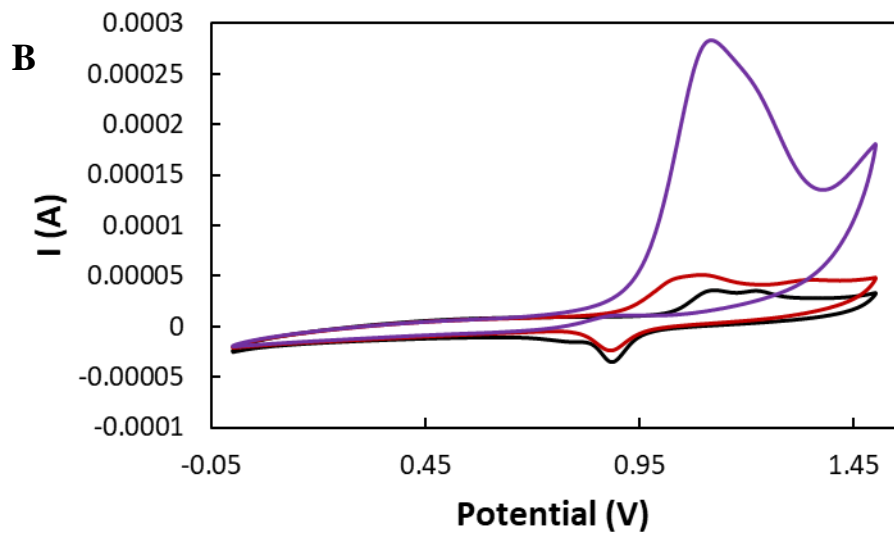
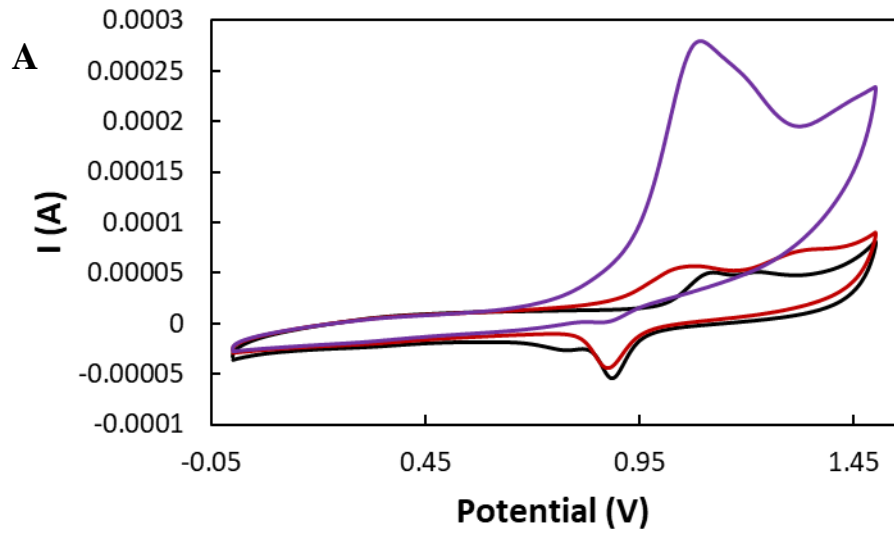


Figure 23. Bar charts showing the oxidative response of (A) 1 mM and (B) 10 mM NAC at the bare GCE, bare PtE, bare AuE and GCEs modified with 10 μL of 1 mg mL^{-1} , 0.1 mg mL^{-1} , 0.05 mg mL^{-1} and 0.02 mg mL^{-1} oxi-BN-doped CNOs. The NAC response was recorded between 1.36 – 1.45 V at the bare and each oxi-BN-doped CNO modified GCE while the NAC peak was measured at 1.12 and 1.11 V for the bare PtE and bare AuE respectively.

The combination of AuNPs with oxi-BN-CNOs were investigated at GCEs modified with 10 μL of each oxi-BN-doped CNO samples (1 mg mL^{-1} , 0.1 mg mL^{-1} , 0.05 mg mL^{-1} and 0.02 mg mL^{-1}). This was carried out by firstly drop-casting the CNOs onto the fresh GCE surface. Once dried, the AuNPs were electrochemically deposited using the optimised multi-pulse potentiostatic method, as described in sections 4.2 and 4.3. Once the AuNPs were deposited onto each oxi-BN-doped CNO/GCE, the resulting AuNP@oxi-BN-CNO/GCE were tested with 1 mM and 10 mM NAC samples in 0.1 M H_2SO_4 by cyclic voltammetry from 0 – 1.5 V at 100 mV s^{-1} (**Figure 24 (A) – (D)**). Both NAC concentrations were compared (**Figure 25 (A) – (B)**) with the greatest response observed with the AuNPs electrodeposited at the GCE modified with 10 μL of the 0.02 mg mL^{-1} of the oxi-BN-doped CNO suspension, thus identifying the optimum AuNP@oxi-BN-doped CNO. This may have been due to a large amount of CNOs at the surface of the GCE. At lower concentrations, the oxi-BN-doped CNO solutions were more homogeneously suspended, which gave rise to more uniform loadings each time onto the GCE. This thinner layer may have been beneficial to the AuNP electrodeposition process as more active sites on the CNO surface would have been accessible to Au^{3+} ions in solution. At higher oxi-BN-doped CNO concentrations, the CNOs clumped together which resulted an ununiform CNO coating which would thus impact the electrodeposited AuNPs.



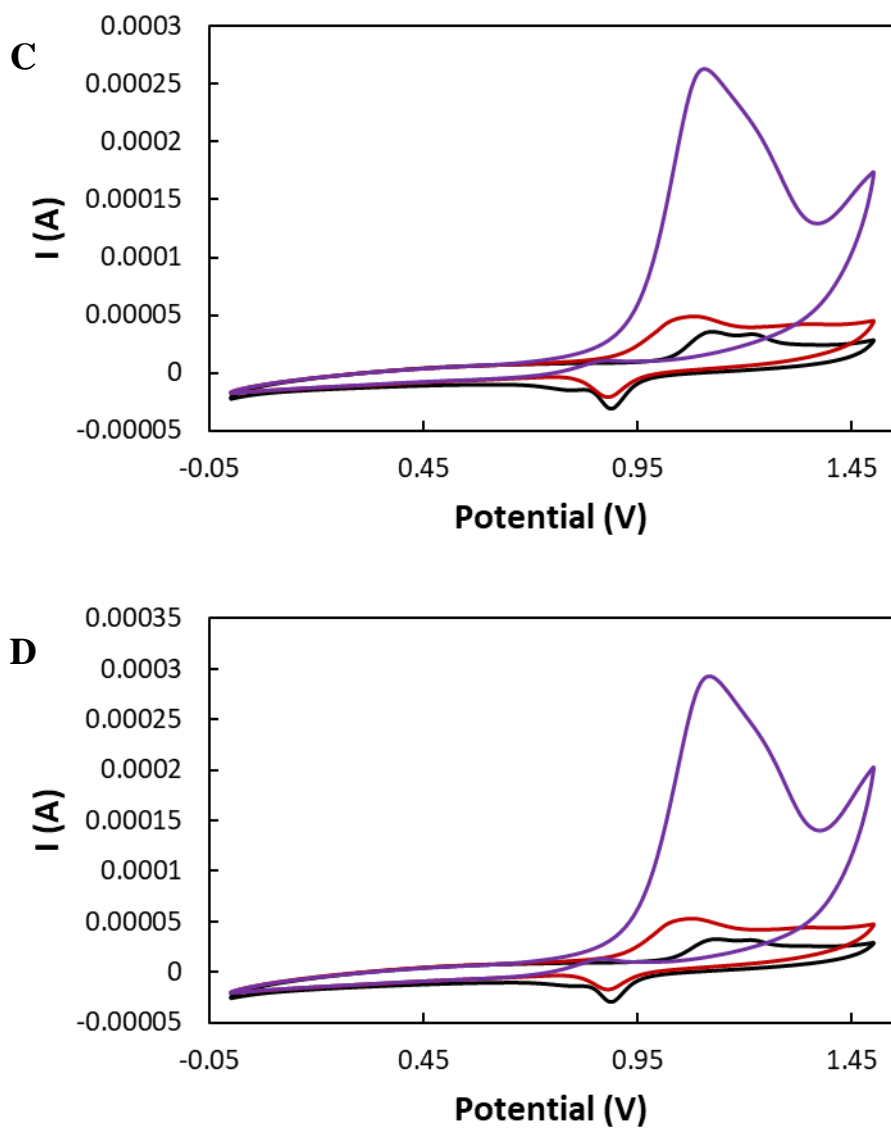


Figure 24. Voltammetry of 1 mM NAC (red) and 10 mM NAC (purple) in 0.1 M H_2SO_4 (black) GCEs modified with 10 μL of (A) 1 mg mL^{-1} , (B) 0.1 mg mL^{-1} , (C) 0.05 mg mL^{-1} and (D) 0.02 mg mL^{-1} oxi-BN-doped CNOs and the optimised AuNPs from 0 – 1.5 V at 100 mV s^{-1} .

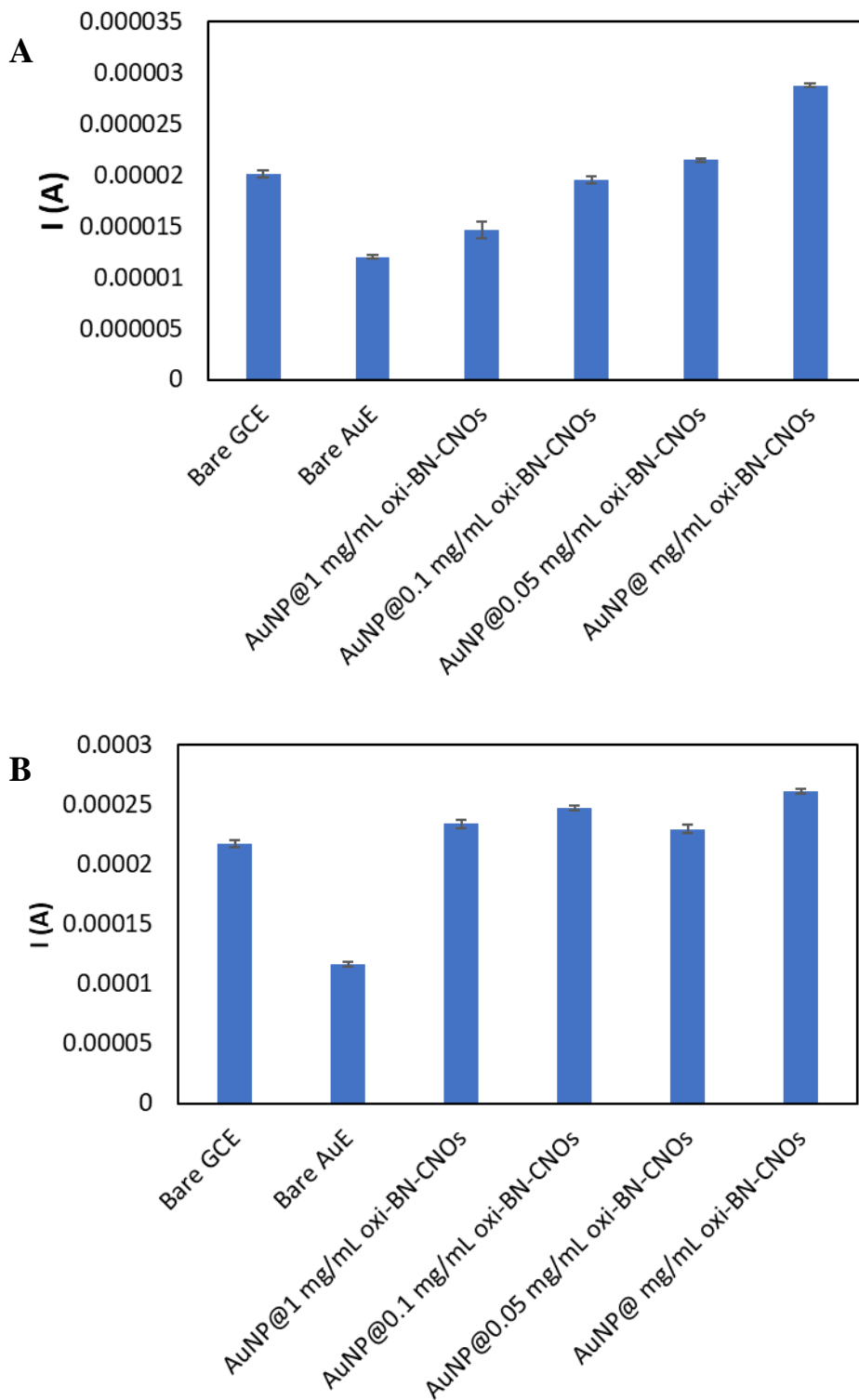


Figure 25. Bar charts showing the oxidative response of (A) 1 mM and (B) 10 mM NAC at the bare GCE, bare AuE and AuNP@ 10 μL of 1 mg mL^{-1} , 0.1 mg mL^{-1} , 0.05 mg mL^{-1} and 0.02 mg mL^{-1} oxo-BN-doped CNO/ GCEs.

Firstly, the AuNP@oxi-BN-doped CNO/GCE electroactive surface area was determined by estimating the charge passed during the Au reduction process and comparing to the gold charge density factor ($340 \mu\text{C cm}^{-2}$)⁴⁵. The resulting electroactive surface area of the AuNP@oxi-BN-doped CNO/GCE was calculated as 0.111 cm^2 (relative to 0.0822 cm^2 for the bare AuE). The AuNP@oxi-BN-doped CNO/GCE was then characterised electrochemically via scan rate studies, redox probe and subsequently EIS analyses. Firstly, a scan rate study was performed at the AuNP@oxi-BN-doped CNO/GCE. This was carried out from $0.4 - 1.5 \text{ V}$ over $10 - 200 \text{ mV s}^{-1}$. In this study the anodic and cathodic faradaic processes were monitored with respect to increasing scan rate. The anodic and cathodic responses increased linearly with respect to increasing scan rate (**Figure 26 (B)**). Equation 4 was used to estimate the surface coverage (Γ) of the AuNP@oxi-BN-doped CNO/ GCE which was found to lie within $1.775 - 1.609 \times 10^{-10} \text{ mol cm}^{-2}$.

$$I_p = \frac{n^2 F^2}{4RT} A v \Gamma \dots\dots\dots(4)$$

where I_p is the peak current (A), n is the number of electrons exchanged, F is Faraday's constant ($96,485.33212 \text{ C mol}^{-1}$), R is the universal gas constant ($8.3145 \text{ J K}^{-1} \text{ mol}^{-1}$), T is temperature (K), A is the electrode surface area (cm^2), v is the scan rate (V s^{-1}) and Γ is the surface coverage value (mol cm^{-2}).

An anionic redox probe which comprised of $5 \text{ mM } [\text{Fe}(\text{CN})_6]^{3/4-}$ in 0.1 M NaOH was used to further characterise the AuNP@oxi-BN-doped CNOs. The voltammogram of the redox probe in **Figure 27 (A)** displayed similar effects to that at the AuNP/GCE in **Figure 11 (A)** where the peak separation drastically decreased in the presence of the AuNP@oxi-BN-doped CNOs, indicating that the electron transfer process was much easier at the modified GCE. The $[\text{Fe}(\text{CN})_6]^{3/4-}$ anodic and cathodic peaks were also more prominent at the AuNP@oxi-BN-doped CNO/GCE than at the bare GCE, further indicating that the presence of Au on the electrode surface increased the accessibility of the surface.

EIS investigations followed using $5 \text{ mM } [\text{Fe}(\text{CN})_6]^{3/4-}$ in 0.1 M NaOH over $0.01 - 100,000 \text{ Hz}$ with an amplitude of 5 mV . Information regarding the initial resistance (R_s) and the charge transfer resistance (R_{ct}) of the AuNP@oxi-BN-doped CNO GCE were obtained, which were slightly lower than those obtained at the AuNP/GCE. The capacitances were also obtained at each electrode. In each case the capacitances of the

AuNP and the AuNP@oxi-BN-doped CNO/GCEs were higher than that of the bare GCE as expected (**Table 5**) possibly due to the capacitive nature of the oxi-BN-doped CNOs used in the AuNP@oxi-BN-CNO/GCE.

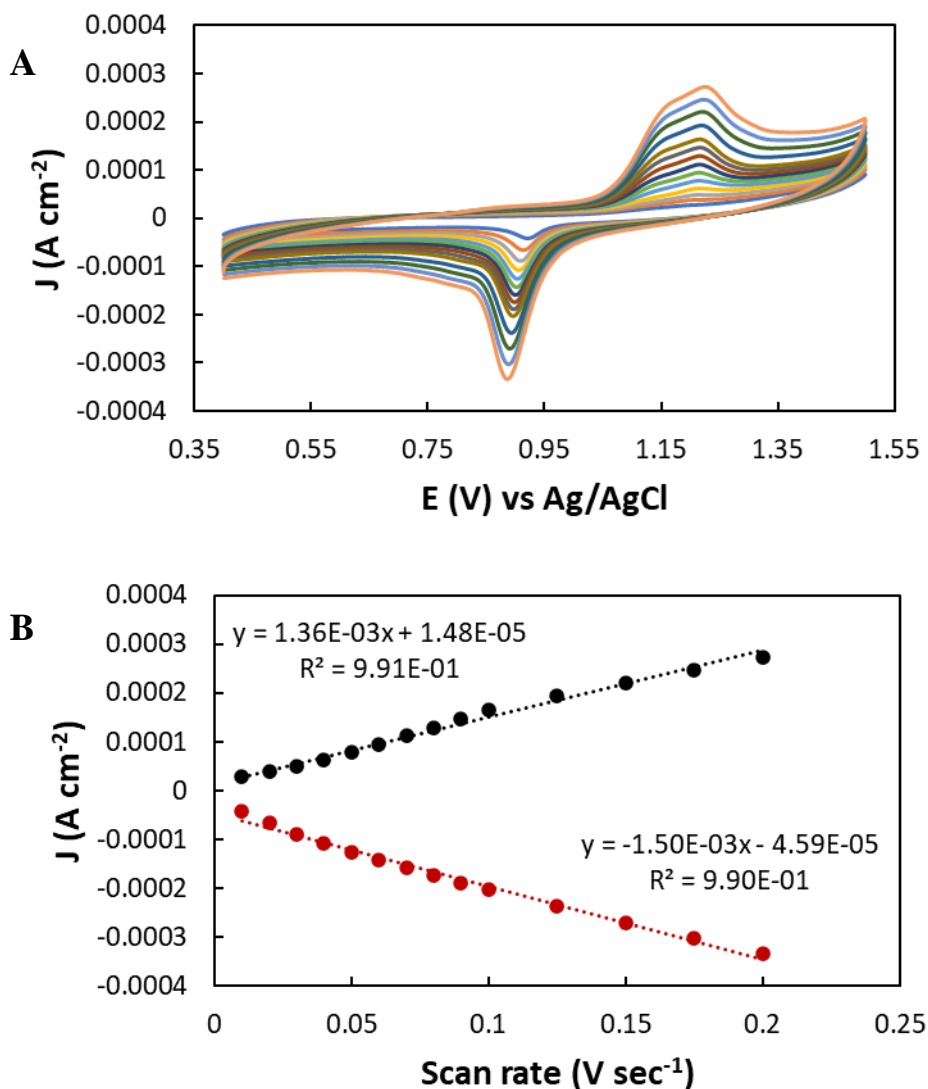
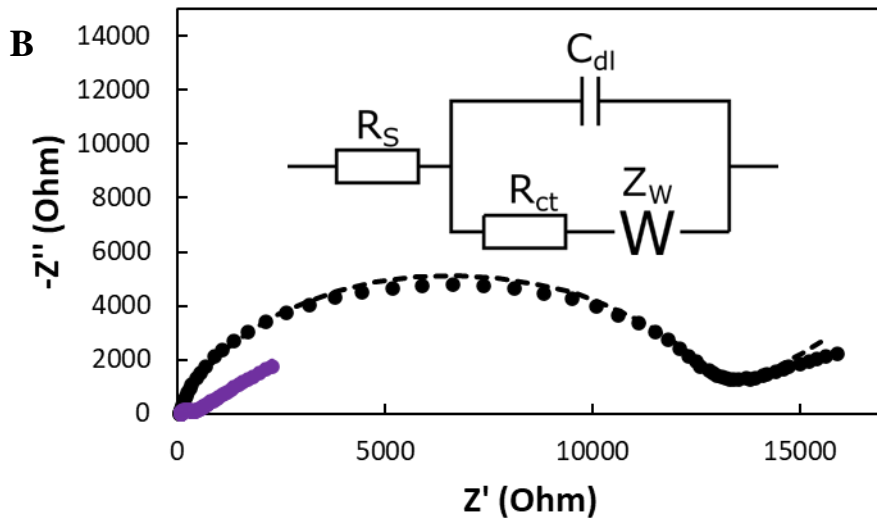
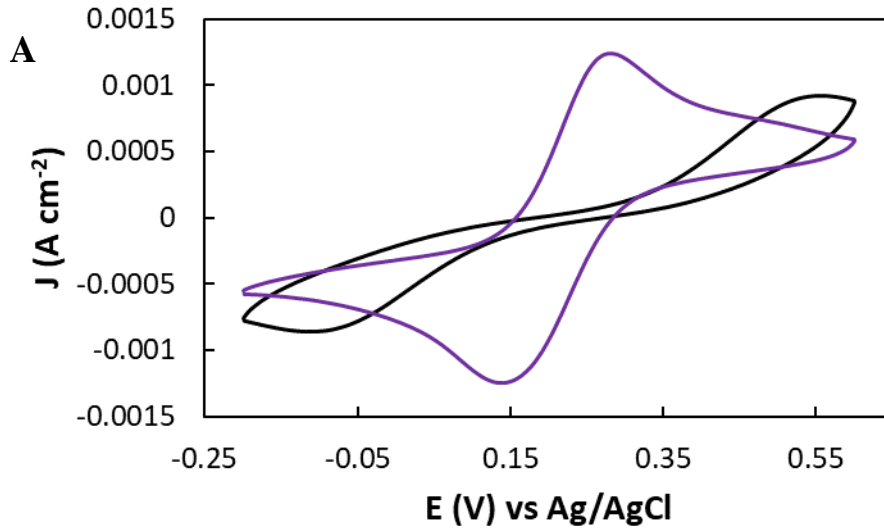


Figure 26 (A) Voltammetry of the AuNP@oxi-BN-doped CNO/GCE in 0.1 M H₂SO₄ from 0.4 – 1.5 V from 10 – 200 mV s⁻¹. (B) Plot of scan rate vs current density monitoring the anodic and cathodic faradaic Au responses of the AuNP@oxi-BN-doped CNO/GCE.



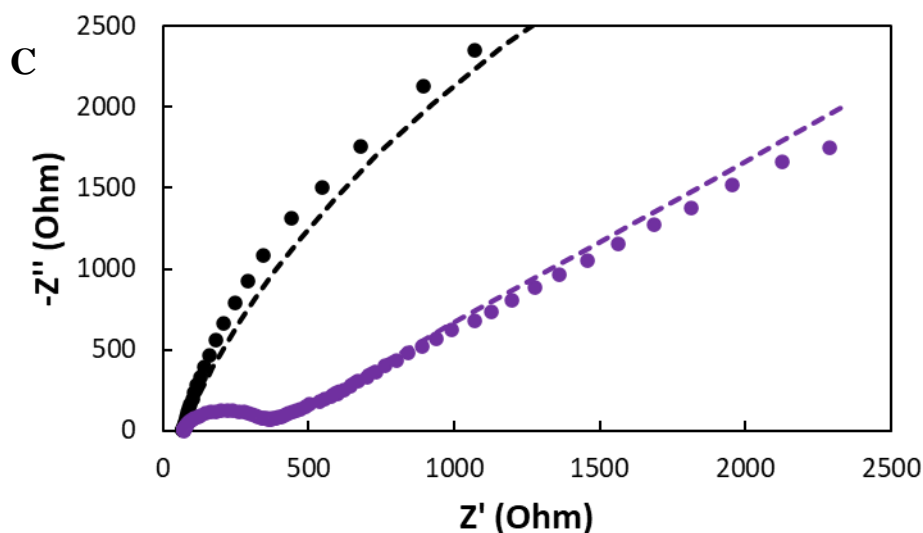


Figure 27 (A) Voltammetry of 5 mM [Fe(CN)₆]^{3/4-} in 0.1 M NaOH at the bare (black) and AuNP@oxi-BN-doped CNO/GCE (purple) from -0.2 – 0.6 V at 100 mV s⁻¹. (B) Nyquist plot of the bare GCE (black) and the AuNP@oxi-BN-doped CNO/GCE (purple) in 5 mM [Fe(CN)₆]^{3/4-} in 0.1 M NaOH with ω from 0.01 – 100,000 Hz with an amplitude of 5 mV. Simulated EIS data is shown by the dashed line. E = 0.221 V and 0.209 V for the bare and AuNP@oxi-BN-doped CNO/GCEs, respectively. (C) Zoomed in image of the Nyquist plot highlighting the arc from the AuNP@oxi-BN-doped CNO/GCE.

From examining the Bode plots of the bare GCE and AuNP@oxi-BN-doped CNO/GCE (**Figure 28**), the stability of each electrode was demonstrated. Firstly, the Gain Margin of the AuNP@oxiBN-CNO-doped GCE was calculated as 2.19 Db (2.961 Db for the bare GCE), thus the positive values demonstrate the stability of both electrodes.

From examining the Bode plot in **Figure 28 (B)**, maximum phase was determined as -72.7°, and -35.9° for the bare GCE and AuNP@oxi-BN-doped CNO/GCE, respectively. The high phase angle indicates that the AuNP@oxi-BN-doped CNO/GCE displays some capacitive properties, however conductive properties are more prominent. This was also observed for the AuNP/GCE. The curve for the bare GCE occurs at a larger phase angle at lower frequencies, which suggests lower ionic permeability and therefore greater insulating properties of each of the Au modified GCEs, where the curve occurs at a lower phase angle and at higher frequencies.

The slope of the Bode magnitude plot (**Figure 28 (A)**) gives an indication on the resistance and capacitance of the electrode in question. The slope of the bare GCE was calculated as -0.83, and at higher frequencies it was calculated as 0.0414 at higher frequencies, thus demonstrating the capacitive behaviour of the bare GCE. For the AuNP/GCE, the slope was calculated to be -0.47, and -0.41 at higher frequencies, demonstrating the low capacitance of the CuF/GCE. These results support the highest capacitance of bare GCE followed by the AuNP/GCE.

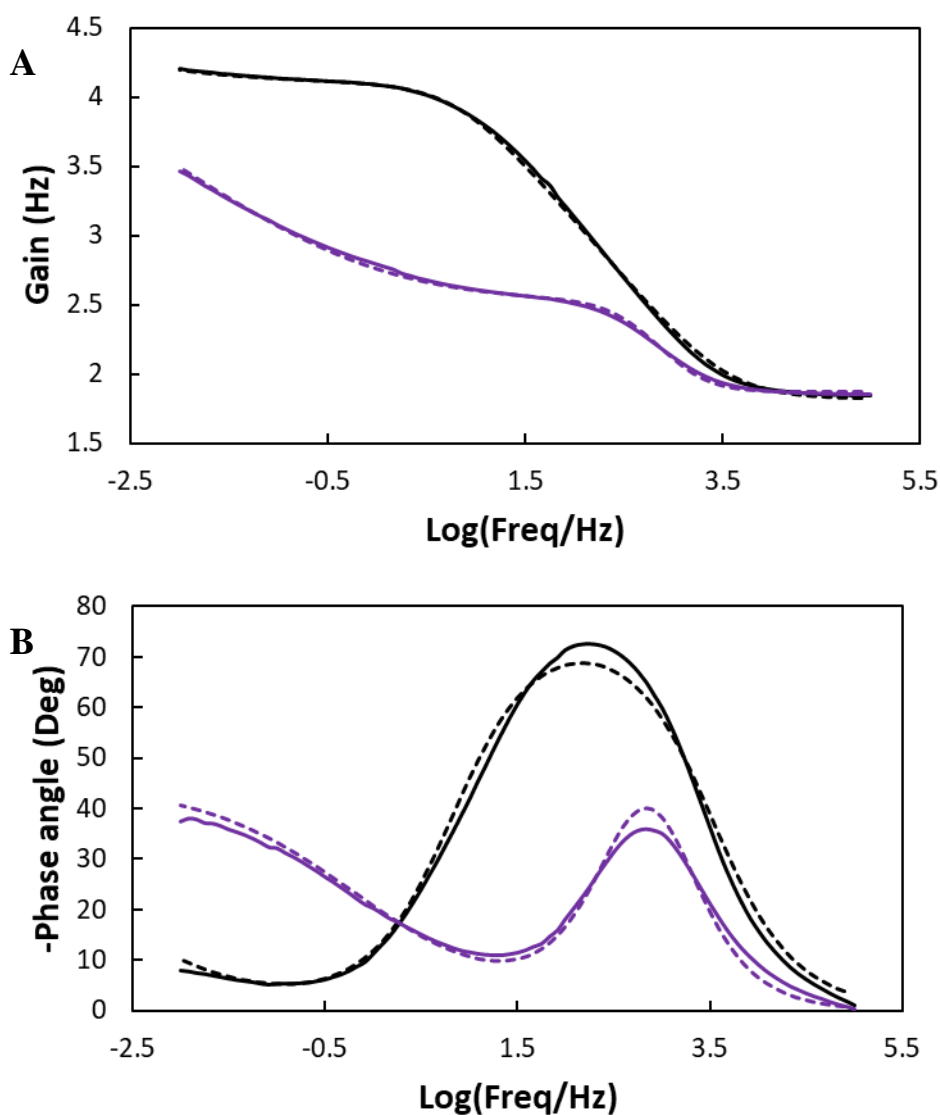


Figure 28. Corresponding experimental (solid lines) and simulated (dashed lines) Bode plots of the AuNP@oxi-BN-doped CNO/GCE (purple) and bare GCE (black) in 5 mM $[\text{Fe}(\text{CN})_6]^{3/4-}$ in 0.1 M NaOH with n from 0.01 – 100,000 Hz with an amplitude of 5 mV, where (**A**) shows the log of the frequency vs gain and (**B**) shows the log of the frequency vs the phase angle.

Table 8. Comparison of the peak heights and potentials of 5 mM [Fe(CN)₆]^{3/4-} at the bare and AuNP@oxi-BN-doped CNO/GCEs.

	$J_p(a)$ (A cm ⁻²)	$E_p(a)$ (V)	$J_p(c)$ (A cm ⁻²)	$E_p(c)$ (V)	ΔE_p (V)	$E_p(1/2)$ (V)	$J_p(a)/J_p(c)$
Bare GCE	8.61×10^{-4}	0.554	7.89×10^{-4}	-0.112	0.666	0.221	1.092
AuNP@oxi-BN-doped/GCE	1.17×10^{-3}	0.28	1.07×10^{-3}	0.137	0.143	0.209	1.094

Table 9. Comparison of the R_s , R_{ct} and capacitances obtained from the EIS spectra for both simulated and experimental data obtained at the bare and AuNP@oxi-BN-doped CNO/GCE.

	Bare GCE		AuNP@oxi-BN-doped CNO/GCE	
	Experimental	Simulation	Experimental	Simulation
R_s (Ohm)	69.30 ± 0.66	67.30 ± 0.77	70.72 ± 1.18	73.90 ± 0.89
R_{ct} (Ohm)	13560.70 ± 389.86	13662.64 ± 391.97	305.28 ± 17.22	304.10 ± 18.02
Capacitance (F)	$7.56 \pm 0.24 \times 10^{-7}$	$6.33 \pm 0.25 \times 10^{-7}$	$1.31 \pm \times 10^{-6}$	$1.74 \pm \times 10^{-6}$
Gain Margin (Db)	2.96 ± 0.03	2.95 ± 0.04	2.191 ± 0.03	2.226 ± 0.02
Phase Margin (°)	55.9 ± 1.1	59.1 ± 1.5	20 ± 1.3	22.8 ± 1.2

3.3.8. Surface analysis of the electrodeposited gold nanoparticles on oxi-BN doped carbon nano-onion modified electrodes

From examining the HR-SEM images of the AuNP@oxi-BN-CNO/GCEs, clear Au structures were visible on the GCE surface (**Figure 29 (A) – (D)**). The structures were dendritic, irregularly shaped coral-like gold structures with gold protrusions radiating from a central point. Unlike the AuNP/GCE, the AuNP@oxi-BN-CNOs appeared to be much larger in size and seemed to join up in chains and clusters, forming a network-like structure at the GCE surface. The larger size of the AuNP@oxi-BN-CNOs may have been due to more nucleation sites for AuNP seeding

to occur. The abundance of nucleation sites has increased for two main reasons: 1) the CNOs would allow for a larger electrode surface area, and so more Au could be electrodeposited onto this larger area; and 2) the oxi-BN-doped CNOs have negatively charged carboxylic acid functional groups on their surface, which would have an affinity for the positively charged Au^{3+} ions in solution, thus allowing for a larger quantity of Au to be electrodeposited resulting in the larger particle size. This also accounts for how the gold protrusions radiate from a central nucleation point, with an oxi-BN-doped CNO at its centre. The oxi-BN-CNOs that were initially drop-casted onto the GCE were not visible at the surface post AuNP electrodeposition due to the carboxylic acid functional groups having an affinity for the Au^{3+} ions, ensuring that all oxi-BN-doped-CNOs being covered in gold.

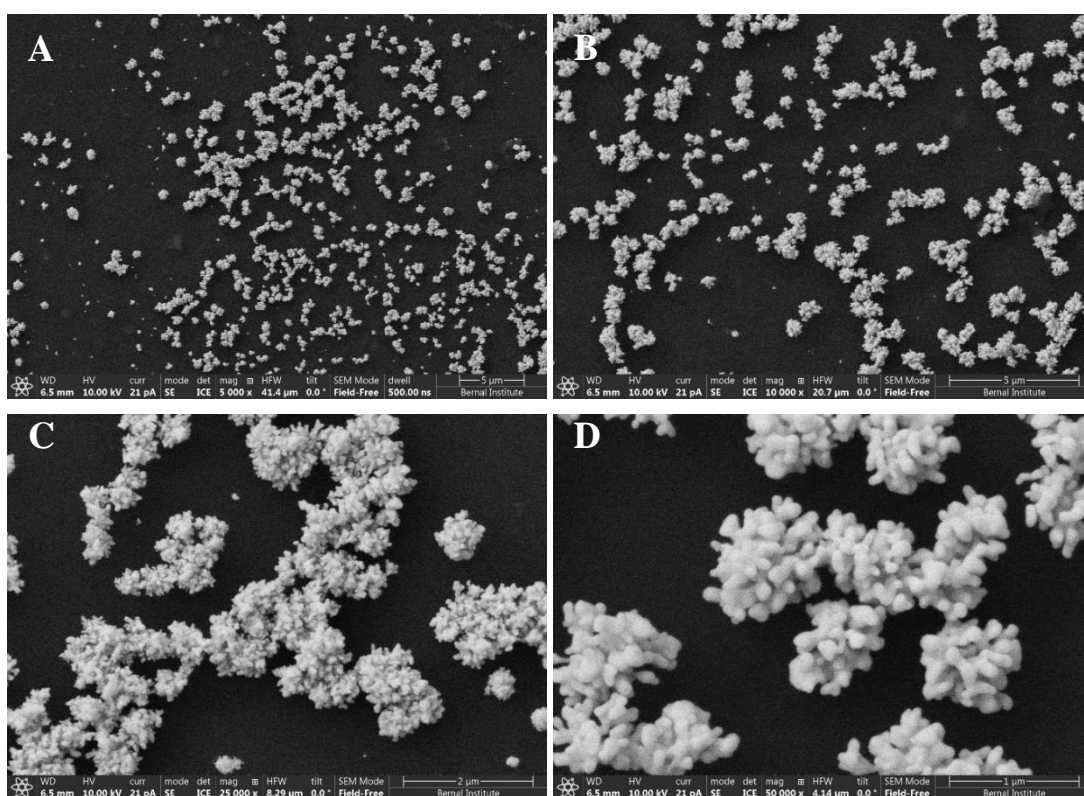


Figure 29. HR-SEM images of the AuNP@oxi-BN-CNO/GCE at 5,000 × (A), 10,000 × (B), 25,000 × (C) and 50,000 × (D) magnifications.

3.3.9. Electrochemical determination of N-acetyl-L-cysteine at the AuNP@oxi-BN-doped CNO modified GCE

Firstly, 1 mM NAC was examined by CV at the optimum AuNP@oxi-BN-doped CNO/GCE. A very clear NAC oxidative response was observed at 1.05 V vs

Ag/AgCl, as shown in **Figure 30**. It was also noteworthy that the Au reduction peak was suppressed in the presence of NAC. This was then studied over $10 - 200 \text{ mV s}^{-1}$ and from plotting the scan rate against the peak height, it was clearly deduced that the process was adsorption controlled. A clear dependence on scan rate was observed as there was a 144 mV anodic shift of the NAC oxidative process (**Figure 31 (A) – (C)**). The AuNP@oxi-BN-doped CNO/GCE was then cycled in 1 mM NAC (**Figure 32 (A)**) and the response was monitored in **Figure 32 (B)**, where the NAC oxidative signal decreased significantly during cycles 1 – 5. After this point the signal continued to decrease but to a much smaller degree. This may have been due to adsorption of NAC to the Au on the GCE surface, diminishing the amount of NAC that could access the electrode surface, thus lowering the NAC response. NAC was then calibrated using two supporting electrolytes, the first being in 0.1 M H_2SO_4 and secondly in 0.1 M sodium acetate buffer (pH 4.45). These calibration studies employed constant potential coulometry where $E_{\text{app}} = 1.15 \text{ V}$ for 5 s.

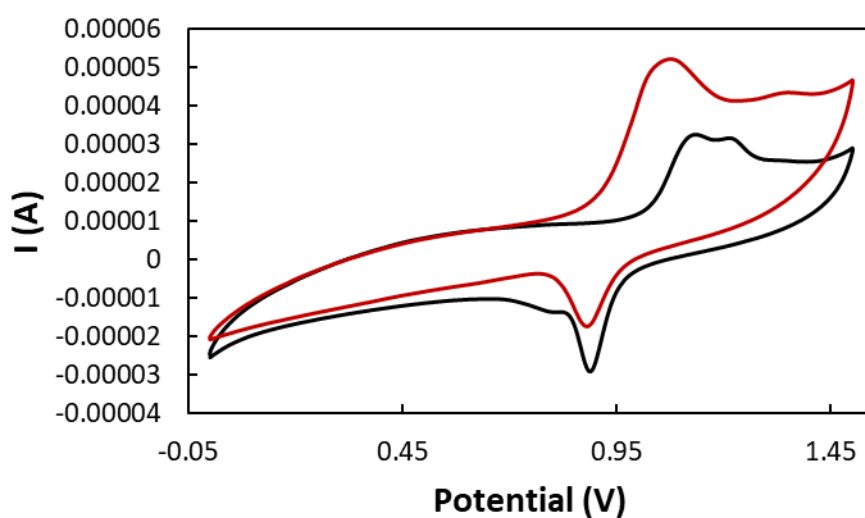
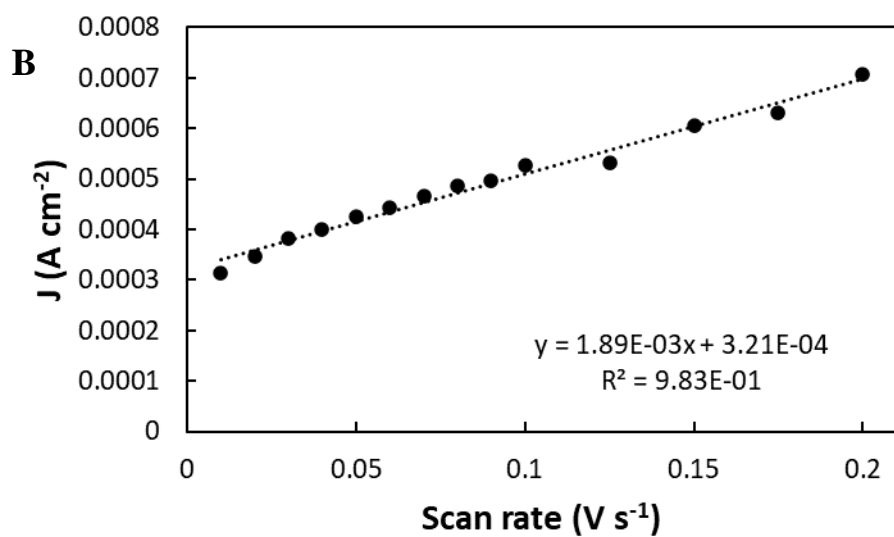
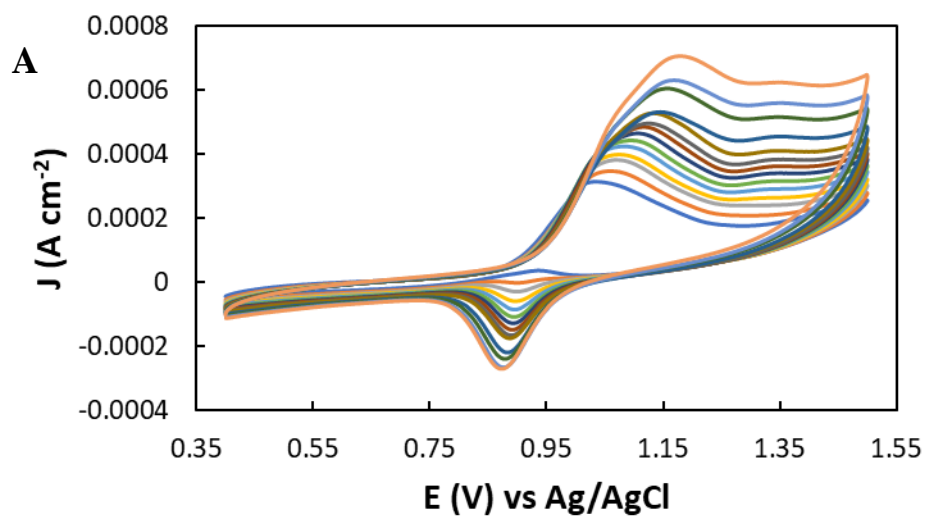


Figure 30. Voltammetry of 1 mM NAC (red) in 0.1 M H_2SO_4 (black) at the AuNP@oxi-BN-doped CNO/GCE from 0 – 1.5 V at 100 mV s^{-1} .



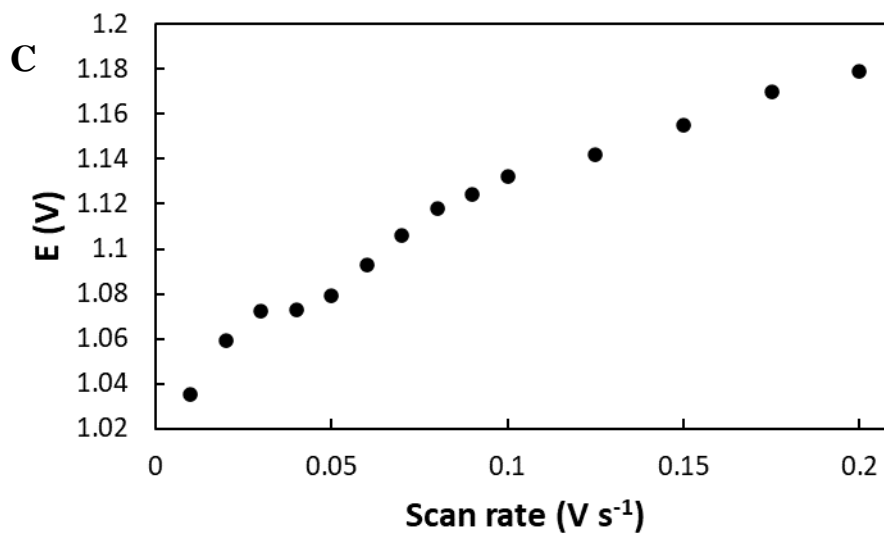


Figure 31 (A) Voltammetry of 1 mM NAC in 0.1 M H_2SO_4 at the AuNP@oxi-BN-doped CNO/GCE from 0.4 – 1.5 V at 100 mV s^{-1} . (B) Plot of the scan rate vs current density. (C) plot of the scan rate vs peak potential.

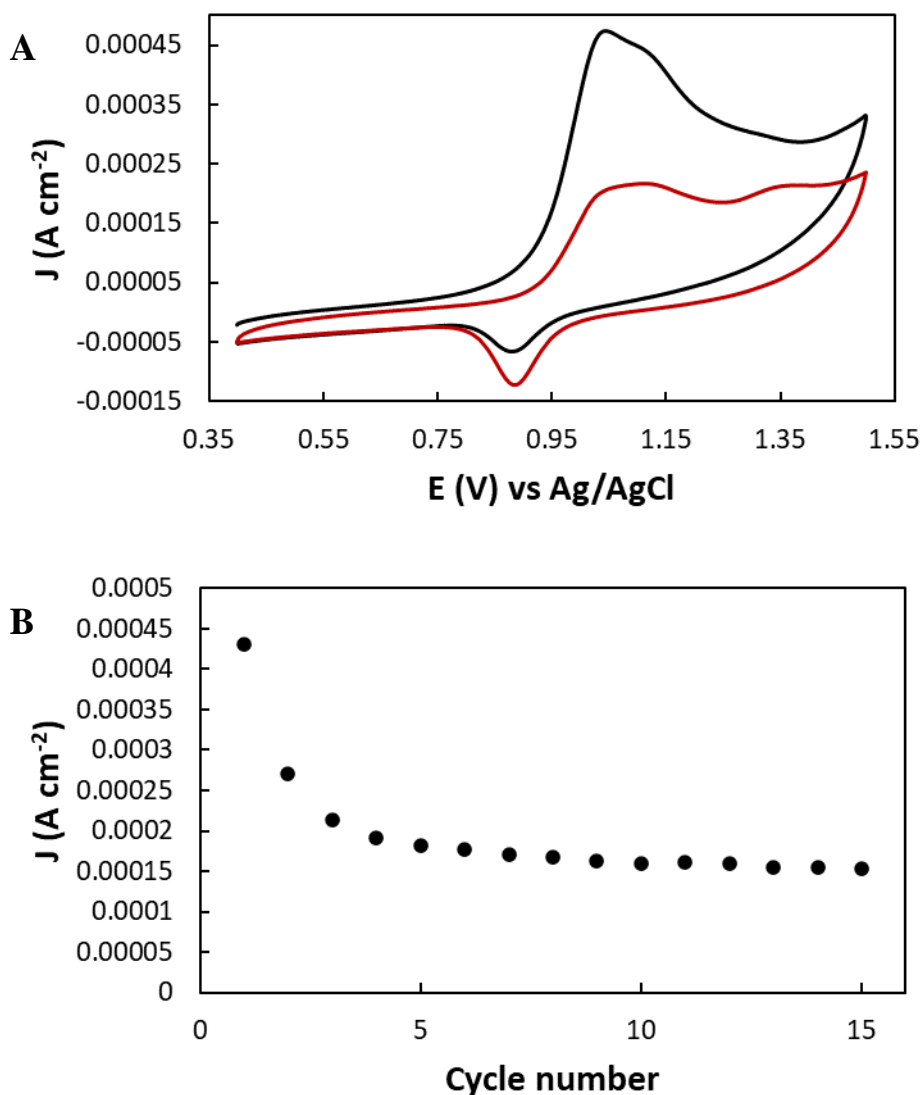


Figure 32 (A) Voltammetry of 1 mM NAC in 0.1 M H₂SO₄ at the AuNP@oxi-BN-doped CNO/GCE from 0.4 – 1.5 V at 100 mV s⁻¹ for 15 cycles, cycles 1 and 15 shown in black and red respectively. **(B)** Plot monitoring the NAC response over 15 cycles.

Firstly, NAC calibration studies were performed in H₂SO₄ at three electrodes in triplicate: at the bare AuE, the oxi-BN-doped GCE and at the AuNP@oxi-BN-doped CNO/GCE (**Figure 33 (A) – (B)**). The oxi-BN-doped CNO/GCE displayed the lowest sensitivity at $1.39 \pm 0.43 \times 10^{-4} \text{ Q cm}^{-2} \text{ mM}^{-1}$ ($n = 3$), followed by the bare AuE ($6.25 \pm 0.49 \times 10^{-4} \text{ Q cm}^{-2} \text{ mM}^{-1}$) ($n = 3$) and the AuNP@oxi-BN-doped CNO/GCE ($1.11 \pm 0.95 \times 10^{-3} \text{ Q cm}^{-2} \text{ mM}^{-1}$) ($n = 3$). Secondly, NAC calibration was performed at the oxi-BN-doped CNO and at the AuNP@oxi-BN-doped CNO/GCEs in 0.1 M sodium acetate buffer (pH 4.45) (**Figure 34 (A) – (B)**). The oxi-BN-doped CNO/GCE yielded a sensitivity of $8.18 \pm 1.64 \times 10^{-5} \text{ Q cm}^{-2} \text{ mM}^{-1}$ while the AuNP@oxi-BN-

doped CNO/GCE resulted in sensitivity of $4.76 \pm 0.126 \times 10^{-4} \text{ Q cm}^{-2} \text{ mM}^{-1}$. There was an overall 6-fold increase in sensitivity at the AuNP@oxi-BN-doped CNO/GCE relative to the oxi-BN-doped CNO/GCE.

In both cases the AuNP@oxi-BN-doped CNO/GCE yielded the highest sensitivity. Although the sensitivity was higher in the 0.1 M H₂SO₄, the sensor in the sodium acetate buffer solution was chosen as the background electrolyte in order to avoid the more acidic conditions. The limit of detection (LOD) and (LOQ) values were then calculated as follows:

$$LOD = \frac{3 \times \sigma (\mu\text{C cm}^{-2} \text{ mM}^{-1})}{\text{Sensitivity } (\mu\text{C cm}^{-2} \text{ mM}^{-1})} \dots\dots\dots(5)$$

$$LOQ = \frac{10 \times \sigma (\mu\text{C cm}^{-2} \text{ mM}^{-1})}{\text{Sensitivity } (\mu\text{C cm}^{-2} \text{ mM}^{-1})} \dots\dots\dots(6)$$

This resulted in LOD of $50.5 \pm 0.13 \text{ }\mu\text{M}$ for the AuNP@oxi-BN-doped CNO/GCE while $774 \pm 90.93 \text{ }\mu\text{M}$ was estimated in the case of the the oxi-BN-doped CNO/GCE, indicating that the AuNP@oxi-BN-doped CNO/GCE can detect NAC at concentrations 15.33 times lower than the oxi-BN-doped CNO/GCE. The LOQ value was also significantly lower at the AuNP@oxi-BN-doped CNO/GCE at $168 \pm 0.44 \text{ }\mu\text{M}$ (LOQ = $2,581 \pm 303 \text{ }\mu\text{M}$ for the the oxi-BN-doped CNO/GCE), indicating that NAC can be quantified 15.36 times lower than at the oxi-BN-doped CNO/GCE using this electroanalytical technique (comparison of sensitivities, LOD and LOQ values for the AuNP@oxi-BN-doped CNO/GCE and oxi-BN-doped CNO/GCE shown in **Table 10**).

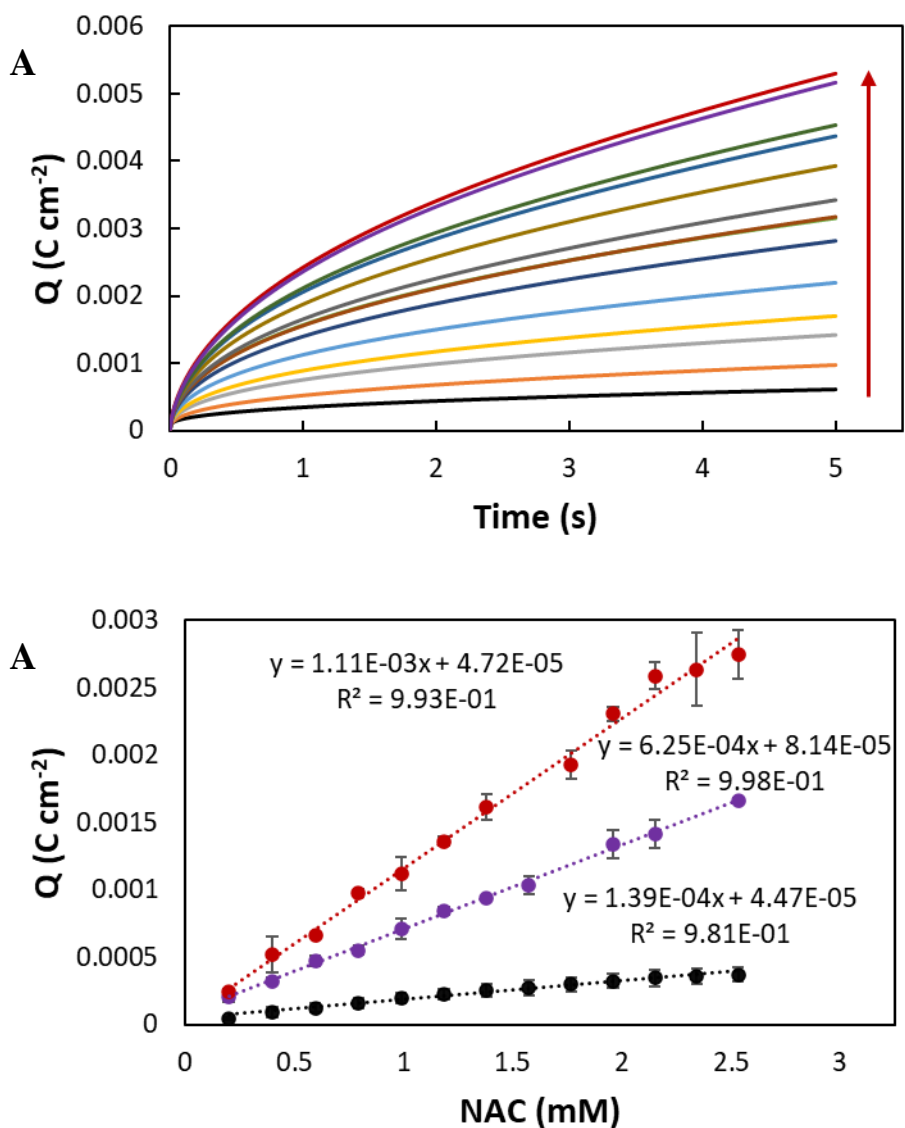


Figure 33 (A) Coulometry of 0.199 – 2.53 mM NAC in 0.1 M H₂SO₄ at the AuNP@oxi-BN-doped CNO/ GCE **(B)** Corresponding calibrations of 0.199 – 2.53 mM NAC in 0.1 M H₂SO₄ at the oxi-BN-doped CNO (black) AuNP@oxi-BN-doped CNO (red) modified GCE and bare AuE (purple) with E = 1.15 V for 5 s. (n = 3)

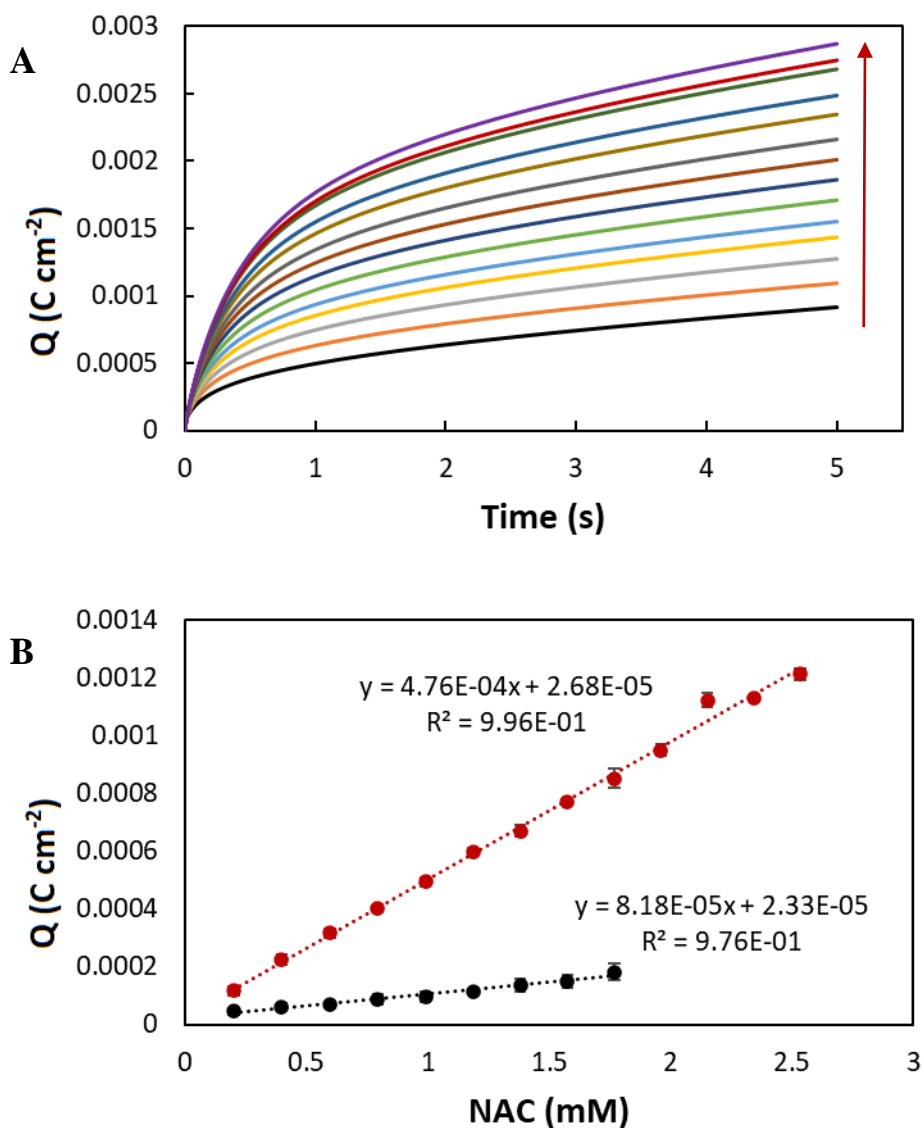


Figure 34 (A) Coulometry of 0.199 – 2.53 mM NAC in 0.1 M sodium acetate buffer (pH 4.45) at the AuNP@oxi-BN-doped CNO/GCE (B) Corresponding calibrations of 0.199 – 2.53 mM NAC in 0.1 M acetate buffer (pH 4.45) at the oxi-BN-doped CNO (black) and the AuNP@oxi-BN-doped CNO (red) modified GCE with $E = 1.15\ V$ for 5 s. ($n = 3$)

Table 10. Comparison of the sensitivities, LOD's and LOQ's of the oxi-BN-doped CNO modified GCE and the AuNP@oxi-BN-doped CNO/GCE in 0.1 M sodium acetate buffer (pH 4.45)

Electrode	Sensitivity ($\mu\text{C cm}^{-2} \text{ mM}^{-1}$)	LOD (μM)	LOQ (μM)
oxi-BN-doped CNO/GCE	81.8 \pm 16.4	774.0 \pm 90.93	2581.0 \pm 303
AuNP@oxi-BN-doped CNO/GCE	476.0 \pm 12.6	50.5 \pm 0.13	168 \pm 0.44

3.3.1.0. N-acetyl-L-cysteine sample analysis

Tablets containing 600 mg NAC were analysed where NAC was extracted such that the resulting solutions contained 1 mM and 2 mM NAC. The samples were analysed using coulometry via standard addition of 0.1 M NAC (**Figure 35 (A)**). The resulting calibration curve was then plotted (**Figure 35 (B)**) and the NAC concentration was calculated by allowing $y = 0$. Each sample was carried out in triplicate under the same conditions. The resulting sample recoveries was between 89.14 – 108.85 % with percentage variability between 2.66 – 10.07 %.

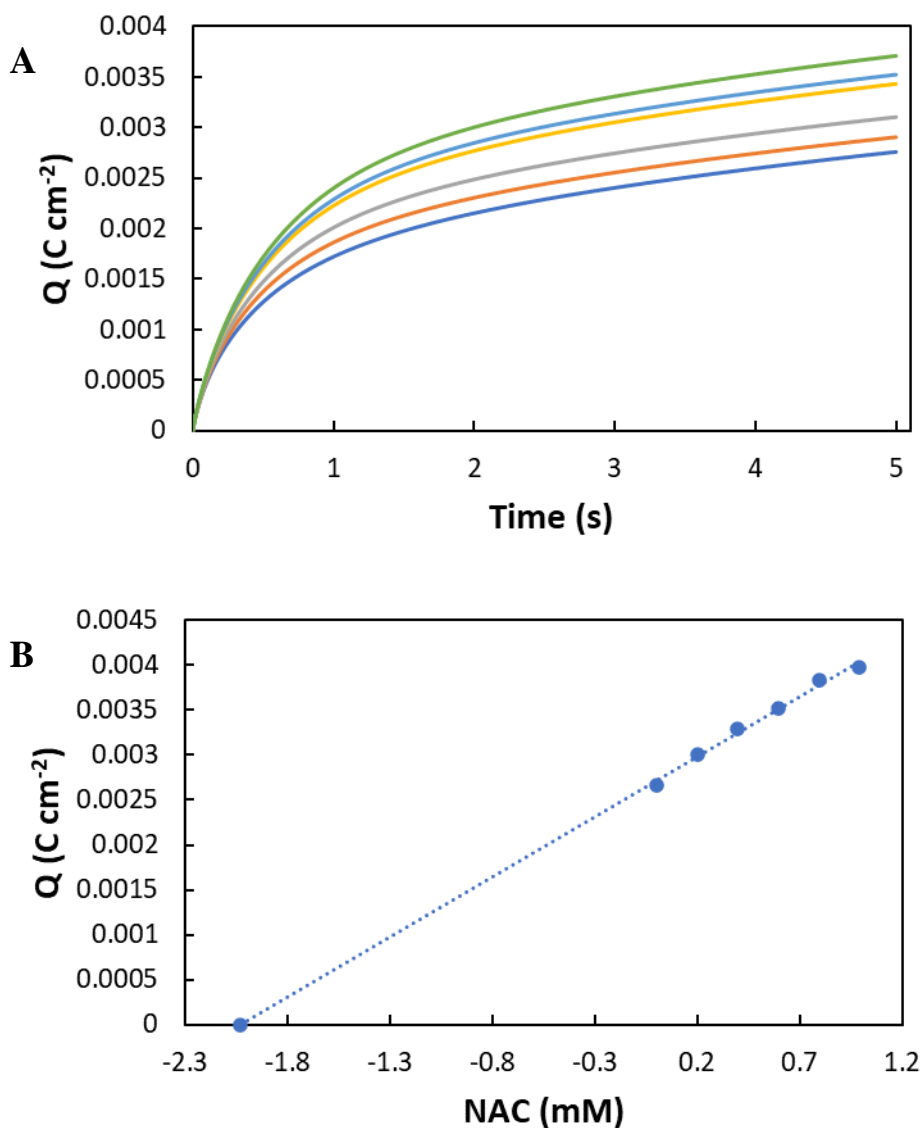


Figure 35 (A) Coulometry of an NAC sample (blue) with 5 subsequent additions of a 0.1 M NAC standard in 0.1 M sodium acetate buffer (pH 4.45) at the AuNP@oxi-BN-doped CNO/GCE (B) Corresponding plot showing the NAC concentration series, where the sample concentration was observed where $y = 0$. ($n = 3$)

Table 11. NAC sample analysis showing the expected NAC concentration, the NAC recovered and the % recovery of samples 1 – 5.

Sample number	Expected NAC concentration (mM)	NAC recovered (mM)	% Recovery of NAC
1	1.97	1.982	100.63 ± 9.66
2	1.979	1.764	89.14 ± 10.07
3	2.0248	2.0017	98.86 ± 2.66
4	0.99	0.971	98.05 ± 3.89
5	1.0125	1.071	105.85 ± 7.47

3.4.0. Conclusions

In conclusion, NAC was initially investigated at a bare GCE and AuE, where the proton dependant irreversible electro-oxidation process was investigated. From these investigations, the AuE showed the greatest NAC oxidative response and thus, led to investigating the use of gold nanoparticles (AuNPs) in maximising this response. A multi-potentiostatic pulse technique using 1 mM HAuCl₄ in 0.1 M HCl was used in AuNP electrosynthesis. These were optimised by testing the resulting AuNPs with a 1 mM NAC standard and altering the electrodeposition parameters. Once the optimum conditions were identified, the optimum AuNPs were characterised using various electrochemical methods and techniques such as by using scan rate studies, redox probe analysis and electrochemical impedance spectroscopy. The combination of the AuNPs with CNOs were then investigated. Four CNO types, p-CNOs, BN-doped CNOs, oxi-CNOs and oxi-BN-doped CNOs, were firstly characterised with the aid of scan rate studies and redox probe analyses, where it was found that the cathodic response at each CNO was favoured. The electroactive surface areas were also analysed, where the oxi-CNOs were found to have the greatest electroactive surface area, while the BN-doped-CNOs had the lowest. Their capacitances were also estimated where the oxi-BN-doped CNOs displayed the highest capacitance and the p-CNOs had the lowest. The oxi-BN-doped CNOs were selected to be used with the AuNPs to give AuNP@oxi-BN-doped CNO/GCEs. While developing the sensor, different concentrations of CNOs were applied and the optimum sensor was identified by testing with NAC standards. The optimum AuNP@oxi-BN-doped CNO/GCE was then characterised with the aid of scan rate studies, redox probes, and electrochemical impedance spectroscopy. A NAC calibration was then obtained via coulometry in both 0.1 M H₂SO₄ and 0.1 M sodium acetate buffer (pH 4.45) with sensitivities $1.11 \times 10^{-3} \text{ Q cm}^{-2} \text{ mM}^{-1}$ and $4.76 \times 10^{-4} \text{ Q cm}^{-2} \text{ mM}^{-1}$, respectively. Although the signal was higher in the H₂SO₄, the calibration was more reproducible in the sodium acetate buffer and the standard deviation was much lower for each data point. NAC commercial samples were then analysed in 0.1 M sodium acetate buffer with a recovery of 89 – 105 % and combined standard deviation of 6.75 %.

3.5.0. References

1. Mokhtari, V.; Afsharian, P.; Shahhoseini, M.; Kalantar, S. M.; Moini, A., A Review on Various Uses of N-Acetyl Cysteine. *Cell Journal* **2016**, *19* (1), 11-17.
2. Elgindy, E. A.; El-Huseiny, A. M.; Mostafa, M. I.; Gaballah, A. M.; Ahmed, T. A., N-acetyl cysteine: could it be an effective adjuvant therapy in ICSI cycles? A preliminary study. *Reprod Biomed Online* **2010**, *20* (6), 789-96.
3. Gaucher, C.; Boudier, A.; Bonetti, J.; Clarot, I.; Leroy, P.; Parent, M., Glutathione: Antioxidant Properties Dedicated to Nanotechnologies. *Antioxidants (Basel)* **2018**, *7* (5).
4. Dilger, R. N.; Baker, D. H., Oral N-acetyl-l-cysteine is a safe and effective precursor of cysteine1. *Journal of Animal Science* **2007**, *85* (7), 1712-1718.
5. De Flora, S.; Balansky, R.; La Maestra, S., Rationale for the use of N-acetylcysteine in both prevention and adjuvant therapy of COVID-19. *FASEB J* **2020**, *34* (10), 13185-13193.
6. Barus, C.; Gros, P.; Comtat, M.; Daunes-Marion, S.; Tarrow, R., Electrochemical behaviour of N-acetyl-l-cysteine on gold electrode—A tentative reaction mechanism. *Electrochimica Acta* **2007**, *52* (28), 7978–7985.
7. Raoof, J. B.; Ojani, R.; Amiri-Aref, M.; Chekin, F., Catechol as an electrochemical indicator for voltammetric determination of N-acetyl-l-cysteine in aqueous media at the surface of carbon paste electrode. *Journal of Applied Electrochemistry* **2010**, *40* (7), 1357-1363.
8. Acelino Cardoso de Sá, L. L. P., Urquiza de Oliveira Bicalho, Devaney Ribeiro do Carmo, Determination of N-Acetylcysteine by Cyclic Voltammetry Using Modified Carbon Paste Electrode with Copper Nitroprusside Adsorbed on the 3–Aminopropylsilica. *International Journal of Electrochemical Science* **2011**, *6*, 3754 - 3767.
9. Mohamed Tunesi, M.; Soomro, R. A.; Ozturk, R., The in situ growth of CuO nanostructures on an ITO substrate and its application as a highly sensitive electrode for the electrochemical determination of N-acetyl-l-cysteine. *Journal of Materials Chemistry C* **2017**, *5* (10), 2708-2716.

10. Zhang, J.; Chang, Y.; Dong, C., Electrocatalytic oxidation and sensitive determination of N-acetyl-L-cysteine at cyclodextrin-carbon nanotubes modified glassy carbon electrode. *Surface Engineering and Applied Electrochemistry* **2015**, *51* (2), 111-117.
11. Kuyumcu Savan, E., Electrochemical determination of N-acetyl cysteine in the presence of acetaminophen at multi-walled carbon nanotubes and nafion modified sensor. *Sensors and Actuators B: Chemical* **2019**, *282*, 500-506.
12. Wang, L. H.; Huang, W. S., Electrochemical oxidation of cysteine at a film gold modified carbon fiber microelectrode its application in a flow-through voltammetric sensor. *Sensors (Basel)* **2012**, *12* (3), 3562-77.
13. Zare, H. R.; Chatraei, F., Preparation and electrochemical characteristics of electrodeposited acetaminophen on ruthenium oxide nanoparticles and its role as a sensor for simultaneous determination of ascorbic acid, dopamine and N-acetyl-L-cysteine. *Sensors and Actuators B: Chemical* **2011**, *160* (1), 1450-1457.
14. Sperling, R. A.; Gil P. R.; Zhang, F.; Zanella, M.; Parak, W. J., Biological applications of gold nanoparticles. *Chemical Science Reviews* **2008**, *37* (9), 1745–2140.
15. Wang, Y.; Zeiri, O.; Raula, M.; Le Ouay, B.; Stellacci, F.; Weinstock, I. A., Host-guest chemistry with water-soluble gold nanoparticle supraspheres. *Nat Nanotechnol* **2017**, *12* (2), 170-176.
16. Guin, S. K.; Parvathi, K.; Ambollikar, A. S.; Pillai, J. S.; Maity, D. K.; Kannan, S.; Aggarwal, S. K., An insight into the electrocatalysis of uranyl sulphate on gold nanoparticles modified glassy carbon electrode. *Electrochimica Acta* **2015**, *154*, 413-420.
17. Guin, S. K.; Pillai, J. S.; Ambollikar, A. S.; Saha, A.; Aggarwal, S. K., Template-free electrosynthesis of gold nanoparticles of controlled size dispersion for the determination of lead at ultratrace levels. *RSC Advances* **2013**, *3* (39).
18. Pingarrón, J. M.; Yáñez-Sedeño, P.; González-Cortés, A., Gold nanoparticle-based electrochemical biosensors. *Electrochimica Acta* **2008**, *53* (19), 5848-5866.
19. Kimling, J.; Maier, M.; Okenve, B.; Kotaidis, V.; Ballot, H.; Plech, A., Turkevich Method for Gold Nanoparticle Synthesis Revisited. *Journal of Physical Chemistry B*. **2006**, *110* (32), 15700-15707.

20. Verma, H. N.; Singh, P.; Chavan, R. M., Gold nanoparticle: synthesis and characterization. *Veterinary World* **2014**, *7* (2), 72-77.
21. Deraedt, C.; Salmon, L.; Gatard, S.; Ciganda, R.; Hernandez, R.; Ruiz, J.; Astruc, D., Sodium borohydride stabilizes very active gold nanoparticle catalysts. *Chem Commun (Camb)* **2014**, *50* (91), 14194-6.
22. Cioffi, N.; Colaianni, L.; Ieva, E.; Pilolli, R.; Ditaranto, N.; Angione, M. D.; Cotrone, S.; Buchholt, K.; Spetz, A. L.; Sabbatini, L.; Torsi, L., Electrosynthesis and characterization of gold nanoparticles for electronic capacitance sensing of pollutants. *Electrochimica Acta* **2011**, *56* (10), 3713-3720.
23. Yanilkin, V. V.; Nastapova, N. V.; Nasretdinova, G. R.; Fazleeva, R. R.; Osin, Y. N., Molecular oxygen as a mediator in the electrosynthesis of gold nanoparticles in DMF. *Electrochemistry Communications* **2016**, *69*, 36-40.
24. Yang, J.; Kim, S. H.; Kwak, S. K.; Song, H. K., Curvature-Induced Metal-Support Interaction of an Islands-by-Islands Composite of Platinum Catalyst and Carbon Nano-onion for Durable Oxygen Reduction. *ACS Appl Mater Interfaces* **2017**, *9* (28), 23302-23308.
25. Suryawanshi, S. R.; Kaware, V.; Chakravarty, D.; Walke, P. S.; More, M. A.; Joshi, K.; Rout, C. S.; Late, D. J., Pt-nanoparticle functionalized carbon nano-onions for ultra-high energy supercapacitors and enhanced field emission behaviour. *RSC Advances* **2015**, *5* (99), 80990-80997.
26. Lu, H.; Eggers, P. K.; Gibson, C. T.; Duan, X.; Lamb, R. N.; Raston, C. L.; Chua, H. T., Facile synthesis of electrochemically active Pt nanoparticle decorated carbon nano onions. *New Journal of Chemistry* **2015**, *39* (2), 915-920.
27. Bartelmess, J.; Quinn, S. J.; Giordani, S., Carbon nanomaterials: multi-functional agents for biomedical fluorescence and Raman imaging. *Chem Soc Rev* **2015**, *44* (14), 4672-98.
28. Plonska-Brzezinska, M. E.; Echegoyen, L., Carbon nano-onions for supercapacitor electrodes: recent developments and applications. *Journal of Materials Chemistry A* **2013**, *1* (44).
29. Zuaznabar-Gardona, J. C.; Frago, A., Electrochemistry of redox probes at thin films of carbon nano-onions produced by thermal annealing of nanodiamonds. *Electrochimica Acta* **2020**, 353.
30. Breczko, J.; Plonska-Brzezinska, M. E.; Echegoyen, L., Electrochemical oxidation and determination of dopamine in the presence of uric and ascorbic acids

using a carbon nano-onion and poly(diallyldimethylammonium chloride) composite. *Electrochimica Acta* **2012**, *72*, 61-67.

31. Thomas, M. P.; Wanninayake, N.; De Alwis Goonatilleke, M.; Kim, D. Y.; Guiton, B. S., Direct imaging of heteroatom dopants in catalytic carbon nano-onions. *Nanoscale* **2020**, *12* (10), 6144-6152.

32. Mohapatra, D.; Muhammad, O.; Sayed, M. S.; Parida, S.; Shim, J.-J., In situ nitrogen-doped carbon nano-onions for ultrahigh-rate asymmetric supercapacitor. *Electrochimica Acta* **2020**, *331*.

33. Mykhailiv, O.; Brzezinski, K.; Sulikowski, B.; Olejniczak, Z.; Gras, M.; Lota, G.; Molina-Ontoria, A.; Jakubczyk, M.; Echegoyen, L.; Plonska-Brzezinska, M. E., Boron-Doped Polygonal Carbon Nano-Onions: Synthesis and Applications in Electrochemical Energy Storage. *Chemistry* **2017**, *23* (29), 7132-7141.

34. Chmiola, J.; Yushin, G.; Gogotsi, Y.; Portet, C.; Simon, P.; Taberna, P. L., Anomalous Increase in Carbon Capacitance at Pore Sizes Less than 1 Nanometer. *American Association for the Advancement of Science* **2006**, *313* (5794), 1760-1763.

35. Bartelmeß, J.; Giordani, S., Carbon nano-onions (multi-layer fullerenes): chemistry and applications. *Beilstein J Nanotechnol* **2014**, *5*, 1980-98.

36. Hezard, T.; Fajerweg, K.; Evrard, D.; Collière, V.; Behra, P.; Gros, P., Gold nanoparticles electrodeposited on glassy carbon using cyclic voltammetry: Application to Hg(II) trace analysis. *Journal of Electroanalytical Chemistry* **2012**, *664*, 46-52.

37. Elgrishi, N.; Rountree, K. J.; McCarthy, B. D.; Rountree, E. S.; Eisenhart, T. T.; Dempsey, J. L., A Practical Beginner's Guide to Cyclic Voltammetry. *Journal of Chemical Education* **2017**, *95* (2), 197-206.

38. Xu, X.; Makaraviciute, A.; Pettersson, J.; Zhang, S.-L.; Nyholm, L.; Zhang, Z., Revisiting the factors influencing gold electrodes prepared using cyclic voltammetry. *Sensors and Actuators B: Chemical* **2019**, *283*, 146-153.

39. Laschuk, N. O.; Easton, E. B.; Zenkina, O. V., Reducing the resistance for the use of electrochemical impedance spectroscopy analysis in materials chemistry. *RSC Adv* **2021**, *11* (45), 27925-27936.

40. Moussa, G.; Matei Ghimbeu, C.; Taberna, P.-L.; Simon, P.; Vix-Guterl, C., Relationship between the carbon nano-onions (CNOs) surface chemistry/defects and their capacitance in aqueous and organic electrolytes. *Carbon* **2016**, *105*, 628-637.

41. Camisasca, A.; Sacco, A.; Brescia, R.; Giordani, S., Boron/Nitrogen-Codoped Carbon Nano-Onion Electrocatalysts for the Oxygen Reduction Reaction. *ACS Applied Nano Materials* **2018**, *1* (10), 5763-5773.
42. Mutuma, B. K.; Matsoso, B. J.; Momodu, D.; Oyedotun, K. O.; Coville, N. J.; Manyala, N., Deciphering the Structural, Textural, and Electrochemical Properties of Activated BN-Doped Spherical Carbons. *Nanomaterials (Basel)* **2019**, *9* (3).
43. Takagi, K.; Natsui, K.; Watanabe, T.; Einaga, Y., Increasing the Electric Double-Layer Capacitance in Boron-Doped Diamond Electrodes. *ChemElectroChem* **2019**, *6* (6), 1683-1687.
44. Liu, Y.; Kim, D. Y., Enhancement of Capacitance by Electrochemical Oxidation of Nanodiamond Derived Carbon Nano-Onions. *Electrochimica Acta* **2014**, *139*, 82-87.
45. Kim, J. Y.; Han, M. G.; Lien, M. B.; Magonov, S.; Zhu, Y.; George, H.; Norris, T. B.; Kotov, N. A., Dipole-like electrostatic asymmetry of gold nanorods. *Sci Adv* **2018**, *4* (2), e1700682.

Chapter 4: Conclusions and future work

Table of Contents

4.1.0. Conclusion.....202

4.2.0. Future Work205

4.3.0. Poster Presentations and Conferences Attended.....206

4.4.0. Manuscripts at Draft Stage207

4.5.0. Modules and Credits Gained.....208

4.1.0. Conclusion

In conclusion, this project expanded on the limited studies on the electrochemical determination of dexamethasone (DEX) and N-acetyl-L-cysteine (NAC), and the electrochemical characterisation of four novel types of carbon nano-ions (CNOs), which included p-CNOs, BN-doped-CNOs, oxi-CNOs and oxi-BN-doped CNOs with applications as electrode modifiers. The electrochemical synthesis of various metal nanoparticles was also investigated for the purpose of generating a sufficiently sensitive sensor for either DEX or NAC.

This work advanced the electrochemical understanding of DEX under a variety of conditions. Firstly, a non-aqueous system, which comprised of 0.1 M LiClO₄ in MeOH, was applied to quantify DEX, where an oxidative response was observed at 1.3 V vs Ag/Ag⁺. The diffusion-controlled nature of this electrochemical oxidation process was demonstrated with the aid of a scan rate study. This anodic process was monitored at a bare GCE over the range 0.83 – 3.07 mM, which resulted in a sensitivity of $5.42 \times 10^2 \mu\text{A cm}^{-2} \text{mM}^{-1}$ and $R^2 = 0.998$. DEX was then examined at an unmodified GCE under alkaline conditions (0.1 M NaOH), where a distinct reduction signal was observed at -1.54 V vs Ag/AgCl, where with the aid of a scan rate study, the diffusion-adsorption controlled behaviour was demonstrated. DEX quantitation was achieved over the range 0.0781 – 5 mM with sensitivity of $2.78 \times 10^1 \mu\text{A cm}^{-2} \text{mM}^{-1}$ at an unmodified electrode (reduction process monitored). Optimum electro-synthesised copper film modified GCE were formed through a dual pulse potentiostatic method, where two oxidation processes at $E_{(a)} = -0.1 \text{ V}$ and -0.4 V vs. Ag/AgCl and two reduction processes at $E_{(c)} = -0.35 \text{ V}$ and -0.8 V vs. Ag/AgCl were observed respectively, resulting in surface coverage values in the range $3.492 - 2.065 \times 10^{-9} \text{ mol cm}^{-2}$. Electrosynthesis of optimised CuMP/GCE using a triple pulse potentiostatic approach was also investigated, which resulted in two oxidation and two reduction processes resulting in surface coverage values within the range $1.69 - 6.32 \times 10^{-9} \text{ mol cm}^{-2}$. The optimum CuMPs and CuF were then characterised using a variety of electrochemical methods, scan rate studies, redox probe analysis and electrochemical impedance spectroscopy (EIS). When investigating the electrochemical behaviour of DEX at each Cu nanostructure modified GCE, an anodic shift in the cathodic response was observed accompanied by a second reduction process on the return cycle, which has been attributed to the dimerisation of two adjacent DEX molecules adsorbed to

the Cu surface. A quantitative study was then carried out via CV over 0.0781 – 5 mM at both Cu nanostructure modified GCEs, which resulted in sensitivities of $2.00 \times 10^2 \mu\text{A cm}^{-2} \text{mM}^{-1}$ and $1.13 \times 10^2 \mu\text{A cm}^{-2} \text{mM}^{-1}$ for the CuF and CuMP modified GCEs respectively. With the CuF/GCE identified as the optimum electrode, DEX was extracted from a tablet sample made in house, which resulted in a recovery of 77.46 – 87.91 %, with a 1.93 – 4.97 % variance between each sample.

Secondly, electrochemical investigations into N-acetyl-L-cysteine (NAC) were carried out with the overarching goal to achieve a highly sensitive electrochemical sensor to be used in NAC quantitative applications. Initially, NAC was investigated via CV at an unmodified GCE and AuE, demonstrating the irreversible proton-dependant electro-oxidation process. This was carried out in various electrolyte solutions, where the acidic media was shown to be most favourable, and in each case the AuE produced the greatest NAC response. This led onto investigations where gold nanoparticles (AuNPs) would be exploited to maximise the NAC oxidative response. A multi-potentiostatic pulse technique using 1 mM HAuCl_4 in 0.1 M HCl was employed for the electrodeposition of uniformly sized AuNPs. Optimisation was carried out through alteration of the electrodeposition parameters followed by testing the resulting AuNPs with 1 mM NAC standard. The optimum AuNPs were then characterised using a variety of electrochemical methods, scan rate studies, redox probe analysis and electrochemical impedance spectroscopy (EIS). The AuNPs were then combined with the use of CNOs to help increase the NAC response further. Firstly, four CNO types, p-CNOs, BN-doped CNOs, oxi-CNOs and oxi-BN-doped CNOs, were characterised using scan rate studies, chronoamperometry (CA) and redox probe analysis, where the cathodic response was favoured at each CNO. The electroactive areas were estimated via CA, and the oxi-CNOs were shown to have the greatest electroactive area, whereas the BN-doped-CNOs had the lowest. Estimation of their capacitances was also performed where the oxi-BN-doped CNOs displayed the highest capacitance and the p-CNOs had the lowest. The oxi-BN-doped CNOs were then selected to be used in combination with the AuNPs, resulting in AuNP@oxi-BN-doped CNO/GCEs. Different CNO concentrations were investigated in development of this sensor, and each resulting sensor was then tested with a 1 mM NAC standard. The optimum AuNP@oxi-BN-doped CNO/GCE was then characterised with the aid of scan rate studies, redox probes, and electrochemical

impedance spectroscopy. A NAC calibration was then carried out via coulometry in H_2SO_4 and 0.1 M sodium acetate buffer with sensitivities $1.11 \times 10^{-3} \text{ Q cm}^{-2} \text{ mM}^{-1}$ and $4.76 \times 10^{-4} \text{ Q cm}^{-2} \text{ mM}^{-1}$, respectively. Despite the higher sensitivity obtained in the H_2SO_4 , there was a large standard deviation between each point, whereas in the sodium acetate buffer, the standard deviation was much lower for each data point. The more reproducible calibration in the sodium acetate buffer was then used to analyse NAC commercial samples, where a sample recovery of $89 - 105 \% \pm 6.75 \%$ was obtained.

4.2.0. Future Work

Going forward, future work could extend to further surface characterisation of the optimal electrodeposited CuF and CuMPs. DEX electroanalysis could also be carried out using DPV and constant pulse methodologies with the view to examine co-analysis potential with respect to related and interfering molecules. Cu modified GCEs could be extended to the electrochemical determination of other compounds, with the aim to develop highly sensitive sensors that can be applied to the analysis of alternative pharmaceutical and wastewater samples. Alternatively, the combination of CuMPs with other nanomaterials, such as CNOs, or CNTs, would potentially change the morphology of the resulting Cu materials. These resulting nanomaterials could then be used in the quantitation of other compounds.

Similarly, the AuNPs and AuNP@oxi-BN-doped CNO/GCE could be characterised further and applied to the quantitation of other compounds that contain thiol groups, such as D-penicillamine. An investigation into the combination of electrodeposited AuNPs with other CNMs could also be investigated in terms of their morphology and effectiveness in the quantitation of NAC and other thiol-containing drugs. Finally, interference studies could be established AuNP@oxi-BN-doped CNO/GCE to assess the selectivity and overall performance of the sensor.

Overall, there is huge potential for the development of high performance electrochemical sensors to quantitatively analyse therapeutic small molecules, biomarkers, drug samples, pollutants and contaminants in water, where samples can be analysed quickly and efficiently, where future work investigating their selectivity will ensure the reliability of such electrochemical sensors.

4.3.0. Poster Presentations and Conferences Attended

- Attended European Cooperation in Science and Technology Action ASAP 10 – 11th February 2021
- “Electroanalysis of small molecule therapeutics relevant to COVID-19” ISE/RSC Electrochemistry Irish Meeting for Early Career Researchers, 27th May 2021
- “Dexamethasone Electroanalysis at Copper Nanoparticle Modified Electrodes formed using a Potentiostatic Triple Pulse Sequence” 240th ECS meeting, 11th October 2021
- “Dexamethasone Electroanalysis at Copper Particle Modified Electrodes formed using a Potentiostatic Dual-Pulse Sequence” SCI Electrochem Postgraduate Conference, Loughborough University, The United Kingdom, 25th May 2022
- “Dexamethasone Electroanalysis at Copper Particle Modified Electrodes formed using a Potentiostatic Dual-Pulse Sequence” 73rd Irish Universities Chemistry Colloquium, UCD, Ireland, 15 – 16th June 2022

4.4.0. Manuscripts at Draft Stage

1. *Dexamethasone Electroanalysis at Copper Particle Modified Electrodes with Pharmaceutical Sample Analysis*, E. Murphy, S.K. Guin, E. Dempsey, in preparation for submission to *Electroanalysis*.
2. *Electrochemical Sensing of N-acetyl cysteine at Nanogold Modified Electrodes*, E. Murphy, S.K. Guin, E. Dempsey, in preparation for submission to *The Analyst*.

4.5.0. Modules and Credits Gained

Code	Module Title	Credits
CH801	Core Skills and Research Techniques in Chemistry	5
CH803	Teaching Skills in Chemistry	5
FM808	Seminar Series	5
GST1	Professional Development and Employability	5
	Total Credits = 20	